

1-1-2014

Combustion Visualization And Particulate Matter Emission Of A Gdi Engine By Using Gasoline And E85

Po-I Lee
Wayne State University,

Follow this and additional works at: http://digitalcommons.wayne.edu/oa_dissertations



Part of the [Other Mechanical Engineering Commons](#)

Recommended Citation

Lee, Po-I, "Combustion Visualization And Particulate Matter Emission Of A Gdi Engine By Using Gasoline And E85" (2014). *Wayne State University Dissertations*. Paper 897.

This Open Access Dissertation is brought to you for free and open access by DigitalCommons@WayneState. It has been accepted for inclusion in Wayne State University Dissertations by an authorized administrator of DigitalCommons@WayneState.

**COMBUSTION VISUALIZATION AND PARTICULATE MATTER EMISSION OF A
GDI ENGINE BY USING GASOLINE AND E85**

by

PO-I LEE

DISSERTATION

Submitted to the Graduate School

of Wayne State University,

Detroit, Michigan

in partial fulfillment for the requirements

for the degree of

DOCTOR OF PHILOSOPHY

2014

MAJOR: MECHANICAL ENGINEERING

Approved by:

Advisor

Date

DEDICATION

To my wife, Yanning, and my sons, Isaac and Randy

ACKNOWLEDGEMENTS

I would like to give my deepest gratitude to my academic advisor, Dr. Ming-Chia Lai, as his invaluable guidance and support were irreplaceable for the progress of this research work. In addition, I am also thankful to my committee members, Dr. Naeim Henein, Dr. Trilochan Singh, Dr. Marcis Jansons, and Dr. Catherine Lebiedzki, for their suggestions and contributions.

The assistance provided from my former and current Wayne State University colleagues, Dr. Xingbin Xie, Dr. Amy Peterson, Dr. Atsushi Matsumoto, Dr. Yi Zheng, Dr. Kan Zha, Mr. Xin Yu, Mr. Ziliang Zheng, Mr. Xiaoce Feng, Mr. Fengkun Wang, Mr. Xi Luo, and Mr. Jinqiao Wang, are also acknowledged as well as the help on machining by Mr. Eugene Snowden and Mr. Marvin Santure. Dr. Simon Ng, Dr. Haiying Tang, and Mr. Craig DiMaggio (currently at Chrysler) in Chemical Engineering and Dr. Chang Liu in Computer Science have also greatly assisted this work.

Special thanks to Mr. Nick Polcyn at Denso North America for lending the equipment; otherwise, most of the current work could not have been accomplished. Also, the support from Delphi, Mr. Keith Confer, Mr. Wayne Moore, and Mr. Matt Foster is greatly appreciated. Mr. Rick Davis and Mr. Ed Groff from GM are also acknowledged for the engine support and presentation invitation. Besides that, I am thankful to my current Chrysler colleagues, Mr. Rick Collins, Mr. Tim Ponkowski, Mr. Dennis Soltis, and Mr. Charles Allen III, for extending my research work.

Last but not least, I would like to thank for my family, my parents and especially, my wife, Dr. Yanning Wu, for the endless encouragement and support.

TABLE OF CONTENTS

Dedication.....	ii
Acknowledgements.....	iii
List of Tables	vii
List of Figures	viii
Nomenclature	xviii
CHAPTER 1 INTRODUCTION	1
1.1 Background.....	1
1.2 Scopes and Objectives of the Study	3
CHAPTER 2 LITERATURE REVIEW.....	6
2.1 Overview of Gasoline Direct Injection (GDI) Engines.....	6
2.2 Air-Fuel Mixing Process of GDI Engines	8
2.3 Combustion Process of GDI Engines.....	12
2.4 Optical Diagnostics of Flame Propagation in GDI Engines	17
2.5 Emissions in GDI Engines.....	20
2.5.1 CO and HC Emissions in GDI Engines.....	22
2.5.2 NO _x Emission in GDI Engines.....	24
2.5.3 PM Emission in GDI Engines with Optical Diagnostics.....	25
2.6 E85 in GDI Engines.....	29
2.7 3-D CFD Simulations GDI Engines	31

CHAPTER 3 STUDY METHODOLOGY AND EXPERIMENTAL SETUP	32
3.1 Fuel.....	32
3.2 Experimental Setup and Apparatus for Engine Testing.....	33
3.2.1 GDI Engine with Optical Access.....	33
3.2.2 Emission Measurement Equipment.....	55
3.3 Cameras and Imaging Process Methods	63
3.3.1 High Speed Camera - Color	63
3.3.2 High Speed Camera - Monochrome	67
3.3.3 Low Speed Camera - Spectrometer	70
3.3.4 Image Process Methods.....	72
3.5 CFD Simulation Setup - CONVERGE	81
CHAPTER 4 RESULTS AND DISCUSSIONS	84
4.1 Engine Start-up Flame Propagation	84
4.2 E0 and E85 on Flame Propagation	88
4.3 No-Valve and 1-Valve Deactivation (Intake) on Flame Propagation	95
4.4 Combustion Cycle-to-Cycle Variation and Flame Propagation.....	109
4.5 EGR Effect on Combustion	114
4.6 Engine Speed on Ignition Timing	117
4.7 Injection Timing Effect on Flame Propagation.....	109
4.8 Injection Timing and Ignition Timing on Pre-Ignition.....	132
4.9 Injection Timing Effect on PM Emission	144
4.10 Ignition Timing Effect on PM Emission	155

4.11 Air-Fuel Ratio Effect on PM Emission.....	164
4.12 Spark Energy on Combustion and Emission	171
CHAPTER 5 CONCLUSION	177
5.1 Summary of the Work.....	177
5.2 Recommendation and Future Work.....	182
Appendix A: Combustion Data.....	185
Appendix B: Injection Quantity Difference.....	190
Appendix C: Emission Data	191
Appendix D: Injection Measurement in RCM	197
Appendix E: Port Fuel Injection CNG Application	203
Appendix F: Ethanol-Biodiesel Application	205
Appendix G: CFD Data	214
References	216
Abstract.....	232
Autobiographical Statement.....	234

LIST OF TABLES

Table 3.1.1 Fuel properties of E0, E85, and ethanol.....	32
Table 3.2.1 sOAE specifications	37
Table 3.2.2 mOAE specifications	40
Table 4.7.1 WOT conditions and emissions (ST at 20° bTDC _{fire}).....	126
Table 4.7.2 Throttled conditions and emissions (ST at 20° bTDC _{fire})	127
Table 4.10.1 WOT conditions and emissions (SOI at 180° bTDC _{fire})	158
Table 4.10.2 Throttled conditions and emissions (SOI at 180° bTDC _{fire})	159
Table 4.11.1 WOT conditions (SOI at 300° bTDC _{fire} ; ST at 10° bTDC _{fire})	166
Table 4.11.2 WOT emissions (SOI at 300° bTDC _{fire} ; ST at 10° bTDC _{fire}).....	166
Table B-1 E0 injection quantity	190
Table B-2 E85 injection quantity	190
Table D-1 An example of spray measurement points for RCM test	202
Table F-1 Spray measurement testing matrix (constant volume chamber)	209
Table F-2 Setup of high speed camera.....	210
Table F-3 Diesel engine specification	212
Table F-4 Diesel engine test matrix	213

LIST OF FIGURES

Figure 2.1 Injector positions and types	10
Figure 2.2 Homogeneous charge and stratified charge	11
Figure 2.3 Otto cycle.....	13
Figure 2.4 AHRR curve of a GDI engine.....	15
Figure 2.5 MBF curve of a GDI engine	16
Figure 2.6 Emission formation locations	21
Figure 2.7 PM distribution	25
Figure 2.8 PM emission from different types of engines	26
Figure 2.9 Different locations of wall impingement for (a)early SOI and (b)late SOI in an optical accessible engine	28
Figure 2.10 Raw (left) and DPF (right) images of PM formation study.....	28
Figure 3.2.1 sOAE setup	
(a) different view angles of the sOAE.....	35
(b) no-valve deactivation	36
(c) one-valve deactivation	36
Figure 3.2.2 mOAE setup	
(a) high speed camera and LNG engine	38
(b) one-valve deactivation optical access.....	39
(c) side-mounted endoscope adaptor.....	39
Figure 3.2.3 sOAE devices	
(a) LabVIEW control board.....	43
(b) in-spark-plug pressure transducer	43
(c) MAP pressure transducer	44
(d) high pressure fuel tank (top) and regulator (bottom).....	45
(e) shop air pressure and flow gauges with EGR system.....	46

Figure 3.2.4 mOAE devices	
(a) MoTeC M800 ECU	49
(b) AND Redline CAS II.....	50
(c) NI PCI-6602 (for injection and camera control)	50
(d) Kistler 2613B encoder (top) and its outputs (bottom).....	51
(e) MoTeC Lambda sensor	52
(f) Kistler pressure amplifier and conditioner	52
(g) high pressure fuel tank	53
 Figure 3.2.5 Signals of mOAE (yellow: spark; purple: crankshaft; blue: intake camshaft)	 54
 Figure 3.2.6	
(a) MKS HS2030	57
(b) Dry air system.....	57
(c) Heated sampling line system	58
 Figure 3.2.7	
(a) TSI EEPS 3090 (left) and the cyclone (right)	60
(b) EEPS schematic	61
 Figure 3.2.8 TSI EEPS 3090 flow schematic	 62
 Figure 3.2.9 Dilution tunnel	 63
 Figure 3.3.1 Phantom V310 (color)	 65
 Figure 3.3.2 Spectral response of Phantom V310 (color) with V7.3 (monochrome)	 65
 Figure 3.3.3 Monochrom image from Phantom V310	 66
 Figure 3.3.4 Filter configuration of Phantom V310.....	 66
 Figure 3.3.5 Phantom V7.1 (monochrome).....	 67
 Figure 3.3.6 Spectral response of Phantom V7.1 (monochrome) with V310 (color) and intensifier	 68
 Figure 3.3.7 Intensifier	 69
 Figure 3.3.8 Spectral response of the intensifier.....	 69

Figure 3.3.9 PI-MAX2 with the spectrometer	70
Figure 3.3.10 Calibration spectra of the spectrometer	71
Figure 3.3.11 Method A illustration	73
Figure 3.4.12 Method B illustration	75
Figure 3.3.13 Method C illustration	77
Figure 3.3.14 Method D illustration	78
Figure 3.3.15 Method E illustration	80
Figure 3.4.1	
(a) sOAE piston with cylinder head	81
(b) mOAE piston.....	82
(c) combustion chamber.....	82
Figure 4.1.1	
(a) E0 combustion at 1 st cycle	85
(b) E0 combustion after 1 st cycle (5 th cycle shown)	86
Figure 4.1.2 E0 flame contours at 1 st cycle (left) and 5 th cycle (right)	87
Figure 4.1.3 E0 flame speed of the first six cycles (Y-axis normalized by the mean piston speed).....	87
Figure 4.2.1	
(a) E0 combustion after 1 st cycle (5 th cycle shown)	91
(b) Spectra of E0 combustion at TDC _{fire} and 15° aTDC _{fire}	92
Figure 4.2.2	
(a) E85 combustion (1 st cycle).....	93
(b) E85 combustion after 1 st cycle (5 th cycle shown)	94
Figure 4.3.1	
(a) No-valve deactivation (1 st cycle)	97
(b) One-valve deactivation (1 st cycle).....	98
Figure 4.3.2	
(a) No-valve deactivation flame development	100

(b) One-valve deactivation flame development	101
(c) One-valve deactivation flame development in mOAE (600 rpm; view from the deactivated intake valve).....	102
Figure 4.3.3	
(a) One-valve deactivation CFD simulation: local-rich zone is shown in red.....	104
(b) One-valve deactivation CFD simulation: local-rich zone is shown in red.....	105
(c) No-valve deactivation CFD simulation: no local-rich zone is shown ..	106
Figure 4.3.4	
(a) No-valve deactivation experiment v.s. simulation	107
(b) One-valve deactivation experiment v.s. simulation (the grey circle represents the deactivated intake valve)	108
Figure 4.4.1 $COV_{P_{cyl}}$ comparison of (a) motoring and (b) combustion	111
Figure 4.4.2 Method C cycle-to-cycle variation of flame propagation:	
(a) No-valve deactivation; ST 20° bTDC _{fire} (numbers in the corner represent ° aTDC _{fire}).....	112
(b) One-valve deactivation; ST 45° bTDC _{fire} (numbers in the corner represent ° aTDC _{fire}).....	113
Figure 4.5.1	
(a) EGR effect on in-cylinder pressure (lean)	115
(b) EGR effect on in-cylinder pressure (rich).....	115
Figure 4.5.2 (a, left) 10% EGR (rich); (b, right) 30% EGR (rich).	116
Figure 4.6.1	
(a) IMEP and COV_{IMEP} of ignition timing sweep (sOAE; 600 rpm)	120
(b) CA0-10 and CA10-90 of ignition timing sweep (sOAE; 600 rpm).....	120
Figure 4.6.2 Ignition timing: (a) 40° (b) 35° (c) 30° (d) 25° (e) 20° (f) 15° bTDC _{fire} (sOAE; 600 rpm)	121
Figure 4.6.3	
(a) IMEP and COV_{IMEP} of ignition timing sweep (mOAE; 1200 rpm)	122
(b) CA0-10 and CA10-90 of ignition timing sweep (mOAE; 1200 rpm) ..	122
Figure 4.6.4 Ignition timing: (a) 30° (b) 25° (c) 20° (d) 15° bTDC _{fire} (mOAE; 1200 rpm).....	123

Figure 4.7.1 Method D at different SOI (test condition: Throttled; Stoich; ST 20° bTDC _{fire})	
(a) SOI: 300° bTDC _{fire}	128
(b) SOI: 180° bTDC _{fire}	129
Figure 4.7.1 CFD v.s. Method E (test condition: Throttled; Stoich; ST 10° bTDC _{fire})	
(a) SOI: 300° bTDC _{fire}	130
(b) SOI: 180° bTDC _{fire}	131
Figure 4.8.1	
(a) Early injection (baseline; SOI 300° bTDC _{fire} ; ST 20° bTDC _{fire})	133
(b) Late injection (SOI 60° bTDC _{fire} ; ST 20° bTDC _{fire})	134
Figure 4.8.2	
(a) Late burn after a misfire cycle (SOI 60° bTDC _{fire} ; ST 20° bTDC _{fire})....	136
(b) Fast burn after a late burn cycle (SOI 60° bTDC _{fire} ; ST 20° bTDC _{fire})	137
Figure 4.8.3 Misfire, late burn, and pre-ignition pressure traces (consecutive cycles)	139
Figure 4.8.4 Pre-ignition v.s. normal pressure trace	140
Figure 4.8.5	
(a) Pre-ignition images	141
(b) Pre-ignition images (1° after ST).....	142
Figure 4.8.6 (a) E0 and (b) E85 pre-ignition pressure traces (out of 100 cycles) ...	143
Figure 4.9.1 Particle size distribution of (a) WOT and (b) Throttled conditions at different SOI [° bTDC _{fire}]	145
Figure 4.9.2 (a) Total concentration and (b) total mass of PM emission at different SOI [° bTDC _{fire}]	147
Figure 4.9.3 Raw and Method E images of E85 at different SOI: 300° bTDC _{fire} (left); 180° bTDC _{fire} (right) (numbers in the corner represent ° aTDC _{fire} ; test condition: Throttled; Stoich; ST 20° bTDC _{fire})	148
Figure 4.9.4 Raw and Method E images of E0 (left) and E85 (right; notice E85 images at different °) (numbers in the corner represent ° aTDC _{fire} ; test condition: WOT; Rich; ST 30° bTDC _{fire})	150

Figure 4.9.5 Particle size distribution of (a) E0 and (b) E85 at different SOI [$^{\circ}$ bTDC _{fire}]	152
Figure 4.9.6 (a) Total concentration and (b) total mass of PM emission at different SOI [$^{\circ}$ bTDC _{fire}]	153
Figure 4.9.7 Raw and Method E images of E0 (left) and E85 (right) with late injection timing (numbers in the corner represent $^{\circ}$ aTDC _{fire} ; test condition: Throttled; Stoich; SOI 60 $^{\circ}$ bTDC _{fire} ; ST 10 $^{\circ}$ bTDC _{fire})	154
Figure 4.10.1 (a) Total concentration and (b) total mass of PM emission at different ST [$^{\circ}$ bTDC _{fire}]	160
Figure 4.10.2 Particle size distribution: (a) WOT and (b) Throttled conditions at different ST [$^{\circ}$ bTDC _{fire}]	161
Figure 4.10.3 (a) Raw and Method E images of E0 (left) and E85 (right) (numbers in the corner represent $^{\circ}$ aTDC _{fire} ; test condition: WOT; Lean; SOI 180 $^{\circ}$ bTDC _{fire} ; ST 30 $^{\circ}$ bTDC _{fire})	162
(b) Raw and Method E images of E0 (left; enhanced due to low intensity) and E85 (right) (numbers in the corner represent $^{\circ}$ aTDC _{fire} ; test condition: WOT; Lean; SOI 180 $^{\circ}$ bTDC _{fire} ; ST 10 $^{\circ}$ bTDC _{fire})	163
Figure 4.11.1 (a) Total concentration and (b) total mass of PM emission at different lambda	167
Figure 4.11.2 Particle size distribution of (a) E0 and (b) E85 at different lambda ..	168
Figure 4.11.3 (a) Raw and Method E images of E0 (left) and E85 (right) (numbers in the corner represent $^{\circ}$ aTDC _{fire} ; test condition: WOT; Rich; SOI 300 $^{\circ}$ bTDC _{fire} ; ST 10 $^{\circ}$ bTDC _{fire})	169
(b) Raw and Method E images of E0 (left) and E85 (right) (numbers in the corner represent $^{\circ}$ aTDC _{fire} ; test condition: WOT; Lean; SOI 300 $^{\circ}$ bTDC _{fire} ; ST 10 $^{\circ}$ bTDC _{fire})	170
Figure 4.12.1 Spark energy on (a) IMEP	173
(b) COV _{IMEP}	173
(c) CA10-50	174
(d) CA50-90	174
(e) HC emission	175

Figure 4.12.2	
(a) Spark energy on flame kernel radius	175
(b) Flame kernel development with different spark energy	176
Figure A-1 IMEP of (a) WOT and (b) Throttled conditions	185
Figure A-2 COV_{IMEP} of (a) WOT and (b) Throttled conditions	186
Figure A-3 CA00-10 of (a) WOT and (b) Throttled conditions	187
Figure A-4 CA10-50 of (a) WOT and (b) Throttled conditions	188
Figure A-5 CA50-90 of (a) WOT and (b) Throttled conditions	189
Figure C-1 CO of (a) WOT and (b) Throttled conditions	191
Figure C-2 CO_2 of (a) WOT and (b) Throttled conditions	192
Figure C-3 HC of (a) WOT and (b) Throttled conditions	193
Figure C-4 Formaldehyde of (a) WOT and (b) Throttled conditions	194
Figure C-5 Acetaldehyde of (a) WOT and (b) Throttled conditions	195
Figure C-6 NO of (a) WOT and (b) Throttled conditions (NO ₂ is nominal)	196
Figure D-1 RCM schematic	197
Figure D-2 Combustion chamber schematic (top) and details (bottom)	198
Figure D-3 Schlieren optics setup	199
Figure D-4 RCM system	199
Figure D-5 Pressure trace of RCM	201
Figure D-6 Images at different test points (right after SOI)	202
Figure E-1 CNG tank (left) and injector (right)	203
Figure E-2 Particle size distribution of air, E0, and CNG	204

Figure F-1 Viscosity curve of different ethanol-biodiesel blending	206
Figure F-2 Densities of different ethanol-biodiesel blending	206
Figure F-3 Spray experiment setup schematic (constant volume chamber)	208
Figure F-4 Customized common rail fueling system	209
Figure F-5 Diesel engine setup schematic.....	211
Figure F-6 Example results	213
Figure G-1 Pressure traces and AHRR curves for (a) Fig. 4.7.2(a) and (b) Fig. 4.7.2(b).....	214
Figure G-2 CFD v.s. Method E (test condition: Throttled; Stoich; SOI 60° bTDC _{fire} ; ST 10° bTDC _{fire}).....	215
Figure G-3 Pressure traces and AHRR curves for Fig. G-2	215

NOMENCLATURE

AHRR	Apparent heat release rate
AMP	Accumulation mode particles
aTDC _{fire}	After the top dead center between the compression and the expansion strokes
BDC _{intake}	The bottom dead center after the intake stroke
BG ratio	The blue-green value ratio from the color camera spectra at certain wavelength
BR ratio	The blue-red value ratio from the color camera spectra at certain wavelength
bTDC _{fire}	Before the top dead center between the compression and the expansion strokes
CA50	The crank angle degree for 50% heat release
CA##-##	The crank angle degrees needed for ##% to ##% of fuel to be burnt
CAD or °	Crank angle degree
CAFÉ	Corporate average fuel economy
CAS	Combustion analysis system
CCD	Charge coupled device
CH	Carbon-hydrogen bond
CH ₄	Methane
CH ₂ O	Formaldehyde
CH ₃ CHO	Acetaldehyde

CMOS	Complementary metal-oxide semiconductor
CO	Carbon monoxide
CO ₂	Carbon dioxide
CNG	Compressed natural gas
DAQ	Data acquisition
DOHC	Dual overhead cam
E0	Pure gasoline
E85	85% ethanol and 15 % gasoline mixed volumetrically
E##B##	Volumetric percentage of ethanol and bio-diesel blending
EcoBoost	A turbocharged GDI engine family by Ford
ECU	Engine control unit
EEPS	Engine exhaust particle sizer
EGR	Exhaust gas recirculation
FID	Flame ionization detector
FPGA	Field-programmable gate array
FSI	Fuel stratified injection
FT-IR	Fourier-transform infrared
GDI	Gasoline direct injection
HC/THC	Hydrocarbons/total hydrocarbons
IMEP	Indicated mean effective pressure
KBr	Potassium bromide
KH-RT	Kelvin-Helmholtz and Rayleigh-Taylor
Lambda	Realistic air-fuel ratio / stoichiometric air-fuel ratio

Lean	Lean air-fuel ratio condition in the current work (λ ~1.15)
LES	Large eddy simulation
LNF	A type of engine by General Motor
LNT	Lean NO _x trap
LSPI	Low-speed pre-ignition
MAP	Manifold absolute pressure
MBF	Mass burnt fraction
mOAE	Production metal engine with optical access in the current work
OEM	Original equipment manufacturer
OH*	Hydroxyl radical
OHV	Overhead valve
P_{cyl}	In-cylinder pressure
PDF	Probability density function
PFI	Port fuel injection
PLIF	Planar laser induced fluorescence
PM	Particulate matter
PN	Particle number
ppm	Parts per million
RANS	Reynolds-averaged Navier-Stokes equations
RCM	Rapid compression machine
RGB	Red, green, and blue colors

rpm	revolution per minute
NMP	Nuclei mode particles
NO	Nitric oxide
NO ₂	Nitrogen dioxide
NO _x	Mono-nitrogen oxides
Rich	Rich air-fuel ratio condition in the current work (lambda ~0.9)
RON	Research octane number
SCR	Selective catalytic reduction
SOI	Start of injection
sOAE	Single-cylinder optically accessible engine in the current work
ST	Spark timing
Stoich	Stoichiometric air-fuel ratio condition in the current work (lambda ~1)
Throttled	Throttled condition in the current work (MAP ~0.5 bar)
UV	Ultra violet spectral range (10 nm to 400 nm)
VIPE	Variable ignition pattern equipment
VVT	Variable valve timing
WOT	Wide open throttle condition in the current work (MAP ~1 bar)

CHAPTER 1 INTRODUCTION

1.1 Background

Personal transportation has changed the ways of living for human beings in the world since last century. In 2010, it was reported that the total quantity of vehicles was over one billion globally, and the two-billion mark is predicted to be achieved around 2020 [1, 2]. The usage of petroleum-based fuel, such as gasoline and diesel, has also been increasing with the increment of passenger cars, light-duty trucks, and other vehicles. Nowadays, about 95% of energy for transportation comes from petroleum-based liquid fuels. Many researchers have suggested that such fuels still be the primary energy source in the future [3]. Moreover, it is also predicted that the energy utilization in 2040 could be 40% higher than the energy demand in 2010 [4-7]. Therefore, fuel economy and emission reduction of vehicle transportation are very important and have been the recent major research objectives in academia, industry, and governmental regulations. According to the data from the U.S. Environmental Protection Agency (EPA), more than 95% CO₂ emission is from burning petroleum-based fuels, and gasoline-fueled internal combustion engines are responsible for about 60% CO₂ emission in the U.S. The transportation is also responsible for the majority of CO and NO_x emissions [8]. In recent years, particulate matter (PM) emission has been studied extensively, and relative regulations have been proposed or applied, especially in Europe [9]. However, more detailed study on PM emission is still necessary due to some concerns and uncertainty in the current measurement method [10].

In order to comply with government emission regulations as well as to accomplish environment sustainability, researchers are focusing on increasing the thermal and fuel efficiency of engines as well as reducing engine-out or tailpipe-out emission. Optimizing engine combustion is always the challenge and essence in research and product development. In the past decade, gasoline-directed-injection (GDI) engines were popularized gradually due to its higher power density (with the usage of turbocharge or supercharge) and fuel efficiency (therefore, lower CO₂ emission) over conventional port-fuel-injection (PFI) gasoline engines. Furthermore, GDI engines also have the advantages of implementing advanced engine control strategies, such as stratified charge and lean-burn combustion, and possibly reducing or eliminating the throttle loss. However, engine control on GDI engines are more complicated, and more advanced technologies are required on them as well.

On the other hand, GDI engines have encountered many challenges. First of all, the air-fuel mixing preparation is critical to combustion quality since the fuel is injected directly into the cylinder with limited time to mix with air. Secondly, wall-wetting (fuel impingement on cylinder wall or piston top) is more serious also due to the directly injected fuel; therefore, unburned hydrocarbons (HC) and PM emissions may be higher. Thirdly, the air-fuel mixture may be overall lean due to the injection strategies, which means that the conventional three-way catalyst could not work well in the lean condition. Fourthly, knocking and pre-ignition are also the concerns in GDI engines, especially with the presence of turbocharger or supercharger.

Besides, advanced or complicated control strategies and technologies represent higher production cost.

Because of the limited resource of petroleum-based fuels, alternative energy has been in discussion in the past few decades. Many alternative fuels have been studied, and some are used in the percent. In gasoline engines, ethanol is deemed as the alternative fuel due to its availability, renewability, and gasoline-like properties. E85, 85% ethanol mixed with 15% gasoline in volume, is a common “Flexfuel” in the U.S., and 10% v/v of ethanol in gasoline is also a requirement by the U.S. government. Nonetheless, ethanol is also known for its lower energy content (LHV ~ 27 MJ/kg) that the fuel economy would decrease if such a fuel is used, and ethanol may also increase the potential of pre-ignition. In spite of that, lower HC, CO, NO_x, and PM emissions may be achieved with the presence of ethanol in fuel.

To investigate the combustion process in a GDI engine, optically accessible engines are often used in modern research to gain the “insight” of combustion. Along with high speed imaging techniques, detailed combustion could be captured by cameras for analysis. In addition, computational fluid dynamics (CFD) modeling also provides necessary information for researchers. With engine-out emission measurement, the analysis of GDI combustion process could be more in-depth.

1.2 Scopes and Objectives of the Study

The present study is focused on visualizing GDI combustion with different fuels (E0 and E85) along with engine-out emission measurement. Different engine operation conditions are taken into consideration to study the effects on engine performance in terms of engine start-up, combustion quality and variation, and

engine-out emission. High speed imaging techniques are used for visualizing the combustion process, and high speed emission measurement devices are used for engine-out emission study. PM emission is the primary focus in the current study on emissions with the assistance of in-cylinder visualization to identify the location of diffusion flame where the soot is formed. CFD modeling is also implemented to analyze the air-fuel mixture preparation as well as the combustion process.

Engine control parameters considered in the study are listed below:

- Fuel (E0 and E85)
- Injection timing (start of injection, SOI)
- Ignition timing (spark timing, ST)
- Air-fuel ratio (λ)
- Valve deactivation
- Exhaust gas recirculation (EGR)
- Spark energy

The literature review is described and discussed in Chapter 2 as GDI engines, GDI spray and wall impingement, GDI combustion strategies, and GDI emissions. Experiment results from previous research work are also mentioned. The review of alternative fuels used in the study is also included in the chapter as well as optical diagnostics and emission measurement.

Chapter 3 contains the study methodology. All experiment equipment and setup are addressed in this section. An optically accessible single-cylinder engine and a modified production engine are used with three different optical accesses. Two high speed cameras are used (color and monochrome) with an intensifier as

well as a spectrometer. Variable Ignition Pattern Equipment (VIPE) is used to generate different spark energy. A high speed Fourier-transform infrared (FT-IR) based gas analyzer and an Engine Exhaust Particle Sizer (EEPS) spectrometer are used for engine-out emission measurement.

The results are demonstrated and discussed in Chapter 4, and Chapter 5 concludes all the research work. The future work is also suggested at the end of the thesis, and some appendices are attached as well.

CHAPTER 2 LITERATURE REVIEW

2.1 Overview of Gasoline Direct Injection (GDI) Engines

As the proposal of the US government on Corporate Average Fuel Economy (CAFE) for cars and light-duty trucks by model year 2025, the fuel economy standard will be 54.5 miles per gallon. Therefore, more advanced engine technologies will have been applied in order to meet the regulation requirements. One of the new technologies is gasoline direct injection (GDI) engines. Since its debut in mass production in 1996, GDI engines have been considered as the next generation spark ignited engines to replace the conventional PFI engines [11]. In recent years, major automotive manufacturers have produced new vehicle models with such application. For example, Ford is predicting more than 90% of its global vehicle production equipped with its EcoBoost engine technology by 2013 [12].

The primary benefit of implementing GDI engine technology is to reduce throttle loss (pumping loss) and to obtain more precise air-fuel mixing process. The conventional PFI engines have the injectors mounted at the intake ports, and the fuel is injected at the same location with low injection pressure, which is normally around 3 to 5 bar [13]. Most fuel droplets vaporize and atomize before entering into the cylinder to create homogeneous air-fuel mixture. During the intake stroke, the mixture is breathed into the cylinder through the intake valves. Therefore, possible liquid fuel deposit is on the intake port surface and valves, which indicates some fuel would not enter the cylinder for combustion; thus, higher fuel consumption is expected. Moreover, the engine load is controlled by the throttle position that serious pumping loss will be inevitable. Unlike diesel engines, conventional PFI

gasoline engines are known that a part of the power output is consumed by the pumping loss, which also represents higher fuel consumption [14]. In addition to aforementioned drawbacks, PFI engines could only run in stoichiometric charge regime ($\lambda \sim 1$) because the fuel and air are mixed homogeneously prior to entering the cylinder. The stoichiometric condition is suitable for the three-way catalyst operation, but the stratified charge (or lean burn) strategy would not be applicable.

Unlike the conventional PFI engines, GDI engines have the injectors mounted either on the side of cylinder wall or on the top of the combustion chamber adjacent to the spark plug. The air-fuel mixing process is more like diesel engines. Since the fuel is injected into the cylinder, no liquid fuel would be wasted at the intake port to worsen the fuel economy. Throttle may also be eliminated with the usage of variable valve timing and lifts to control the air flow. Besides, precise injection control could be achieved that stratified charge (lean burn) combustion is feasible to improve fuel economy. Volkswagen is known for its FSI engines with the stratified charge application [15]. Homogeneous charge combustion is also doable in GDI engines with many advantages. Many researchers have indicated that power output of GDI engines in homogeneous mode could increase about 15% with the utilization of a turbocharger or supercharger. Fuel consumption may be up to 5% lower comparing to PFI engines [16, 17]. With early injection timing, usually at the beginning of intake valve opening, the fuel and air will have sufficient time to mix before the spark occurs. A significant benefit of GDI engines running homogeneous charge is the charge cooling effect [18]. The phenomenon is due to the fuel vaporization process

that the in-cylinder temperature decreases as the energy is absorbed to overcome the latent heat of vaporization of the liquid fuel; therefore, the volumetric efficiency of the engine is improved (since air density is higher at lower temperature), and the engine knocking possibility could be reduced due to lower peak temperature at the end of compression stroke.

2.2 Air-Fuel Mixing Process of GDI Engines

Unlike the homogeneous charge formed in a PFI engine, the air-fuel mixing process in a GDI engine is critical and will affect the ensuing combustion process and engine-out emission. Many studies have focused on GDI spray and air-fuel mixture preparation [13, 18, 19], and the process could be improved and optimized with advanced technologies, e.g. variable valve timing. Although such technologies have been applied on PFI engines, their influences are more significant on GDI ones.

Since the injection happens inside the engine cylinder, the flexibility of valvetrain is high in a GDI engine with high effectiveness on air flow regulation. Modern GDI engines have mostly 4 valves – 2 intake ones and 2 exhaust ones. The shape of the combustion chamber is often dome-shape or pent-roof type with center-mounted spark plug. Theoretically, a spherical shape combustion chamber would benefit the uniformity of flame propagation that more complete combustion may be achieved.

Variable valve timing (VVT) is a means to change the opening and close timing of the valves at different crank angle degree (CAD) with respect to the top

dead center between the exhaust stroke and intake one (TDC_{intake}). The sprockets on the camshafts are coupled with “phasers” that could be actuated by hydraulic mechanism or electrical device. The need of different valve timing is due to different engine speed and load that the air quantity needed for the optimal combustion varies. With the VVT application, engine volumetric efficiency could be maximized in a wide range. Moreover, negative valve overlap (NVO) is carried out with the technology that controlling internal exhaust gas recirculation (EGR) would be possible quantitatively [20].

In addition to VVT, variable valve lift, duration, and valve deactivation are also applicable in modern GDI engines [21-25]. With extra lobes attached on the camshafts, low valve lift and high valve lift are controlled; the different valve opening duration could be done with different lobe profiles. As for valve deactivation, one of the intake valves would stop working that the air is forced to enter the cylinder through the other one. Strong swirl motion is therefore created. Another method to achieve similar effect is positioning an extra “throttle” in one of the intake ports that the air is blocked when the throttle is closed. With the aforementioned valvetrain technology, engine performance will be enhanced and emission can be reduced due to lower pumping loss, higher volumetric efficiency, better air-fuel mixing process, controlled EGR effects, and more complete combustion.

The positions of the injector in the GDI engine are categorized in two ways: side-mounted and center-mounted. As directly explained by the names, a side-mounted injector is placed on the side of combustion chamber, usually in between the two intake valves; a center-mounted injector is located at the center of the

combustion chamber roof with the spark plug in the vicinity. Figure 2.1 illustrates the two positions of GDI injectors. Furthermore, injection from a side-mounted injector could be either wall-guided or air-guided dependent on the design of piston top that the air-fuel mixing process is assisted or directed by the piston top or by the in-cylinder air motion. A center-mounted injector is spray-guided that the fuel evaporates around the spark plug.

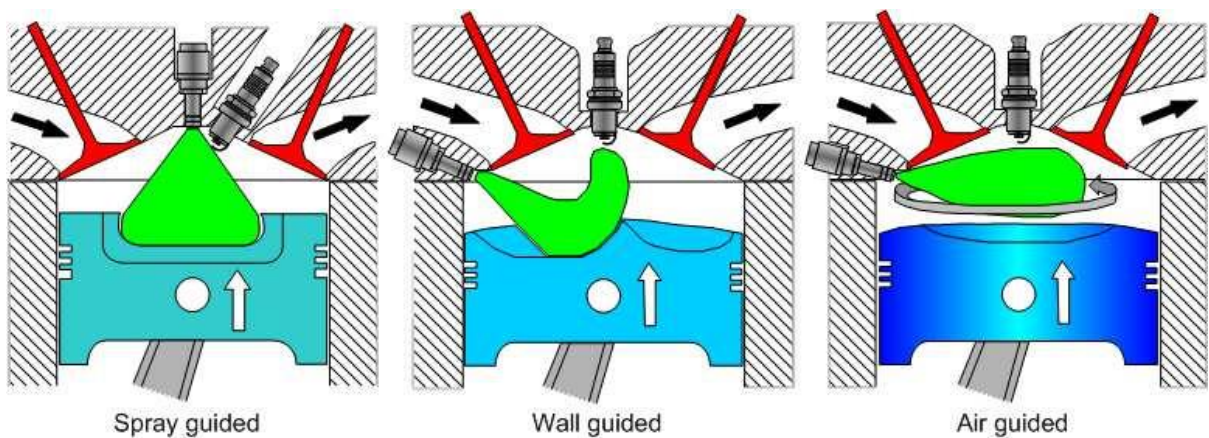


Figure 2.1 Injector position and injection types [26]

During the air-fuel mixture preparation, the charge is more homogeneous if the fuel is injected early ($\sim 300^\circ$ bTDC_{fire}); conversely, the charge is more heterogeneous or “stratified” if the injection is late ($\sim 60^\circ$ bTDC_{fire}). Homogeneous charge would represent uniform air-fuel mixture with air-fuel ratio is kept close to stoichiometry that all fuel atoms are assumed to have enough air in the surroundings. Once ignited by the spark plug, the mixture is burnt uniformly throughout the combustion chamber; so the combustion is considered more complete. Stratified charge is also known as lean burn, which the fuel is injected

near the firing TDC. With proper design of piston top to interact with air and fuel, the air-fuel ratio around the spark plug is richer and gets leaner farther away from the spark plug. The overall air-fuel ratio is lean so that less fuel injection is expected and therefore better fuel economy may be realized. Figure 2.2 shows the concept of these two charge types.

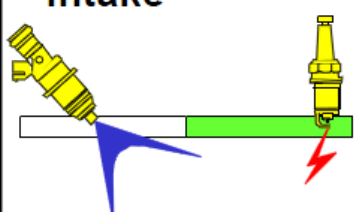
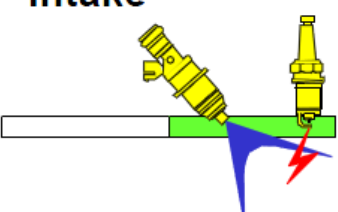
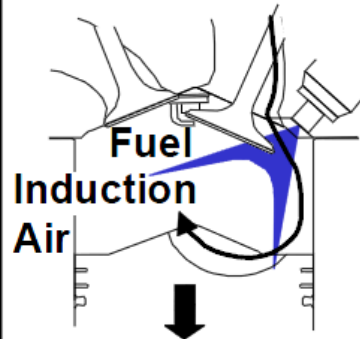
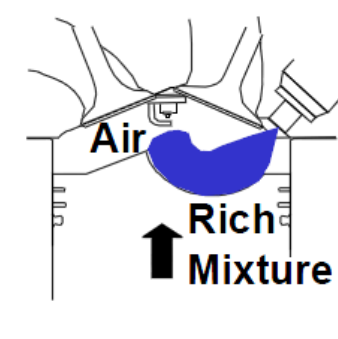
Mode	Homogeneous	Stratified Lean Burn
Injection Schedule	<p>Intake</p>  <p>Compression</p>	<p>Intake</p>  <p>Compression</p>
Mixing	 <p>Fuel Air Induction</p>	 <p>Air Rich Mixture</p>
A/F	12 - 14.7	> 24
Target	High Power	Fuel Economy

Figure 2.2 Homogeneous charge and stratified charge [27]

2.3 Combustion Process of GDI Engines

The combustion of a four-stroke spark-ignited engine is initiated by a “spark”, typically from a spark plug, to convert the chemical energy of the fuel to the mechanical work and heat. Thermodynamically, the conventional spark-ignited engines are Otto cycle, which is shown as the ideal Otto cycle P-V diagram in Fig. 2.3. In the figure, Process 2-3 is the constant volume combustion in which the energy is inputted [14]. Ideally, combustion is initiated and most fuel is burned in this period, where the piston is at the TDC position. However, the time from the spark, early flame kernel development, to rapid combustion is not infinitely short since the chemical reactions require certain durations to complete. Therefore, the control of spark timing, spark energy, and spark direction are very critical for the early flame kernel development as well as the ensuing combustion process besides the aforementioned air-fuel mixing process. As a result, a spark-ignited engine is commonly found with higher cycle-to-cycle variations than a compression-ignited engine [28, 29].

To study the cycle-to-cycle variations, the coefficient of variation (COV) of the in-cylinder pressure (P_{cyl}) or indicated mean effective pressure (IMEP) could be used to indicate the variability of the combustion [30]. IMEP is calculated by the work done by the piston over the cylinder displacement, which is shown in Eq. 2.1. The equation for COV calculation is listed in Eq. 2.2. In normal engine operation conditions, COV_{IMEP} should be no greater than 3% to be considered as acceptable combustion. During warm-up periods, less than 10% COV_{IMEP} would be accepted.

If COV_{IMEP} exceeds 10%, the driveability of the vehicle and combustion stability will be problematic [31].

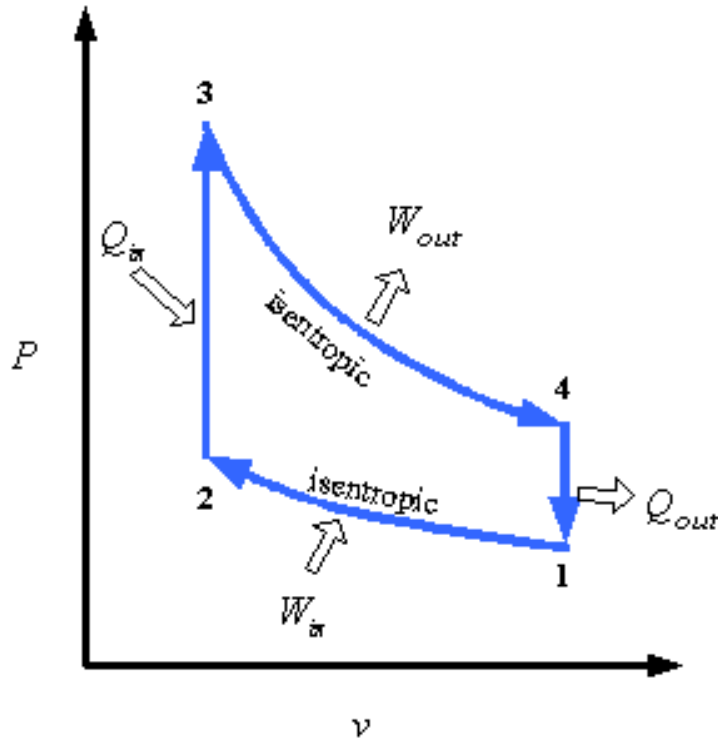


Figure 2.3 Otto cycle

- $IMEP = \frac{W_{C,E,i}}{V_d} = \frac{m_f Q_{LHV} \eta_{f,i}}{V_d}$ Equation 2.1

, where $W_{C,E,i}$ is the indicated work per cycle calculated from the summation of the work in the compression stroke and that in the expansion stroke; V_d is the total displacement volume; m_f is the mass of injected fuel in one cycle; Q_{LHV} is the lower heating value of the fuel; $\eta_{f,i}$ is the indicated fuel conversion efficiency

$$\bullet \quad COV_{IMEP} = \frac{\sigma_{IMEP}}{\mu_{IMEP}} \times 100 = \frac{\left(\frac{1}{n-1} \sum_{i=1}^{i=n} (IMEP_i - \mu_{IMEP})^2\right)^{1/2}}{\mu_{IMEP}} \times 100 \quad \text{Equation 2.2}$$

, where σ_{IMEP} is the standard deviation of the IMEP of the n samples; μ_{IMEP} is the mean IMEP of the n samples; $IMEP_i$ is the i^{th} IMEP of the n samples

The indicated work from Eq. 2.1 is done by the piston and can be calculated from Eq. 2.3 with respect to crank angle degree (CAD).

$$\bullet \quad \frac{dW_{C,E,i}}{d\theta} = \frac{\gamma}{\gamma-1} P_{cyl} \frac{dV}{d\theta} \quad \text{Equation 2.3}$$

, where θ is the crank angle degree; γ is the ratio of specific heats; P_{cyl} is the measured in-cylinder pressure

During combustion, the chemical energy stored in the fuel is released and converted to work on the piston and heat transferred through the combustion chamber wall and coolant. From the measured pressure traces, one could calculate the apparent heat release rate (AHRR) curves by Eq. 2.4. One example of AHRR curve is shown in Fig. 2.4, where two distinguishable regions are seen and denoted. Most energy is released in Region (1), which is also known as the premix combustion. Region 2 is called diffusion combustion, where most soot formation happens during this combustion process. It should be noticed that Region (2) in Fig. 2.4 is usually not apparently observed in PFI engines since the combustion is more homogeneous without serious wall impingement in the combustion chamber; however, it may be seen as in the figure from GDI engines due to wall wetting.

- $$\frac{dQ}{d\theta} = \frac{\gamma}{\gamma-1} P_{cyl} \frac{dV}{d\theta} + \frac{1}{\gamma-1} V \frac{dP_{cyl}}{d\theta} \quad \text{Equation 2.4}$$

, where Q is the apparent heat release

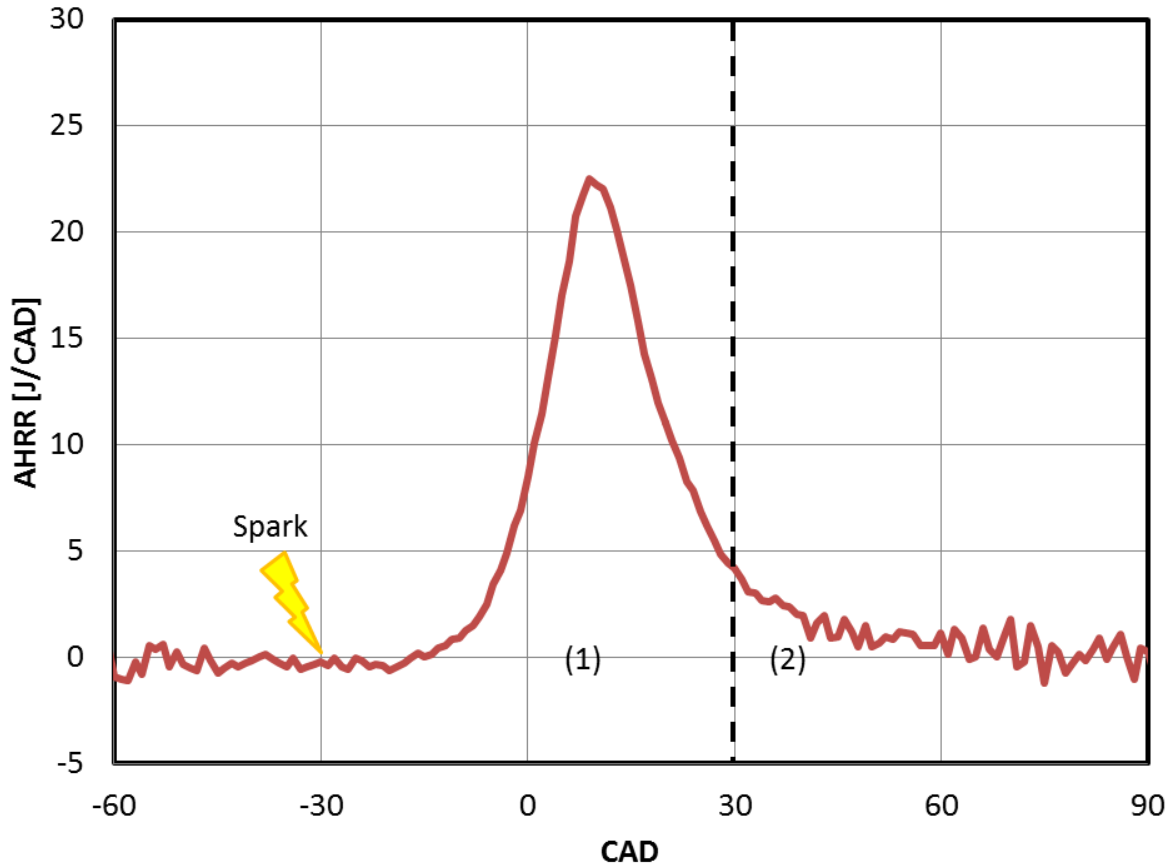


Figure 2.4 AHRR curve of a GDI engine

Dividing the AHRR curve by the maximal AHRR, the mass burnt fraction (MBF) could be obtained. Figure 2.5 shows the MBF calculated from Fig. 2.4. CAXX is usually used to denote XX% mass burnt at that crank angle degree, for example, $CA50 = 10^\circ \text{ aTDC}_{\text{fire}}$ represents 50% mass of injected fuel is burnt at 10°

after the TDC between the compression and expansion stroke (firing TDC). CAXX-YY typically denotes the duration for the engine to burn the fuel from XX% to YY% by mass, e.g. CA10-50 = 20° means that it takes 20° to burn 10% to 50% fuel mass fraction. The information is very important in SI engine applications to control the combustion phasing. In general, CA50 at between 5 and 10° aTDC_{fire} is considered the maximum brake torque (MBT) point, where the engine is running most efficiently.

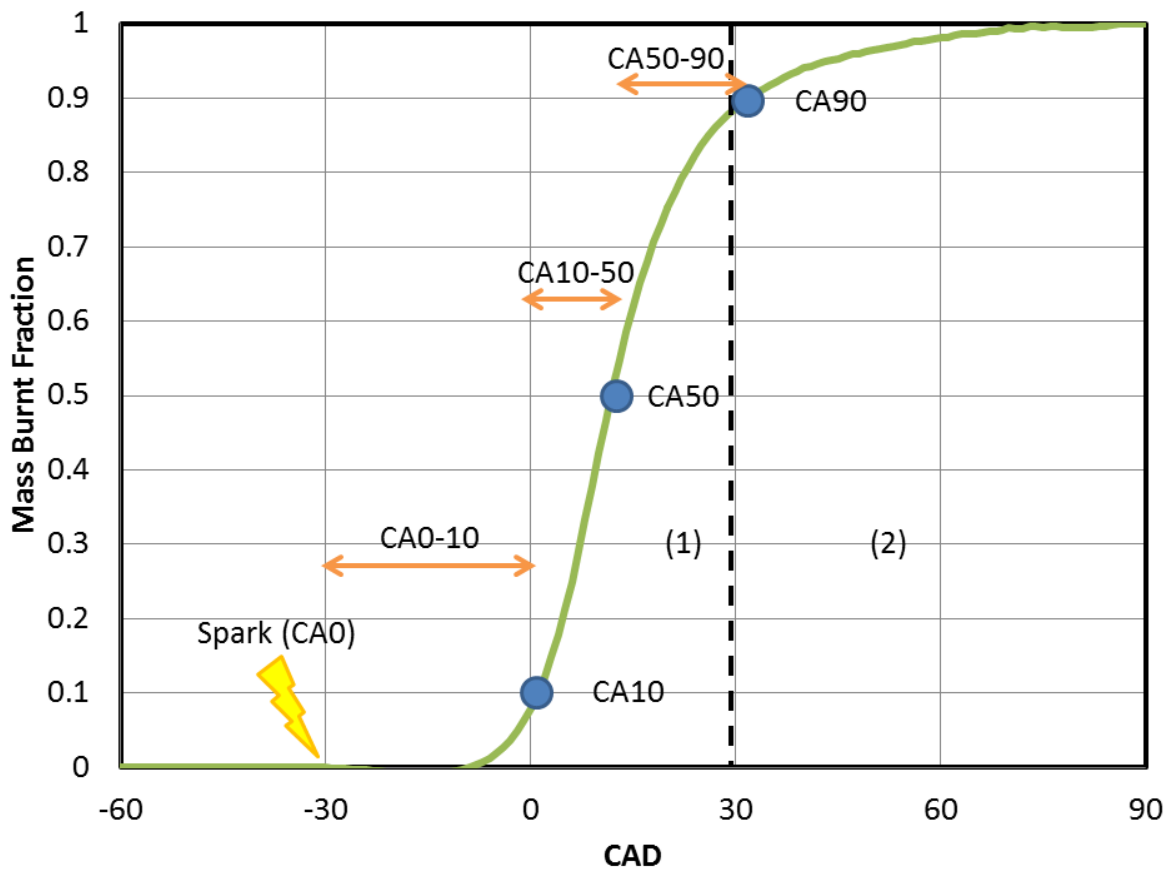


Figure 2.5 MBF curve of a GDI engine

2.4 Optical Diagnostics of Flame Propagation in GDI Engines

Because the complexity of the combustion process in SI engines, researchers have been focusing on different approach to study the subject more in-depth as many have focused on the flame kernel development by using different study methods, such as optical engines or CFD simulation to improve the analysis. The benefit of implementing an optically accessible engine (OAE) is the direct visualization of the combustion chamber. The dynamical process of combustion could be captured by high speed imaging technologies, e.g. a high speed camera. If a window is placed on the piston top, more thorough insight could be accessed even though the fuel-wall interaction or in-cylinder air flow may be compromised. Excessive crevice volume is also found in an OAE as well as the robustness of the whole engine system. Nevertheless, more and more research implements such engines for optical diagnostics. Other methods may be applied through different optical setup, such as fiber optics via the spark plug or endoscopy through the cylinder wall.

Ault and Witze studied the flame kernel growth by implementing fiber optics around the spark plug to detect the light intensity [32]. Their tests were focused on lean conditions where the luminosity of the flame is low. Although, the relationship of flame kernel growth rate and convection velocity was studied in their paper, they concluded that the noise from the spark plug may well impact the measurement. Therefore, direct imaging would still be needed for better comparison on flame propagation study. Lipatnikov and Chomiak [33] analyzed the randomness of the flame kernel development in a turbulent gas mixture by using simplified

mathematical models. Probability density functions were used with experimental data to check the variations in the initial stage of the flame kernel development due to turbulence effects. Ancimer et al. conducted experiments in a high swirl production SI engine to study the flame kernel growth [34]. A modified spark plug with fiber optics was also used in their study. They measured secondary voltages from the ignition system as anemometers in the combustion chamber to detect the in-cylinder flow, which could affect the direction of the spark “arc.” Their results indicated that the flame growth rate could be calculated as the averaged expansion rate where the ignition point is the center. However, the point may not coincide with the center of the flame kernel in turbulence due to high convective flow. Subramanian et al. also characterized the flame development in a PFI engine by using similar fiber optics in the spark plug [35].

Song and Sunwoo did numerical approach along with experiments in a constant volume combustion chamber to study the initial flame kernel development and its propagation [36]. They concluded that the speed of engine and the MAP are proportional to the initial flame kernel development velocity. If the air-fuel mixture is lean, the flame expansion velocity would decrease. They also found that higher spark energy increased the initial flame radius with a little temperature change. In addition, the increase of the spark plug gap would enhance the flame kernel development as well as the increase of the spark dwell time.

Researchers from Honda [37] studied the cycle-to-cycle variation of combustion in lean conditions by imaging the early flame kernel development of the combustion process in an optically accessible single-cylinder engine. Side and

bottom views of the combustion chamber were accessible to visualize the ignition points. They concluded that the various directions of the spark from the electrodes were the causes of cyclic variation of combustion. Pajot and Mounaim-Rousselle also conducted their experiments in an optical engine to verify the effect of in-cylinder flow on the early flame kernel development [38]. Particle Imaging Velocimetry (PIV) was used in the study to visualize the in-cylinder flow field. Their conclusion is that the flame kernel is subject to the predominant in-cylinder flow. Similar results could be found in [39] that in-cylinder flow has strong effects on the initial flame kernel development.

Ikeda et al. developed an in-spark-plug flame sensor (similar to aforementioned fiber optics in other research) to measure the local chemiluminescence from the initial flame kernel [40]. The flame front structure and the cyclic variation of combustion were correlated. Chemical radicals, such as OH^* , CH^* , and C_2^* , found in the flame front were detected for engine combustion analysis. It was concluded that the flame propagates faster in stoichiometric conditions.

Lee and Boehler [41] used different spark plug electrode configurations in a constant volume combustion chamber with Schlieren imaging technique to study the early flame kernel development. They also used the same spark plugs in a PFI engine to verify the effects of different electrode configurations. In their paper, it was concluded that the combustion is better with less conductive mass of the spark plugs; moreover, a specific spark plug configuration (J-gap design) performed better especially in lean conditions. Their engine testing also verified that the specific type of spark plug had the best performance. Researchers from Southwest Research

Institute also studied the effects of spark plug design on the initial flame kernel development [42]. False color scale was implemented in their imaging results to improve the readability of the images. They found that the size of the electrode is important on flame kernel growth that smaller electrodes produced more rapid flame kernel development.

It is concluded that the flame kernel development could be enhanced or distorted significantly by the in-cylinder air motion, spark energy and duration, local air-fuel ratio, and the shape of spark plug. The variation of the flame kernel development could be high if strong swirl or tumble motion is present in the cylinder. However, it is unclear how the flame would propagate in a GDI engine since the air-fuel mixing process occurs inside the cylinder with less homogeneity than that in a PFI engine. The injection timing is expected to have an impact on the combustion process as well as the fuel-wall interaction [13]. By experimenting in optical engines or measuring flame growth via optical methods with the assistance of computer programming on image processing, the study of early flame kernel development could be more direct; more “insight” could be acquired at the same time.

2.5 Emissions in GDI Engines

This section will review emissions of GDI engines in literature. Regulated emissions are the primary focus in this study, so CO, CO₂, THC, NO_x, and PM will be discussed in the following content. It should be addressed that PM emission has not yet been regulated by EPA in the U.S. due to the complexity of standardizing the measurement procedures even though the regulation has recently been proposed

and implemented in Europe. In spite of that, many researchers have investigated the emission extensively since it is harmful to human aspiratory system. Figure 2.6 shows the formation locations of different emissions (except for PM) inside the combustion chamber of gasoline engines.

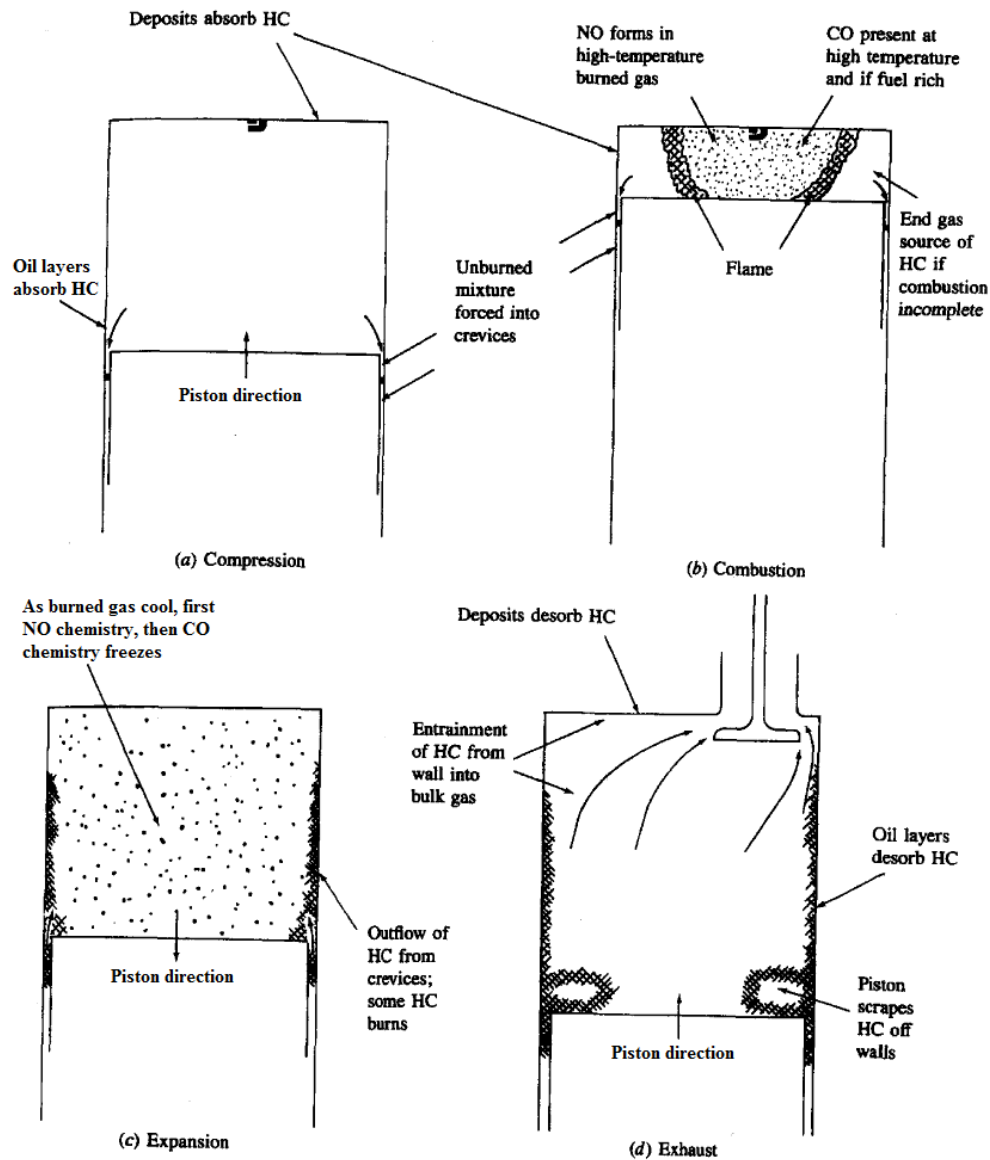


Figure 2.6 Emission formation locations [31]

2.5.1 CO and HC Emissions in GDI Engines

CO and HC emissions are formed because of incomplete combustion [43]. In gasoline engines, the locations of CO and HC formation are usually along with the cylinder wall where quench zones are present due to relatively cooler temperature of the wall. If the air-fuel mixture is rich, CO could also be present if the temperature is high. Air-fuel ratios are the primary factor of their formation [44]. In rich conditions, the level of the two emissions is very high due to insufficient oxygen that partial reactions are more prevalent to form intermediate combustion products. Engine start-up period emits high HC and CO since the engine is purposely running in rich conditions. In lean conditions, excessive oxygen would help the combustion to be more complete that HC and CO emissions are usually very low when the equivalence ratio is around 0.9. However, if the engine is running too lean, combustion would be deteriorated to misfire that HC emission will increase due to high level of unburned hydrocarbons. At the same time, CO emission will still be low due to no reaction between the carbon atoms and oxygen atoms.

Crevice volumes are another source for HC emission. Some fuel molecules could go into the crevice volumes, such as the volume between the piston and the cylinder wall, during the compression stroke. Those molecules will come out later in the expansion stroke due to the piston motion, but the flame front will have propagated as the end of combustion process that these molecules could not be burned at all or completely. Therefore, the position of the spark plug is important that it is at the center of the combustion chamber in most engines to create more uniform flame propagation. Furthermore, the spark timing is also critical that flame

front passes earlier through the combustion chamber with advanced spark timing, so the unburned hydrocarbons will miss it once they are out from the crevice volume. Nonetheless, if the spark timing is too retarded, incomplete combustion could occur [45, 46].

Fuel and oil deposits on the cylinder wall could also increase the HC emission [47]. In GDI engines, wall impingement is inevitable since the fuel is directly injected inside the cylinder. The emission is found higher in a GDI engine than in a PFI one when stratified injection is applied, which is considered one of the drawbacks of GDI applications especially with side-mounted injectors [48, 49]. In order to control the fuel-wall interaction, the injection timing becomes important in GDI engines [50, 51].

Over-mixing or under-mixing of the fuel could happen if improper injection timing is applied. Over-mixing means the outer boundaries of the air-fuel mixture could be too lean to be ignited if the mixing period is too long; on the other hand, under-mixing is defined that there is not enough time for the mixing process – local rich zones could be found if under-mixing is present. HC emission is found high from both phenomena. The former could occur if the in-cylinder flow is too strong, such as high tumble or high swirl air motion. Cold start is also a concern in gasoline engine applications that most HC emission is formed during the period due to more quench zones present [52].

The conclusion is made that the injection timing, air-fuel mixing process, spark timing, and air-fuel ratio as well as engine coolant temperature are critical to reduce CO and HC emissions in a GDI engine.

2.5.2 NO_x Emission in GDI Engines

NO_x emission consists of NO mainly with some NO₂ in presence, which is mostly found in compression-ignition engines but also in spark-ignition ones. The formation of NO_x emission is temperature dependent primarily that the higher the temperature, the more NO_x will be formed if enough oxygen is present. In gasoline engines, the highest NO_x emission is found when the equivalence ratio is about 0.95 [31, 44]. Even though the in-cylinder temperature is high in rich conditions, there is not enough oxygen to react with nitrogen in the air. On the other hand, the combustion is not sustainable in too lean conditions that the in-cylinder temperature is not high enough to cause the reactions.

From the standpoint of the aftertreatment system, the three-way catalyst has been used in the past decades in gasoline engines with profound efficiency in CO, HC, and NO_x reduction simultaneously. However, NO_x reduction could be challenging in GDI engines especially when running lean. The conventional three-way catalyst may not be applicable in lean conditions; so many other methods have been proposed and studied. Lean NO_x Trap (LNT) and passive ammonia selective catalytic reduction (SCR) are the common catalysts proposed by other researchers [53-56].

On the combustion side, different engine control technologies and strategies are important to find the engine operation points with minimal NO_x formation [57, 58]. Lowering the in-cylinder temperature has been considered the means to reduce NO_x formation during the combustion process besides applying a catalyst in the aftertreatment system for the reduction. The addition of EGR in the fresh air-fuel

mixture has been proposed and utilized in internal combustion engines. Some researcher proposed a method that the spark timing is prior to the injection timing to reduce NO_x emission; however, PM emission may increase significantly as the result of heterogeneous combustion by using such a strategy [59].

2.5.3 PM Emission in GDI Engines with Optical Diagnostics

PM emission has been known hazardous to human health; diseases such as asthma are caused primarily by PM in the atmosphere. Thus, the reduction of PM emission is critical in IC engines. To categorize particles in terms of their sizes, nuclei mode particles (NMP) and accumulation mode particles (AMP) are denoted as shown in Figure 2.7 [60].

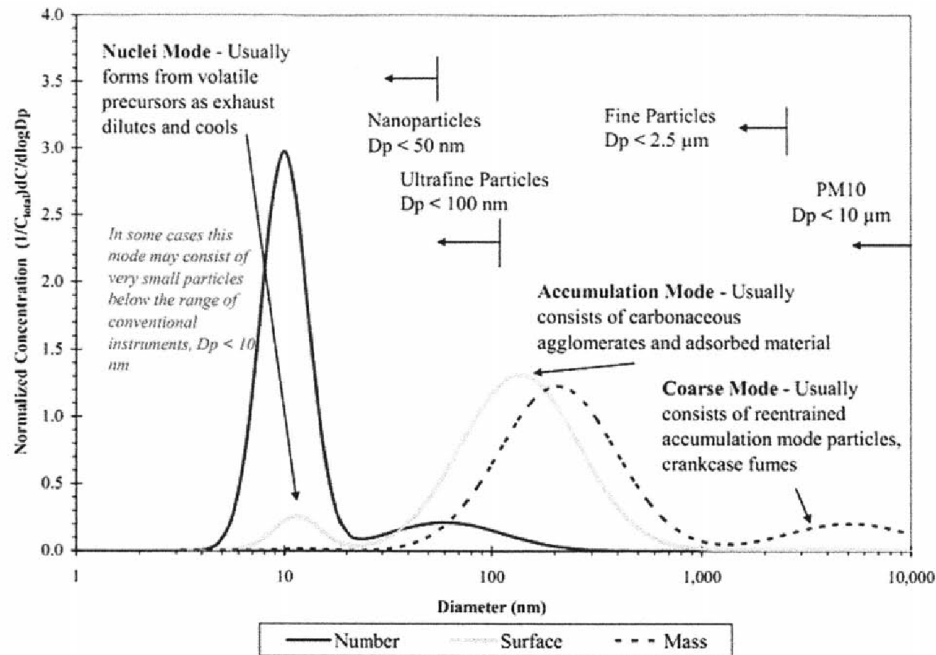


Figure 2.7 PM distribution [60]

Many studies have indicated that GDI engines have a significant drawback on particulate matter (PM) emissions [61, 62] in terms of both mass and particle number (PN) due to the direct injection in the cylinder. As shown in Fig. 2.8 [61], the emission from GDI engines is much worse than that from PFI engines. This is due to less homogeneity found during the air-fuel mixing process in GDI engines as well as more wall-wetting present in GDI engines due to direct injection.

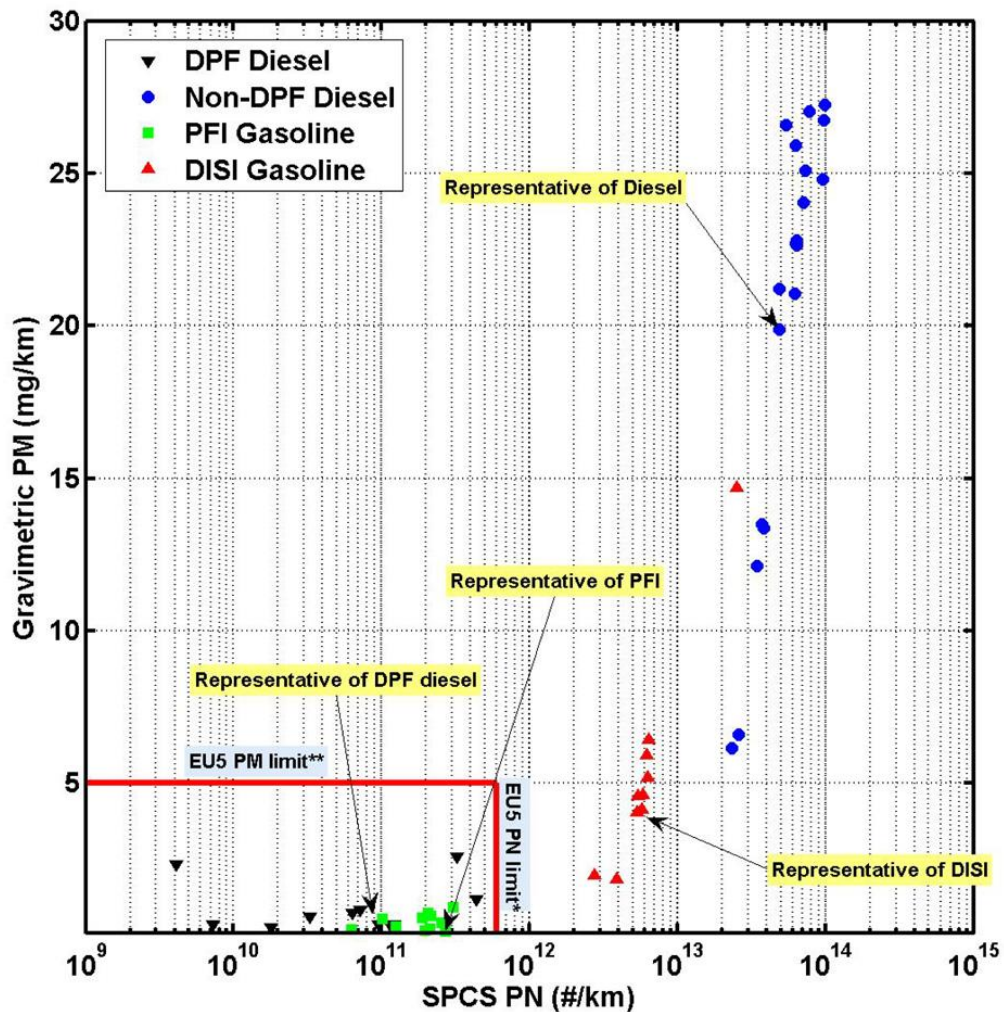


Figure 2.8 PM emission from different types of engines [61]

Researchers in the past decade have been determining the causes and possible locations of soot formation inside the combustion chamber as well as its characteristics with optical access and soot measurement technique [63-67]. Optical diagnostics via an endoscope to visualize the combustion inside a real combustion chamber is considered more realistic than studying from an OAE since the geometry is kept as well as the in-cylinder air-fuel interaction.

Moreover, various engine operation conditions may influence PM emission. The air-fuel ratio, injection timing, and combustion phasing are concluded as very influential on particle concentration [68-72]. Spray pattern and spray-wall interaction are also important on contributing PM emission [71, 73]. Some research also indicated that sophisticate engine control is necessary because most PM emission is generated during cold start and catalyst heating periods [74, 75].

Previous studies have shown that early injection would cause wall impingement on piston top and late injection spray could penetrate to the cylinder liner, as Fig. 2.9 shown [76, 77]. However, the combustion results of different injection timing are unclear since fuel types, ignition timing and air-fuel ratio would also have impacts that more detailed study must be needed since the combustion process is complicated in real GDI engines. With visualization from optical accesses on an engine, possible locations of PM emission formation could be identified after image process and statistical calculation. Figure 2.10 shows an example from [74] that diffusion flame is captured in the images and soot formation is found. Furthermore, flame propagation could also be studied by similar methods.

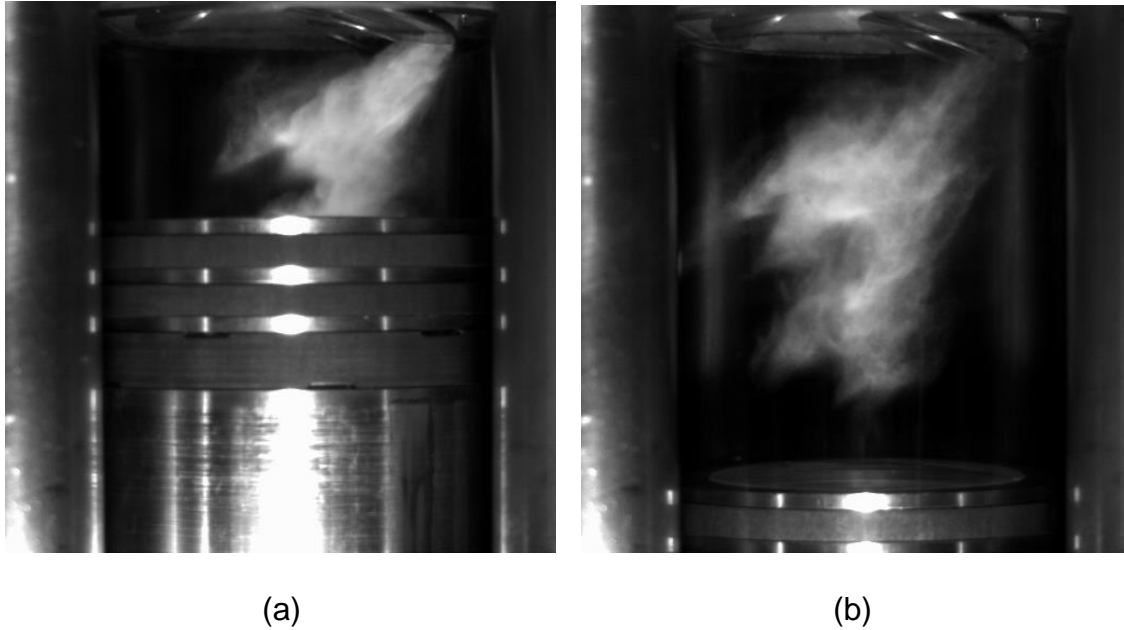


Figure 2.9 Different locations of wall impingement for (a)early SOI and (b)late SOI in an optical accessible engine [76, 77]

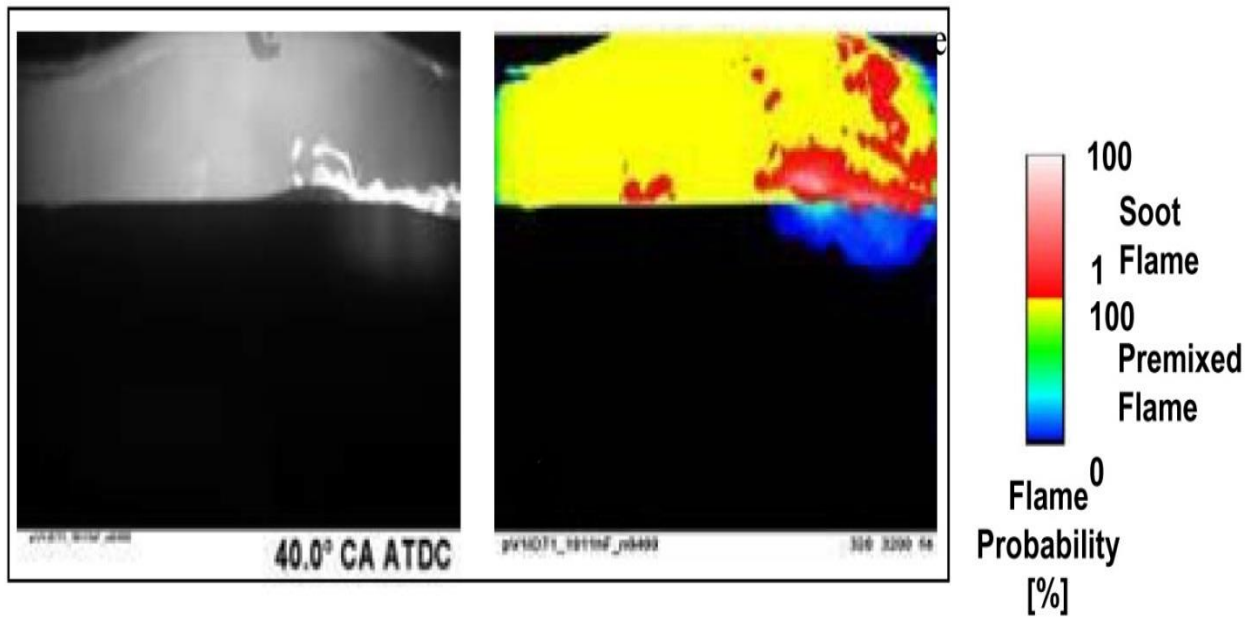


Figure 2.10 Raw (left) and PDF (right) images for PM formation study [74]

2.6 E85 in GDI Engines

Since the energy crisis in the last century, the replacement of petroleum-based fuel has been brought to the focus of researchers in the automotive industry. Fuels with “renewability”, which means they could be recycled in the natural system that their resources are considered sustainable, have been studied intensively and extensively. Among them, ethanol and bio-diesel are the two most popular fuels in gasoline and diesel engine applications, respectively. Besides, the extra oxygen found in their contents is also seen beneficial to the combustion process and therefore the emission reduction.

Ethanol has been mandated up to 10% by volume in gasoline in the U.S. market (low-level blend). Recently, many automotive companies have developed new technologies to adapt up to 85% ethanol in gasoline (high-level blend), which is called “E85” or “FLEXFUEL” [78]. Most ethanol resource in the U.S. is the product of starch-based crops, which may cause the concern of food resource availability; nonetheless, cellulosic ethanol, which is derived from non-food based feedstock, is also undergone research.

The renewability and oxygen content in ethanol are the reasons that it is the focus of gasoline replacement. In addition, there are some benefits of utilizing ethanol in gasoline engines, especially in GDI engines [79, 80]. The research octane number (RON) of ethanol is rated over 100 [81], which indicates its significant knock resistance. The latent heat required for the vaporization of liquid ethanol is also high that charge cooling effect could be emphasized to increase engine volumetric efficiency [82]. Regarding emissions, the presence of ethanol is

mostly beneficial to CO, HC, and PM emissions due to extra oxygen available during the combustion process [83-87]. Besides, ethanol is a short-chain single-component compound that it is easier to be oxidized to CO₂ than long-chain multiple-component compounds, such as gasoline.

However, there are still some concerns while applying the fuel. Lower energy content, i.e. the lower heating value (LHV in MJ/kg) of ethanol, is found in ethanol than in gasoline [88], which is about 27% less. It is therefore inevitable that more fuel will be injected in order to keep the same energy input to an engine if more ethanol is present in the fuel. Furthermore, vehicles with FLEXFUEL capability would require different materials for their parts from regular vehicles since ethanol is deemed harmful to certain materials such as rubber. The aforementioned high latent heat of vaporization could also be a disadvantage when the ambient temperature is too low to vaporize the fuel. Many researchers have addressed the issues and investigated the behavior of the fuel during cold start [89, 90]. Unregulated emissions, especially aldehydes, are found high when ethanol is used as the fuel. PM emission in terms of particle number is also unclear with the presence of ethanol in fuel.

In the recent research, low-speed pre-ignition (LSPI) has been emphasized in GDI engine applications especially using fuels containing ethanol [91-100]. Pre-ignition is an abnormal engine combustion event that the air-fuel mixture is ignited without the assistance of spark plug, which is more like auto-ignition. Engines could be damaged by the abnormal combustion. Many researchers have concluded that this phenomenon could be because of several factors. The local hot spots inside the

combustion chamber, hot oil droplets in the air-fuel mixture, and fuel components. Nonetheless, the detailed mechanism is still not definitely understood.

2.7 3-D CFD Simulations of GDI engines

With more advanced computing technologies, the numerical analysis of engine operations becomes possible in terms of computational speed and accuracy. 3-D computational fluid dynamics (CFD) simulation could be accomplished in a meaningful time span for researchers to access more details that could not be captured by physical experiments.

Due to the requirement of high-performance hardware for large-eddy simulation (LES), the Reynolds-averaged Navier-Stokes equations (RANS) are still used very often in the research field [101]. RANS is a time-averaged method to simulate the motion of fluid flow, and it is suitable to describe turbulence. However, some details would be missing since the results are time-averaged. Recently, CFD software without user-meshing process has been developed to reduce the complication of simulation for the user standpoint [102, 103] that the mesh is generated by the software automatically.

The fuel spray-wall interactions as well as air-fuel mixing process have been analyzed numerically [104-106]. The wall-impingement, local air-fuel ratios, and in-cylinder flow field, which are usually difficult to study in a real engine, could be simulated with 3-D CFD software as well as the turbulence kinetic energy (TKE), tumble ratio, and swirl ratio [13, 19].

CHAPTER 3 STUDY METHODOLOGY AND EXPERIMENTAL SETUP

The study methodology is described in the chapter. All fuels are listed in the first section, and the setup of a production GDI engine with optical accesses is mentioned in the ensuing content. Image processing techniques and numerical simulations are discussed at the end of this chapter.

3.1 Fuel

In the current research work, pure gasoline (E0) and an ethanol-gasoline blend (E85) are used. For E0, RON-93 is used; for ethanol, 100% anhydrous (200 Proof) is used in the study. E85 in the experiment is 85% ethanol blending with 15% pure gasoline volumetrically by the splashing method. The detailed fuel properties are listed in Table 3.1.1, and it should be noticed that pure ethanol data is also listed for comparison.

Table 3.1.1 Fuel properties of E0, E85, and ethanol

	Gasoline	E85	Ethanol
Density [kg/m^3]	737	778	789
Kinematic Viscosity [$10^{-6} \text{ m}^2/\text{s}$]	0.46	-	1.07
Specific Heat C_p [kJ/kg-K] @ 40°C	2.22	2.41	2.72
Latent Heat of Vaporization [kJ/kg]	380 - 500	-	904
Lower Heating Value [MJ/kg]	43.1	29.7	26.8
Research Octane Number	93	-	109

3.2 Experimental Setup and Apparatus for Engine Testing

Detailed experimental setup and apparatus for engine testing are addressed in this section. The current study utilizes a GDI spark-ignited engine to study combustion and emission characteristics with optical accesses and state-of-the-art emission measurement devices.

3.2.1 GDI Engine with Optical Access

The GDI engine used in the current research is from GM EcoTec family coded LNF, which is a 4 cylinder dual-overhead-cam (DOHC) engine. The engine was first introduced in the US in 2007 on Pontiac Solstice and Saturn Sky Red Line. The engine is equipped with a twin-scroll turbocharger and variable valve timing technology on both the intake and exhaust camshafts. The exhaust valves are filled with sodium inside that the material would be liquefied at high temperature to enhance the heat transfer due to improved conductivity. The engine head is made of high strength aluminum alloy to reduce the engine weight. The displacement is 2.0 L with square 86 mm bore and stroke. The injection system was designed to be pressurized by a high pressure fuel pump attached on the intake camshaft, and the injection pressure is ranged from 31 bar (idle) to 155 bar (wide-open throttle). However, due to the limited resource on engine controlling, such as the lack of open ECU or Drivven hardware, VVT, EGR, turbocharger, and the fuel system are disabled in the current study.

Three engine heads are used in the current research with optical accesses at different positions – no modification (for single-cylinder optical engine), optical

access through one intake valve, and optical access through the side wall of Cylinder 4 combustion chamber (for multi-cylinder optical engine).

First, an over-head-valve (OHV) single-cylinder optical engine (denoted as sOAE) with Bowditch piston (elongated piston) is modified to attach a metal liner and an LNF engine head with side window (sapphire) mounted. There is no modification on the engine head that its combustion chamber roof geometry is intact. Nonetheless, a flat quartz window is placed on the Bowditch piston top that the piston is not the same as a production one. A 45-degree mirror with UV-grade coating is located on the bottom of the cylinder block to access the combustion chamber visually. Two views of the single cylinder optical engine are shown in Fig. 3.2.1(a), and the bottom view from the Bowditch piston is shown in Fig 3.2.1(b) and (c) for no-valve deactivation and one-valve deactivation (intake), respectively. The specification of the engine is listed in Table 3.2.1.

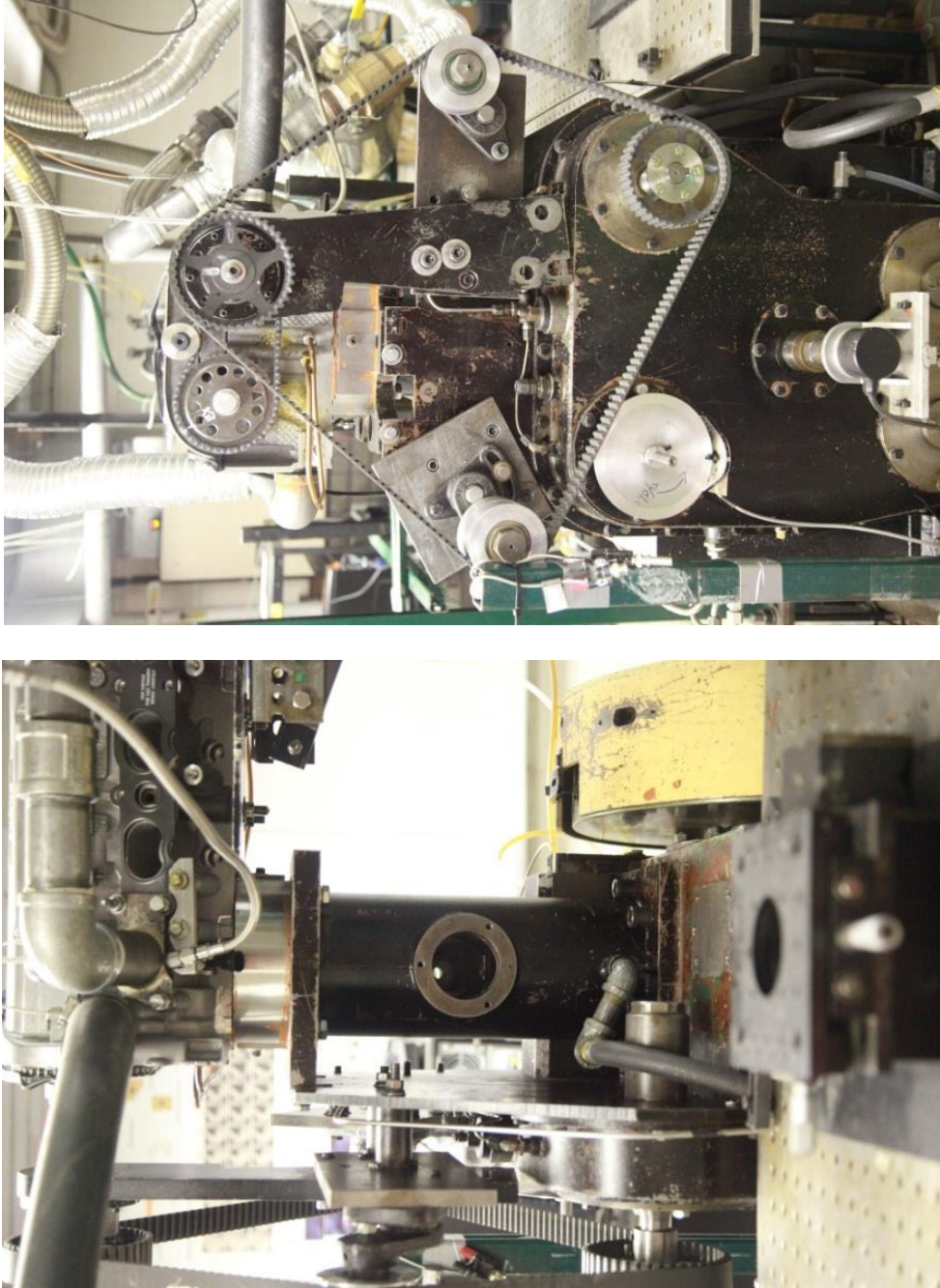
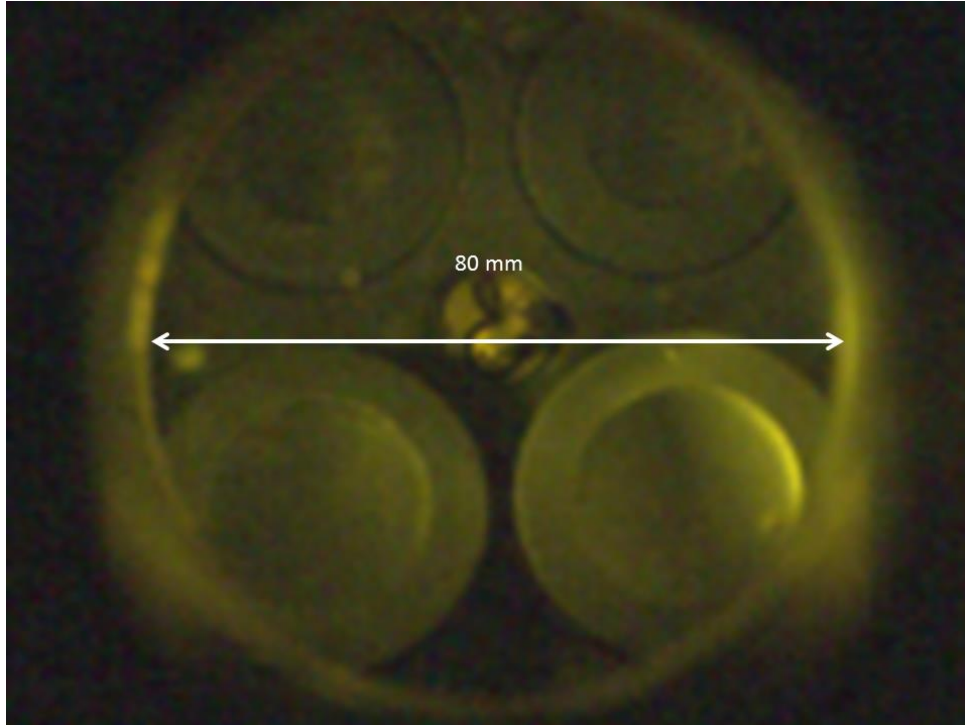
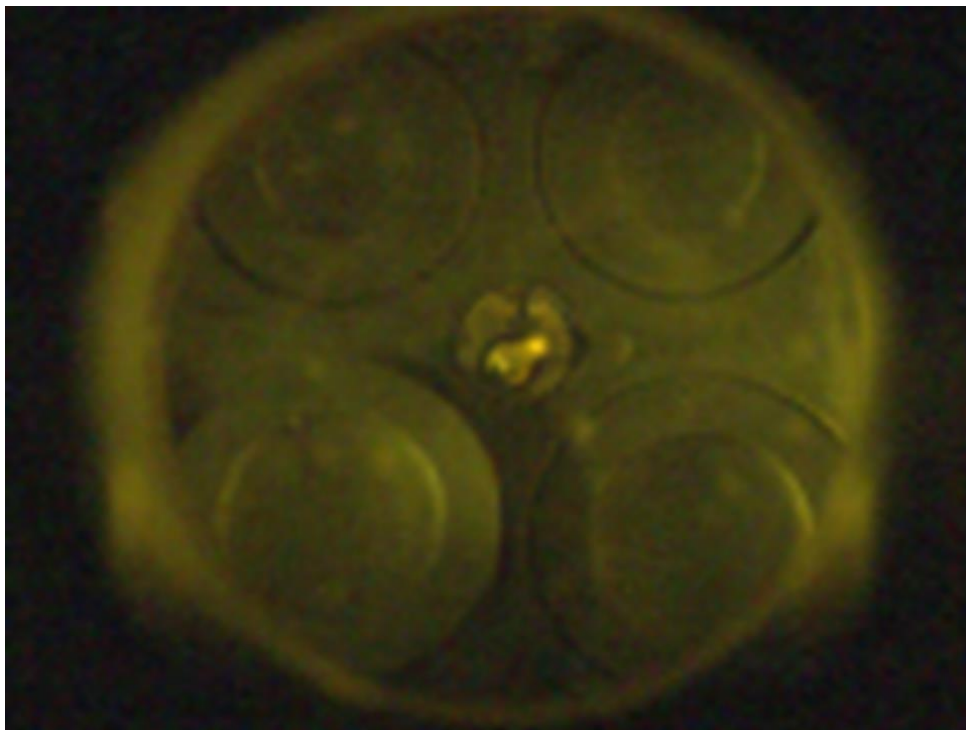


Fig. 3.2.1 sOAE setup: (a) different view angles of the sOAE



(b)



(c)

Fig. 3.2.1 sOAE setup: (b) no-valve deactivation and (c) one-valve deactivation

Table 3.2.1 sOAE specifications

General	Naturally aspirated, single cylinder
Bore X Stroke	86 mm X 108 mm
Compression Ratio	10.47:1
Engine Speed	600 rpm
Intake Valve	
Max Lift	10.3mm @234° bTDC _{fire}
Duration	203.6° @1 mm lash
Exhaust Valve	
Max Lift	10.3mm @240° aTDC _{fire}
Duration	194° @1 mm lash
Injector	6-hole OEM injector (side-mounted)
Fuel	E0(gasoline), E85
Injection Pressure	100 bar
Injection Timing	300° or 180° bTDC _{fire}
Air-Fuel Ratio (Lambda)	Rich (0.9), Stoich (1.0), Lean (1.15), or Very Lean (1.6)
Spark Timing	45° -- 15° bTDC _{fire} with increment of 5°
Spark Dwell Time	4 ms
EGR (if applied)	0-30% with increment of 10%
MAP	~ 1 bar
Intake Temperature	40 °C
Coolant Temperature	80 °C

Secondly, a production LNF engine is used with the other two modified engine heads (denoted as mOAE). Cylinder 1, 2, and 3 of the engine are disabled with Cylinder 4 modified for optical diagnostics. One engine head is modified that one of the intake valves in Cylinder 4 is replaced by a sapphire window; the other head is bored out from the side of Cylinder 4 to insert an adaptor for endoscope access. The former is suitable for one valve deactivation study, and the latter is suitable for flame propagation, spark, and pool fire (diffusion flame) study. It should be noticed that since the modification is done with minimal change on engine geometry, the air motion and crevice volume in the combustion chamber should be nearly identical to a production engine. Therefore, the combustion and emission study is considered practical and similar to the real world conditions. The engine setup is shown in Fig. 3.2.2, and the engine specification is shown in Table 3.2.2.

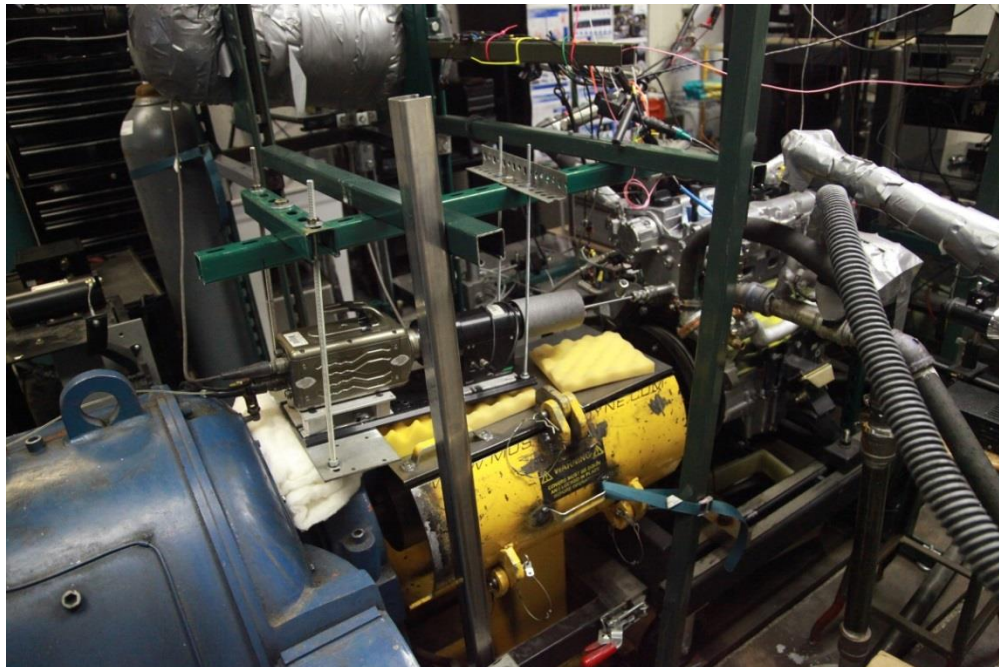


Fig. 3.2.2 (a) mOAE setup: high speed camera and LNF engine

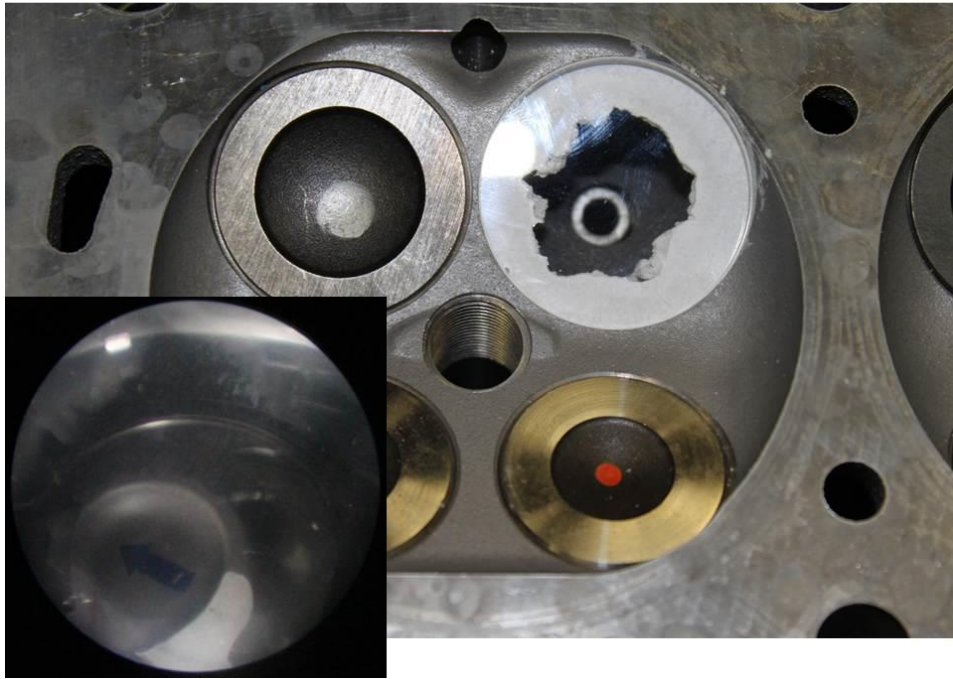


Fig. 3.2.2 (b) mOAE setup: one-valve deactivation optical access

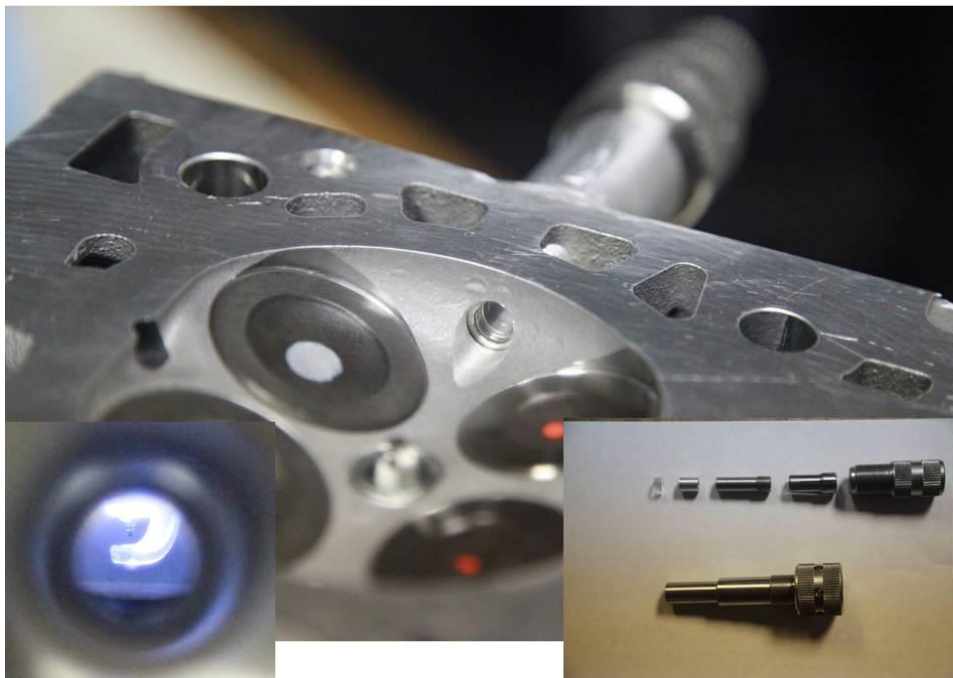


Fig. 3.2.2 (c) mOAE setup: side-mounted endoscope adaptor

Table 3.2.2 mOAE specifications

General	Naturally aspirated, 1-cylinder activated
Bore X Stroke	86 mm X 86 mm
Compression Ratio	9.2:1
Engine Speed	1200 rpm
Intake Valve	
Max Lift	10.3mm @234° bTDC _{fire}
Duration	203.6° @1 mm lash
Exhaust Valve	
Max Lift	10.3mm @240° aTDC _{fire}
Duration	194° @1 mm lash
Injector	6-hole OEM injector (side-mounted)
Fuel	E0(gasoline), E85, CNG
Injection Pressure	100 bar
Injection Timing	300°, 180°, or 60° bTDC _{fire}
Air-Fuel Ratio (Lambda)	Rich (0.9), Stoich (1.0), or Lean (1.15)
Spark Timing	30° -- 10° bTDC _{fire} with increment of 5°/10° aTDC _{fire}
Spark Dwell Time	4 ms
MAP	~ 1 bar or ~0.5 bar
Intake Temperature	25 °C
Coolant Temperature	40 °C

The single-cylinder engine is control by LabVIEW 5 on Windows 98 system as well as the data acquisition (DAQ). This is an open-loop control that the injection and ignition signals are triggered by an Optoschmitt sensor (Honeywell) mounted on the cam, which generates a pulse per 720° (1 signal/four-stroke cycle). The timing is generated by a crank angle encoder at the rate of $0.9^\circ/\text{pulse}$ (equal to 400 signals per revolution). It should be noticed that the crank angle encoder used on sOAE is not a typical one, which is usually set at 1.0 or $0.5^\circ/\text{pulse}$ (360 or 720 signals/revolution, respectively). High speed cameras could also be synchronized with the trigger and the timing signals. The injection system is pressurized by a nitrogen bottle with a high pressure regulator set at 100 bar, and the fuel is stored in a high pressure stainless steel bottle (~ 1 L) directly connect to a GDI injector. In-cylinder pressure is measured by a Kistler spark-plug build-in pressure transducer with an amplifier, and re-pegging is done by MATLAB programming after acquiring the raw data from testing. The manifold absolute pressure (MAP) is measured by a pressure transducer, and MAP at the bottom dead center after the intake stroke ($\text{BDC}_{\text{intake}}$) is used for re-pegging. The intake temperature and the coolant temperature are monitored though thermocouple readouts. Nitrogen is used as EGR to sOAE if applied, which is measured and calculated from a Horiba oxygen sensor at the intake manifold.

Since a single-cylinder optical engine test is very short (10 – 30 cycles at a time) due to the limitation of engine robustness, lambda sensors could not be used to measure the air-fuel ratio. Therefore, the air-fuel ratio is calculated directly from the measured intake air mass flow rate and the injected fuel quantity. The engine

intake air flow is supplied by shop air, and its volumetric flow rate is regulated by a flow meter (Flo-Gauge, RCM Industries) and a pressure gauge at the outlet of the shop air. The intake air flow could be then calculated by Eq. 3.2.1 and Eq. 3.2.2. For example, if the pressure and flow rate are read at the shop air outlet as 15 psi and 12 scfm, respectively, and the MAP is read at 1 bar, the intake air flow rate is estimated at 0.00286 m³/s. With measured temperature, the mass flow rate of air at the temperature could therefore be calculated with corresponding air density, and then the air-fuel ratio could be then assessed by dividing dictated injection quantity in mass. All the devices mentioned above are shown in Fig. 3.2.3.

- $K_P = \sqrt{P_{shop\ air}/P_{Flo-Gauge}}$; $K_T = \sqrt{T_{shop\ air}/T_{Flo-Gauge}}$ (Equation 3.2.1)

,where $P_{Flo-Gauge}$ and $T_{Flo-Gauge}$ are the calibration conditions specified on the device

- $\dot{Q}_{real} = \dot{Q}_{Flo-Gauge}/(K_P \times K_T)$ (Equation 3.2.2)

,where $Q_{Flo-Gauge}$ is the flow rate measurement



Figure 3.2.3 (a) sOAE devices: LabVIEW control board



Figure 3.2.3 (b) sOAE devices: in-spark-plug pressure transducer

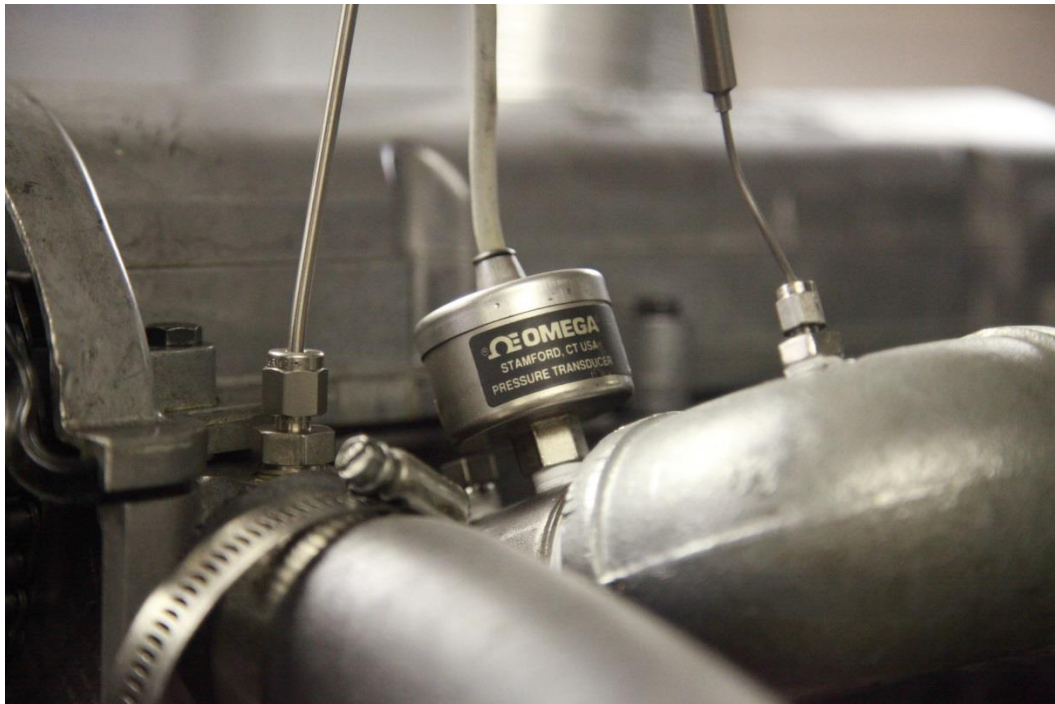
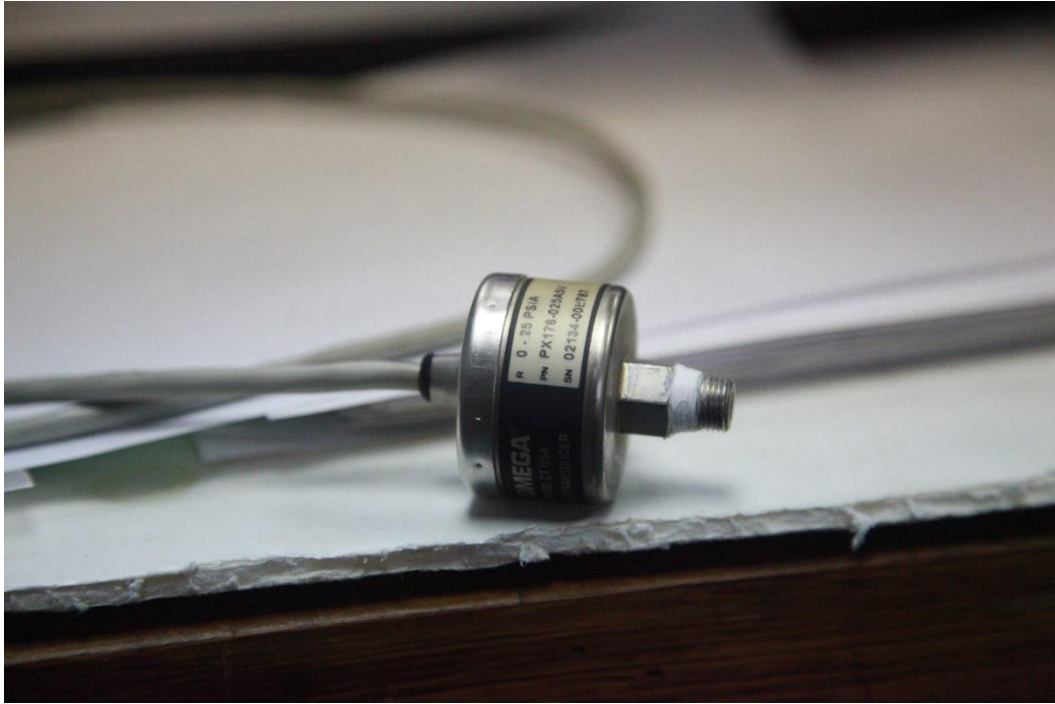


Figure 3.2.3 (c) sOAE devices: MAP pressure transducer



Figure 3.2.3 (d) sOAE devices: high pressure fuel tank (top) and regulator (bottom)



Figure 3.2.3 (e) sOAE devices: shop air pressure and flow gauges with EGR system

On the mOAE, an aftermarket ECU (MoTeC M800) is used for measuring correct crank and cam timing and generating spark signals. The ECU is capable of controlling engines up to eight cylinders that it is suitable for the current application; however, it was originally designed for PFI applications, so the GDI injector control in the present research is bypassed by other control methods mentioned later in the chapter. The in-cylinder pressure is measured by a high-temperature pressure transducer (Kistler Type 6052C with insulated cable) with the measuring range from

0 to 250 bar at operating temperature from -20 to 350 °C. Due to its small dimensions, this type of pressure transducers is ideal in the internal combustion engines with minimal engine modification. It uses a piezoelectric crystal to achieve high sensitivity with good temperature stability while measuring. The signal is conditioned through a Kistler signal conditioning platform (SCP, Type 2854A) and amplified by Kistler Type 5064A). This platform is capable of conditioning a wide range of signals from both piezoelectric or piezoresistive pressure sensors.

The production engine utilizes the signals generated from the two camshafts and the crankshaft to define the engine timing reference for other signals, such as injection signals. The crankshaft signal is generated 1 pulse/6° with two missing signals at the 59th and the 60th, and the signal is falling-edge activated. The TDCs of Cylinder 1 and 4 are at the 14th crankshaft signal, and that of Cylinder 2 and 3 are at the 44th crankshaft signal. The intake and exhaust camshaft signals are four uneven signals. At parking position (no cam phasing), the rising edge of the first exhaust camshaft signal is at the 3rd signal from the crankshaft and its falling edge is at the 8th crankshaft signal. The rising edge of the second exhaust camshaft signal is at the 33rd crankshaft signal, and the falling edge is at the 38th crankshaft signal. The rising edge of the third exhaust camshaft signal is at the 43rd crankshaft signal, and the fall edge is at the 8th crankshaft signal. The fourth rising edge of the exhaust camshaft signal is at the 13th crankshaft signal, and its falling edge is at the 38th crankshaft signal. The rising and falling edges of the first intake camshaft signal are at the 48th and 53rd crankshaft signal, respectively; the edges of the second intake camshaft signal are at the 18th and 23rd crankshaft signal. The rising and falling

edges of the third intake camshaft signal are at the 28th and 53rd crankshaft signal, respectively; the edges of the second intake camshaft signal are at the 58th and 23rd crankshaft signal. The firing order of the engine is 1-3-4-2.

The crank angle encoder used on the mOAE is Kistler Type 2613B. It is an optical encoder system suitable for speed range from 1 to 20000 rpm with a minimal 0.1°/signal resolution. If a remote control unit is used, it could generate two sets of signals: a fixed timing signal at 1°/signal with a trigger signal at 1 signal/revolution rate; an adjustable timing signal from 0.1°/signal to 6°/signal with a trigger signal at 1 signal/revolution rate. Therefore, synchronizing with other instruments, such as a high speed camera, at different timing resolutions is achieved.

The data acquisition (DAQ) of the mOAE is done by CAS Redline II from AND Technology Inc. It is a high-speed real-time data acquisition system with combustion analysis device. Signals, for example in-cylinder pressure traces, are acquired with respect to the timing signals from the crank angle encoder, so data taken at 0.1° rate (7200 data points per combustion cycle) could be achieved in the current study. Nonetheless, 1 data point per degree is set for more stable data acquisition and memory space in the present. In-cylinder pressure trace re-pegging is automatically computed in the system that no MATLAB programming on re-pegging is needed in the post process.

Because of the original design of MoTeC M800 as a PFI application, the injection signal is generated via LabVIEW 2010 programming and a National Instruments counter/timer device (NI PCI-6602) with digital I/O. The device has an 80 MHz source frequency to generate or time signals precisely and accurately.

Injection signals are generated with pre-determined timing and duration and sent to the injector driver provided by Delphi. The driver then sends the signal to the injector; once it is triggered, fuel would be delivered during the specified injection duration. The fuel system is also pressurized by the same setup on the sOAE due to the disabled production fuel pump. The air-fuel ratio is measured in terms of lambda by MoTeC Lambda sensor mounted on the exhaust pipe. All the aforementioned instruments on mOAE are shown in Fig. 3.2.4.



Figure 3.2.4 (a) mOAE devices: MoTeC M800 ECU

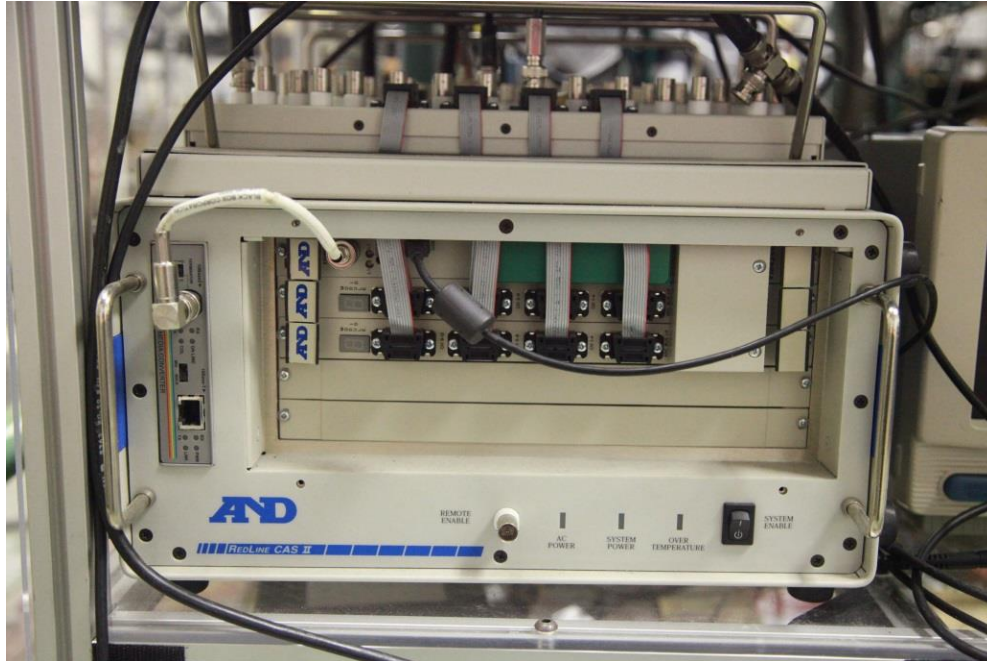


Figure 3.2.4 (b) mOAE devices: AND Redline CAS II

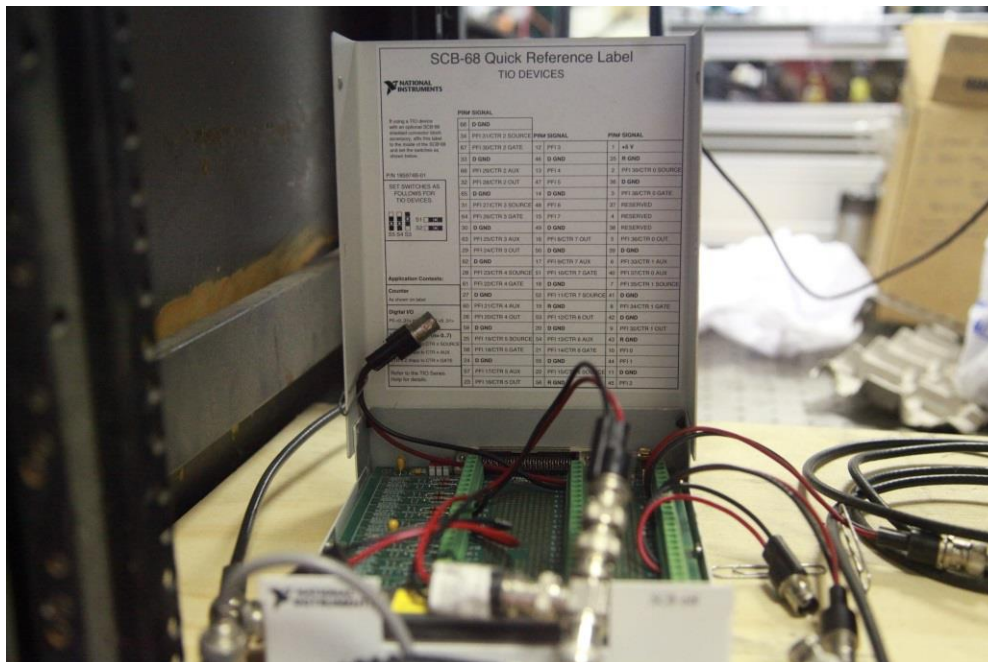


Figure 3.2.4 (c) mOAE devices: NI PCI-6602 (for injection and camera control)

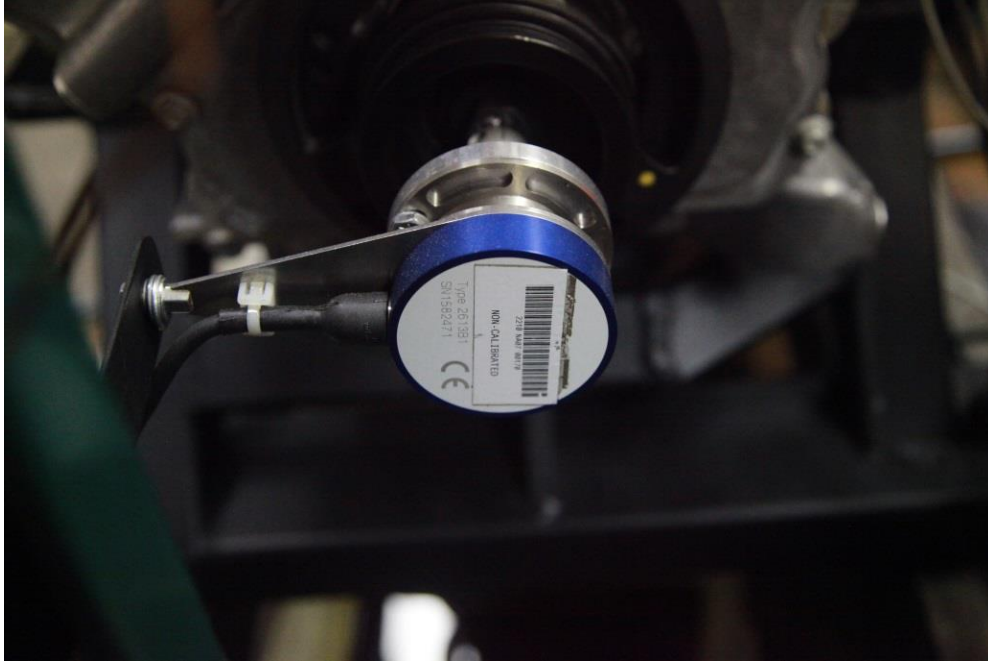


Figure 3.2.4 (d) mOAE devices: Kistler 2613B encoder (top) and its outputs (bottom)

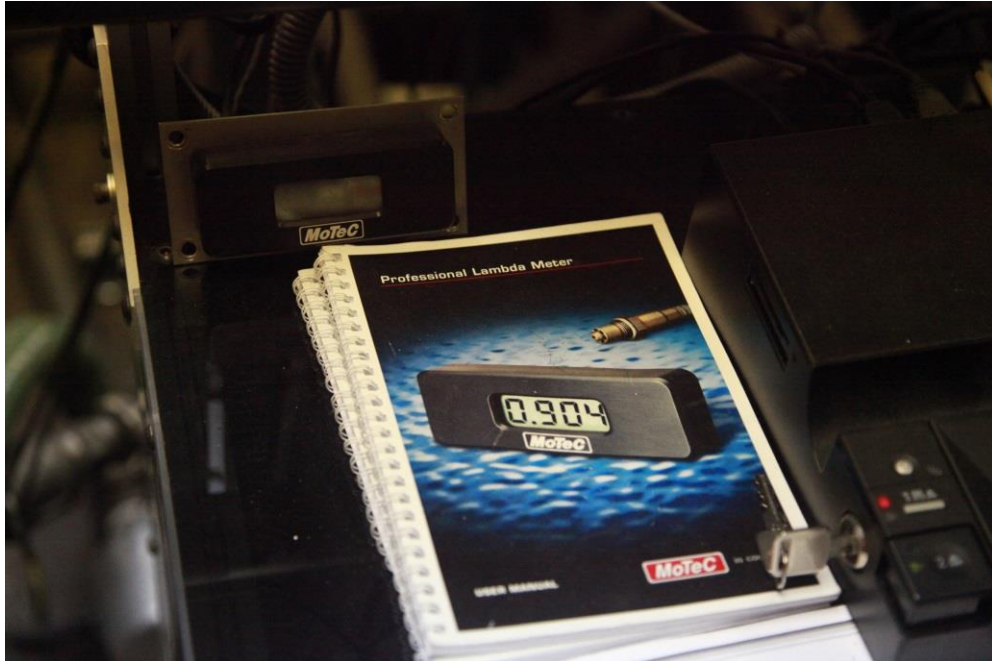


Figure 3.2.4 (e) mOAE devices: MoTeC Lambda sensor

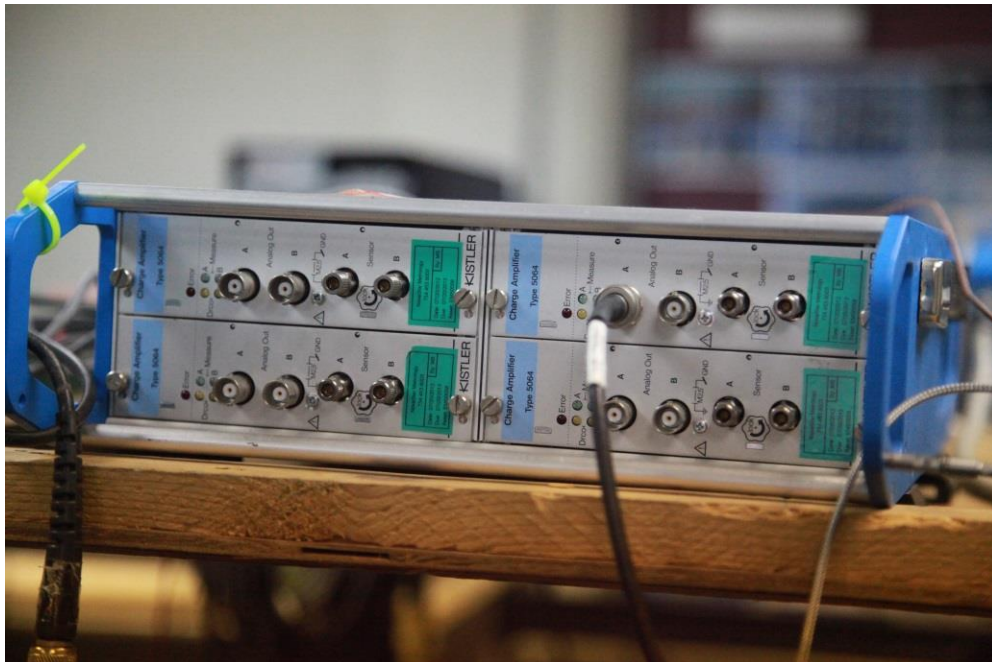


Figure 3.2.4 (f) mOAE devices: Kistler pressure amplifier and conditioner



Figure 3.2.4 (g) mOAE devices: high pressure fuel tank

A specially made device in the present research is the spark energy test bench. It is named Variable Ignition Pattern Equipment (VIPE), which could generate different energy with respect to different coil configuration. Up to eight coils could be configured together as 4-pair coils in parallel (each pair is seen as 2 coils in series) in the study. Energy is outputted through a high voltage cable, which is rated 0 k Ω in the present setup, to the spark plug. Due to intellectual proprietary,

the device could not be presented in figure. The estimated energy output of the OEM coil for this engine is about 50 mJ, and the 8-coil configuration mentioned above could output around 250 mJ. The energy measurement should be performed by using a specific test bench; if it is measured from engine operation, the discharge duration is shorter because of high discharge voltage. The signal needed to trigger the device is the same one to trigger an OEM coil, so there is no modification necessary besides bypassing the original coil. Figure 3.2.5 shows a snapshot of the coil discharge voltage, camshaft and crankshaft timing signals measured from an oscilloscope. Since only Cylinder 4 is activated on the engine, the spark timing is set with respect to the TDC_{fire} of that cylinder.

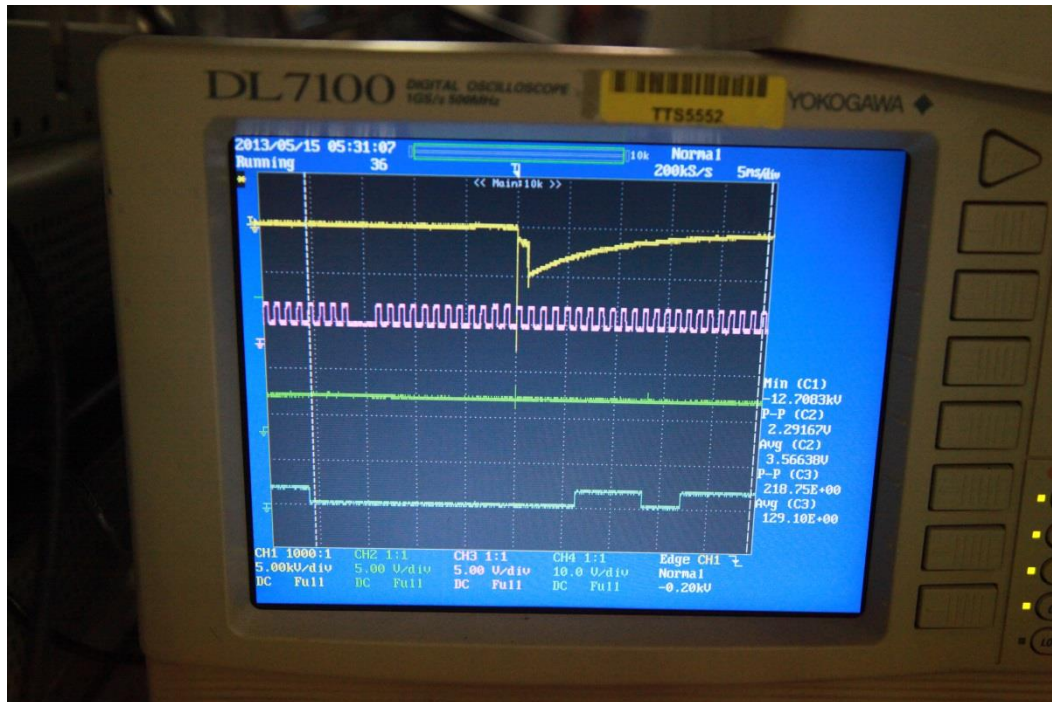


Figure 3.2.5 Signals of mOAE (yellow: spark; purple: crankshaft; blue: intake camshaft)

3.2.2 Emission Measurement Equipment

Three different emission measurement devices are used in the current study for different exhaust gas species. The following content will introduce them in details.

A. MKS MultiGas Analyzer HS-2030

The MKS gas analyzer is a Fourier-transform infrared (FT-IR) based device to measure the concentrations of various gas species from parts-per-billion (ppb) to %. “HS” stands for high speed that it is capable of high speed gas measurement up to 5 Hz sampling rate. FT-IR is a technique that the absorption, emission, or photoconductivity of an infrared spectrum from a gas could be obtained and converted to concentration via Fourier transform algorithm. A Helium-Neon laser is placed in the device as the reference laser. Most molecules could be detected by the device except for N_2 , H_2 , and O_2 . Dry air is provided to the device to purge it and to keep water out from condensation in the gas detecting cell or hazing of the KBr windows. A LabVIEW programming code is used to control the device and to collect the data. “Recipes” for corresponding fuels, such as E85, are provided by the manufacturer for different species measurement. Heated sampling lines and filters should be attached before entering into the device to avoid water and particles from the exhaust gas. This device is capable of measuring a wide range of gas species, so it is suitable for exhaust gas component analysis. Figure 3.2.6 shows the device.

In the current study, the exhaust gases of E0 and E85 from the GDI mOAE are measured and analyzed in ppm. The related recipes are listed below, but it

should be noticed that the recipe ETHANOL is used for E0 measurement since there is no related one provided by the manufacturer.

- ETHANOL recipe

- $\text{THC} = (1.1 \times \text{CH}_4) + (2 \times \text{Acetaldehyde}) + (2.4 \times \text{Acetylene}) + (1.9 \times \text{Ethylene}) + (2 \times \text{Ethane}) + (2 \times \text{Ethanol}) + (2.85 \times \text{Propylene}) + (6.3 \times \text{Toluene})$
- Some calibrations (e.g., "NO 191C") include a correction factor to account for the combustion environment, which provides better absolute accuracy. Dry readings are calculated from wet readings: $\text{Dry} = \text{wet} / (1 - w/100)$, where w = water reading in %.

- ETHANOL HIGH recipe

- $\text{THC} = (1.1 \times \text{CH}_4) + (2 \times \text{Acetaldehyde}) + (2.4 \times \text{Acetylene}) + (1.9 \times \text{Ethylene in high ethanol}) + (2 \times \text{Ethane in high ethanol}) + (2 \times \text{Ethanol}) + (2.85 \times \text{Propylene}) + (6.3 \times \text{Toluene in high ethanol})$
- Some calibrations (e.g., "NO 191C") include a correction factor to account for the combustion environment, which provides better absolute accuracy. Dry readings are calculated from wet readings with the correction mentioned above.



Figure 3.2.6 (a) MKS HS2030

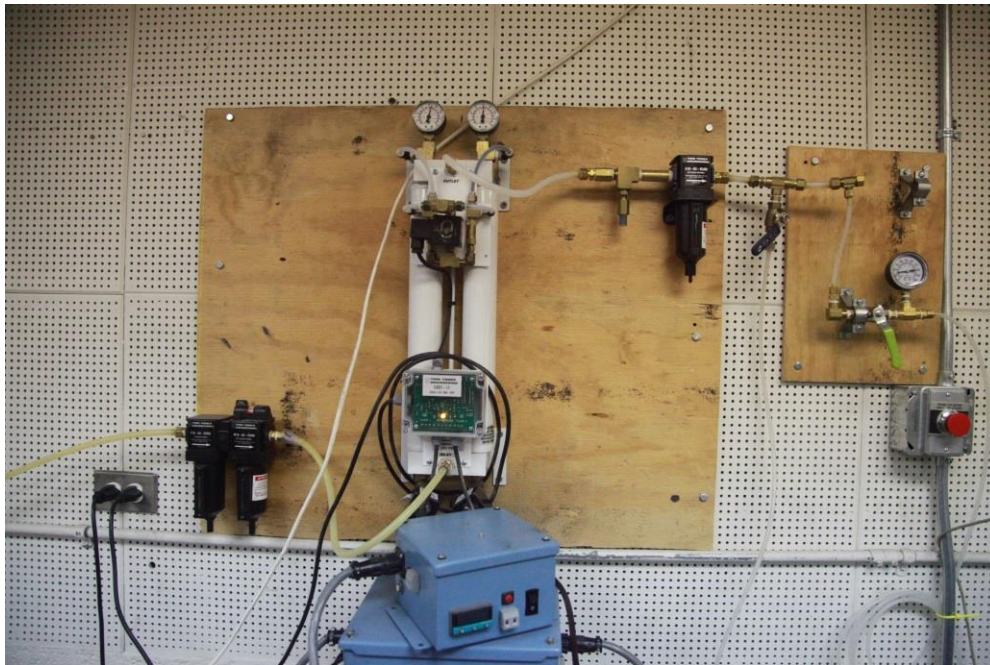


Figure 3.2.6 (b) Dry air system

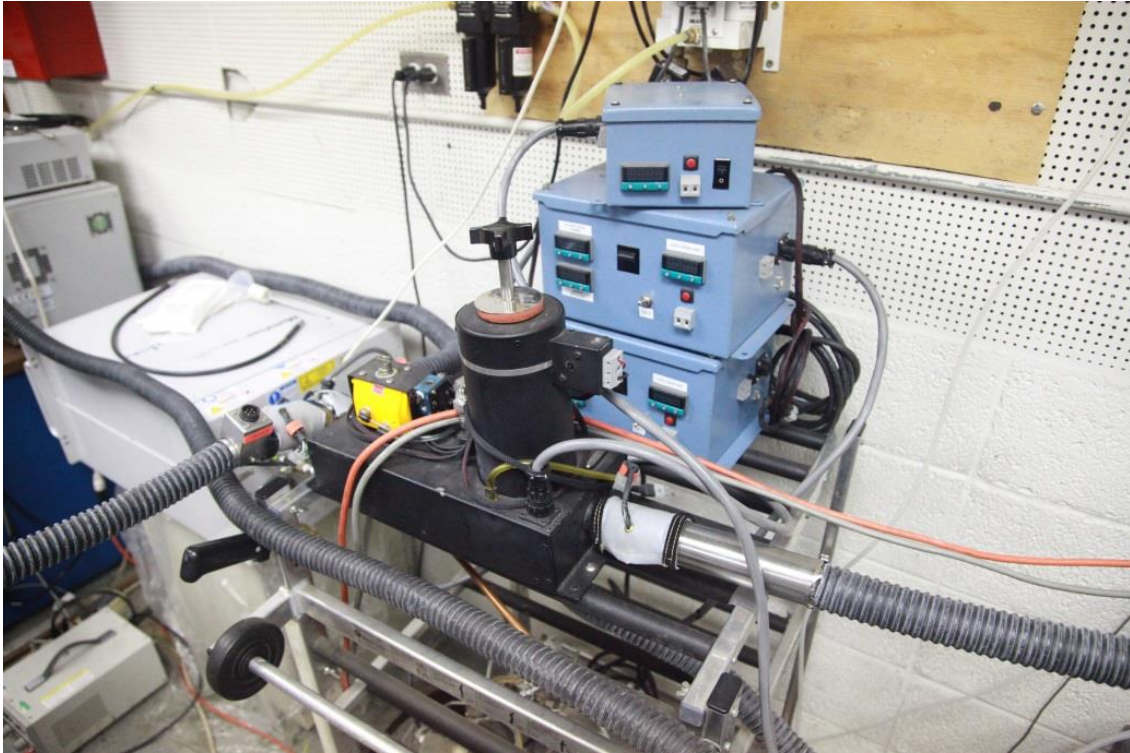


Figure 3.2.6 (c) Heated sampling line system

B. TSI Engine Exhaust Particle Sizer Spectrometer 3090

PM emission is measured by TSI Engine Exhaust Particle Sizer (EEPS) spectrometer 3090 in the current study. It is a special device dedicated to measure engine-out particle size distribution. The range of particle sizes is from 5.6 nm to 560 nm. The equipment is capable of fast measurement with 10Hz of sampling rate. Figure 3.2.7 shows the device, the schematic inside the spectrometer, and the cyclone attached at the inlet.

The exhaust air is pumped into the device through “Aerosol In” in Fig. 3.2.7. A cyclone is attached in front of the inlet, which is shown in Fig. 3.2.7(b), to remove large particles larger than the specified sizes of the instrument. All particles entering into the instrument go through an electrical diffusion charger where ions are

generated. These ions would mix with the particles to create various charge levels with respect to the particle sizes. After passing through the charger on the top of EEPS, all particles go downwards in Fig. 3.2.7. A stream of filtered sheath air will encounter the particles before hitting the measurement column. The particles will be deflected by the High-Voltage Electrode mounted at the center radially outward; since they have been charged with the ions previously, the particles will be collected by the electrodes(electrometers) located on the outer wall. The particle size distribution is then determined based on the electrical current measured by the electrometers. The exhaust flow rate and sheath air flow rate are controlled by the built-in pumps in the device, so all internal flows are regulated that the users only need to be aware of the flow rate at the aerosol flow inlet. The flow schematic of the EEPS spectrometer is shown in Fig. 3.2.8.

The entire EEPS 3090 is automated that there is no hassle for the users to operate the machine. However, the to-be-measured exhaust flow should be diluted prior to entering the device that the particle number should not exceed or below the upper and lower measuring concentration limits to obtain meaningful data. In the current research, a simple dilution tunnel is used with a fixed dilution ratio at 10:1 shown in Fig. 3.2.9.

The exhaust flow is firstly extracted from the exhaust pipe to a buffer container to reduce pulsation flow from the engine by a heated pump. Filtered shop air then is applied to mix with the exhaust flow, and the tunnel is heated to 191 °C to eliminate water condensation. A bypass is placed before the diluted exhaust flow entering into the EEPS spectrometer to get rid of excessive flow. It should also be

noticed that the sampling line is not heated at this point to cool down the flow to room temperature. The reason is that the particle size distribution at room temperature is more realistic that the spectrometer is designed to take the measurement at room temperature.



Figure 3.2.7 (a) TSI EEPS 3090 (left) and the cyclone (right)

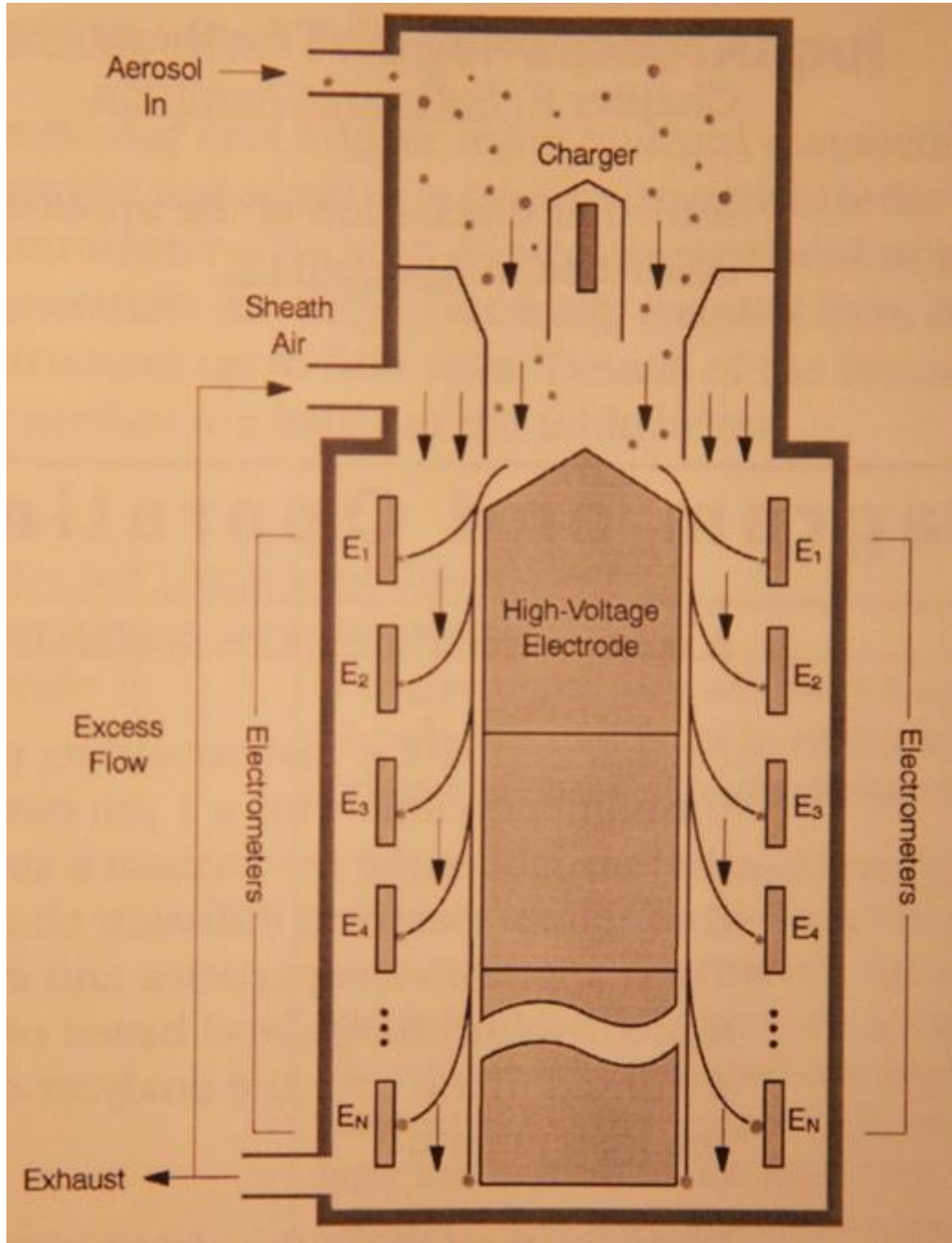


Figure 3.2.7 (b) EEPS schematic [107]

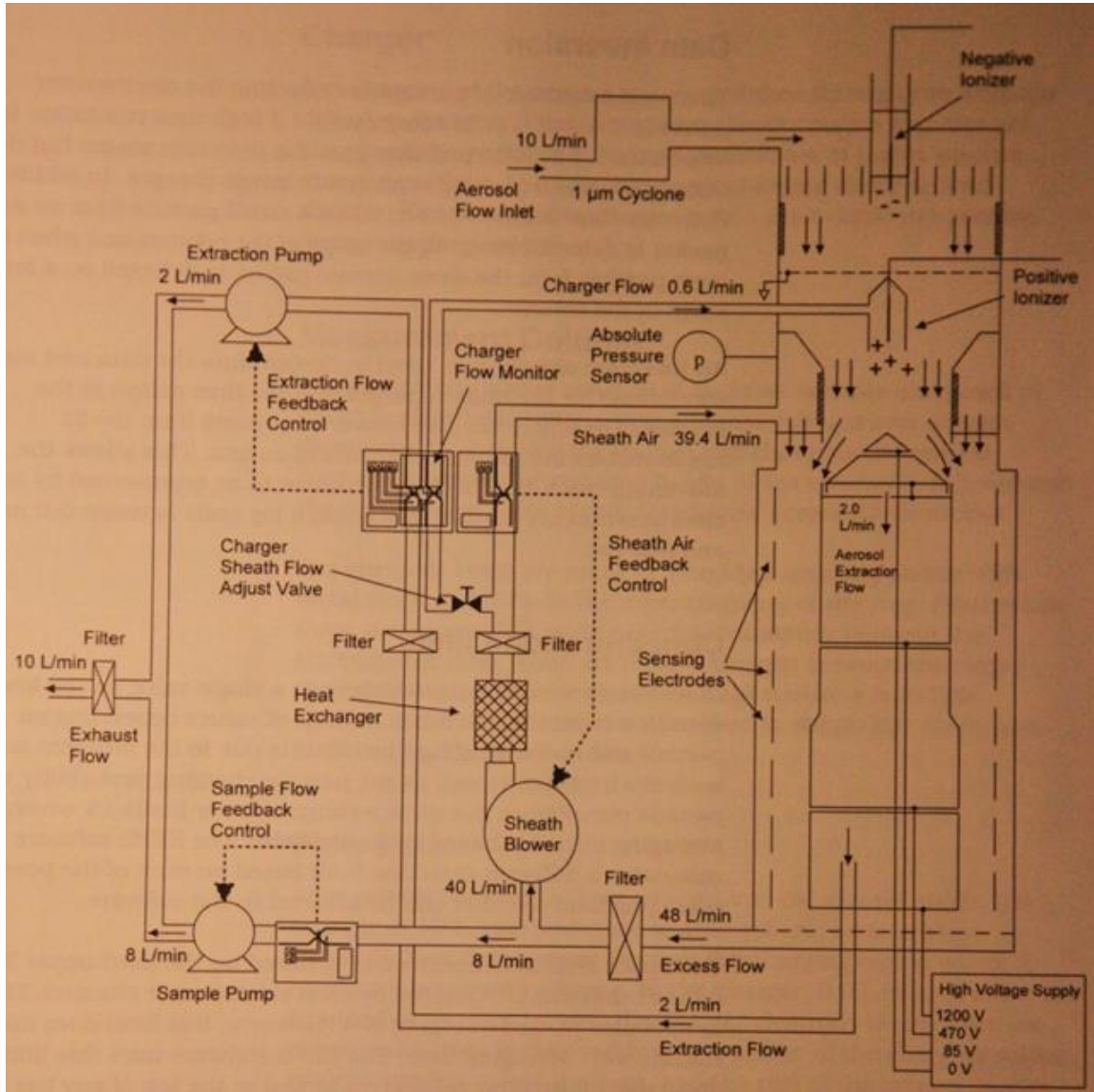


Figure 3.2.8 TSI EEPs 3090 flow schematic [107]



Figure 3.2.9 Dilution tunnel

3.3 Cameras and Imaging Process Methods

The following content will describe the details of image analysis.

3.3.1 High Speed Camera - Color

Figure 3.3.1 shows the high speed color camera (Phantom V310, Vision Research) used in the study. It has the capability up to 1 megapixel, 1280 X 800 resolutions, or 500000 frame per second (fps) speed depending on the setup. A custom-designed CMOS sensor is used inside the camera. It also has the trigger and memory-gate ability to synchronize with an external clock like the crank angle encoder used in the research. The spectral response chart is shown in Fig. 3.3.2. The blue color detected by the camera is ranged from 375 nm to 550 nm

wavelength; the green color is from 450 nm to 650 nm; the red color is from 575 nm to 675 nm. As shown in Fig. 3.3.2, the response of the blue color is lower than the other two colors in this camera, so higher noise in blue would be expected, which is also observed from the image results. An ultra-violet compatible lenses is used (UV-NIKKOR, 105 mm focus, 1:4.5 aperture) in order to capture the UV light from the combustion process.

The camera could also be used as a monochromatic one. The change is done via windows command prompt, which could be found in Accessories folder or by typing “cmd” under Start. The command lines are listed below. 100.100.111.205 is the IP address of the camera, and the “0” or “3” after info.cfa is to switch the camera between color (3) or monochrome (0).

- telnet[space]100.100.111.205[space]7115[enter] [enter]
- set[space]info.cfa[space]0
- set[space]info.cfa[space]3

If the camera is in monochrome mode, the image is presented as shown in Fig. 3.3.3. This is because different filters are used on the camera chip with respect to different color. Figure 3.3.4 shows the filters configuration in an image. The actual spectral responses are obtained in monochrome mode since the color images are the results of interpolation of the monochrome ones. Extra image process will be needed if the conversion to color images is necessary, such as the 2-color method study. In the current study, only the color mode is used to analyze the combustion process. It should be noticed that the most bottom-left pixel is always a red filter regardless of the image size for this specific camera.



Figure 3.3.1 Phantom V310 (color)

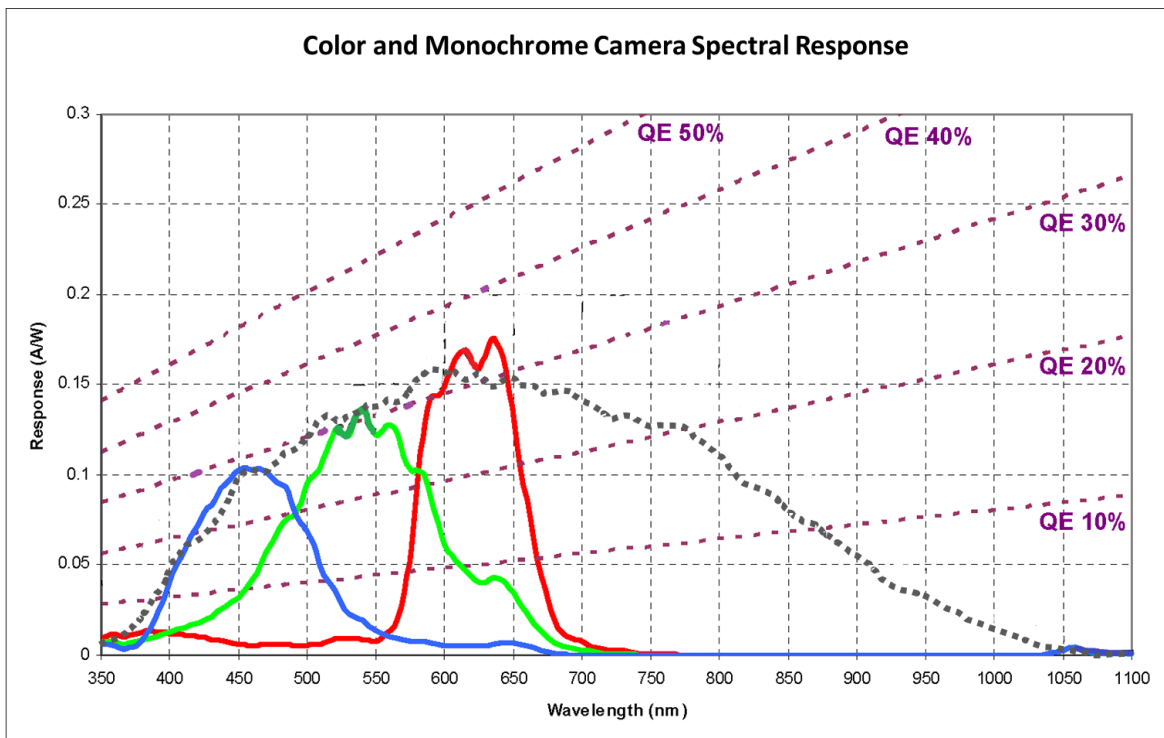


Figure 3.3.2 Spectral response of Phantom V310 (color) with V7.3 (monochrome)



Figure 3.3.3 Monochrome image from Phantom V310

R	G	R	G	R	G	R	G	R	
G	B	G	B	G	B	G	B	G	
R	G	R	G	R	G	R	G	R	
G	B	G	B	G	B	G	B	G	...
R	G	R	G	R	G	R	G	R	
G	B	G	B	G	B	G	B	G	
R	G	R	G	R	G	R	G	R	

Figure 3.3.4 Filter configuration of Phantom V310

3.3.2 High Speed Camera - Monochrome

Phantom V7.1 from Vision Research is used in the current study. It is a monochromatic high speed camera, which is capable of up to 800 X 600 resolutions or 10000 fps depending on the setup. Figure 3.3.5 and 3.3.6 show the camera and its spectral response, respectively. The sensitivity of this camera is higher (much lower noise) than the aforementioned color camera since it only reads black and white. The camera is suitable for the flame propagation or combustion luminosity study from the engine testing and the Schlieren imaging technique for the spray measurement. Synchronization with an external timing source is also possible in this camera.

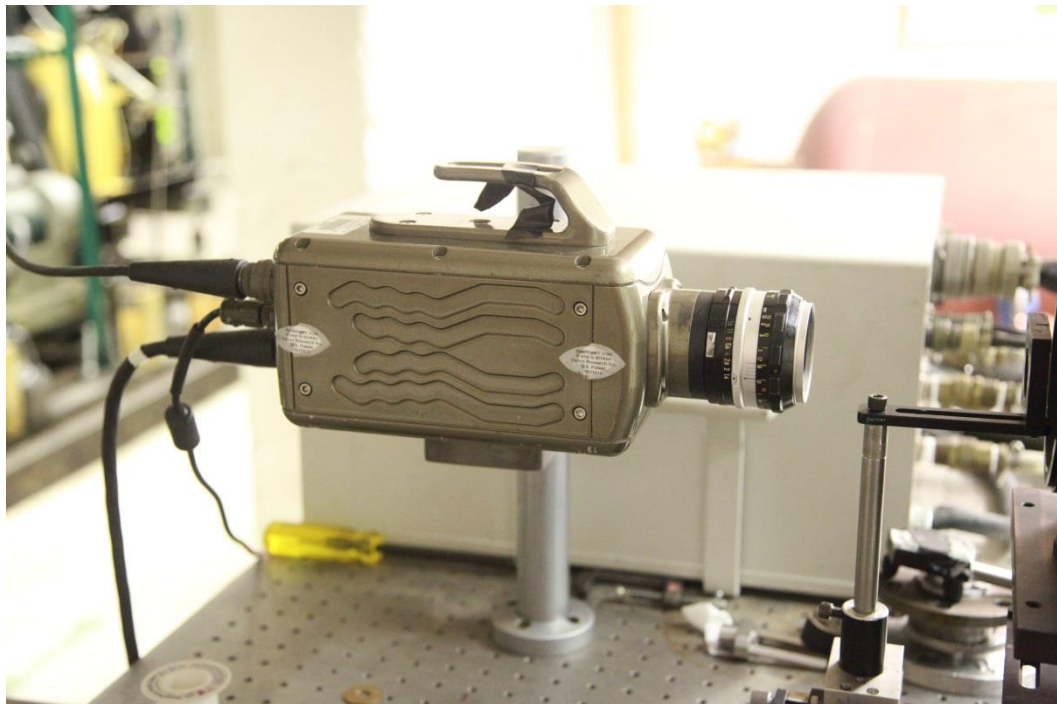


Figure 3.3.5 Phantom V7.1 (monochrome)

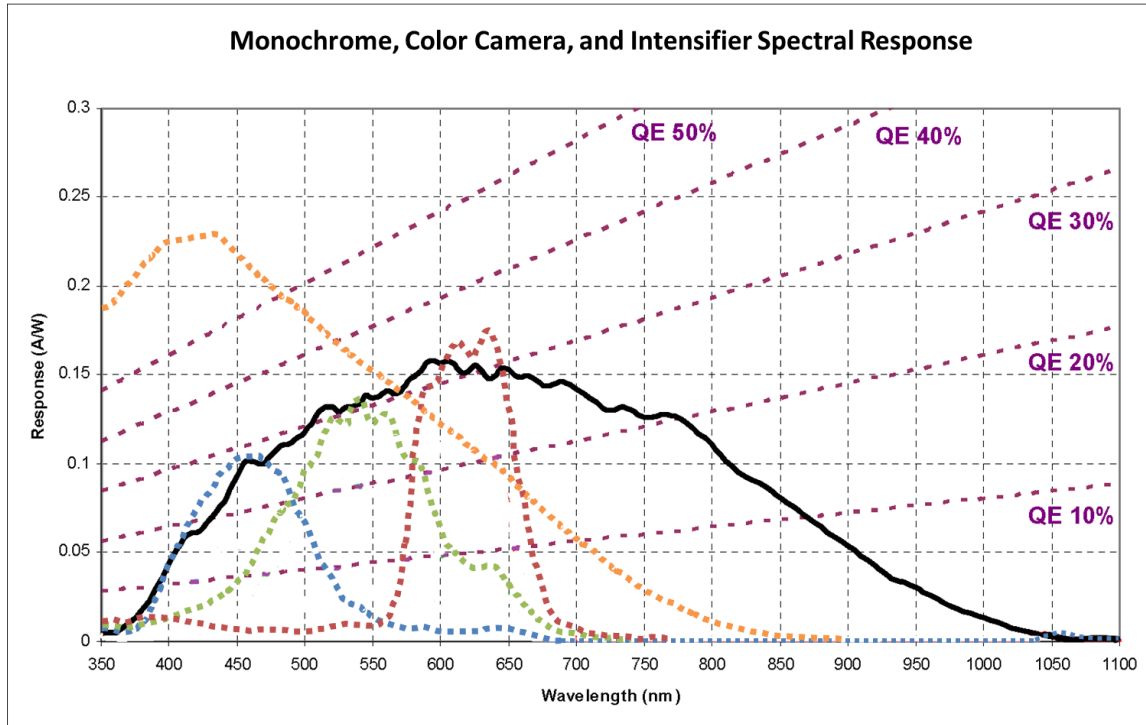


Figure 3.3.6 Spectral response of Phantom V7.1 (monochrome) with V310 (color) and intensifier [109]

An intensifier (HiCATT 18, Lambert Instruments) is used with the monochrome camera in most engine combustion research to enhance the light intensity. The device and its spectral response are shown in Fig. 3.3.7 and 3.3.8, respectively. The near-UV light regime is emphasized by the intensifier. It could also be synchronized with the camera by an external timing source. A NIKKOR 60 mm 1:2.8 lenses is used if the camera and intensifier are used on the mOAE; otherwise, the aforementioned UV lenses is used mostly.



Figure 3.3.7 Intensifier

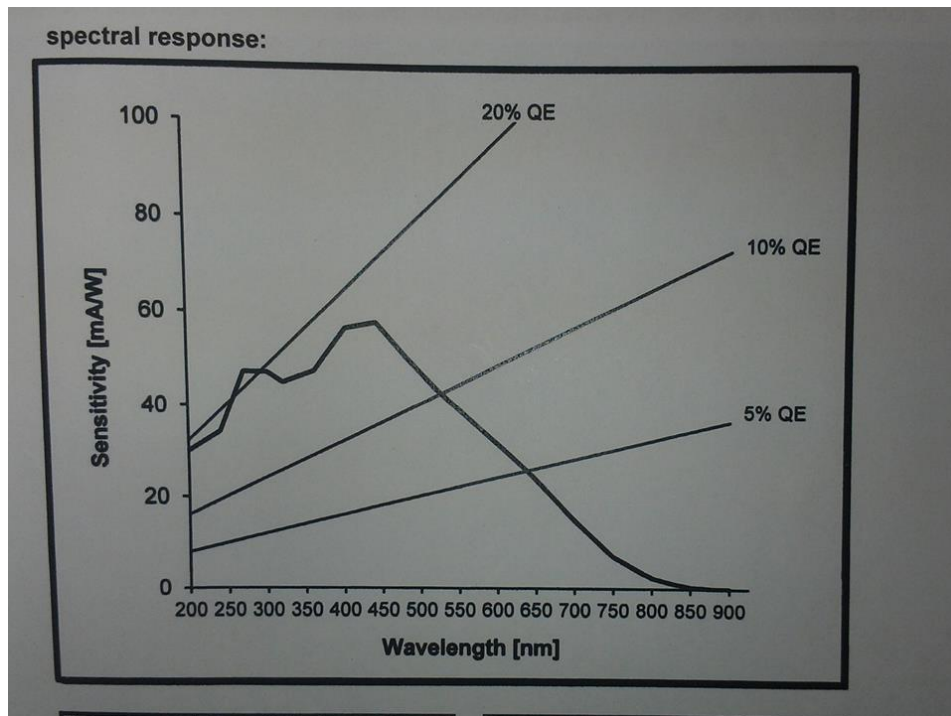


Figure 3.3.8 Spectral response of the intensifier [110]

3.3.3 Low Speed Camera - Spectrometer

A CCD camera coupled with a spectrometer is also used in the current study (PI-MAX 2 with ACTION SpectaPro 2150i, Princeton Instruments). Figure 3.3.9 shows the setup of the camera and spectrometer. It is used on the sOAE via the bottom view to analyze the in-cylinder gas species during the combustion process. Since it is low speed, only one shot per cycle is captured. The system could also be synchronized with an external timing source to capture the image at different crank angle degree; however, multiple tests would be needed due to its low speed. The calibration spectra of the spectrometer are shown in Fig. 3.3.10, which is used for the system calibration by the software; it should be noticed that the system is not calibrated with respect to the lens or gratings.

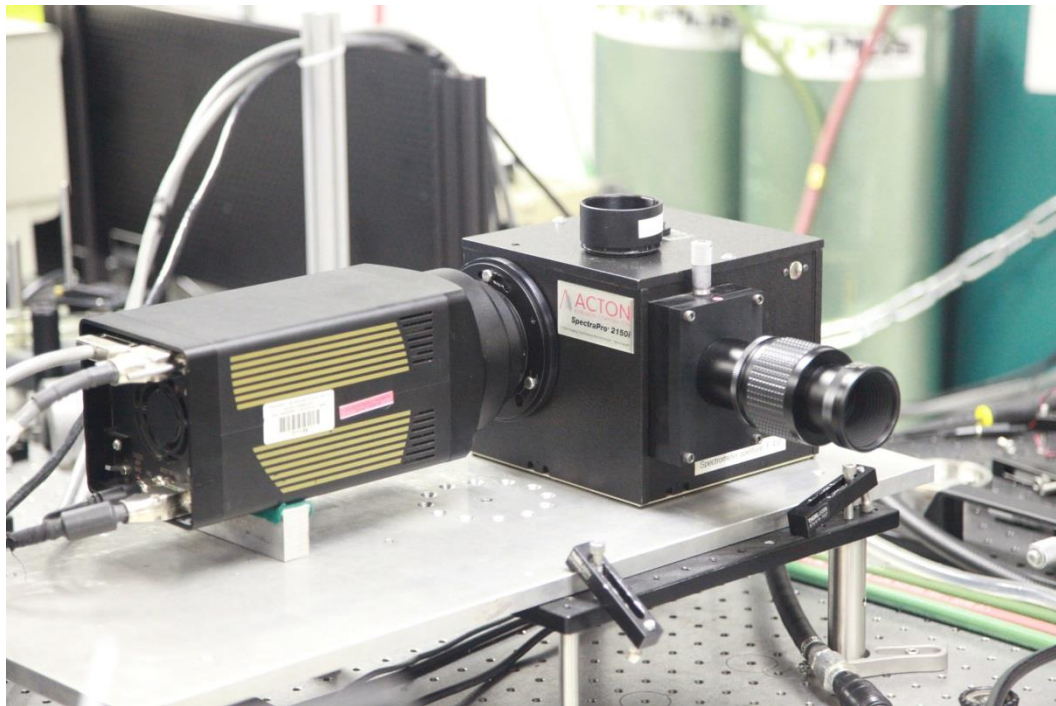


Figure 3.3.9 PI-MAX2 with the spectrometer

3.3.4 Image Process Methods

Several image process methods are implemented in the current study to fulfill various approaches to analyze the combustion process of GDI engines. Raw images directly from the cameras and statistical images calculated based on a set of images are both presented. In general, images from the sOAE are the results of up to 30 cycles of combustion; those from the mOAE are from 50 cycles of combustion. All image process methods are computed through author-developed code in MATLAB.

Method A: Equivalent circle area as the effective flame area (monochrome images)

This method calculates the flame areas directly from the raw images (monochrome) and uses a circle with equivalent areas to represent the flame. Flame in raw images is firstly contoured by setting a threshold to distinguish the black area and the flame in the images. The images then are binarized that pixels inside the contour are numbered 1 (white) and the rest are numbered 0 (black). All pixels with value 1 are counted, and a circle with equivalent pixel count could be generated. The area of the flame is therefore computed. Since the images are captured by the monochromatic camera with the intensifier, the boundary of the flame is clearly identified with minimal inaccuracy. Similar methods have been proposed by other researchers [112]. Figure 3.3.11 illustrates the process.

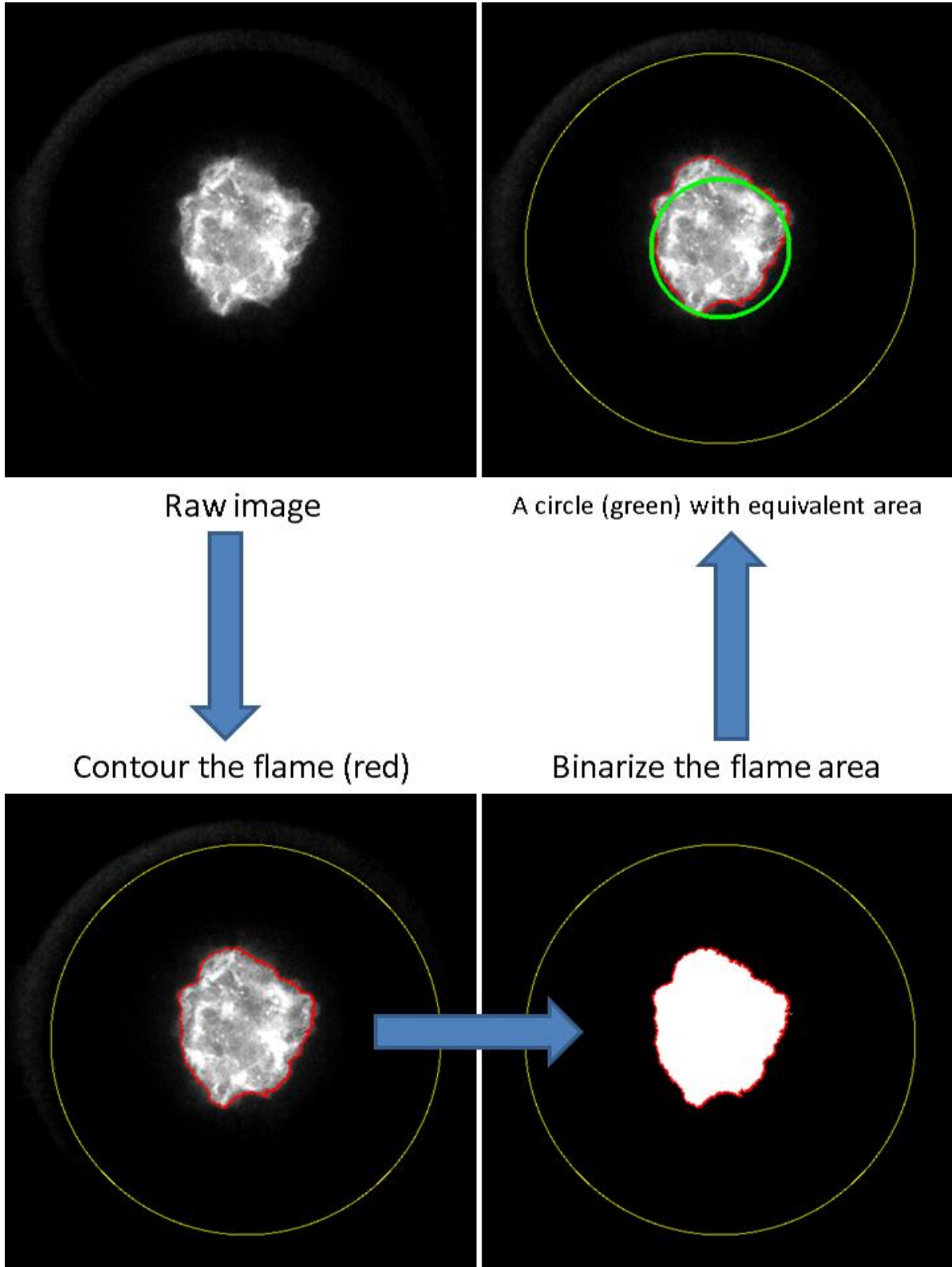


Figure 3.3.11 Method A illustration

Method B: RGB values of images (color images)

Since the color camera could detect three colors of the light with respect to wavelength, Method B utilizes the RGB values captured by the camera. Each color value, red, green, and blue, is summed in the effective view circle from images, and the summed values are then divided by the view area to represent the averaged RGB values in the images. Because the images are synchronized with the crank angle degree, the averaged RGB values could show the progress of the combustion. Even though detailed spatial resolutions are lost in this method, the temporal difference of the combustion process could be compared and studied. Equation 3.3.1 shows the calculation of the averaged RGB values, and the image process method is demonstrated in Fig. 3.3.12.

$$\bullet \quad RGB_{average} = \frac{\sum_{i=1}^{i=n} (Red, Green, or Blue Value)}{Area_{effective}} \quad (\text{Equation 3.3.1})$$

,where Red, Green, or Blue value: the value of a pixel of a raw image based on 16-bit unsigned integer (uint16) from 0 to 65535; Area_{effective}: the area of an image where the actual combustion chamber is shown (RGB values of pixels in the area are computed); i = 1...n: the ith pixel in the effective area; 1 is the first one and n is the last one

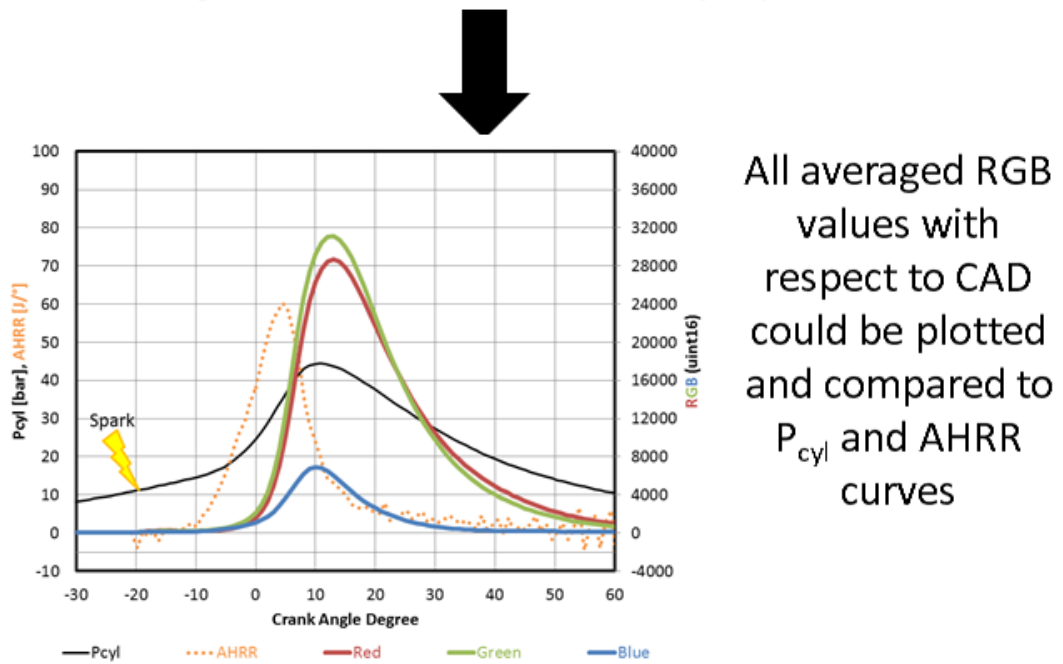
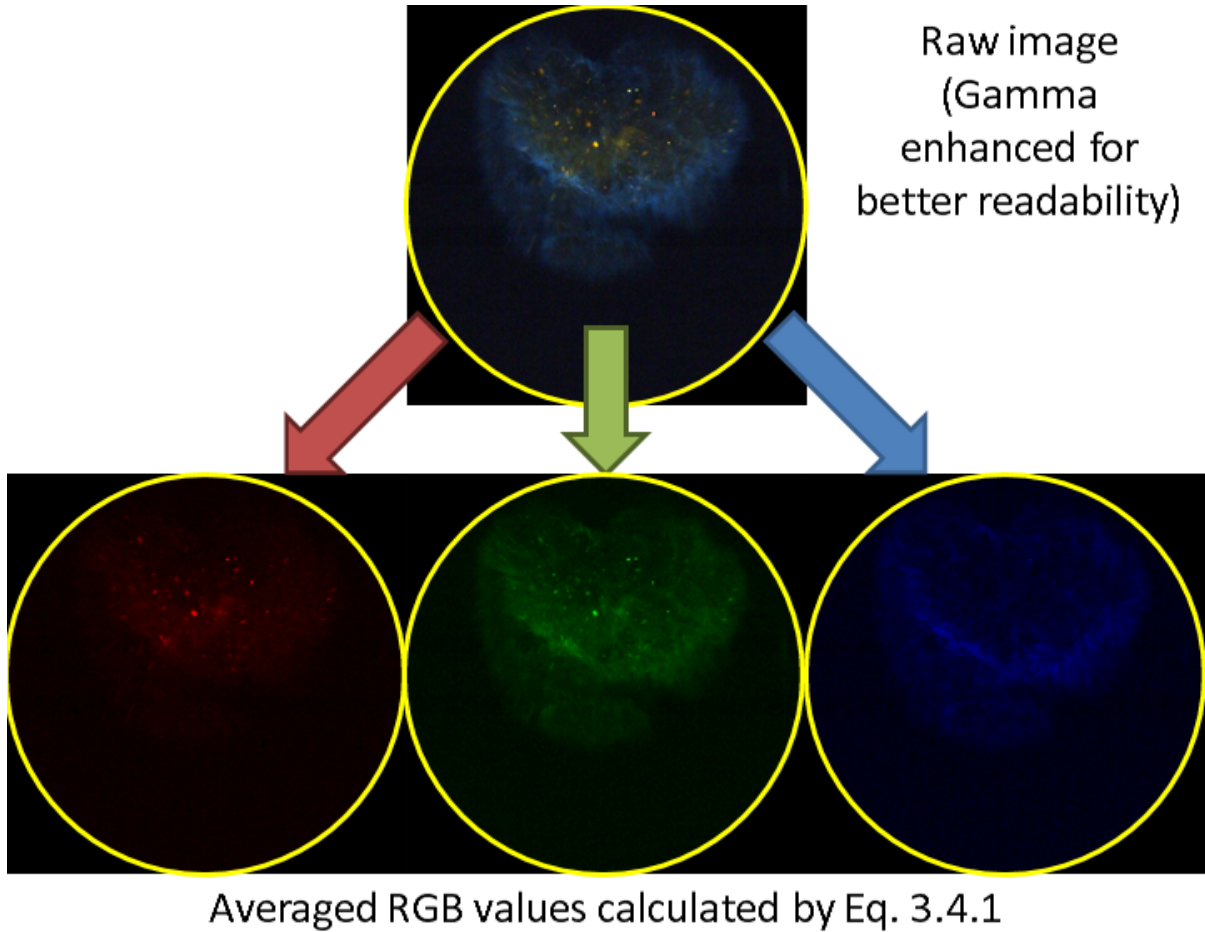


Figure 3.3.12 Method B illustration

Method C: Statistical probability images for sOAE flame propagation

A statistical probability method is used to characterize the flame propagation. Where the flame would be present in the view is computed as the flame probability (progress variable) with respect to crank angle degree. For example, if 10 cycles of combustion images are obtained in a test, there are 10 images at the same crank angle degree. These 10 images at the same degree are binarized to define the contour of the flame, and then a new image could be formed with summed binary values (0 to 10 in this case) on each pixel. After divided by the number of images (10 in this case), the flame probability would be shown as 0 (least likely) to 1 (most likely) on each pixel. This method was used in [113] and is shown in Fig. 3.3.13. In the current study, both monochromatic and color images could be used; however, only the blue color is computed by this method if color images are used.

Method D: 2-D to 1-D flame propagation image in mOAE

The 2-D images acquired from the mOAE are the side view of the combustion chamber; therefore, the flame propagation could be studied if the images are compressed to 1-D. Due to the low luminosity even with the usage of intensifier, the flame propagation could be defined as along with the intake valve side, the exhaust valve side, or at the center (spark plug). Although detailed spatial resolution is sacrificed in this method, the flame propagation could be qualitatively characterized with respect to time. Figure 3.3.14 illustrates the method, and the resultant image could be compared with in-cylinder pressure trace as well as the AHRR curve.

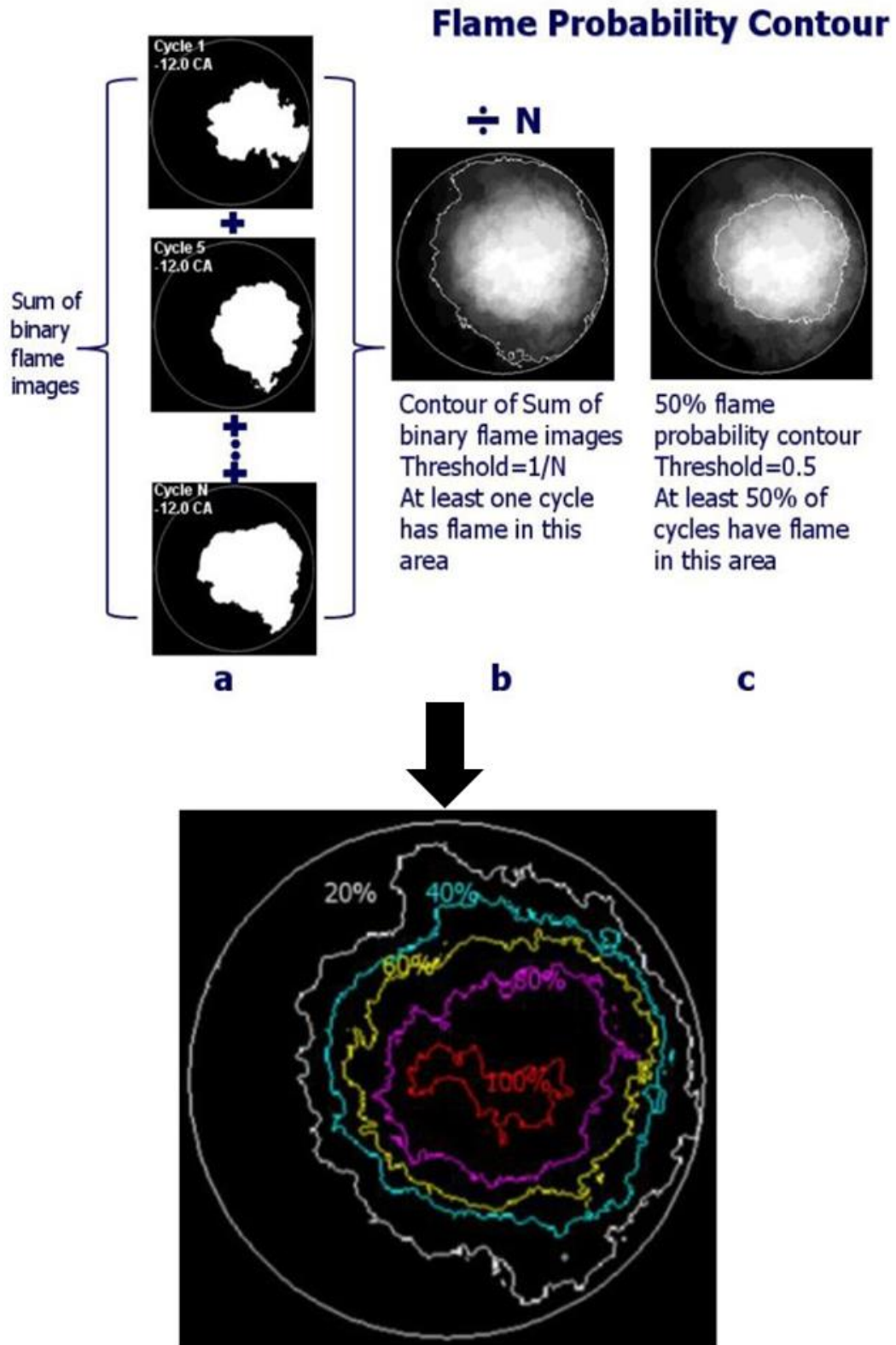
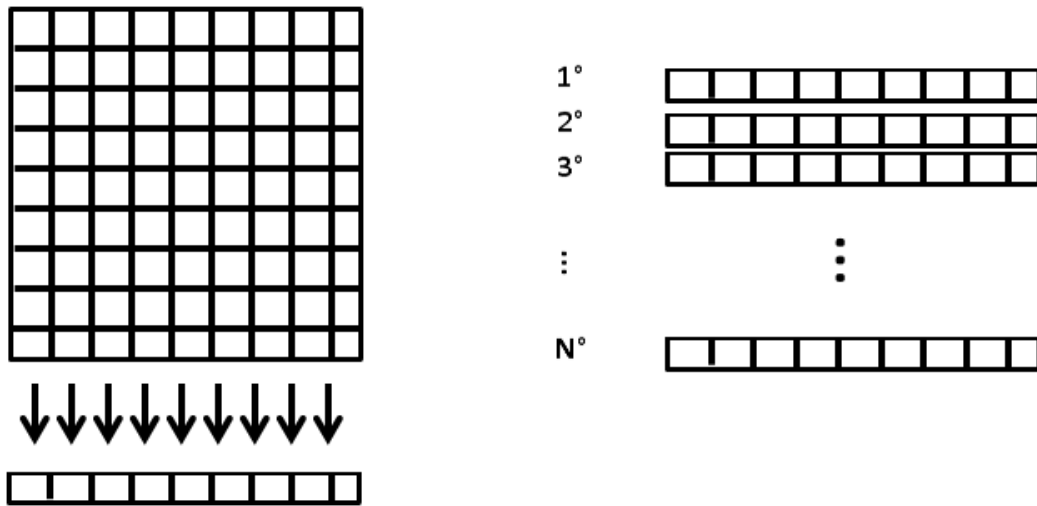
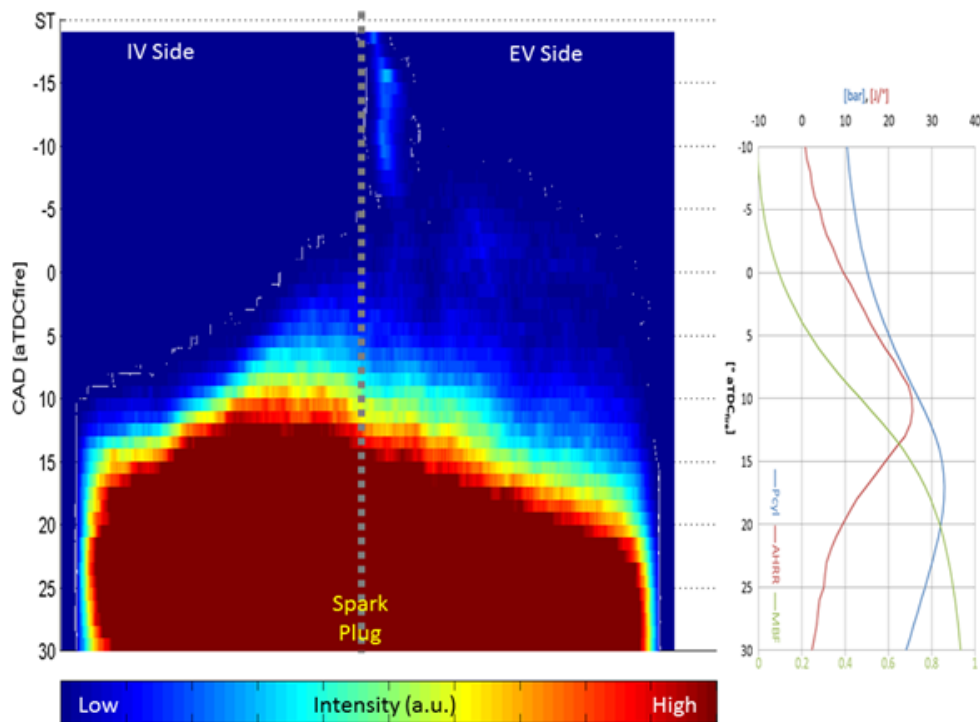


Figure 3.3.13 Method C illustration [113]



(a) Integrating each column of pixels to form a 1-D array

(b) Stacking each array to form a temporal image with 1-D spatial information

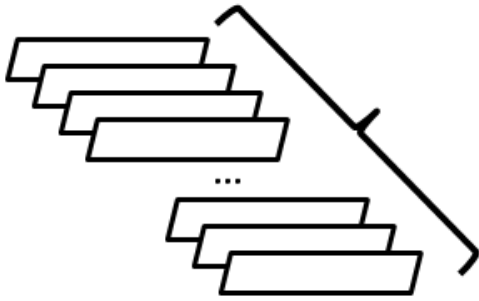


(c) Flame propagation vs CAD with combustion data aside

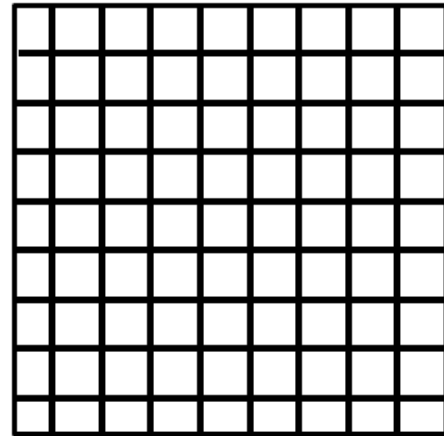
Figure 3.3.14 Method D illustration

Method E: 2-D PDF and standard deviation image in mOAE

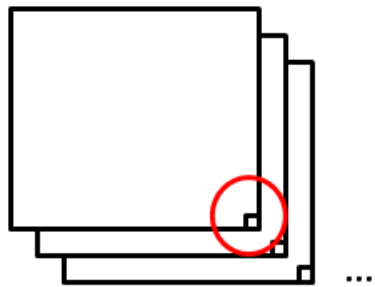
This method utilizes the probability distribution function and standard deviation to characterize the flame propagation. 50 cycles of combustion images are obtained via the high speed camera, so there are 50 images at each crank angle degree. Light intensity at the same pixel on the images is then calculated by the probability distribution function, and the standard deviation is also computed. Two new statistical images are formed to present the most possible light intensity on each pixel (PDF image) and the variation of the intensity values (standard deviation image). This method is the modification of the one found in [114], which only considered an averaged value from each image. The current method is able to retain the spatial and temporal resolution that the combustion process could be therefore analyzed from the beginning to the end. Figure 3.3.15 shows the process of a PDF image.



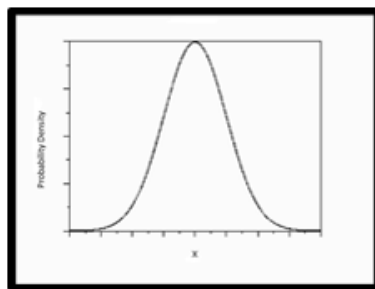
(a) 50 cycles of raw images at the same crank angle degree



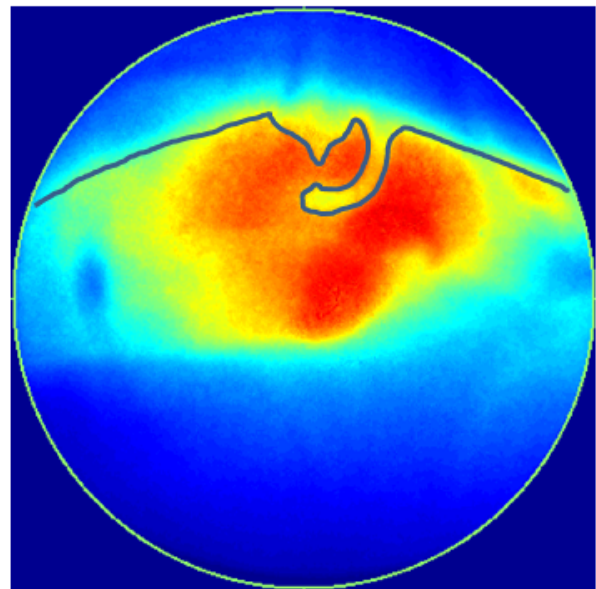
(d) Redraw all pixels with the most possible intensity form a statistical intensity image



(b) 50 intensity values collected at each pixel



(c) Calculate PDF and find the most possible intensity at each pixel



(e) Adapt with artificial colors

Figure 3.3.15 Method E illustration

3.4 CFD Simulation Setup - CONVERGE

The air-fuel mixing and combustion processes are simulated by using CONVERGE in the present study. The software is built by Convergent Science, Inc. The avoidance of the meshing process (grid generation) by users is realized, which will speed up the simulation time for analysis. Many researchers have used the software for in-cylinder fluid dynamics study as well as combustion [13, 19].

Figure 3.4.1 shows the geometry of the single cylinder of the GDI engine with both flat (sOAE) and production (mOAE) piston tops. The mesh size is set 4 mm, and the Adaptive Mesh Refine (AMR), which is a specially designed function in CONVERGE, is also implemented around the critical zones, such as the vicinity of the injector or the spark plug. The mesh size around the injector is 0.25 mm, and that around the spark plug is 0.125 mm by the AMR. The computational time step is set at 0.000001 s (1 μ s).

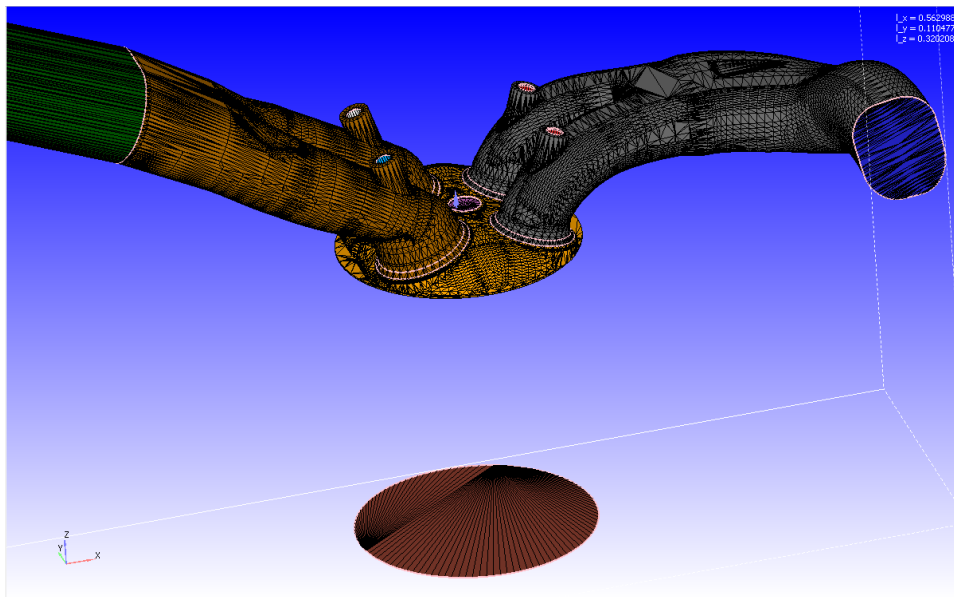


Figure 3.4.1 (a) sOAE piston with cylinder head

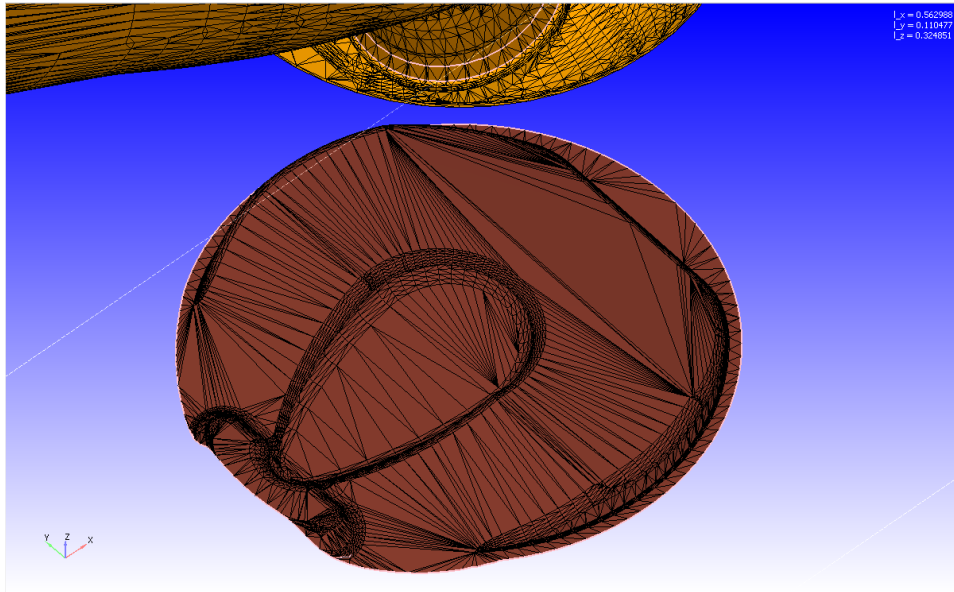


Figure 3.4.1 (b) mOAE piston

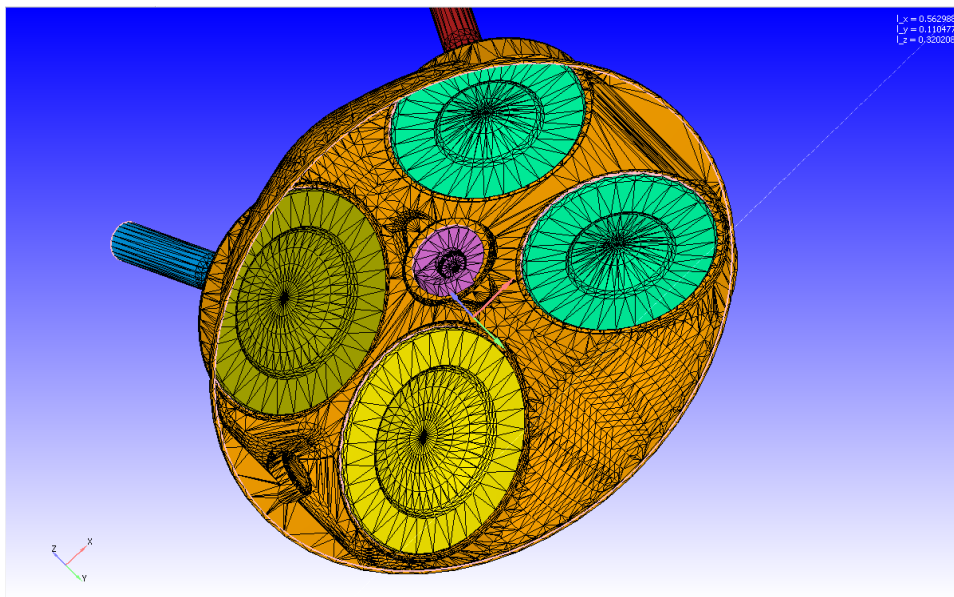


Figure 3.4.1 (c) Combustion chamber

The Kelvin-Helmholtz and Rayleigh-Taylor (KH-RT) combined model is used for the droplet break-up simulation and the No Time Counter (NTC) method is selected for the droplet collision model. Turbulence is simulated by the Renormalization Group (RNG) k - ϵ model, which is a Reynolds-averaged Navier-Stokes (RANS) model. A detailed chemical kinetics model, SAGE, is chosen for combustion simulation as suggested in [115]. Users would be permitted to set up the chemical reaction mechanism by CHEMKIM-formatted input files. A reduced dual component chemical reaction mechanism is used for RON 93 (93% iso-octane and 7% n-heptane by volume). Every zone in the computational domain would have similar thermodynamic conditions to reduce the complication.

CHAPTER 4 RESULTS AND DISCUSSIONS

The research results and discussions are described in this chapter. Various engine operation parameters are used to investigate their effects on combustion and emissions.

4.1 Engine Start-up Flame Propagation

To study the flame propagation through the very first few cycles as engine start-up process, a test condition listed below is implemented. Method A is used for image study.

Test condition:

- 600 rpm; MAP: 1 bar; Lambda: ~ 1.63 ; EGR 0%; 40°C intake air; 80°C coolant
- Injection timing: 300° bTDC_{fire}; injection pressure: 180 bar
- Ignition timing: 30° bTDC_{fire}
- Camera Frame Rate: 6000 fps

Figure 4.1.1 shows the image results of E0 combustion starting from the first cycle, and the flame progression contours of the first and the fifth combustion cycles are shown in Fig. 4.1.2. The images present that the first cycle is relatively weaker than the successive ones; even though the combustion is observed, the flame speed data, normalized with the mean piston speed and shown in Fig. 4.1.3, indicates that the first cycle has relatively slow flame propagation. Once the surrounding is developed, as seen in Fig. 4.1.1(b), the images show higher intensity, and the flame propagates faster as the results shown in Fig. 4.1.3. This test is done in lean condition, so the flame is expected to be faster if the air-fuel mixture is richer.

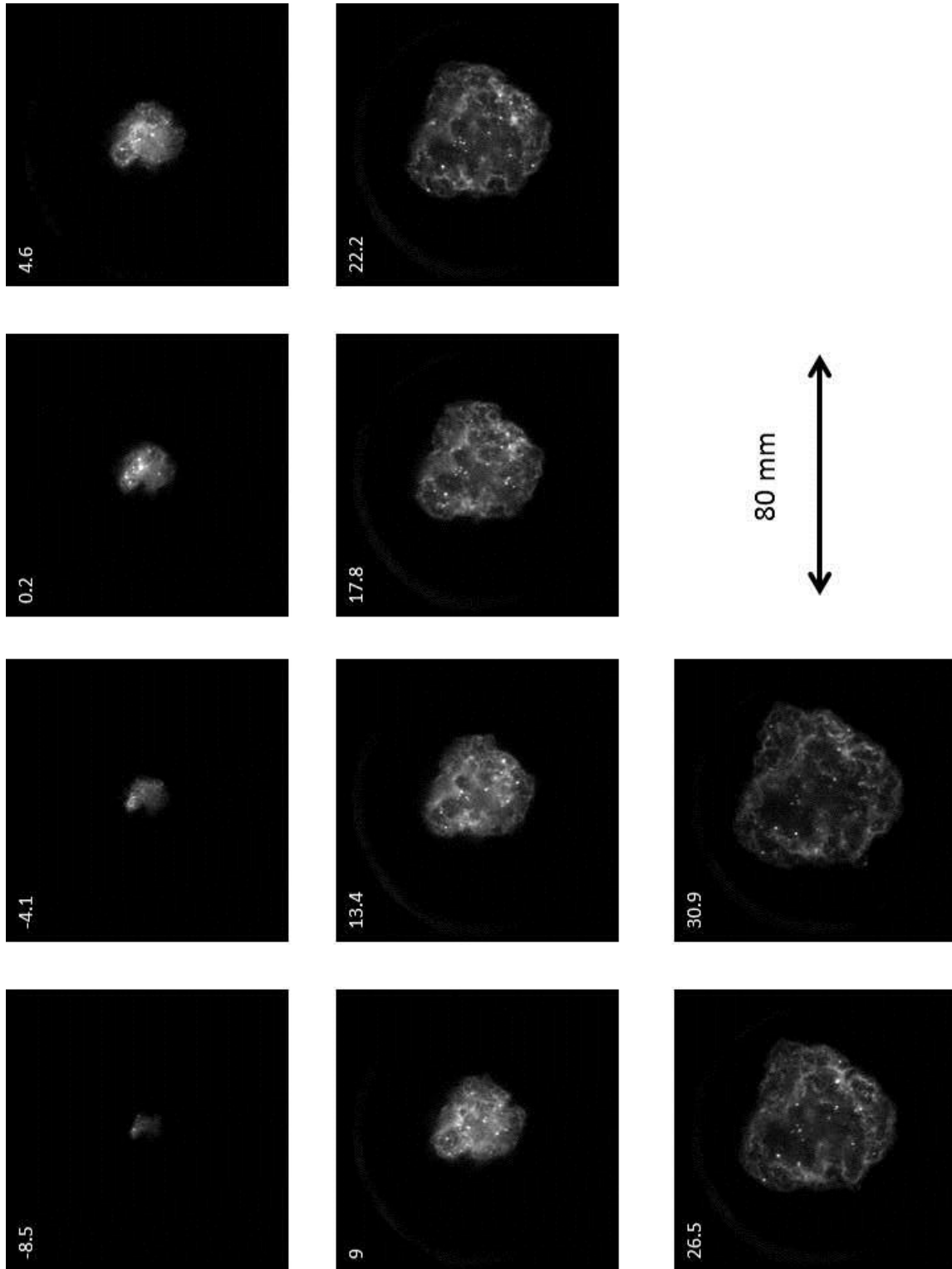


Figure 4.1.1 (a) E0 combustion at 1st cycle

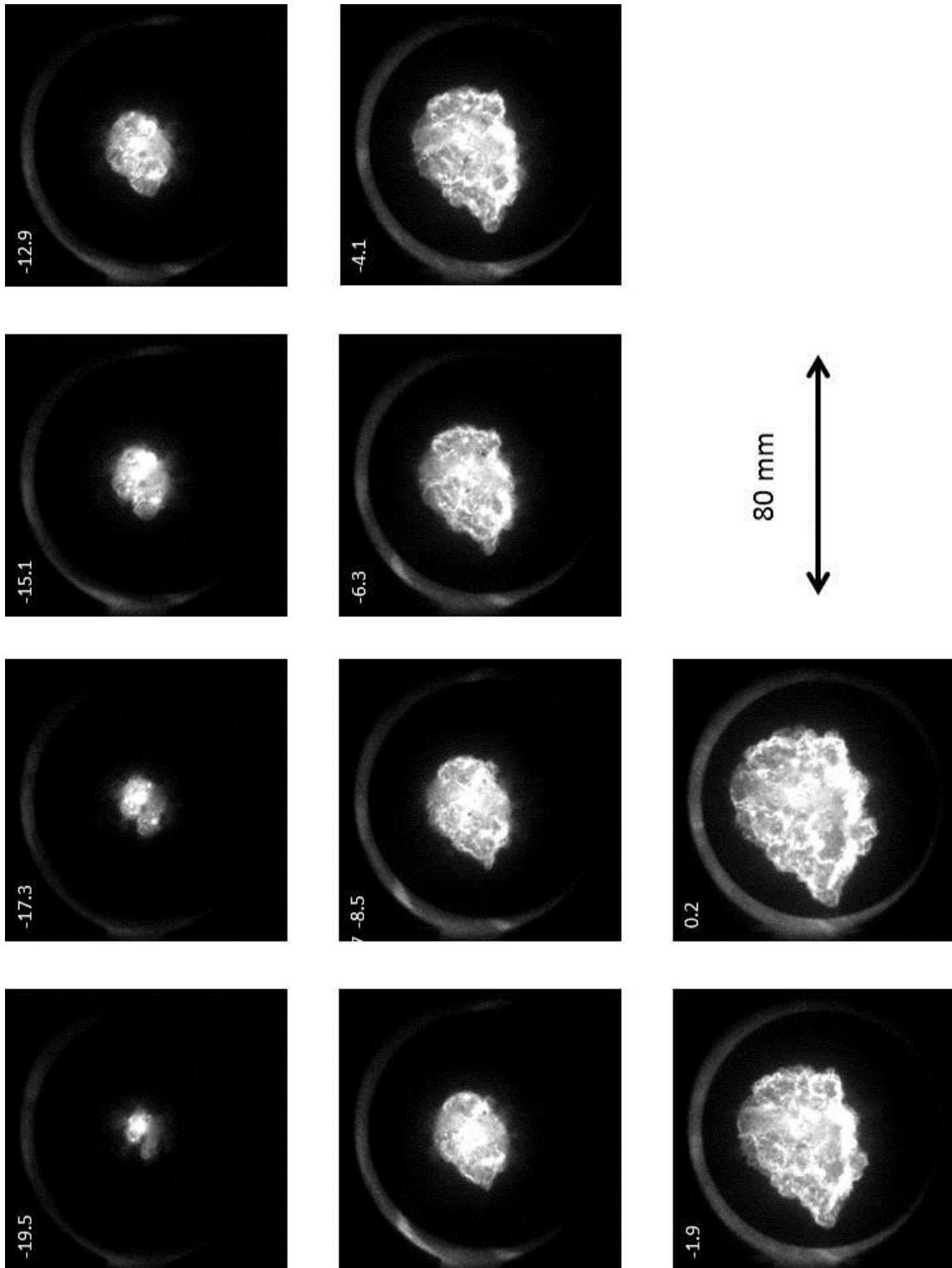


Figure 4.1.1 (b) E0 combustion after 1st cycle (5th cycle shown)

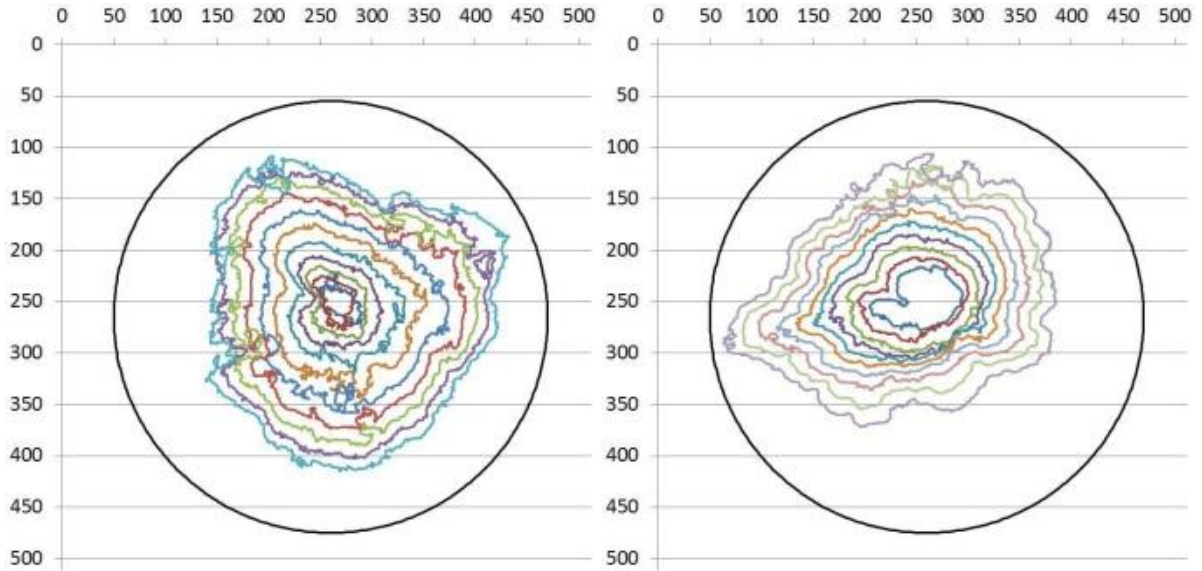


Figure 4.1.2 E0 flame contours at 1st cycle (left) and 5th cycle (right)

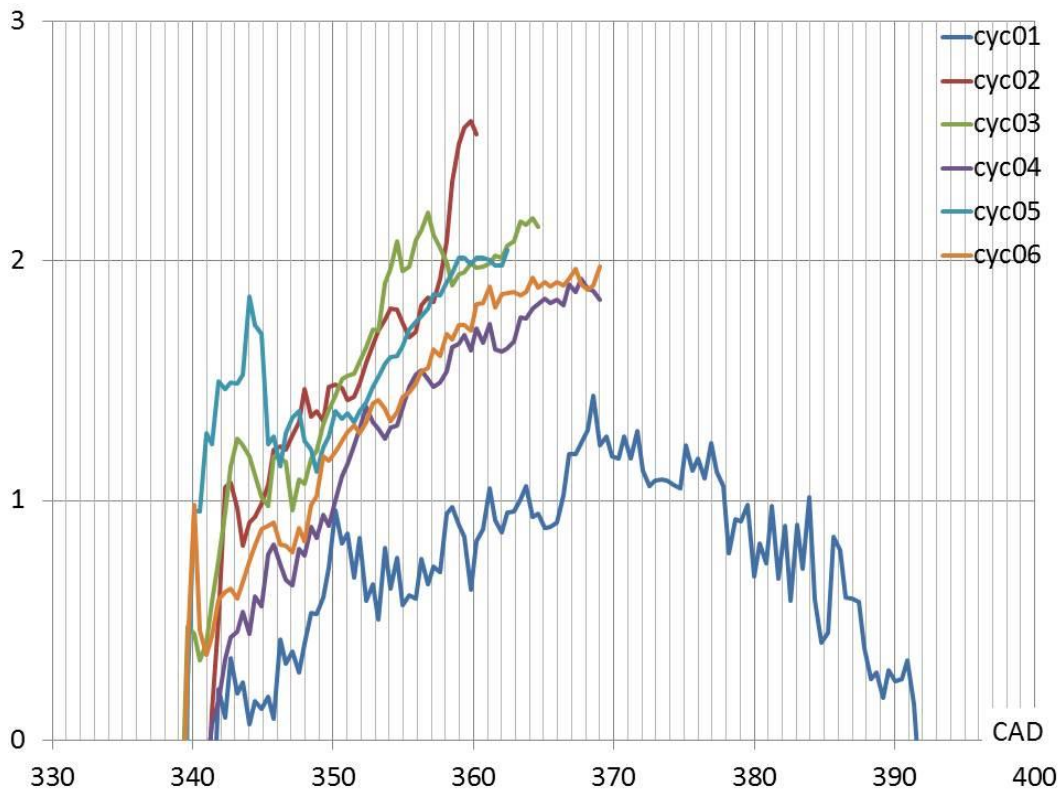


Figure 4.1.3 E0 flame speed of the first six cycles (Y-axis normalized by the mean piston speed)

4.2 E0 and E85 on Flame Propagation

The difference of E0 and E85 combustion is studied and presented in this section. The startability of both fuels is the objective that the first few cycles of combustion are investigated. Test condition is listed as below and Method B is used.

Test condition:

- 600 rpm; MAP: 1 bar; Lambda: ~ 1.63 (E0) and ~ 1.58 (E85); EGR 0%; 40°C intake air; 80°C coolant
- Injection timing: 180° bTDC_{fire}; injection pressure: 100 bar
- Ignition timing: 45° bTDC_{fire}
- Frame Rate: 6000 fps

The images of E0 and E85 combustion are shown in Fig. 4.2.1 and Fig. 4.2.2 along with their RGB values, respectively. The injection started at 180° bTDC_{fire} to signify the difference between E0 and E85 in this test. The averaged IMEP of E0 is 3.72 bar, and that of E85 is 4.51 bar; COV_{IMEP} is 47.76% for E0 and 6.81% for E85.

There is no combustion recorded in the first cycle of E0, so the images of the ensuing cycles are shown in Fig. 4.2.1(a). It is evident that E85 provides much stronger and more stable combustion than E0 does because the RGB values in Fig. 4.2.2 are higher than those in Fig. 4.2.1(a).

The first cycle of E85 is relatively weak comparing with the ensuing cycles. However, E85 provides better startability since there is no combustion in the first cycle using E0. This is because that ethanol has lower boiling temperature than most of the heavy components of E0, which would indicate better fuel vaporization

and atomization; moreover, there is more fuel vapor available for ignition since more E85 fuel is injected than E0 to compensate its lower energy content. The trend may be reversed at even lower ambient temperature when not enough heat in the charge air is available to vaporize the fuel.

It should be noted that the blue values have similar magnitude between all cycles and the two types of fuel. In Fig. 4.2.2, it is seen that the peak of the apparent heat release rate (AHRR) coincides with the blue color. The correlation is not as strong for the E0 case in Fig. 4.2.1(a), but the start of the blue color and AHRR still occur at the same time. This may indicate that the blue flame, which is representative of the lean flame, is correlated to the flame propagation and responsible of most of the heat release.

Comparing the images at 15° bTDC_{fire}, 0° aTDC_{fire}, and 15° aTDC_{fire} (namely, -15, 0, and 15) in Fig. 4.2.1(a) and 4.2.2, it is shown that blue color starts and peaks earlier than the red one, with the green one in between, indicating richer pockets in the later combustion processes, where soot burn-out is taking place. Higher peak pressure is observed for E85 cases than E0 ones because of more complete combustion. Due to better startability, the ensuing experiments are conducted with the utilization of E85 on both the OAE and metal engine.

Figure 4.2.1(b) shows two spectra of the E0 combustion, one at TDC_{fire} and the other one at 15° aTDC_{fire}. It is seen that OH* exists through the period of combustion from the spectrometer measurement; however, CH₂O* and CH* may be covered by the stronger chemiluminescent light from CO-O* and some blackbody radiation from soot particles in the later stage during the combustion. From Fig.

3.3.2 it is known that the blue color from the high speed camera is from 375 nm to 575 nm, so it may partially present some combustion products, such as CH_2O^* and CH^* ; however, OH^* wavelength is beyond the capability of the color camera that it should not be represented by the blue flame (i.e., the blue values) from the camera.

To further study the intermediate combustion species, a simple method is used to estimate according to the blue-to-red ratio (BR ratio) and blue-to-green (BG ratio) ratio from the images. From Fig. 3.3.2, the BR ratios around 380 nm, 500nm, and 650 nm are about 2, 7 and 0.07, respectively; the BG ratios around 380 nm, 500nm, and 650 nm are about 2, 1, and 0.25, respectively. Analyzing the averaged blue, green and red values from Fig. 4.2.1(a) and Fig. 4.2.2(a), it is found that wavelength of 380 nm is predominant at TDC_{fire} , and wavelength of 500 nm or greater is primarily present afterwards. This could be used for quick estimation of in-cylinder intermediate species during a combustion event since setting up a spectrometer could be very cost- and labor- intense.

On the other hand, this simple method may not be applicable if the blue and red/yellow flame is not distinguishable enough, which is usually the case of fast flame propagation, strong combustion, or rich air-fuel ratio conditions. Figure 4.2.2(b) illustrates the limit of this method as the averaged green and red values are high at the beginning of combustion. The BR or BG ratio does not represent the spectra of camera.

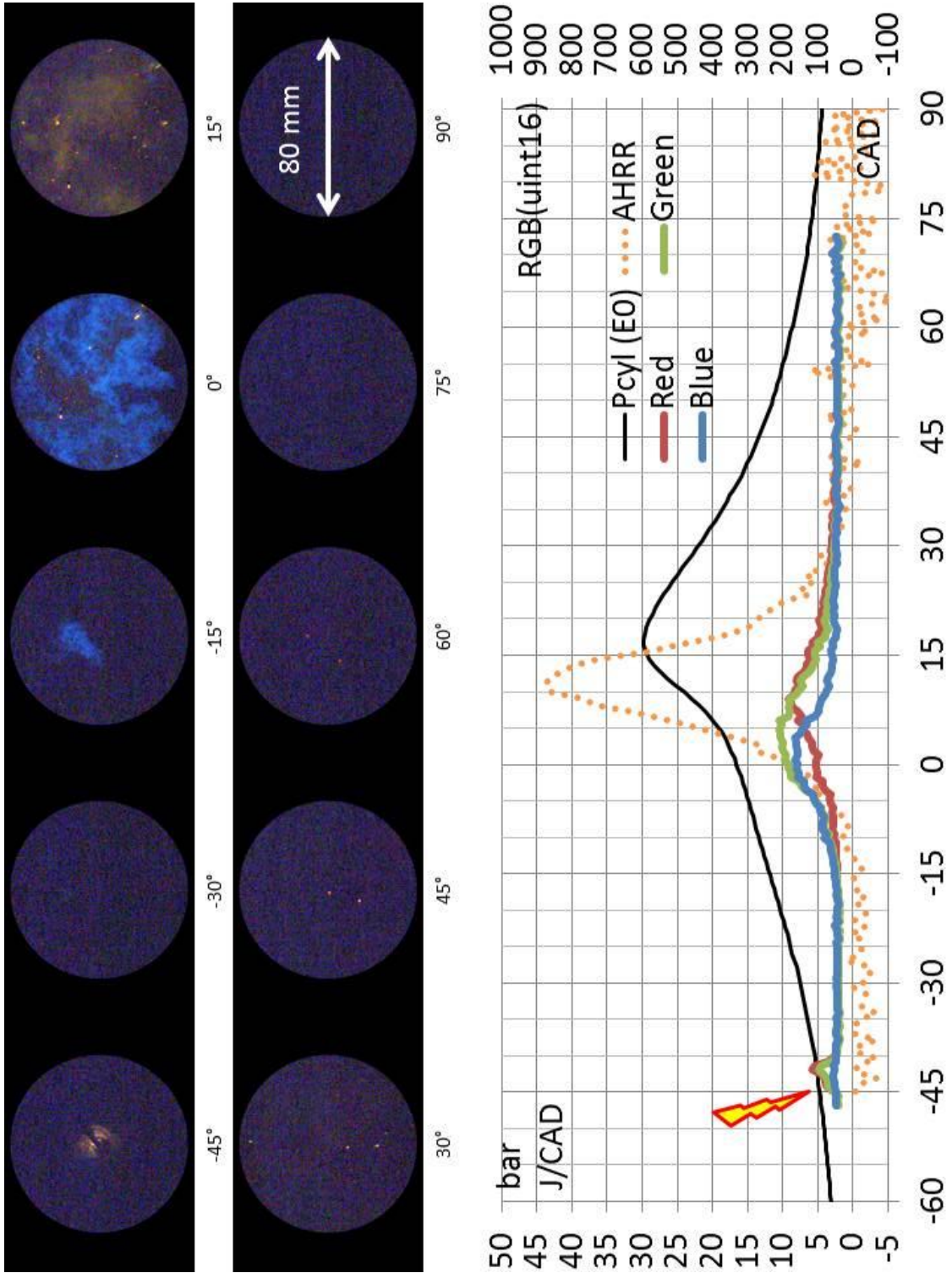


Figure 4.2.1 (a) E0 combustion after 1st cycle (5th cycle shown)

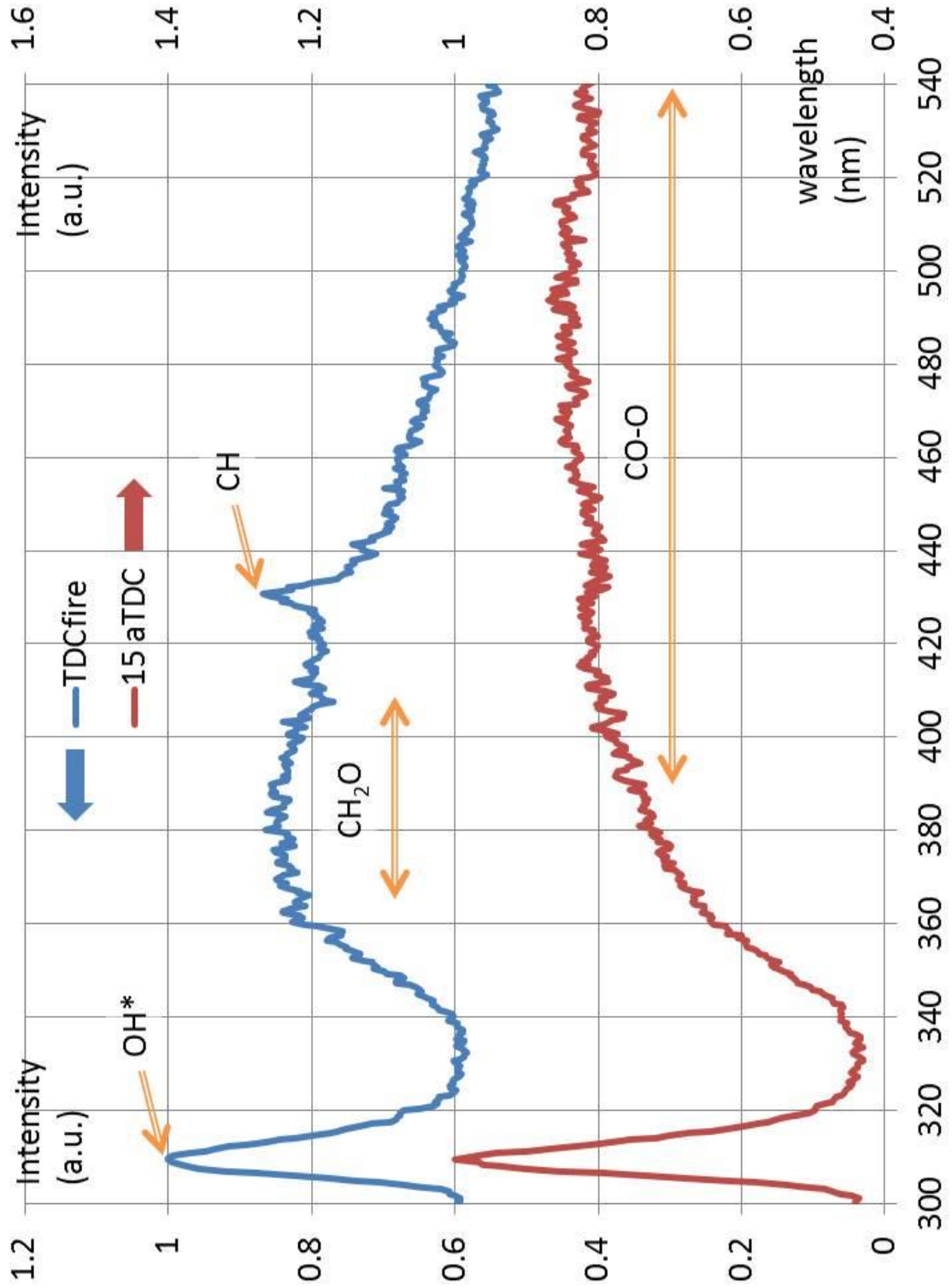


Figure 4.2.1 (b) Spectra of E0 combustion at TDC_{fire} and 15° aTDC_{fire}

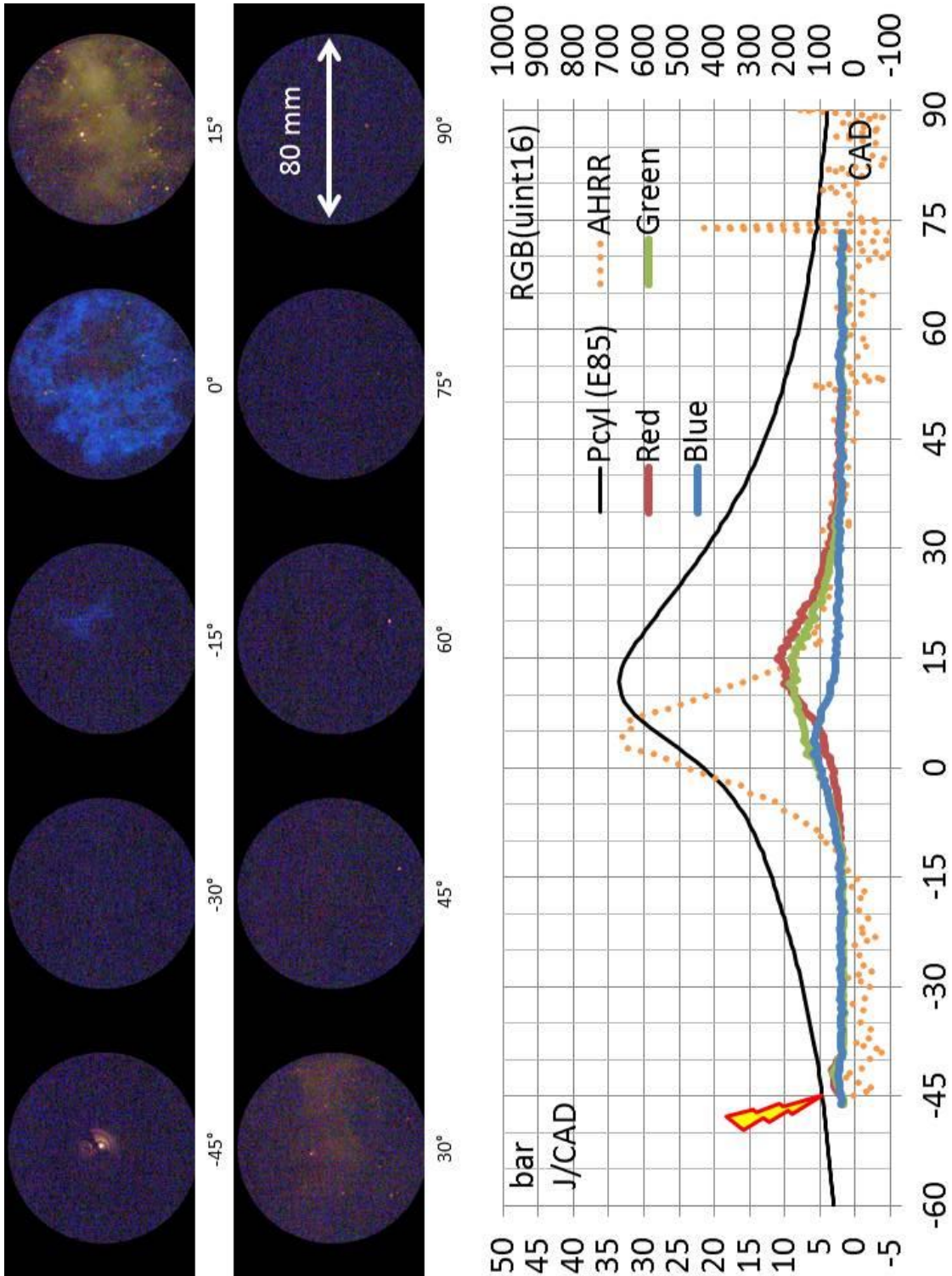


Figure 4.2.2 (a) E85 combustion (1st cycle)

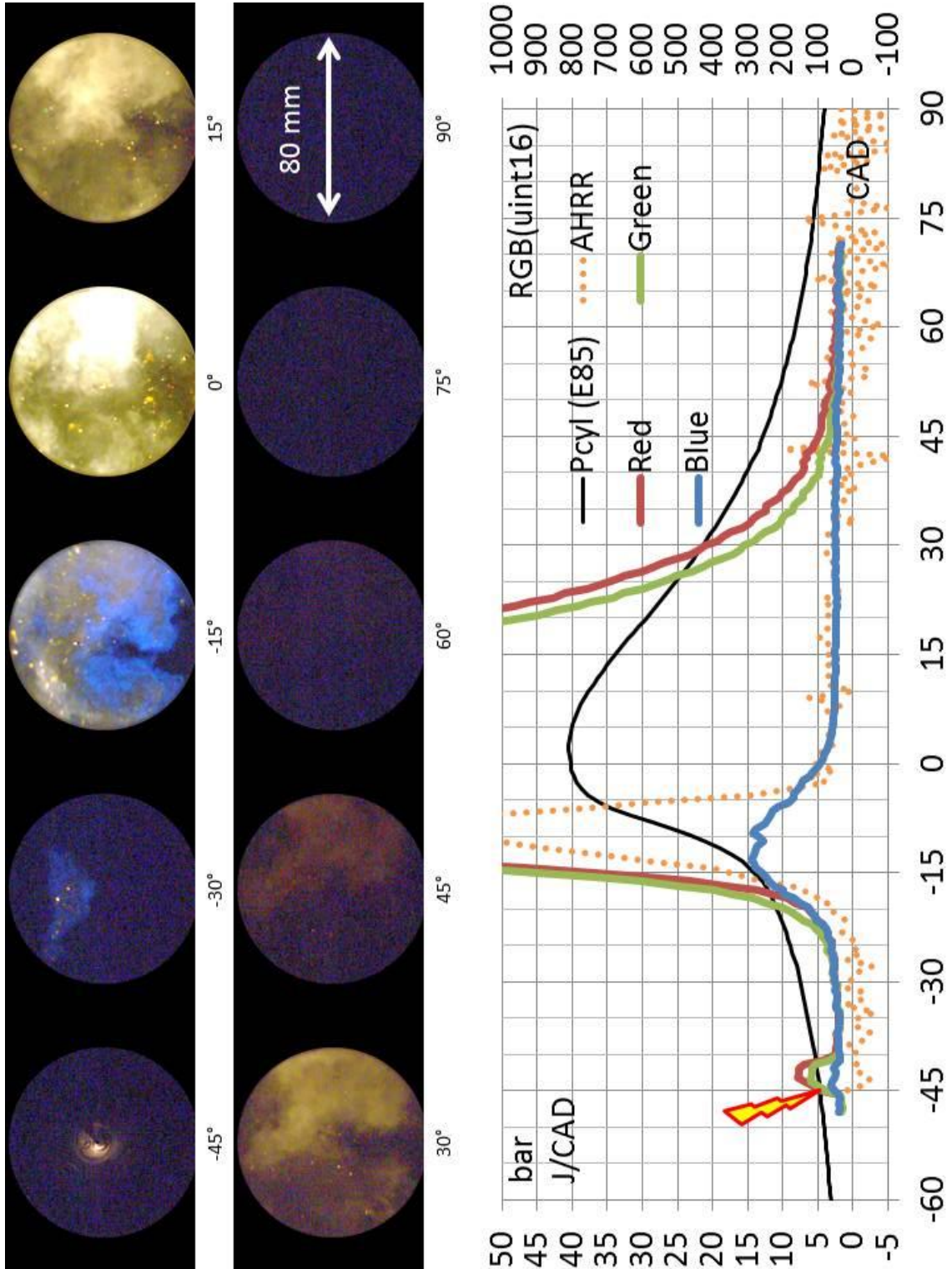


Figure 4.2.2 (b) E85 combustion after 1st cycle (5th cycle shown)

4.3 No-Valve and 1-Valve Deactivation (Intake) on Flame Propagation

This test is experimented with E85 since its startability is better than E0 as discussed previously. Test condition is listed below and Method B is used.

Test condition:

- 600 rpm; MAP: 1 bar; Lambda: ~ 1.20 (E85); EGR 0%; 40°C intake air; 80°C coolant
- Injection timing: 300° bTDC_{fire}; injection pressure: 100 bar
- Ignition timing: 30° bTDC_{fire}
- Camera Frame Rate: 6000 fps

Theoretically, one-valve deactivation creates more swirl motion (swirl-dominant) inside the cylinder due to asymmetric intake air flows, whereas no-valve deactivation has more tumble motion (tumble-dominant) caused by the piston reciprocation. Figure 4.3.1(a) and 4.3.1(b) show the first cycle images of these two modes, no-valve and one-valve deactivation, respectively. One should be noticed that the bottom of the image is the intake valve position and the top of that is the exhaust valve position.

The first cycle of one-valve deactivation has relatively weak combustion, as shown in Fig. 4.3.1(a). On the other hand, the combustion of the first cycle of no-valve deactivation is stronger. Since E85 is the only fuel utilized in this test and its good combustibility is discussed and proven previously, the results indicate the impact of one-valve deactivation on deteriorating the combustion process in this particular engine setup because the IMEP of the first cycle of no-valve deactivation and one-valve deactivation is 6.88 bar and 5.52 bar, respectively. It is also observed

that the combustion process is weaker with one-valve deactivation from the AHRR and RGB values. In addition to that, one-valve deactivation images show strong diffusional flame at the end of the combustion. It is therefore expected that the soot formation is higher with this configuration.

The correlation between the blue color and AHRR also agrees with the observation from the fuel type tests. The peaks of both curves overlap with each other, which indicate that the blue color may be burn rate related. It is also worthy of notice that the averaged blue values are mostly the same in any tangible combustion, but the averaged red values always vary from cycle to cycle depending on the combustion.

Nevertheless, the averaged IMEP of no-valve and one-valve deactivation is 6.58 bar and 6.82 bar; the COV_{IMEP} of them are 3.91% and 6.87%, respectively. This suggests that even though the combustion is more stable while no valve is deactivated. This is in the agreement with the previous study [13] when the engine speed and power output are relatively low (less than 2000 rpm, 1~2 bar BMEP).

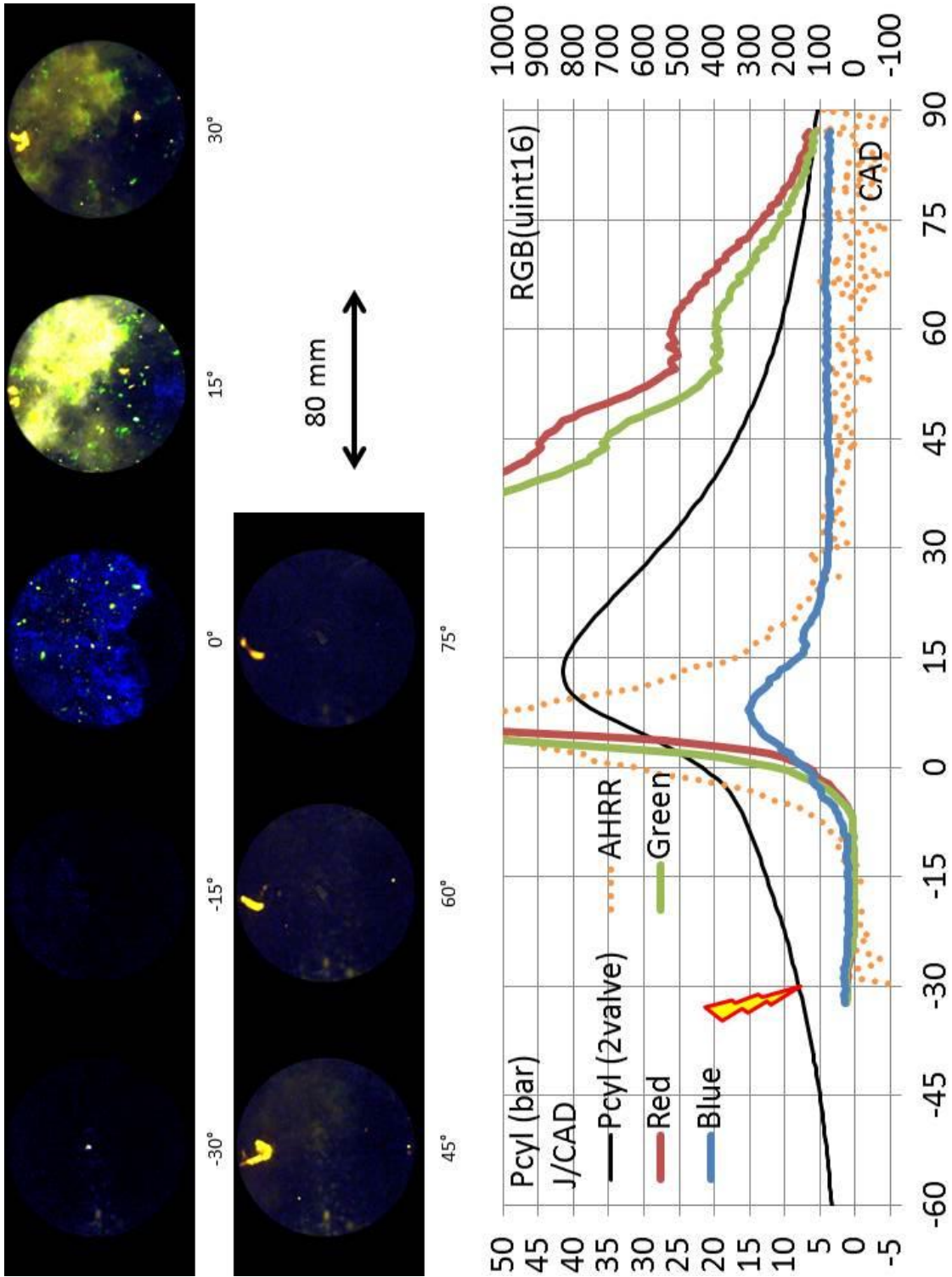


Figure 4.3.1 (a) No-valve deactivation (1st cycle)

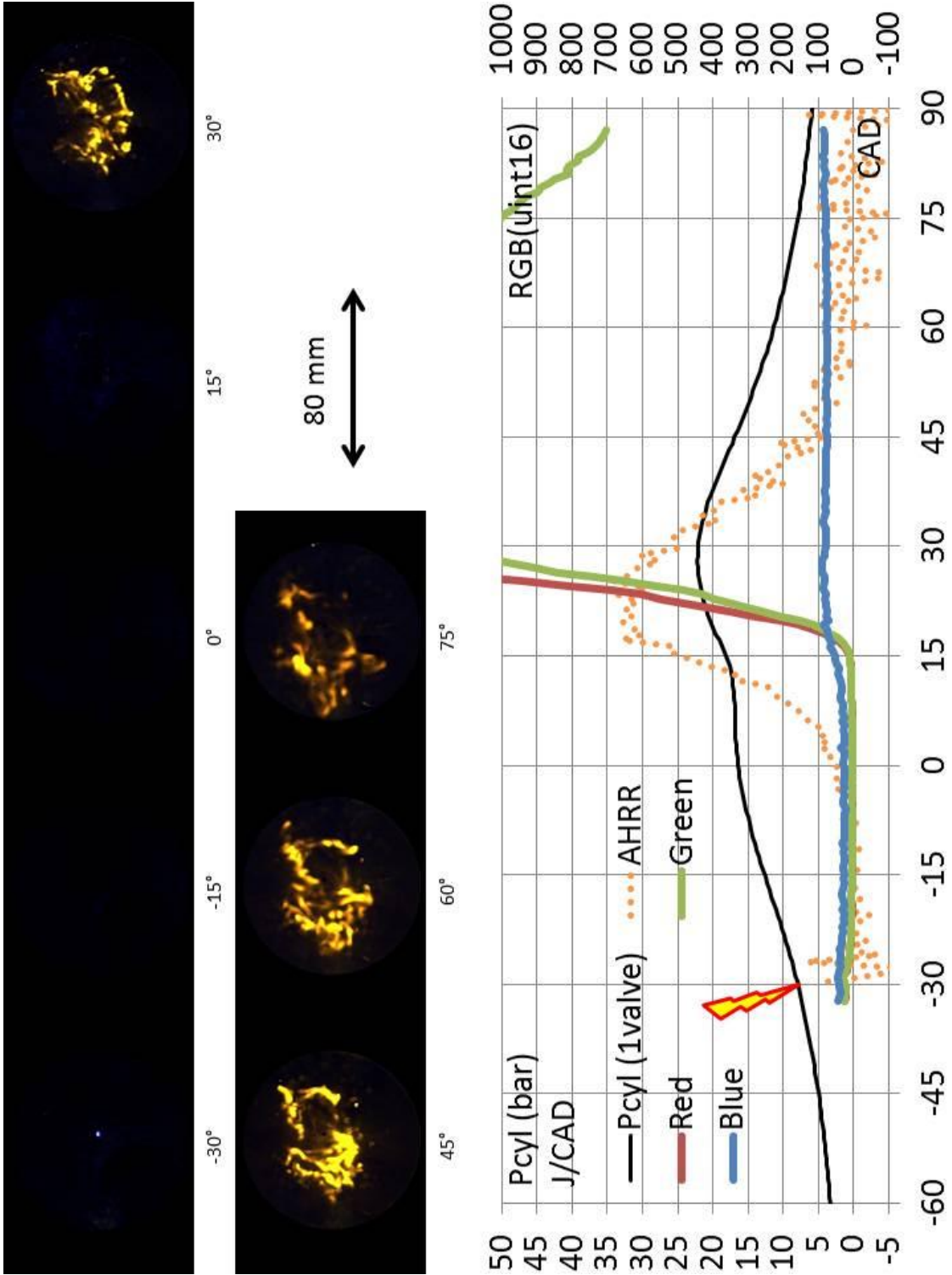


Figure 4.3.1 (b) One-valve deactivation (1st cycle)

In order to study the difference between these two valve configurations, an ultra-lean condition ($\lambda \sim 1.6$) with early spark timing (45° bTDC_{fire}) is conducted in order to focus on the blue flame propagation. The image results shown in Fig. 4.3.2(a) and Fig. 4.3.2(b) are compared side-by-side from the start of ignition (15° bTDC_{fire}) to the TDC_{fire} (0°). It should be noted that the RGB values of the images in Fig. 4.3.2(a) and Fig. 4.3.2(b) are enhanced, so they should not be compared with the images in Fig. 4.3.1.

The flame kernel of one-valve deactivation starts from the bottom-right to the top-left of the image, which is from the deactivated intake valve; the flame kernel of no-valve deactivation starts from the top to the bottom of the image, which is from the exhaust valve side. Figure 4.3.2(c) is the image data taken from the one-valve deactivated cylinder head on the metal engine for qualitative study. Comparing Fig. 4.3.2(b) and Fig. 4.3.2(c), the flame development before TDC (0°) should be seen as the blue flame. Both figures show the same flame development direction, so the shape of piston top is concluded to have minimal impacts. It should be mentioned that the two tests in Fig. 4.3.2(b) and Fig. 4.3.2(c) are set up with the same spark plug at different ignition timing; nonetheless, both results show the same flame development direction.

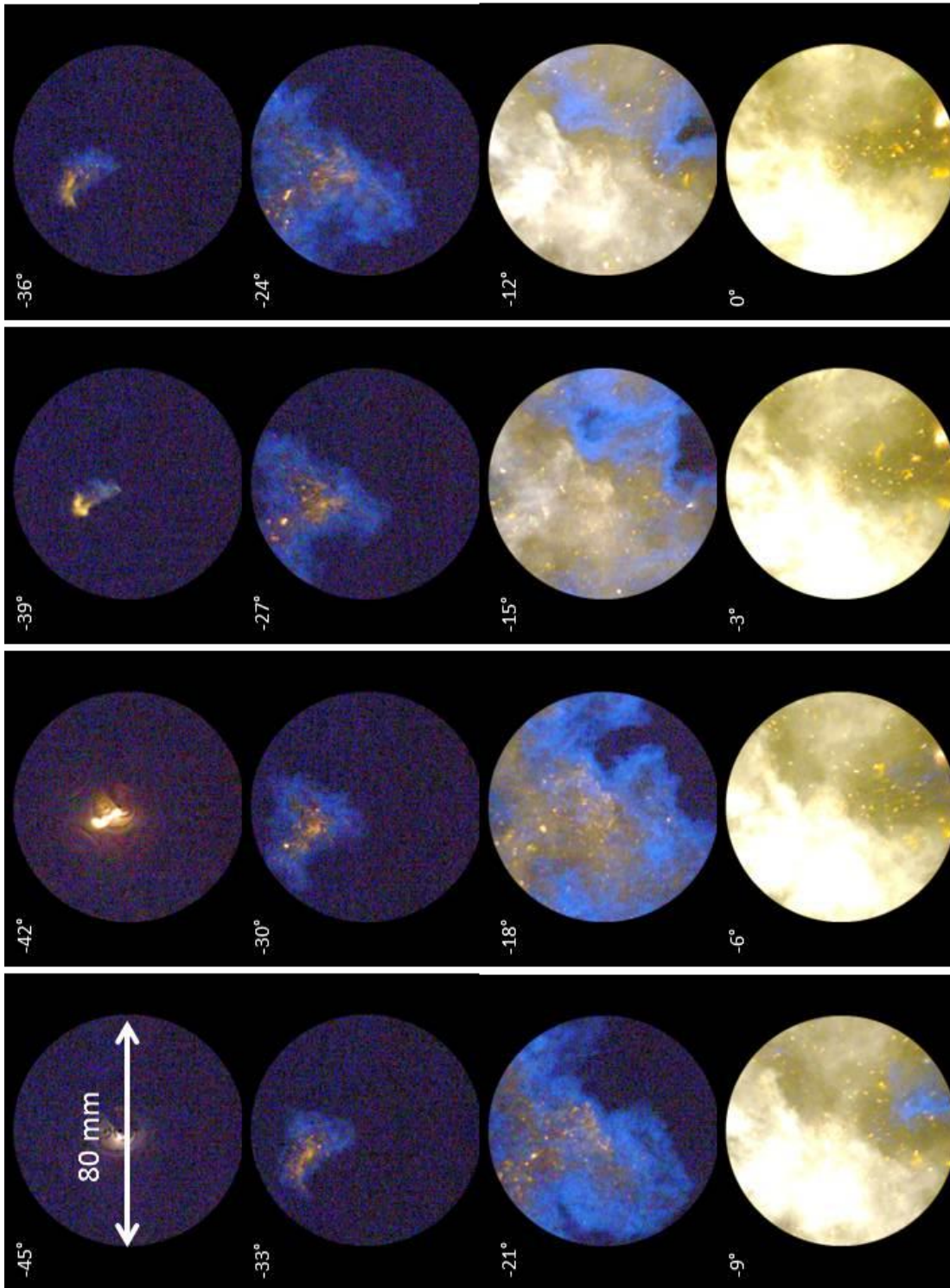


Figure 4.3.2 (a) No-valve deactivation flame development

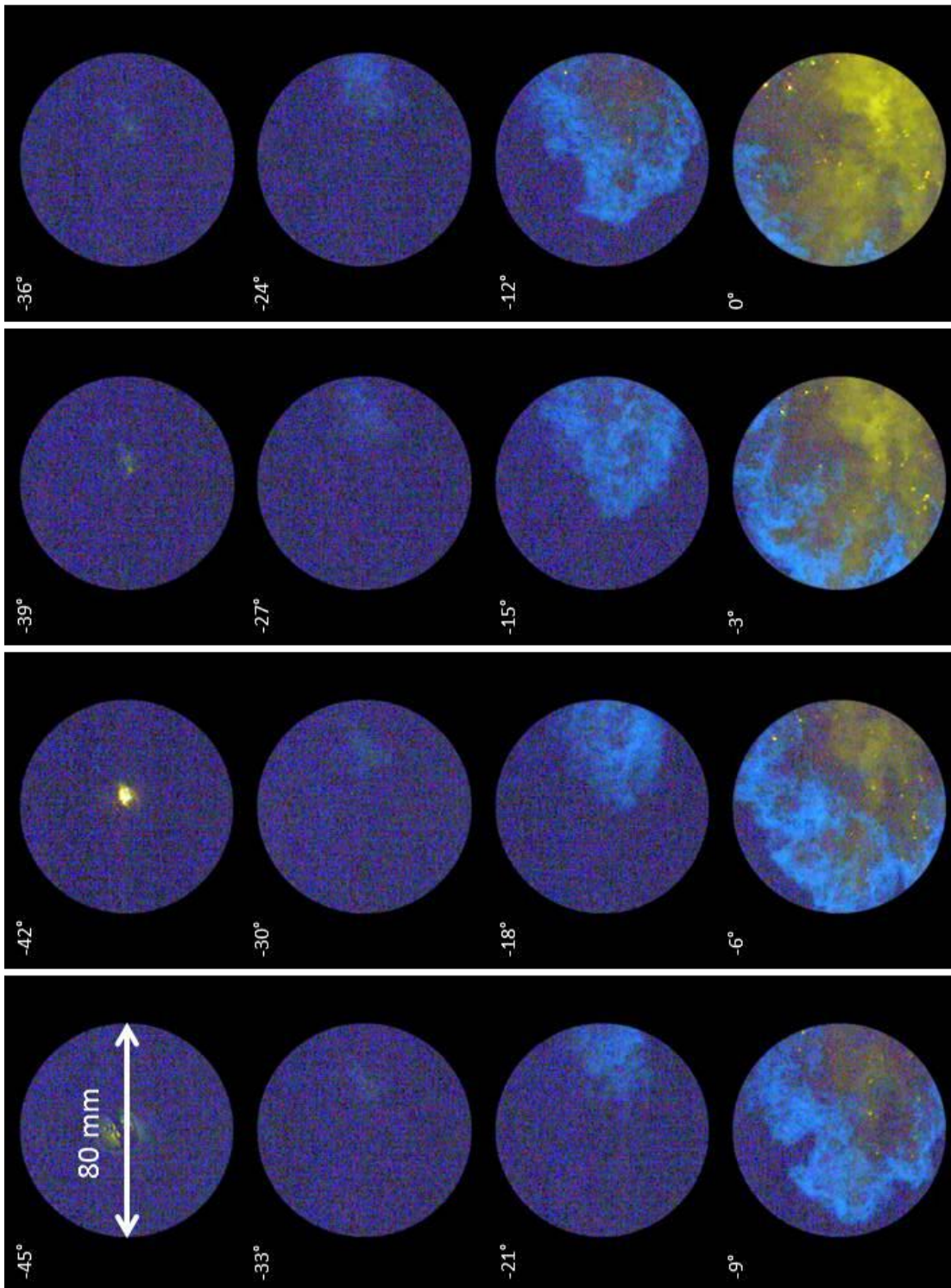


Figure 4.3.2 (b) One-valve deactivation flame development

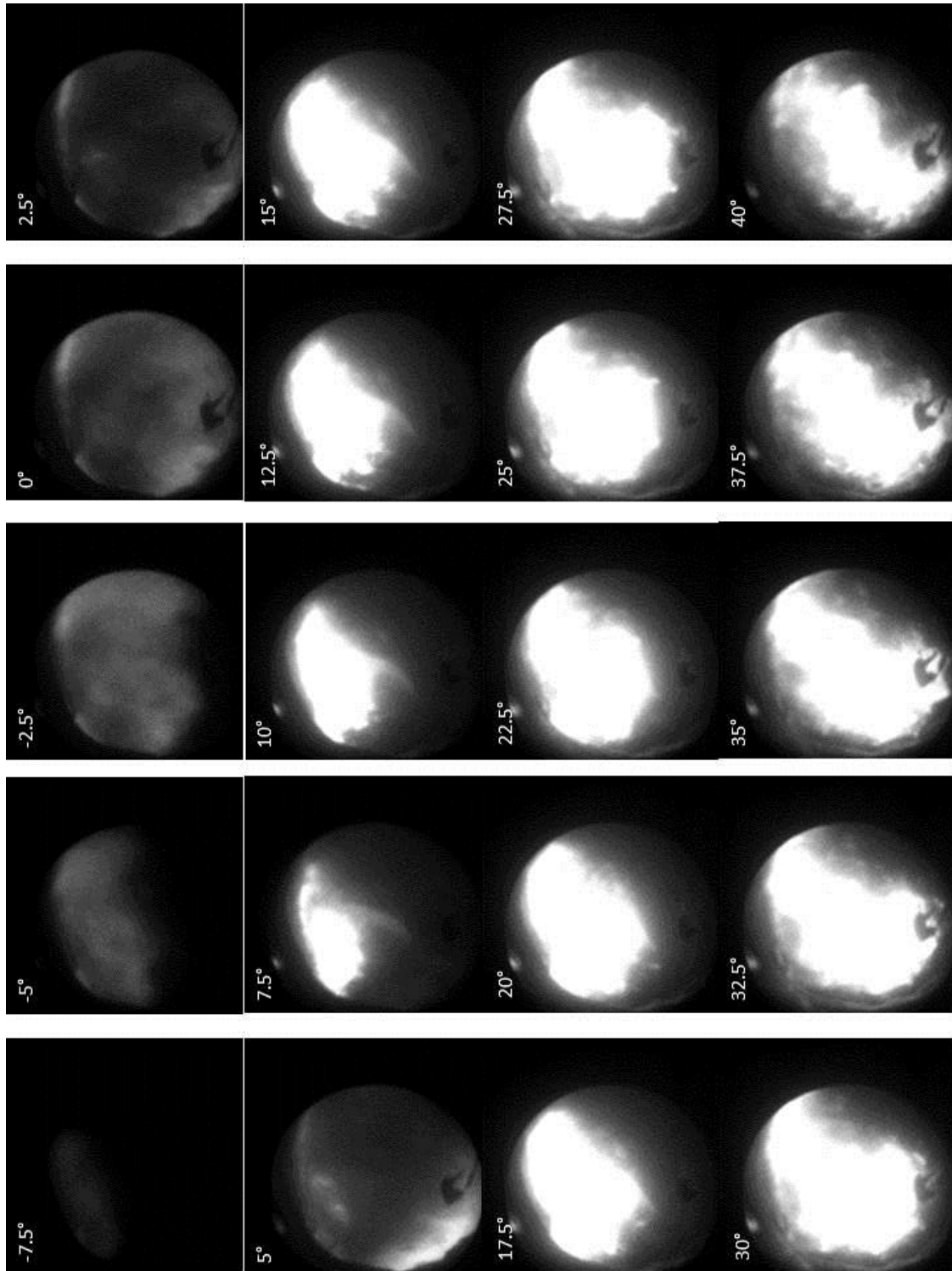


Figure 4.3.2 (c) One-valve deactivation flame development in mOAE (600 rpm; view from the deactivated intake valve)

One explanation of this phenomenon is that the direction of the spark discharge arc does not encounter a local-rich zone. A CFD simulation is done to display the air-fuel ratio inside the combustion chamber before the spark. The result is shown in Fig. 4.3.3(a). It is clear seen that the local-rich zone occurs at the activate intake valve side while the arc is moving towards the deactivated valve. Therefore, the control of the spark arc direction is important in order to encounter a local-rich zone to have better combustion. The flame propagation is directed by the air flow motion where one-valve deactivation is dominated by swirls and no-valve deactivation is controlled by tumbles.

Figure 4.3.3(b) shows another view angle for better illustration. It should be addressed that Fig. 4.3.3(a) and Fig. 4.3.3(b) have different piston geometry to represent the sOAE and mOAE, respectively. Either figure shows that the local air-fuel mixture rich zone (red color) is on the opposite side of the spark direction. This is the evidence of over-mixing as described in the literature review section that the in-cylinder air flow motion pushes richer air-fuel mixture away from the spark; therefore, the combustion is deteriorated. On the other hand, no-valve deactivation does not show asymmetric flame propagation as shown in Fig. 4.3.3(c).

Figure 4.3.4(a) and Fig. 4.3.4(b) show the side-by-side comparison of the experimental images (from Fig. 4.3.2(a) and Fig. 4.3.2(c)) and simulation results for no-valve deactivation and one-valve deactivation, respectively. Even though CO₂ concentration is used in the simulation results and may not represent the flame propagation perfectly, it is still clearly seen that no-valve deactivation has more symmetric flame propagation.

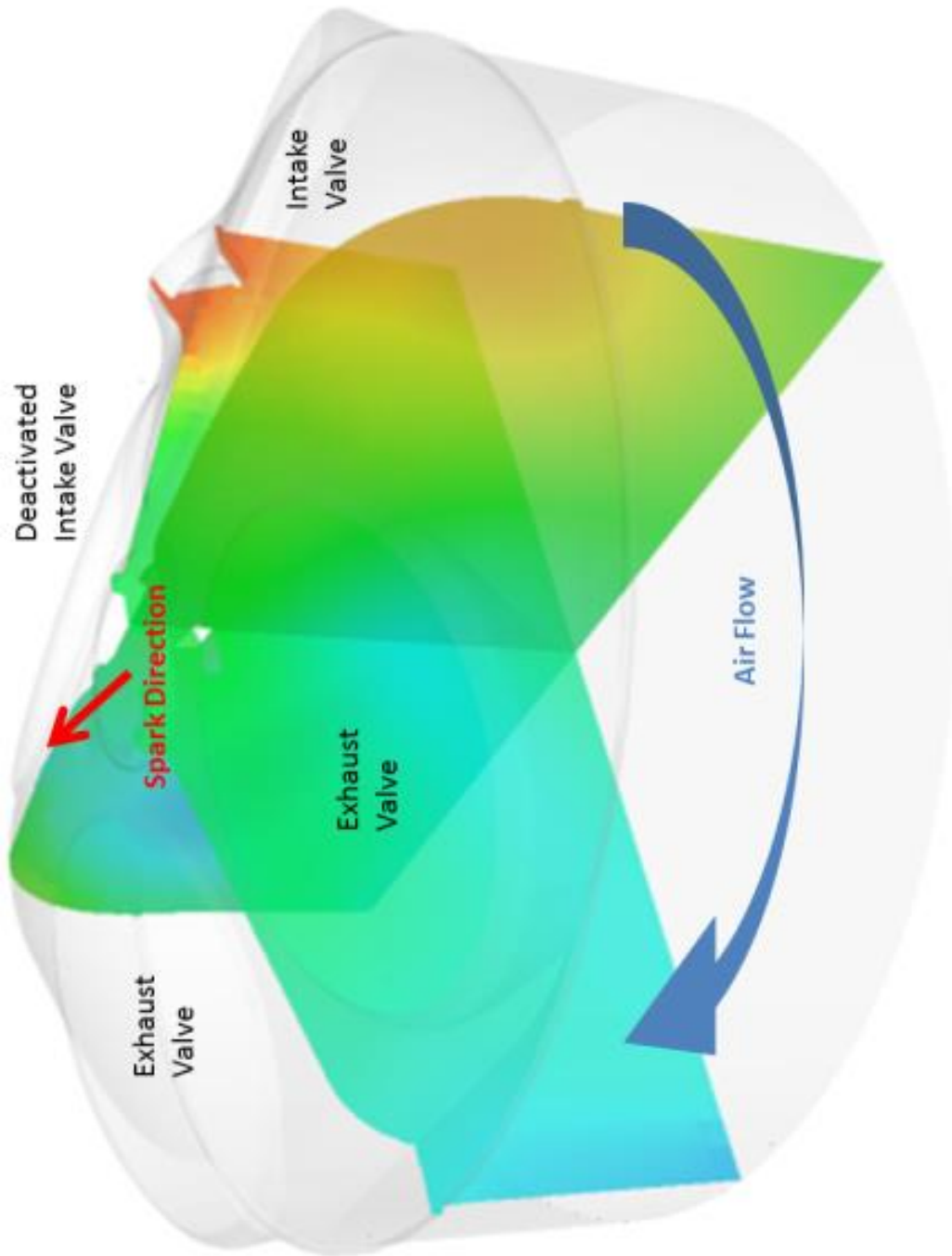


Figure 4.3.3 (a) One-valve deactivation CFD simulation: local-rich zone is shown in red

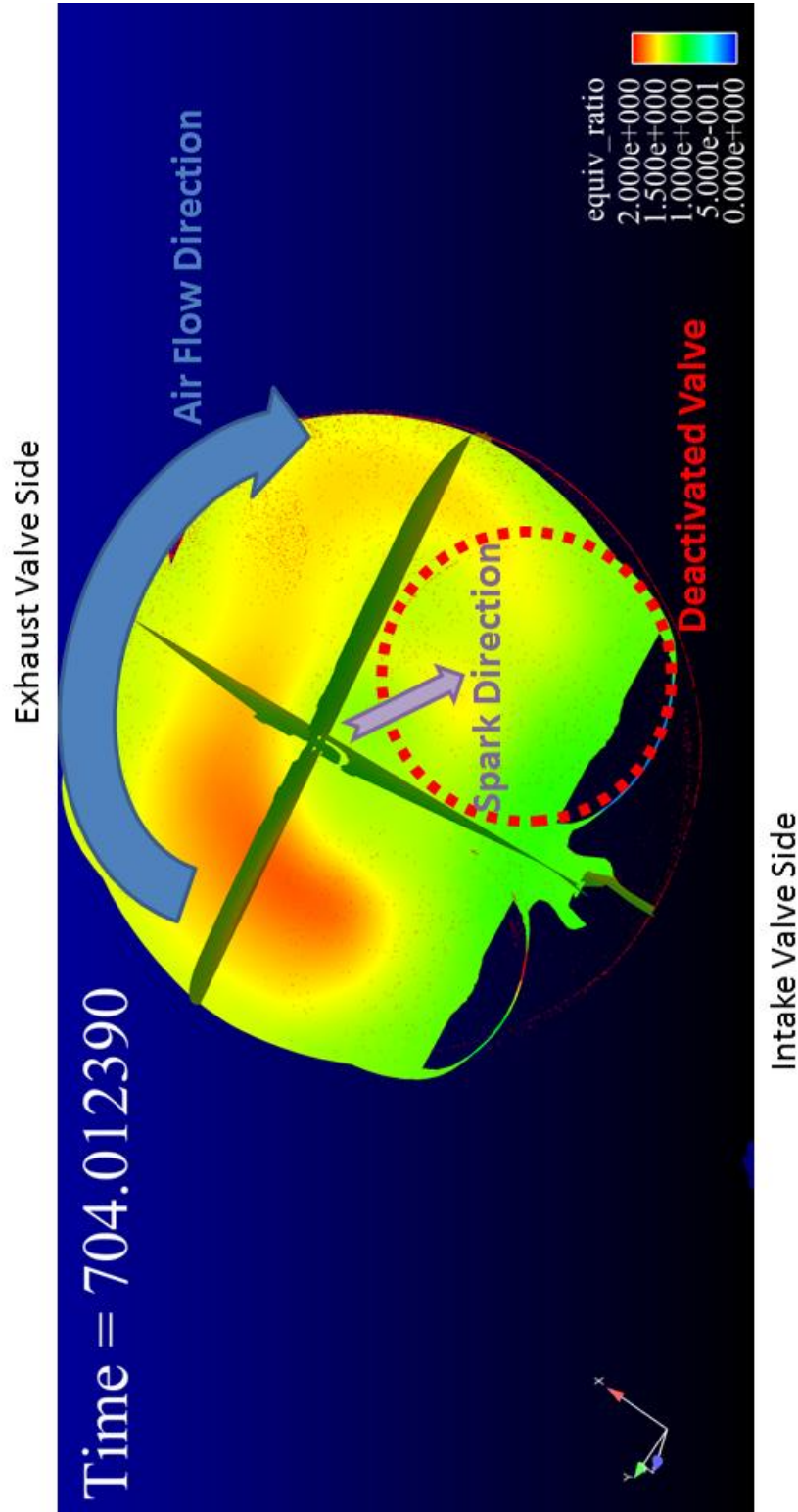


Figure 4.3.3 (b) One-valve deactivation CFD simulation: local-rich zone is shown in red

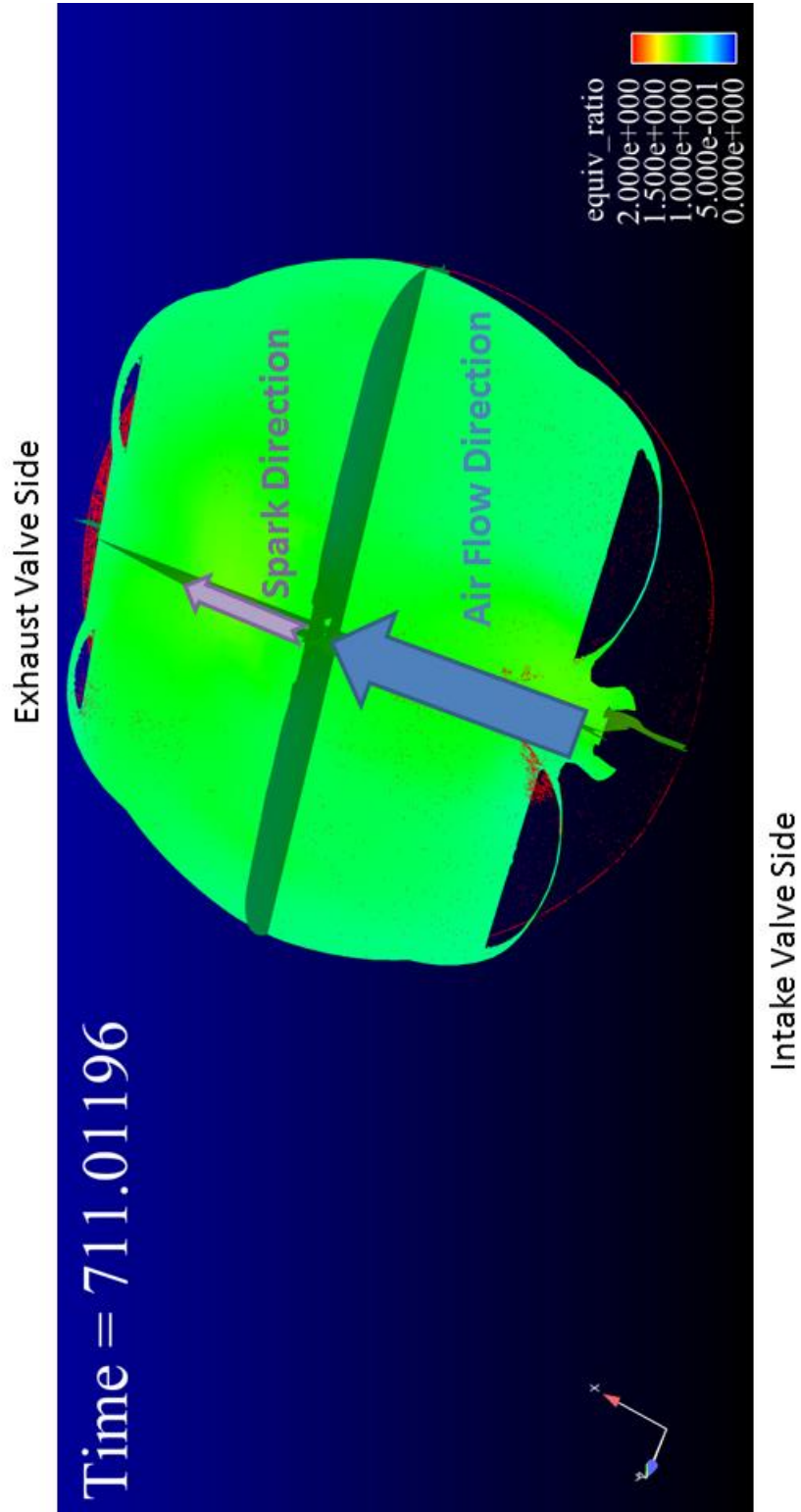


Figure 4.3.3 (c) No-valve deactivation CFD simulation: no local-rich zone is shown

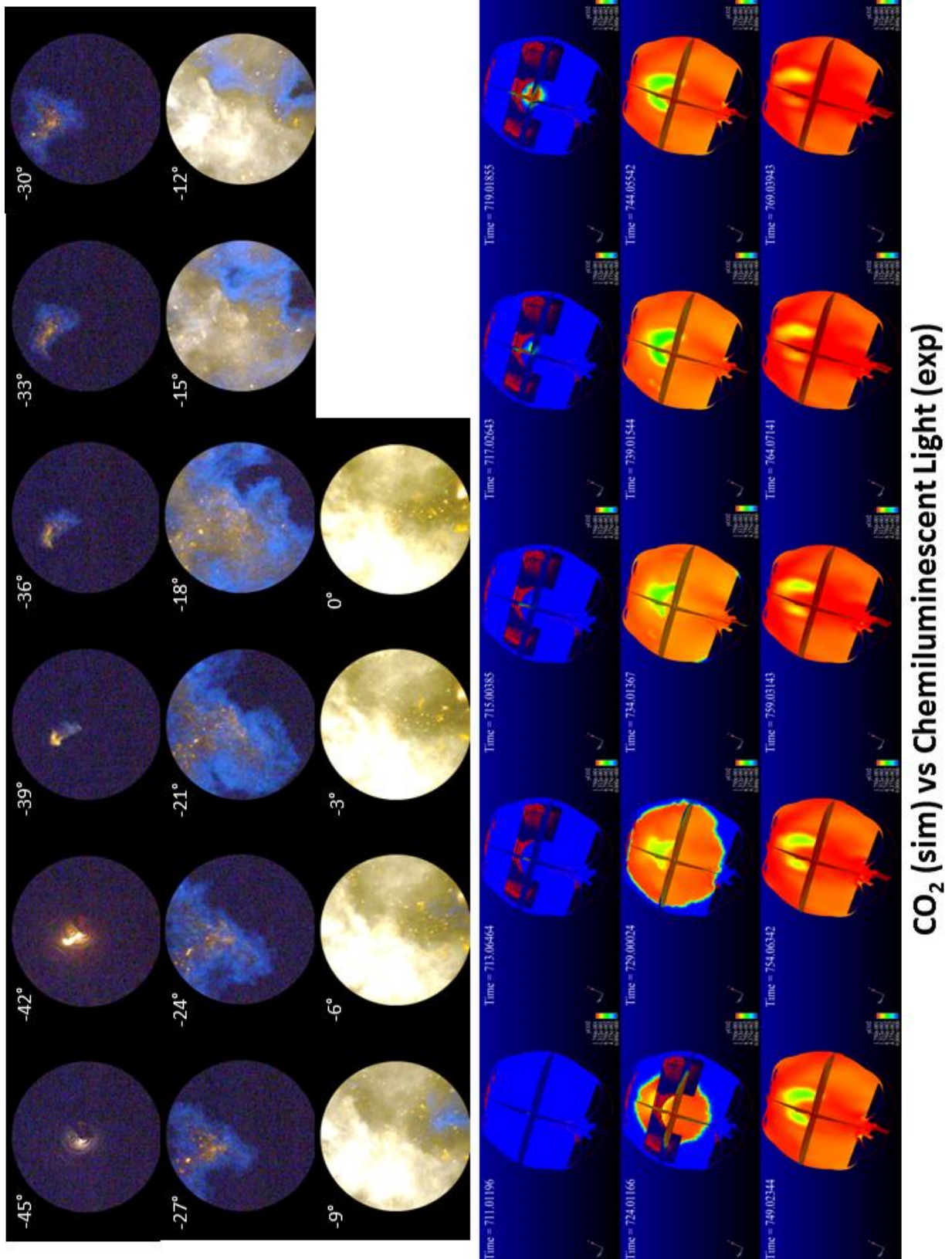


Figure 4.3.4 (a) No-valve deactivation experiment v.s. simulation

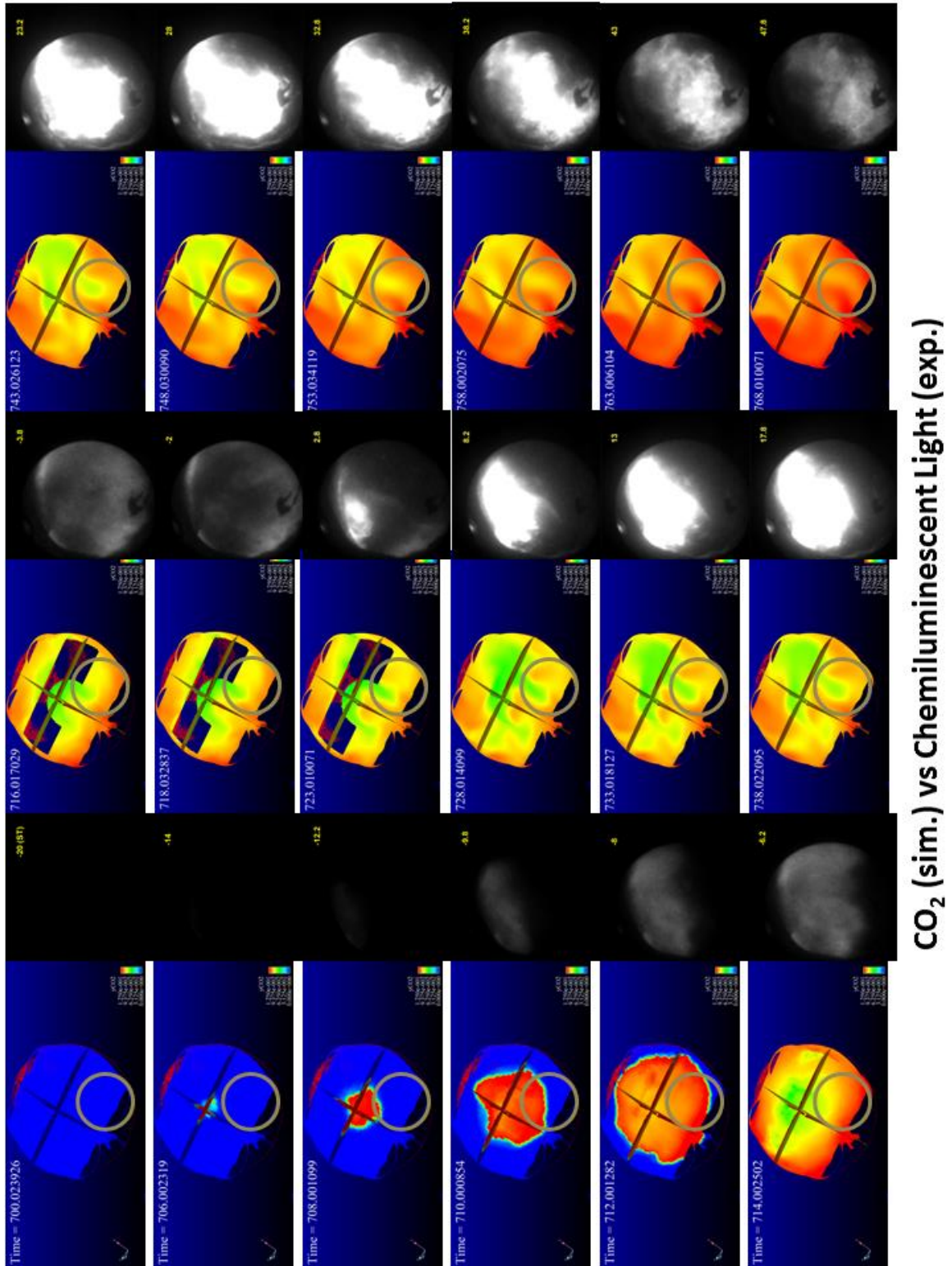


Figure 4.3.4 (b) One-valve deactivation experiment v.s. simulation (the grey circle represents the deactivated intake valve)

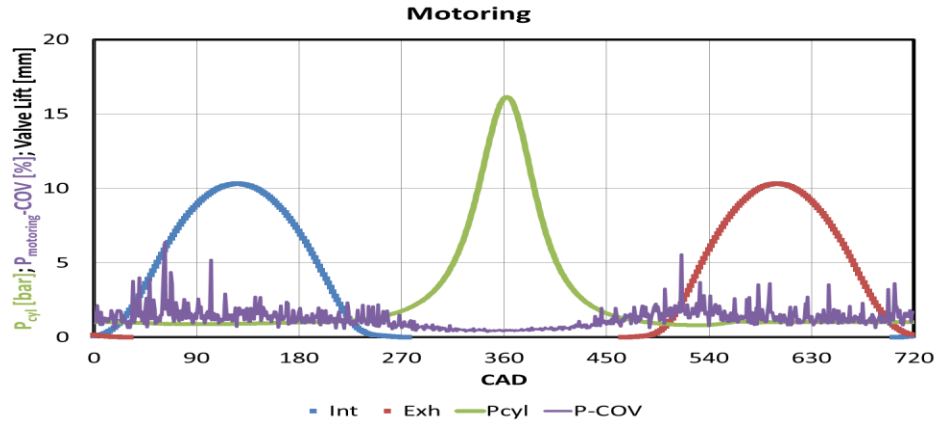
4.4 Combustion Cycle-to-Cycle Variation and Flame Propagation

Gasoline engines are known for their high cycle-to-cycle variation of combustion. Comparing the two flame propagation contours in Fig. 4.1.2, it is clearly seen that their shapes are varied. To study the cycle-to-cycle variation further, 100 cycles of motoring and combustion events are recorded from two separated tests on mOAE. The results are presented in Fig. 4.4.1. The two green lines are the averaged in-cylinder pressure (P_{cyl}), and the blue and red curves represent the intake and exhaust valve lift in mm, respectively. The purple line is the coefficient of variation of the in-cylinder pressure, $COV_{P_{cyl}}$, of the motoring test at each crank angle degree, which is of 100 samples; the orange line is the $COV_{P_{cyl}}$ of the combustion test at each crank angle degree, which is also of 100 samples.

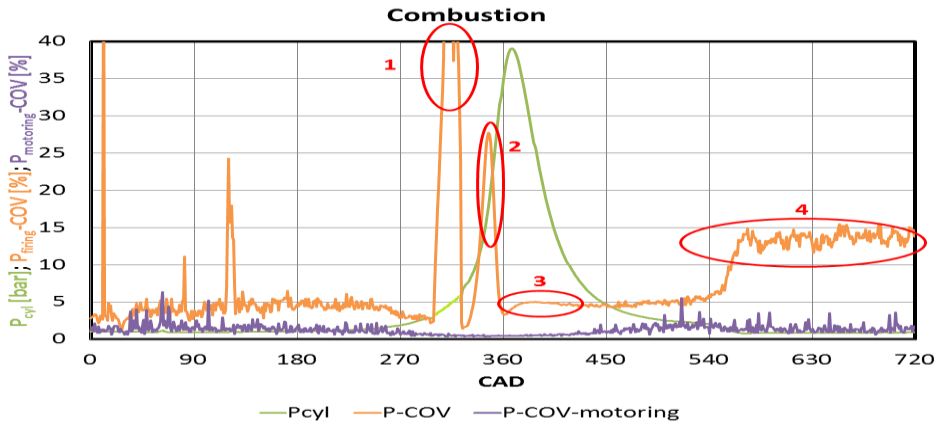
Looking at Fig. 4.4.1(a), the purple line is quite “noisy” between 0 to 270 and 450 to 720 degrees. This is due to the movement of either the intake or exhaust valves. Even though the valve lift curves do not change cycle by cycle, the impact of valve open and close is clearly recorded by the in-cylinder pressure transducer; therefore, the variation is reflected on P_{cyl} . Moreover, the $COV_{P_{cyl}}$ has more variation in the beginning of both the intake and exhaust valve open. This is due to the air motion going into the combustion chamber (intake valve open) or exiting from it (exhaust valve open, as known as blow-down). Between 270 and 450 degrees, there is no valve movement but piston motion. The variation is relatively small (about 1% $COV_{P_{cyl}}$); in other words, the pressure increment and decline are considered “constant.” The peak pressure and its location are also consistent throughout the 100 cycles.

If there is combustion going on in the engine, the results could be very different as shown in Fig. 4.4.1(b). The orange line ($COV_{P_{cyl}}$, combustion) has higher values than the purple one. This is because the air motion in the firing combustion chamber is more turbulent than that in the motoring one. Besides, there are other causes that affect the in-cylinder pressure stability as the four red circles in Fig. 4.4.1(b). The first red circle represents the variation by the spark. Even though the spark timing is fixed in this test, the real discharge timing could vary due to the hardware. Without a good grounding and insulation, which is the case in this study due to the age of the data acquisition devices, the pressure traces could record “false” signals and values. Smoothing the data then becomes necessary, but some calculations like IMEP would be containing more inaccuracy or losing details. The second red circle is due to the start of combustion (i.e. the early flame kernel development). The third one is due to the peak pressure location or diffusion flame, and the fourth one is due to the hot exhaust gas and the blow-down process.

Figure 4.4.2 shows the flame propagation by Method C from sOAE. Although the engines are different, the variation of combustion flame propagation could still be seen. The images shown in Fig. 4.4.2 represent both no-valve and one-valve deactivation. It should be noticed that the color gradient shown in the images represents the “probability” of the flame location, so one should not be misled to consider the color gradient as the “intensity” of the flame. Since the view area is large (the whole combustion chamber from the bottom view), the variation of flame propagation in Fig. 4.4.2 should be correlated to the second red circle in Fig. 4.4.1(b).



(a)



(b)

Figure 4.4.1 $COV_{P_{cyl}}$ comparison of (a) motoring and (b) combustion

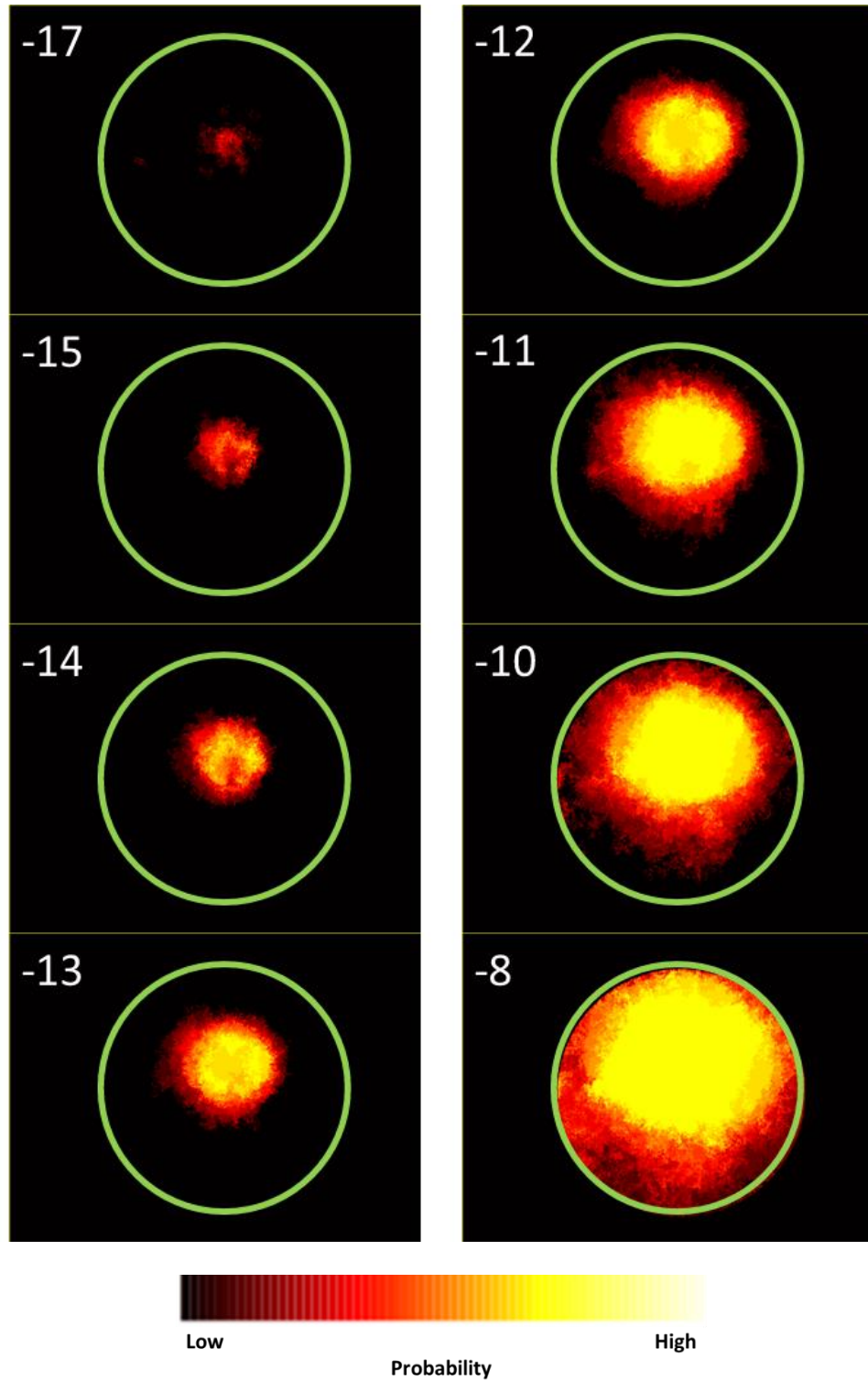


Figure 4.4.2 Method C cycle-to-cycle variation of flame propagation: (a) no-valve deactivation; ST 20° bTDC_{fire} (numbers in the corner represent $^\circ$ aTDC_{fire})

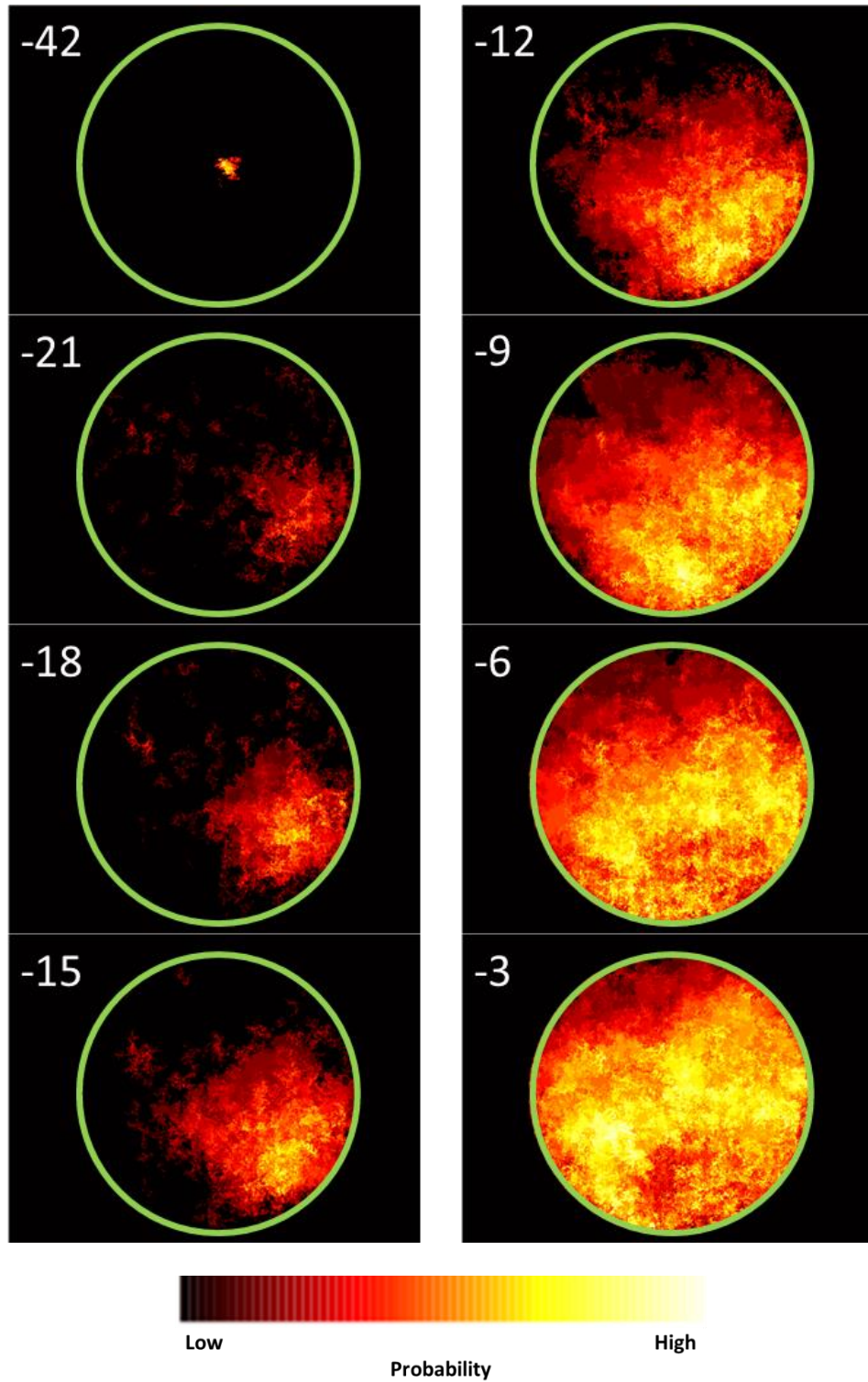


Figure 4.4.2 Method C cycle-to-cycle variation of flame propagation: (b) one-valve deactivation; ST 45° bTDC_{fire} (numbers in the corner represent ° aTDC_{fire})

4.5 EGR Effect on Combustion

Although EGR is usually not present in start-up procedure, it is interesting to see its effects on combustion with respect to the air-fuel ratio. The test condition is listed below.

Test condition:

- 600 rpm; MAP: 1 bar; Lambda: ~ 1.20 (lean) and ~ 0.9 (rich); 40°C intake air; 80°C coolant
- Injection timing: 300° bTDC_{fire}; injection pressure: 100 bar
- Ignition timing: 20° bTDC_{fire}
- EGR: 0%, 10%, 20%, and 30%
- Camera Frame Rate: 6000 fps

Figure 4.5.1 shows the in-cylinder pressure traces of implementing EGR at the intake. It should be noticed that N₂ is used as EGR in the current study. The peak pressure decreases as the increment of EGR as well as IMEP. The effect of changing combustion phase by using EGR is emphasized more in Fig. 4.5.1(b) with rich condition.

Images of two cases are compared, whose spark timing is at 20° bTDC_{fire}. Figure 4.5.2 shows 10% EGR and 30% EGR in rich condition. The image results clearly show the difference, where 30% case shows no smoke-like plume but some bright spots. It is believed that these local spots would result in soot formation. Furthermore, the increase of EGR would also decrease the stability of combustion, which could be verified with COV_{IMEP} (not shown).

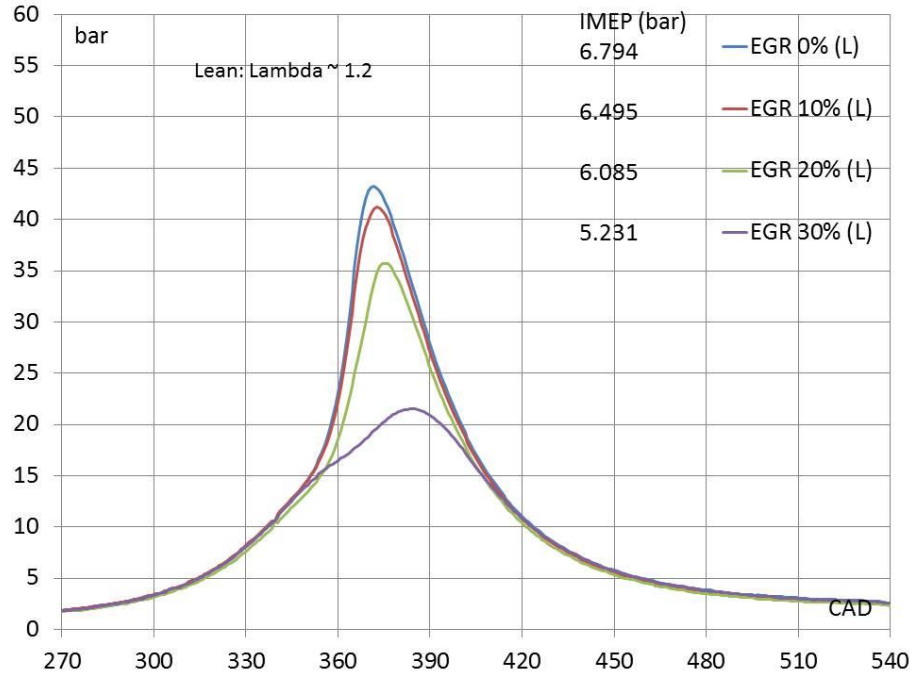


Figure 4.5.1 (a) EGR effect on in-cylinder pressure (lean)

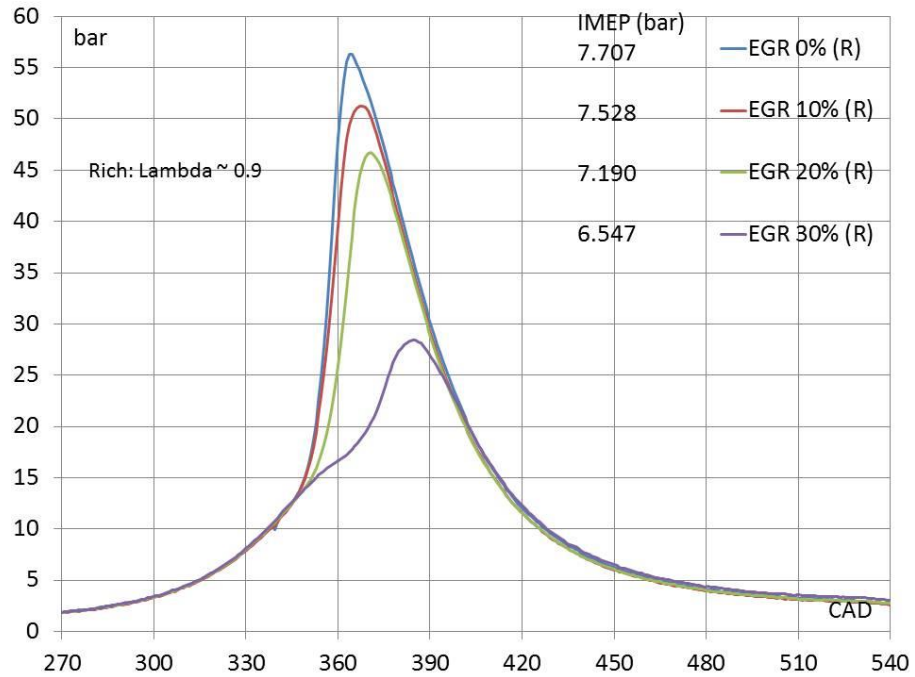


Figure 4.5.1 (b) EGR effect on in-cylinder pressure (rich)

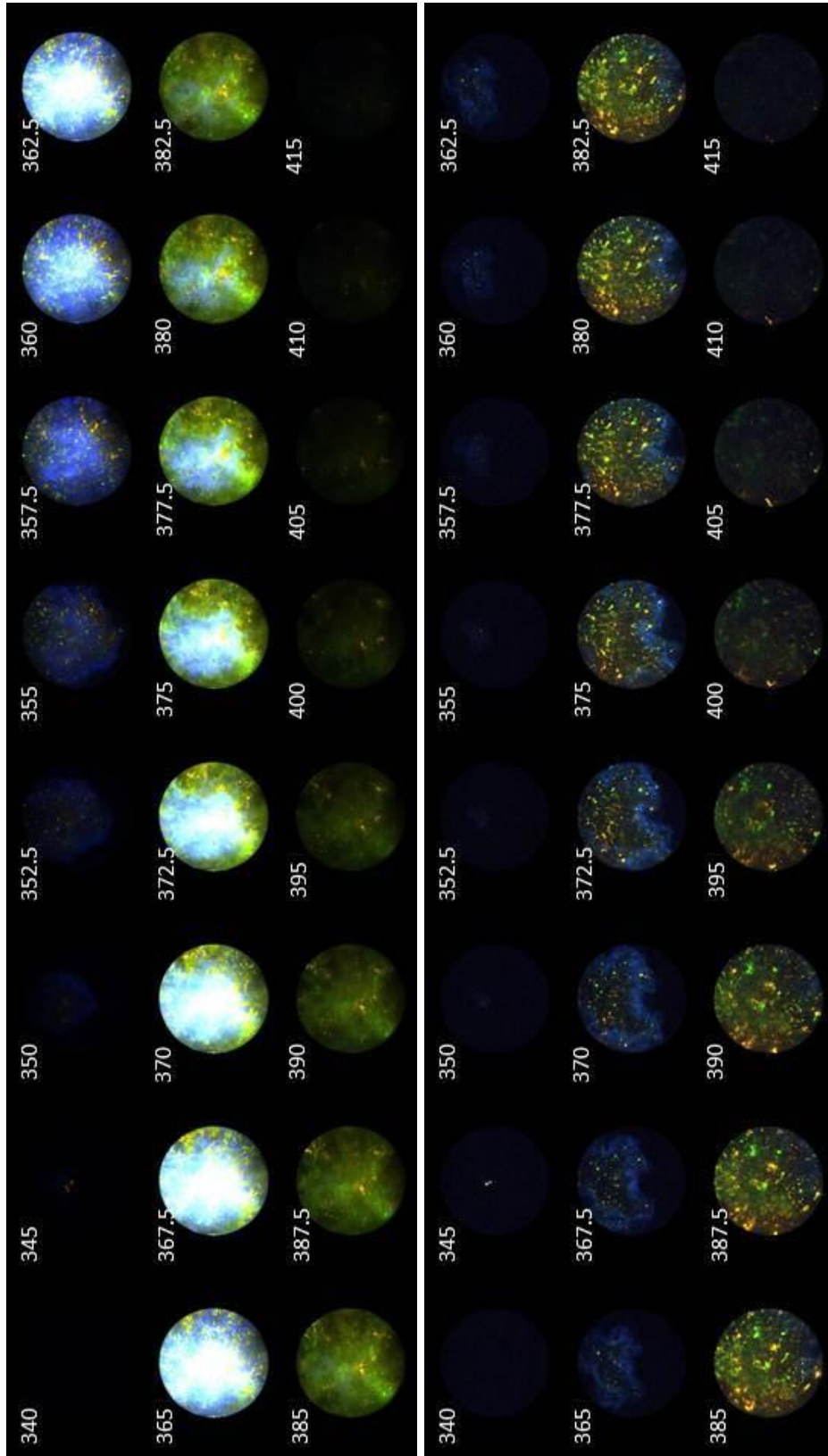


Figure 4.5.2 (a, left)10% EGR (rich); (b, right)30% EGR (rich)

4.6 Engine Speed on Ignition Timing

For engine calibration, different ignition timing (spark timing) is required at different engine speed and load due to the time needed for flame propagation. Too early or too late ignition timing would cause undesired combustion scenarios, for example knocking or unstable combustion. Either low efficiency or high emissions could be the consequences. Due to the limitation on engine operations in the current study, low engine speed on the sOAE and high engine speed on the mOAE results are compared. The test condition is listed below.

Test condition:

- 600 rpm and 1200 rpm; MAP: 1 bar; Lambda: ~ 1.21 ; EGR 0%; 40°C intake air; 80°C coolant
- Injection timing: 300° bTDC_{fire}; injection pressure: 100 bar
- Ignition timing: 40 to 15° bTDC_{fire} (600 rpm) in 5° and 30 to 10° bTDC_{fire} (1200 rpm) in 5°
- Camera Frame Rate: 6000 fps

Figure 4.6.1 shows the IMEP, CA00-10 and CA10-90 of the ignition timing sweep tests from the OAE. The test is done at lean condition (lambda ~ 1.21) with the injection at 300° bTDC_{fire}. The spark timing is set from 40° bTDC_{fire} to 15° bTDC_{fire} in 5° on the OAE at 600 rpm, and 30° bTDC_{fire} to 10° bTDC_{fire} in 5° on the metal engine at 1200 rpm. There is no valve deactivation so that the combustion could maintain the stability.

At the spark timing at 20° bTDC_{fire} and 15° bTDC_{fire}, the engine has high IMEP and low COV_{IMEP} on the OAE at 600 rpm. This indicates that most energy

input is converted to work output, i.e. higher efficiency. The maximum brake torque (MBT) is considered in this range of spark timing. However, the image results demonstrate that the retard spark timing, 20° bTDC_{fire} and 15° bTDC_{fire}, do not have the brightest images as shown in Fig. 13. Therefore, high luminosity may not have a strong correlation to represent high IMEP in this case as the luminosity is considered strong from the images. If the spark timing is too early, like Fig. 13(a), most chemical energy is done against the piston upward motion, the engine would have lower power output and the combustion becomes more unstable as the lower IMEP and higher COV_{IMEP} shown in Fig. 12(a); besides, knocking could occur in a real engine. The CA0-10 and CA10-90 results show that early spark timing causes longer burning duration.

Since the combustion phase is shifted with the advanced spark timing, most mixture could be burnt around TDC. This may explain higher luminosity and the appearance of smoke-like plume in Fig. 4.6.2, especially with advanced spark timing. The components of the plume are not studied in the present but future to identify the actual species of the plume.

Although retarding spark timing may help to improve IMEP and reduce the negative work, Fig. 4.6.2(e) and Fig. 4.6.2(f) show some bright spots after TDC. This could be a concern due to possible soot formation.

Ignition sweep test is also performed on the metal engine with the side-mounted endoscope. This experiment is done at 1200 rpm, which is higher than the one on the OAE (600 rpm). The IMEP and COV_{IMEP} results in Fig. 4.6.3(a) indicate that retarded spark timing has lower IMEP and higher COV_{IMEP}, which is opposite to

the results from the OAE. The MBT is reached with early spark timing. Moreover, the CA0-10 and CA10-90 data shows that the burning rate is slower with retarded spark timing in Fig. 4.6.3(b). This is also a contrast to the OAE test.

One assumption to explain the difference from these two tests is that the air motion by the piston reciprocation would impact the mixture burning rate. The CA0-10 data of early spark timing in both tests shows a flat line, which means the early flame development is not changed with respect to the spark timing – an indication that air is not compressed sufficiently to affect the chemical reaction.

Once the spark timing is retarded, CA0-10 could be faster or slower depending on the engine speed. It is believed that the flame kernel of retarded spark timing has enough time to develop at low speed, so the burning rate is faster. On the other hand, higher engine speed does not provide enough time for the flame kernel to develop thoroughly if the spark timing is retarded; thus, the combustion is deteriorated. It should be noticed that CA0-90 at 600 rpm and 1200 rpm is about 40° at the MBT point, but the burn rate at 1200 rpm is actually faster due to the higher engine speed.

The image results in Fig. 4.6.4 support the assumption described above. Figure 4.6.4(a) and Fig. 4.6.4(b) show very robust combustion, but the chemiluminescent light is not seen much in Fig. 4.6.4(c) and Fig. 4.6.4(d).

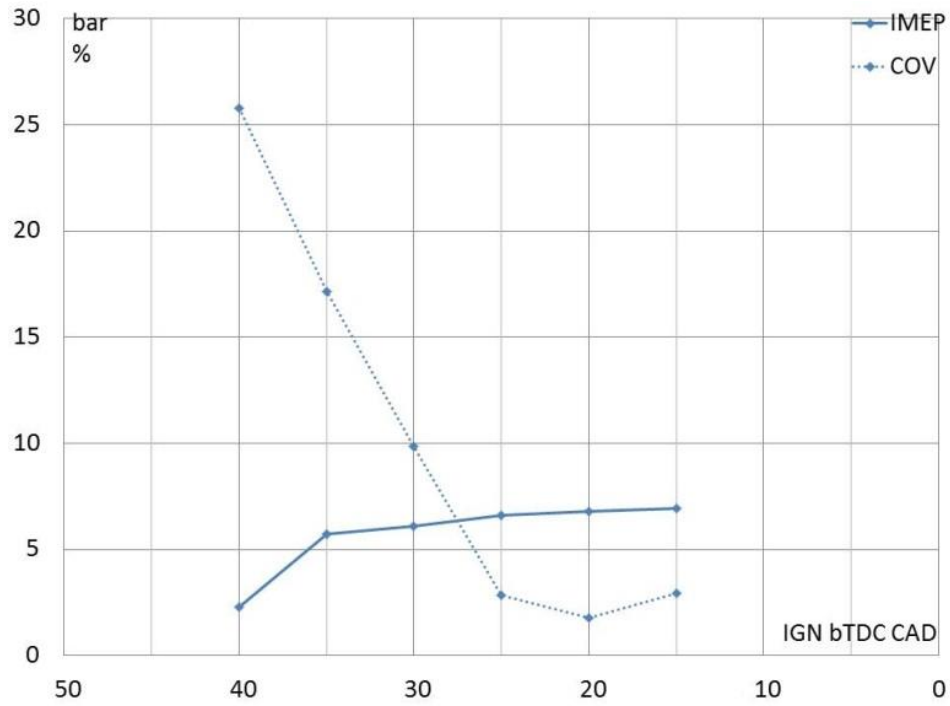


Figure 4.6.1 (a) IMEP and COV_{IMEP} of ignition timing sweep (sOAE; 600 rpm)

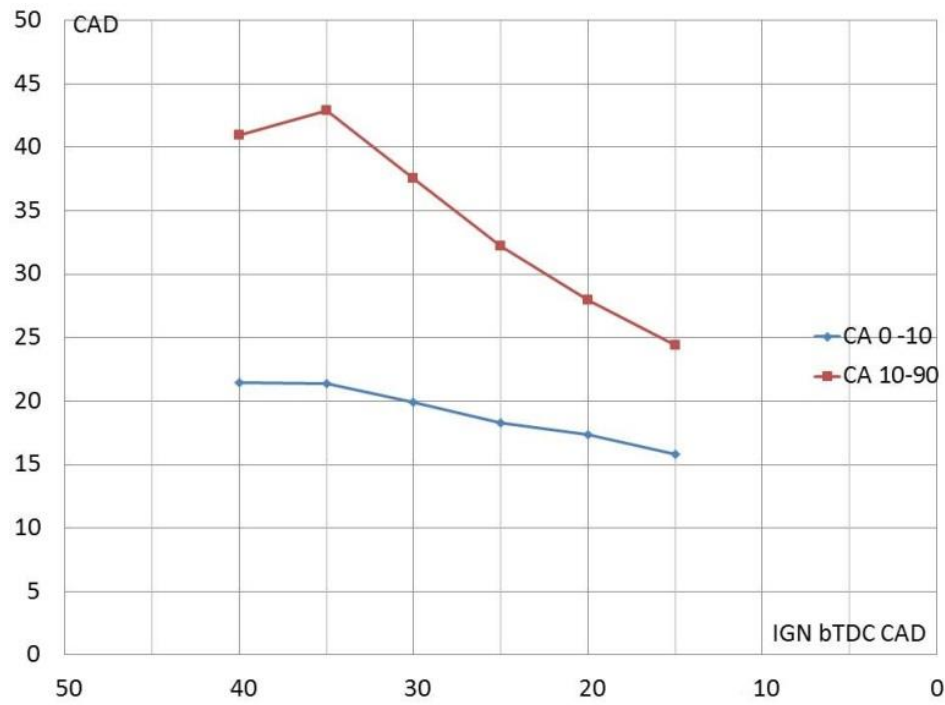


Figure 4.6.1 (b) CA₀₋₁₀ and CA₁₀₋₉₀ of ignition timing sweep (sOAE; 600 rpm)

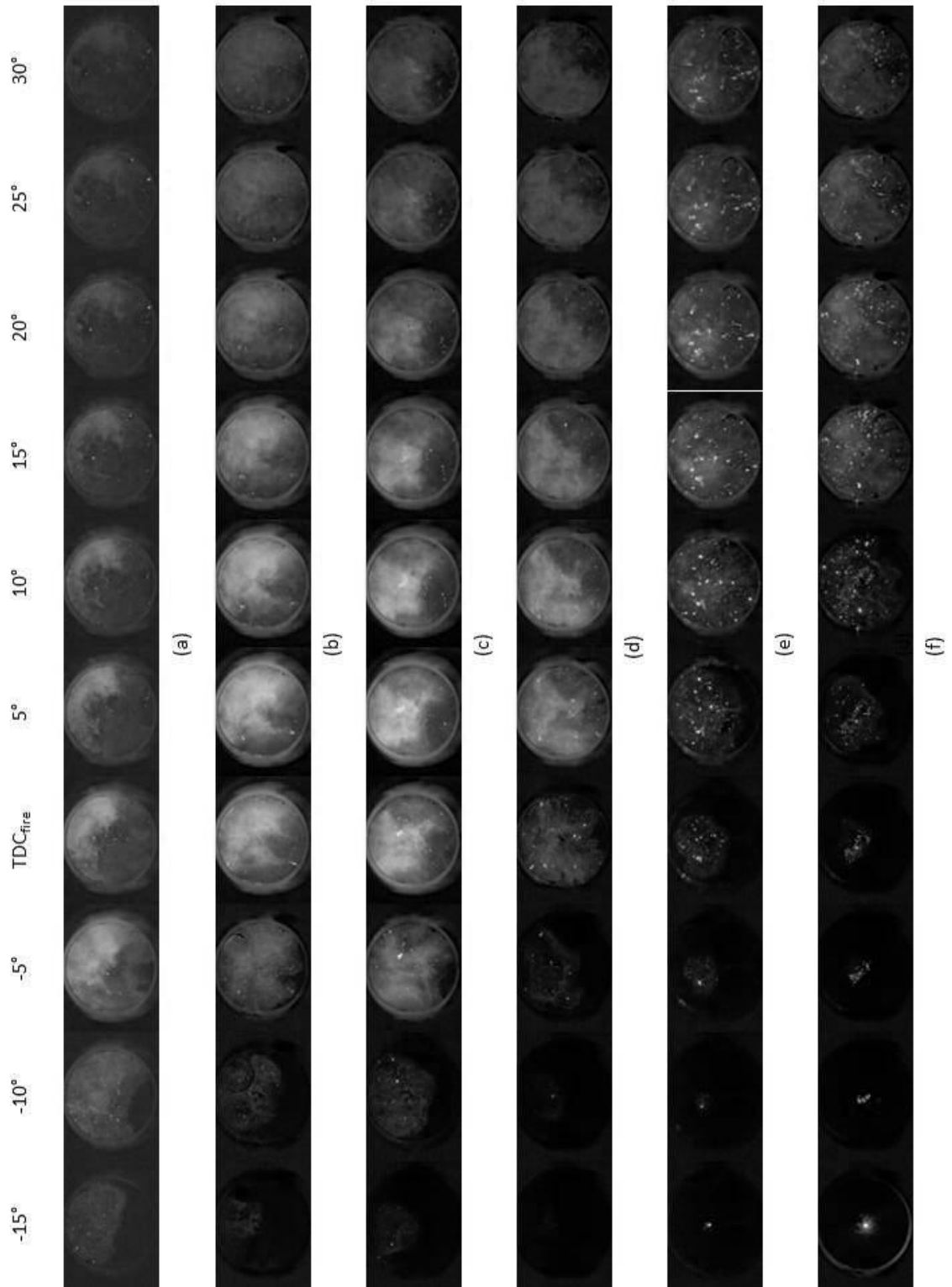


Figure 4.6.2. Ignition timing: (a) 40° (b) 35° (c) 30° (d) 25° (e) 20° (f) 15° bTDC_{fire} (sOAE; 600 rpm)

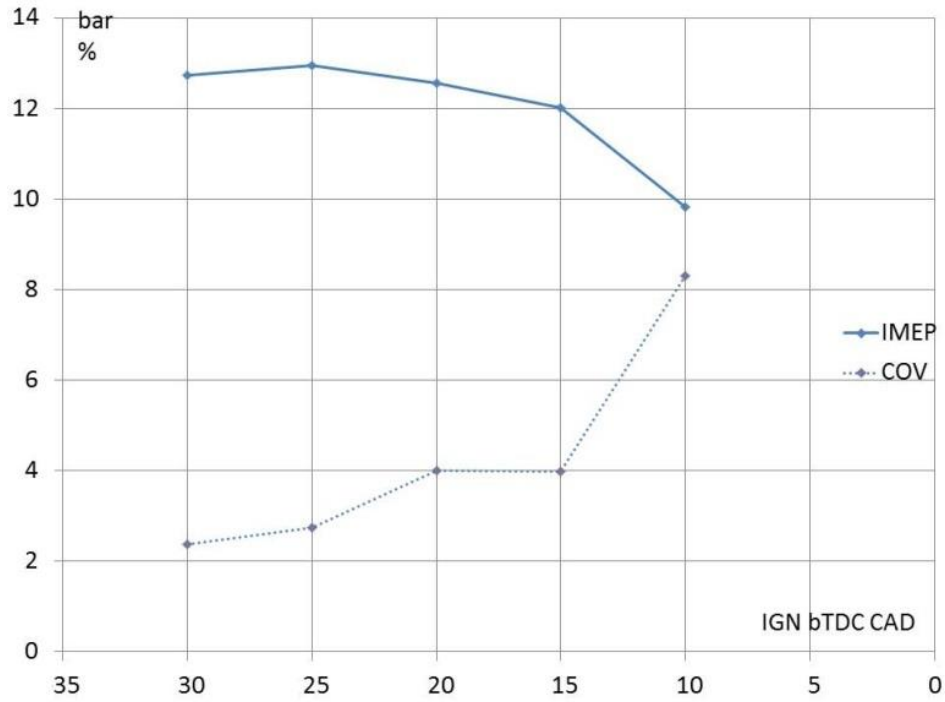


Figure 4.6.3 (a) IMEP and COV_{IMEP} of ignition timing sweep (mOAE; 1200 rpm)

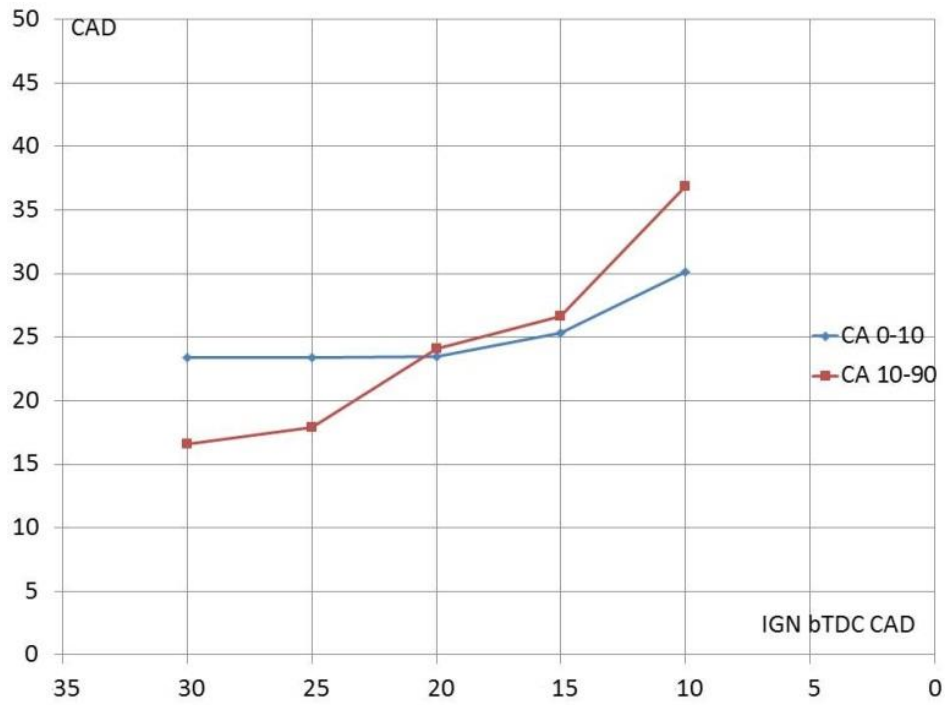


Figure 4.6.3 (b) CA0-10 and CA10-90 of ignition timing sweep (mOAE; 1200 rpm)

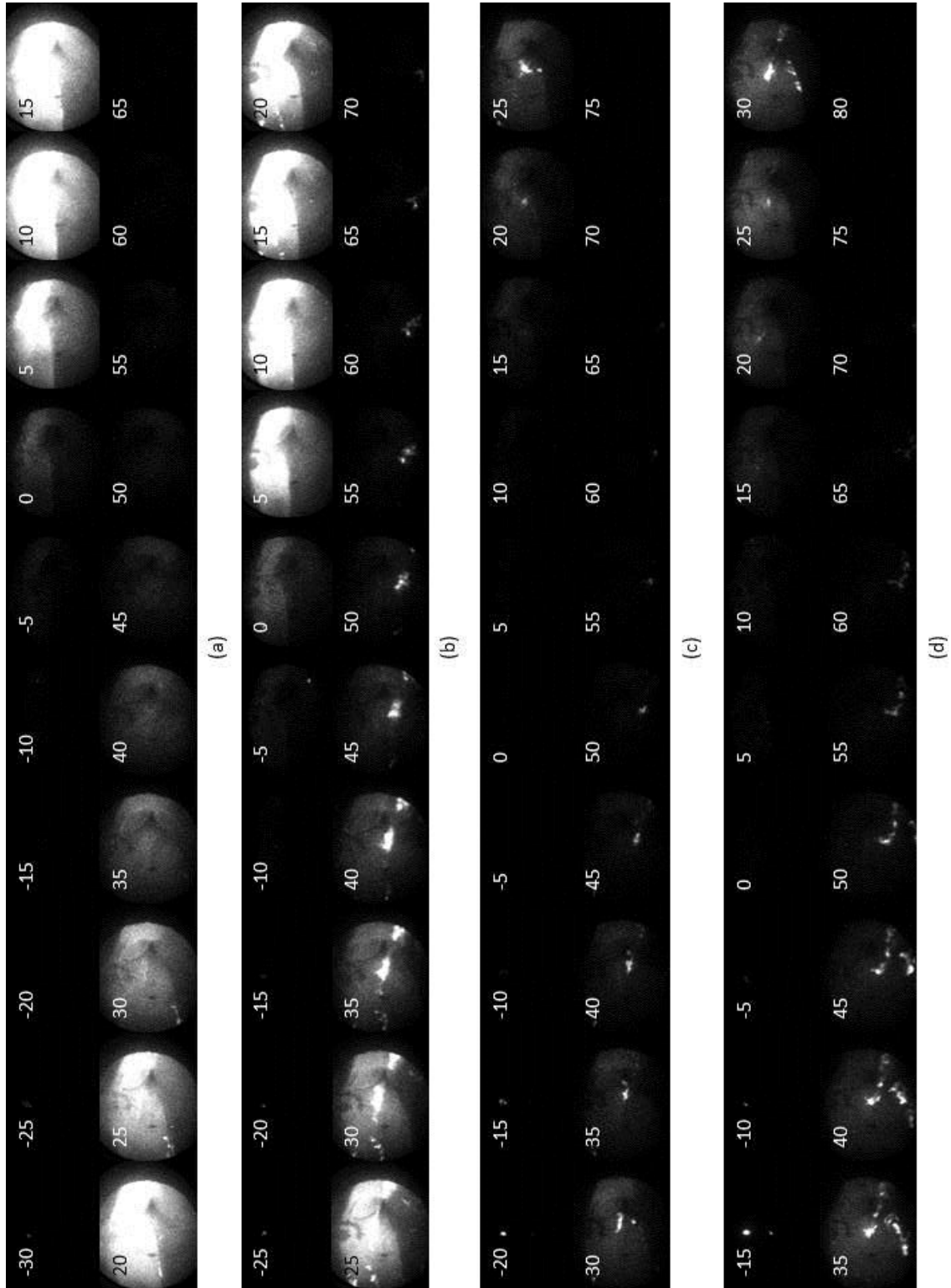


Figure 4.6.4. Ignition timing: (a) 30° (b) 25° (c) 20° (d) 15° bTDC_{fire} (mOAE; 1200 rpm)

4.7 Injection Timing Effect on Flame Propagation

The effects of SOI 300° bTDC_{fire} and 180° bTDC_{fire} are compared in both WOT (high load) and Throttled (low load) conditions listed in Table 4.7.1 and Table 4.7.2. The air-fuel ratios are lean for WOT and stoichiometric for Throttled to show the significance of the injection timing effect on PM emission. However, one should be noticed that a typical production engine would be running in rich air-fuel mixture in WOT or full load condition to avoid undesired engine combustion such as knocking. The spark timing is fixed at 20° bTDC_{fire} so that CA50 in both conditions is around 10° aTDC_{fire}. The COV_{IMEP} of all tests is in the acceptable range for engine operation; namely, it is less than 3%.

Figure 4.7.1 shows Method D images of E85 in Throttled condition. It is seen that the flame spreads out symmetrically from the spark plug position with SOI 300° bTDC_{fire}; on the other hand, it propagates to the intake side of the combustion chamber where higher intensity is seen with SOI 180° bTDC_{fire}. This indicates that most air-fuel mixture may concentrate on the intake side of the combustion chamber. Due to limited fuel-air interaction period with late SOI, the combustion has higher inhomogeneity and would have more unburned hydrocarbons (HC), which is seen in Table 4.7.2 and Table 4.7.4. The asymmetric combustion may apply uneven force to the piston and liner, which could cause extra deformation or wear to the piston and the cylinder liner. In addition, knocking could occur on the slow side of flame propagation, which is the exhaust side in this case, at higher load and engine speed.

In Throttled condition, CA50 and MBF (CA50-90) indicate that late SOI could enhance the flame propagation as suggested from the accumulated intensity images

in Figure 4.7.1; nevertheless, CA50 is somewhat slower for late SOI in WOT condition even though CA50-90 still shows significant decrease. It should be addressed that CA50-90 may represent diffusion flame region, which could be related to soot formation and PM emission, so shorter CA50-90 is usually more desirable. This will be proven and shown in Method E results later.

Comparing the two fuels, injection timing seems to have more impact on E85 as the flame propagation is faster (Throttled) or slower (WOT) depending on the operating conditions. Late SOI also seems to result in more stale combustion (lower COV_{IMEP}), which is contrary to its inhomogeneous flame propagation. Further investigation is needed yet beyond the current objectives.

The CFD results, although in slightly different conditions where ST is at 10° bTDC_{fire} instead of 20° bTDC_{fire}, still show the same flame propagations with respect to the two different injection timings. Figure 4.7.2 shows the results comparing to the image results by Method E. It is clearly seen that early SOI has fuel wall impingement on the piston top (Fig. 4.7.2(a)), and late SOI has asymmetric early flame propagation but no pool fire (Fig. 4.7.2(b)).

Table 4.7.1 WOT conditions and emissions (ST at 20° bTDC_{fire})

Lean	IMEP	COV _{IMEP}	SOI	CA50	CA 50-90
	[bar]	[%]	[° bTDC _{fire}]	[° aTDC _{fire}]	[°]
E0	10.99	1.62	300	9	42
	11.16	1.45	180	10	39
E85	11.67	1.72	300	9	37
	10.62	1.32	180	12	28

Lean.	SOI	CO	HC	NO
	[° bTDC _{fire}]	[%]	[ppm]	[ppm]
E0	300	0.02	737	1869
	180	0.02	1097	1782
E85	300	0.03	382	1274
	180	0.04	591	393

Table 4.7.2 Throttled conditions and emissions (ST at 20° bTDC_{fire})

Stoich.	IMEP	COV _{IMEP}	SOI	CA50	CA 50-90
	[bar]	[%]	[° bTDC _{fire}]	[° aTDC _{fire}]	[°]
E0	5.86	1.92	300	10	20
	5.63	1.7	180	9	23
E85	5.55	2.01	300	10	20
	5.31	2.51	180	8	19

Stoich.	SOI	CO	HC	NO
	[° bTDC _{fire}]	[%]	[ppm]	[ppm]
E0	300	0.42	957	701
	180	0.48	1628	645
E85	300	0.19	512	573
	180	0.12	824	835

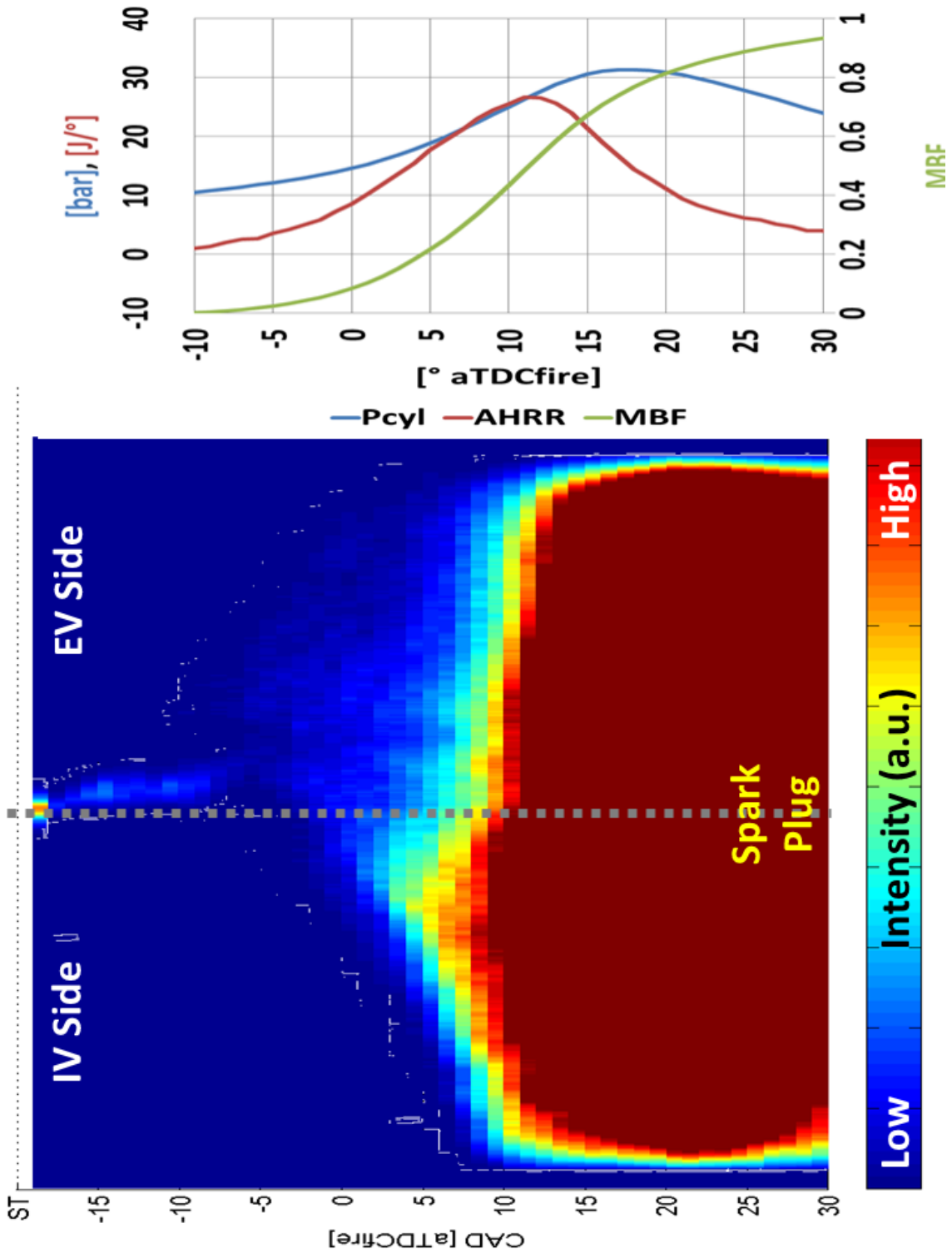


Figure 4.7.1 Method D at different SOI (test condition: Throttled; Stoich; ST 20°

bTDC_{fire}) (a) SOI 300° bTDC_{fire}

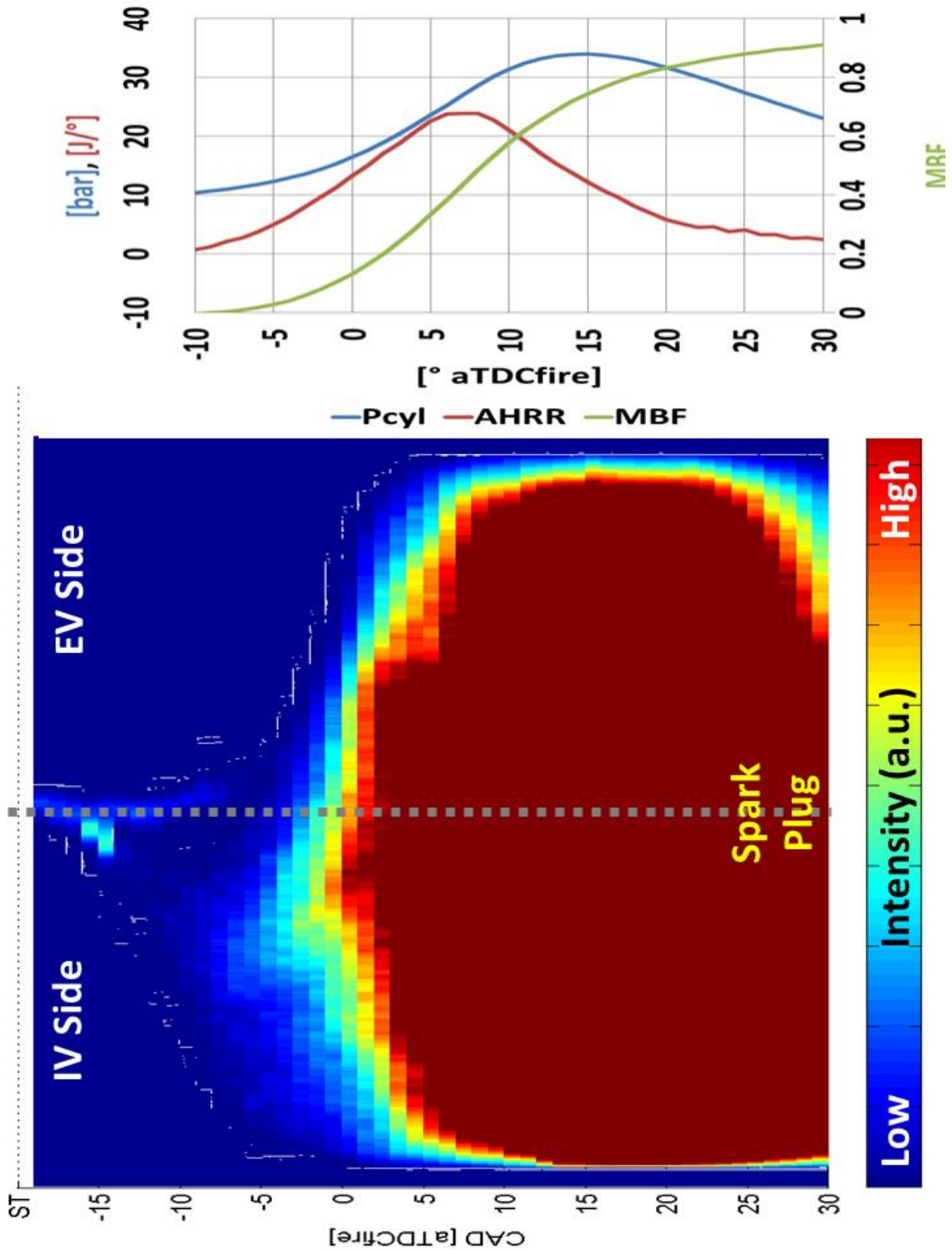


Figure 4.7.1 Method D at different SOI (test condition: Throttled; Stoich; ST 20° bTDC_{fire}) (b) SOI 180° bTDC_{fire}

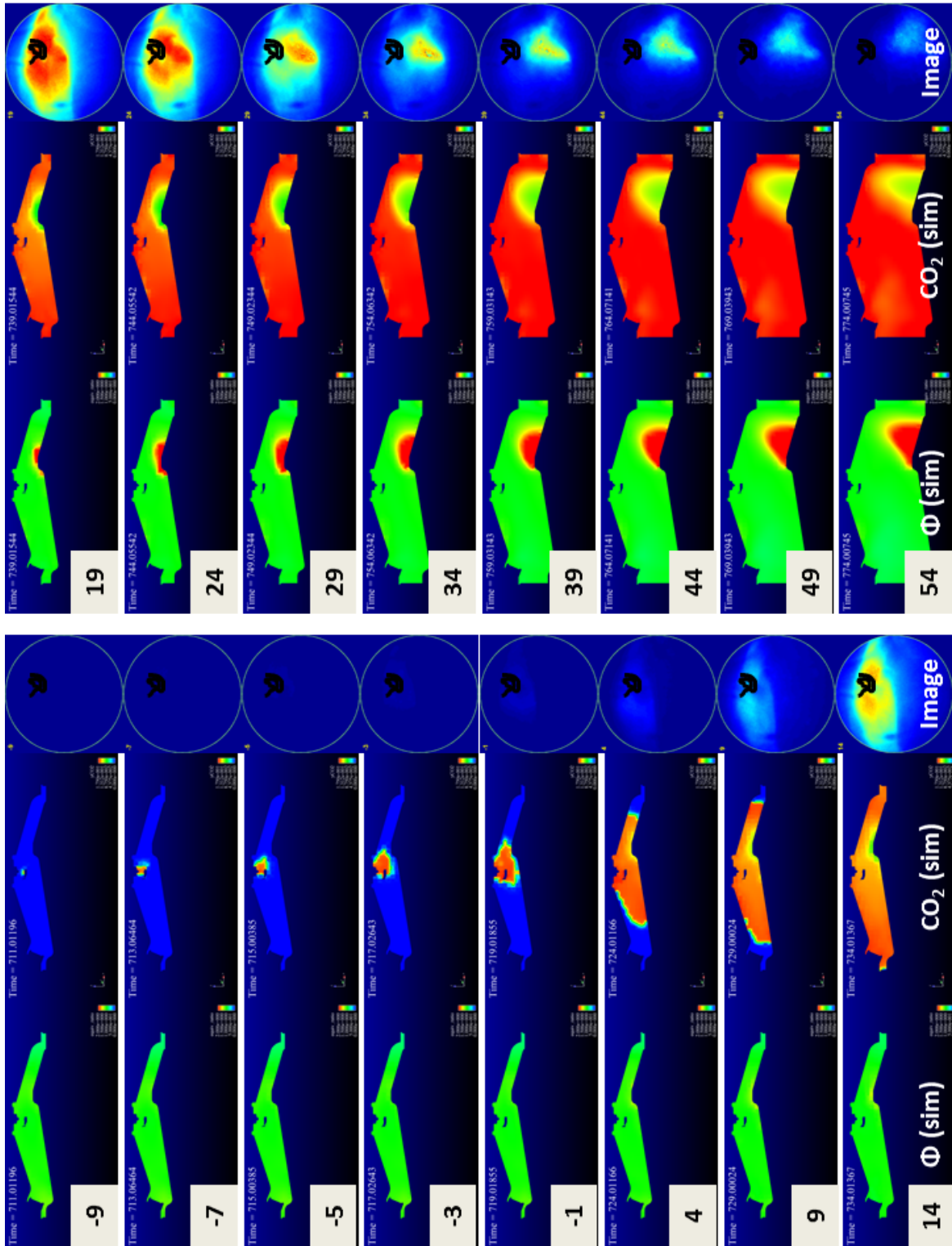


Figure 4.7.2 CFD v.s. Method E (test condition: Throttled; Stoich; ST 10° bTDC_{fire})

(a) SOI: 300° bTDC_{fire}

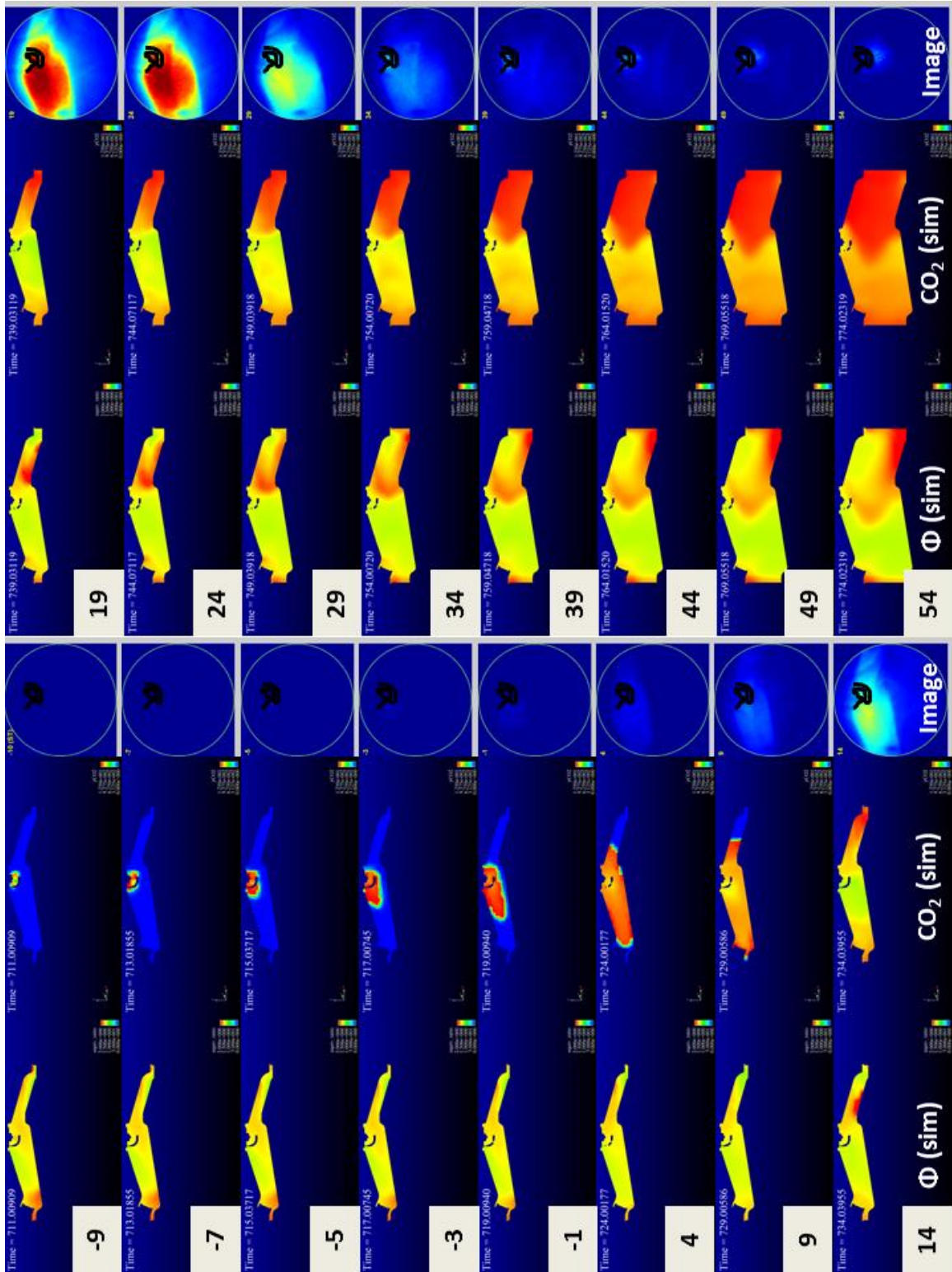


Figure 4.7.2 CFD v.s. Method E (test condition: Throttled; Stoich; ST 10° bTDC_{fire})

(b) SOI: 180° bTDC_{fire}

4.8 Injection Timing and Ignition Timing Effect on Pre-Ignition

Another set of tests is also performed to observe the combustion images with the in-cylinder pressure, apparent heat release rate, and mass burnt fraction curves. SOI at 300° bTDC_{fire} and 60° bTDC_{fire} are chosen to compare homogeneous combustion (premix) and stratified charge combustion, and ST at 20° bTDC_{fire} and 10° aTDC_{fire} are selected. The test conditions are listed as below.

Test condition:

- 1200 rpm; MAP: 1 bar; Lambda: ~ 1.15 ; EGR 0%; 25°C intake air; 40°C coolant
- Injection timing: 300 or 60° bTDC_{fire}
- Injection pressure: 100 bar
- Ignition timing: 20° bTDC_{fire} or $^\circ$ aTDC_{fire}
- Camera Frame Rate: 12000 fps

Due to possible instability concern, the tests are only performed on the metal engine. The baseline results are shown in Fig 4.8.1. Early injection gives the air and fuel enough time to mix more homogeneously as shown in Fig. 4.8.1(a). The IMEP of the case is 13.055 bar, and CA50 is at an optimal position, which is between 5° and 10° aTDC_{fire}. However, once the injection is retarded to 60° aTDC_{fire}, as shown in Fig. 4.8.1(b), the combustion images indicate that the mixture does not have the same mixing quality. The flame is more heterogenous or diffusion-like. IMEP fluctuates more with late injection, and possible pre-ignition or misfire may also occur, which will be presented later.

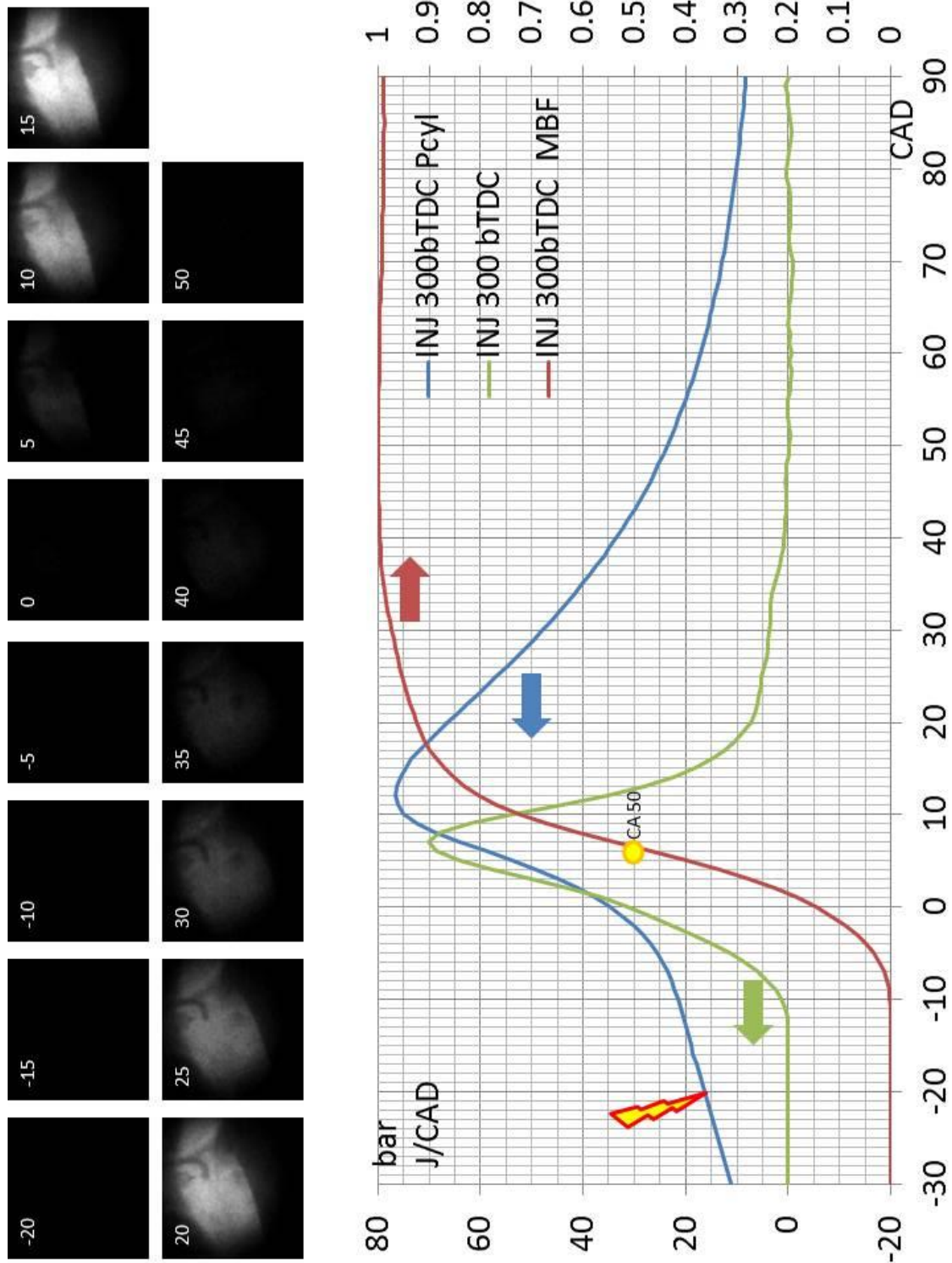


Figure 4.8.1 (a) Early injection (baseline; SOI 300° bTDC_{fire}; ST 20° bTDC_{fire})

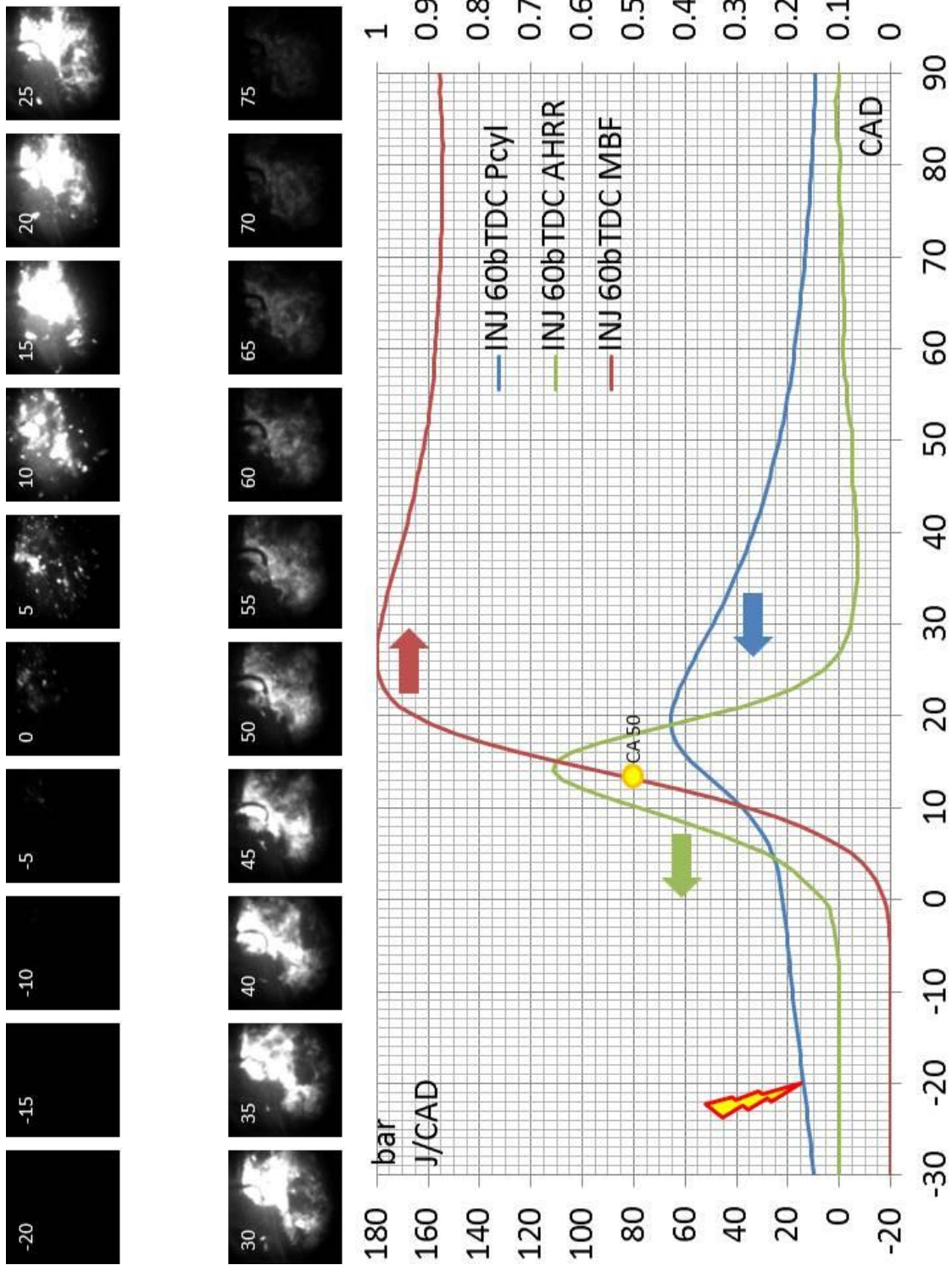


Figure 4.8.1 (b) Late injection (SOI 60° bTDC_{fire}; ST 20° bTDC_{fire})

One noticeable phenomenon of late injection is misfire. From the results of data acquisition, misfire occurs very often with late injection, whereas no misfire is observed with early injection. With the optical access, it is easy to compare the pressure traces and images side-by-side and to discover that once a misfire occurs, the ensuing cycles have the pattern of late-burn to fast-burn. Due to the resolution of data acquisition, the results do not indicate any abrupt pressure rise, excessive peak pressure, or pressure trace fluctuation. Nevertheless, low speed pre-ignition is captured with retarded spark timing as the results shown below.

Figure 4.8.2(a) shows the result of a late-burn cycle, which occur right after a misfire cycle. The images show some visible flame at later crank angle degree. To cause pre-ignition after a late-burn cycle, one hypothesis is considered that the hot burnt gas does not have time to cool down before exiting from the exhaust valves, so the residuals remain higher-than-normal temperature. Once the following cycle starts, the air-fuel mixture is warmed up faster than a fast-burn cycle would therefore occurs as shown in Fig. 4.8.2(b).

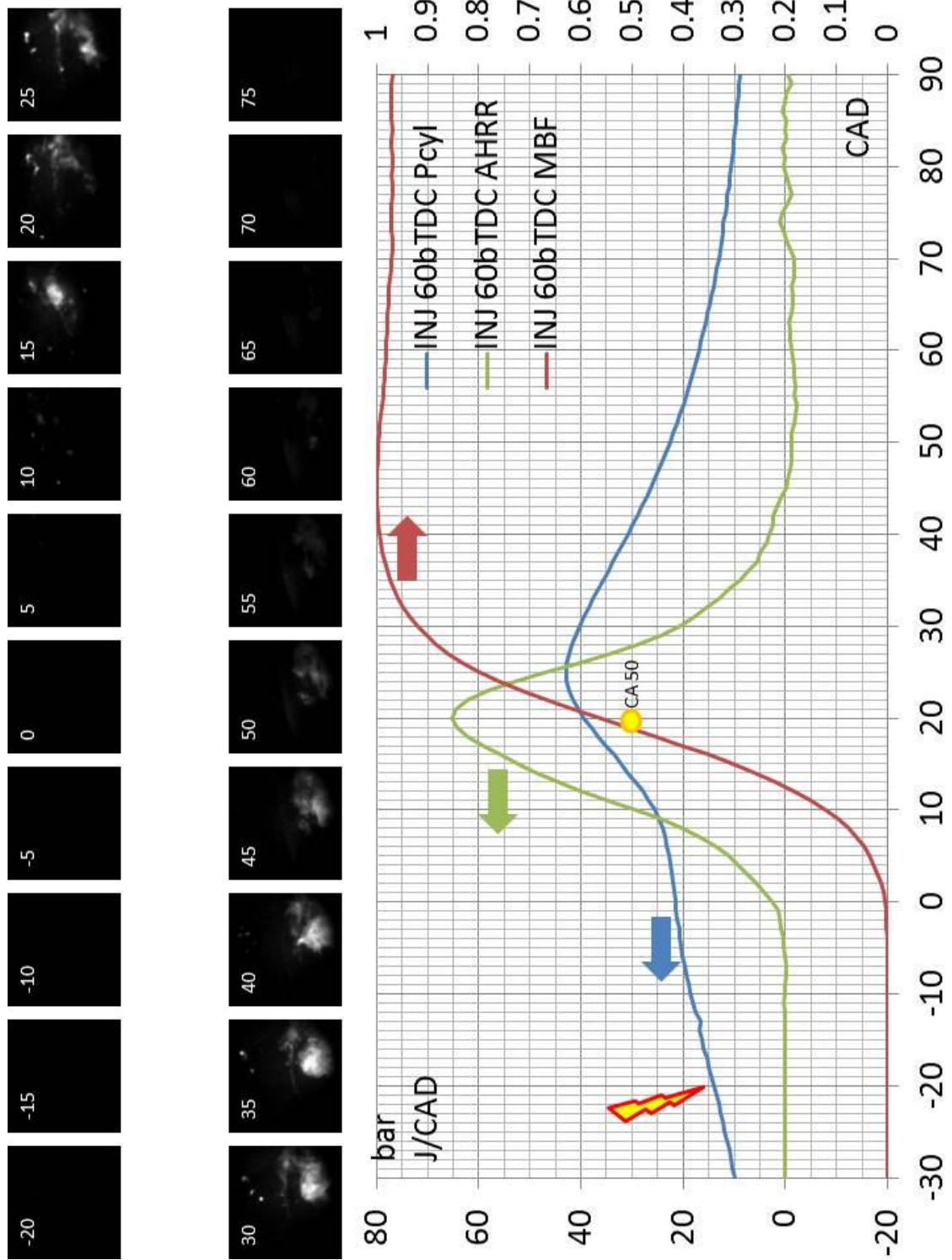


Figure 4.8.2 (a) Late burn after a misfire cycle (SOI 60° bTDC_{fire}; ST 20° bTDC_{fire})

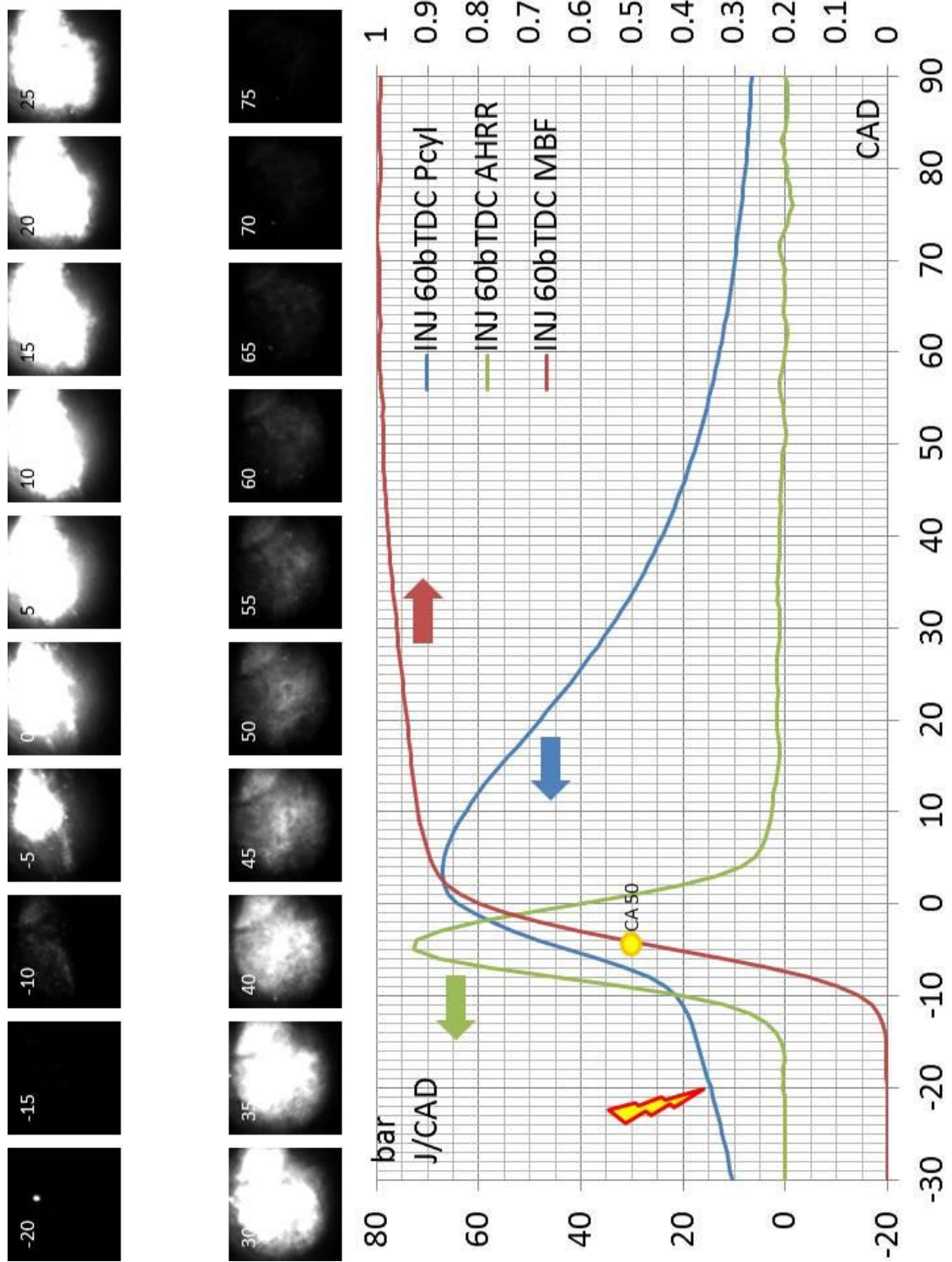


Figure 4.8.2 (b) Fast burn after a late burn cycle (SOI 60° bTDC_{fire}; ST 20° bTDC_{fire})

To confirm the assumption above, the spark timing is set at 10° aTDC_{fire} to cause pre-ignition. Although the pressure traces of all cycles are not shown in the thesis because of its length, it is found that a pre-ignition cycle occurs after a late-burn one as shown in Fig. 4.8.3. Figure 4.8.4 shows the pre-ignition image results and the pressure traces of the pre-ignition and the normal combustion. It is clearly seen that the pre-ignition combustion starts much earlier than the actual spark timing.

The first hump of the normal pressure trace (light blue) in Fig. 4.8.4 could be considered as the motoring pressure trace due to late spark timing, and the second hump is called firing peak pressure. Therefore, the pre-ignition pressure trace suggests that there be endothermic reactions between 60° bTDC_{fire} and 30° aTDC_{fire}. Figure 4.8.5 shows another pre-ignition event (without pressure trace) that clearly presents the combustion (flaming cloud) starts before the onset of spark. The light intensity is very strong that the images are over saturated.

The reactions could be due to fast vaporization process of fuel, which is injected at 60° bTDC_{fire}. The reason for the fuel to vaporize rapidly is that there may be hot residual gas or oil droplets inside the combustion chamber from the previous cycle that causes the auto-ignition for the ensuing cycle. Therefore, the pre-ignition occurs without the spark. Nonetheless, the current study does not find that E85 is more prone to pre-ignition than E0 suggested by other literature. Both fuels show 9 cycles of pre-ignition event out of 100 cycles of data as shown in Fig. 4.8.6. Therefore, more in-depth research is needed to further understand the onset of pre-ignition.

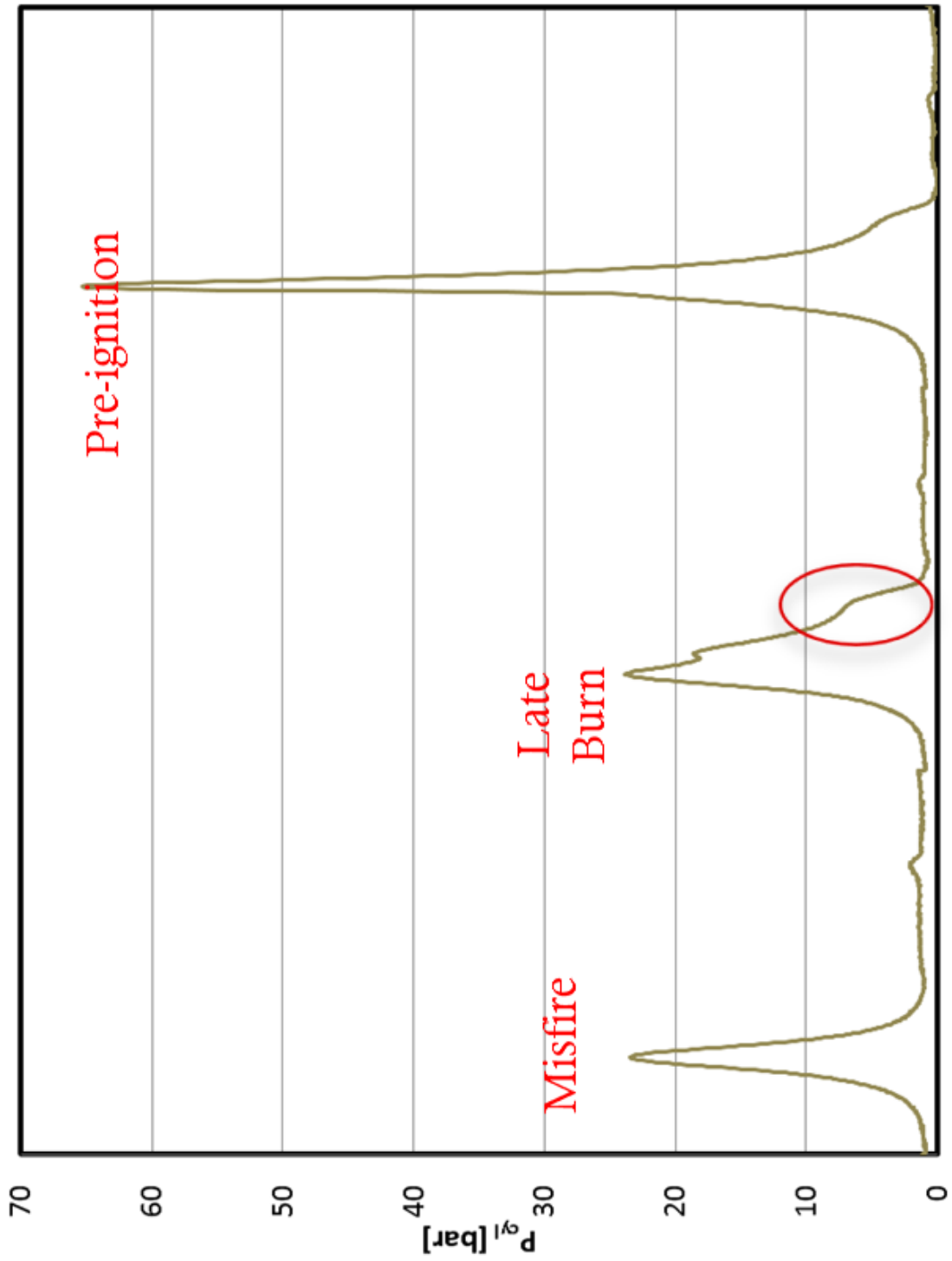


Figure 4.8.3 Misfire, late burn, and pre-ignition pressure traces (consecutive cycles)

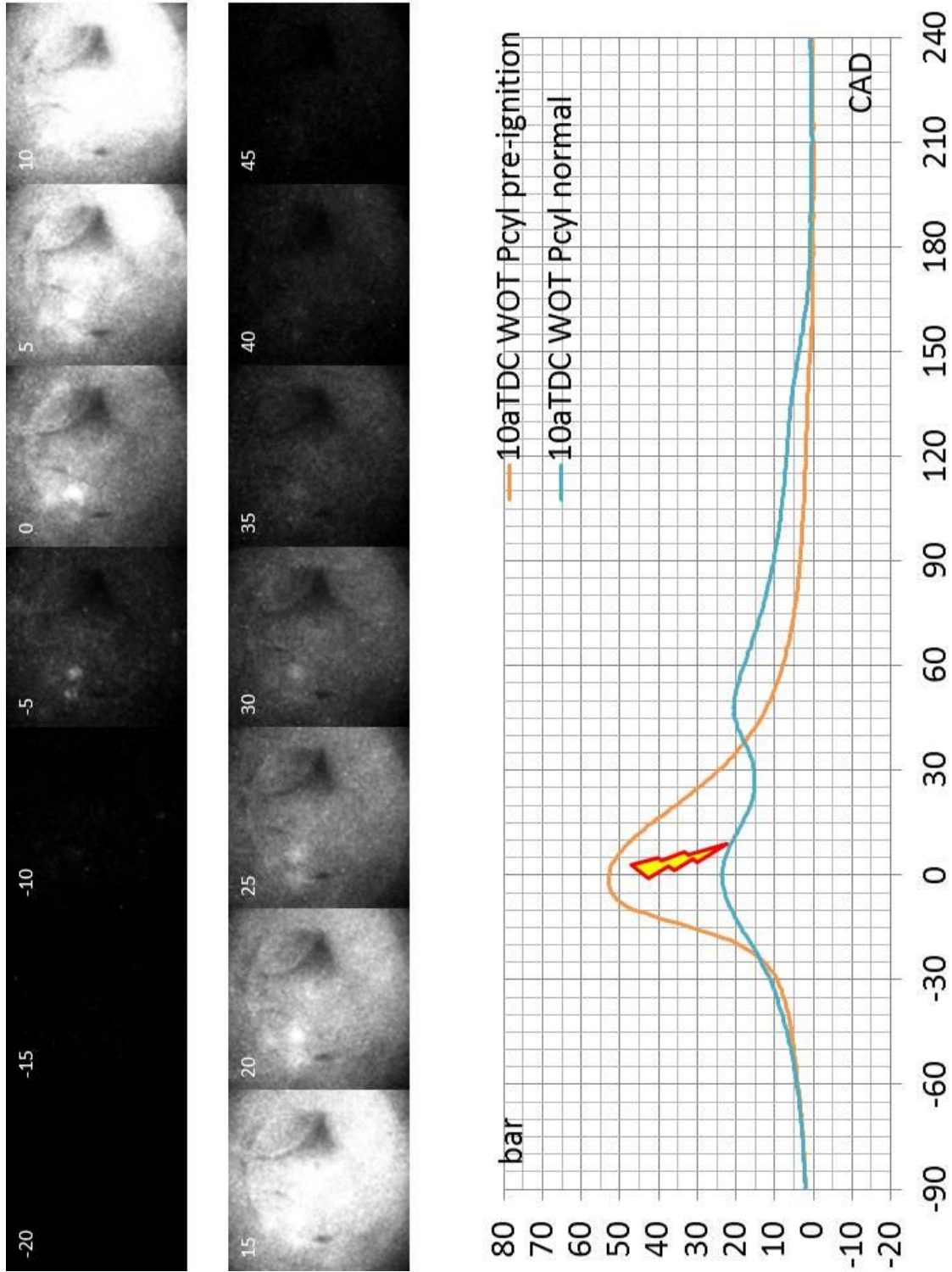


Figure 4.8.4 Pre-ignition v.s. normal pressure trace

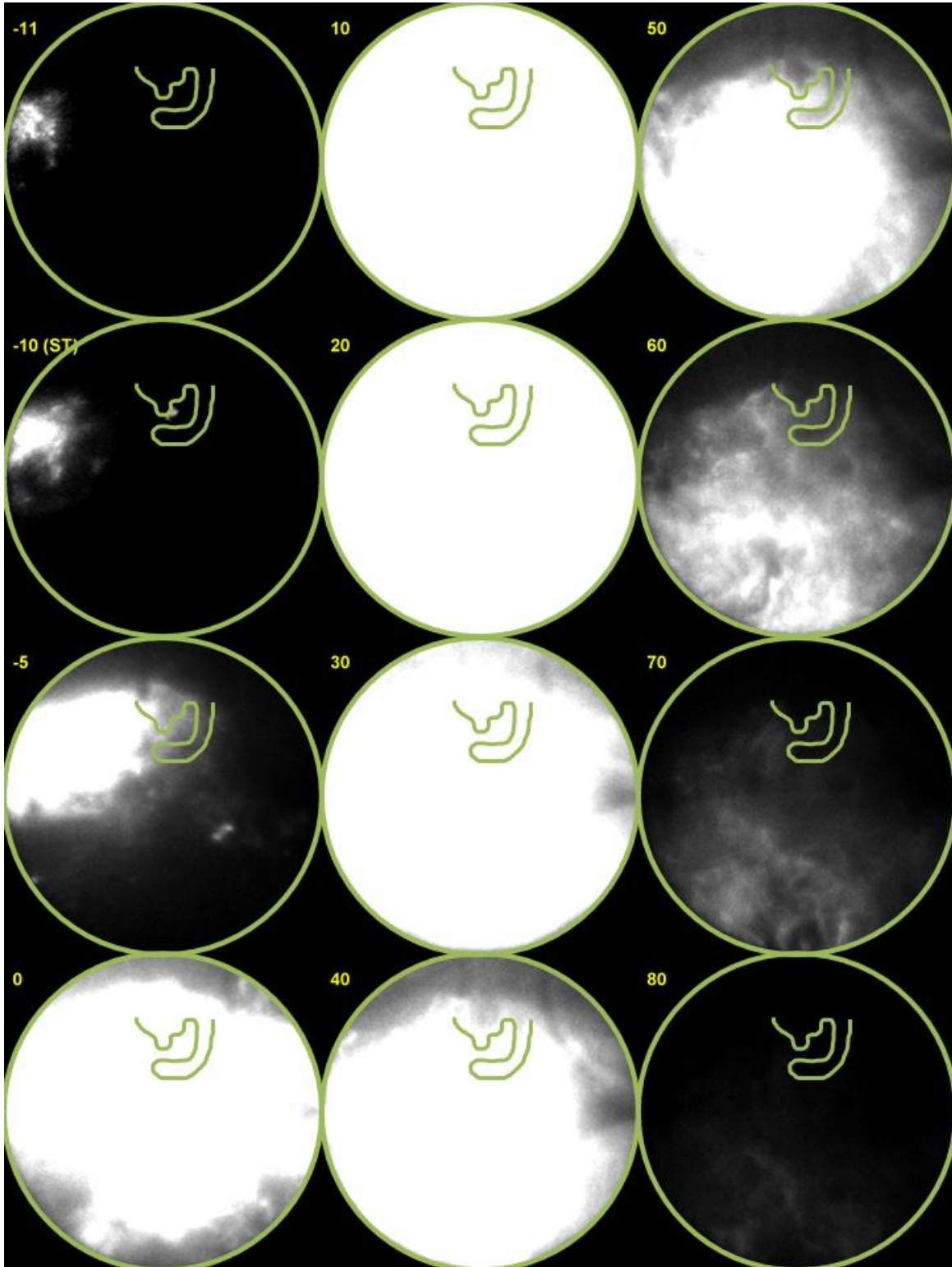
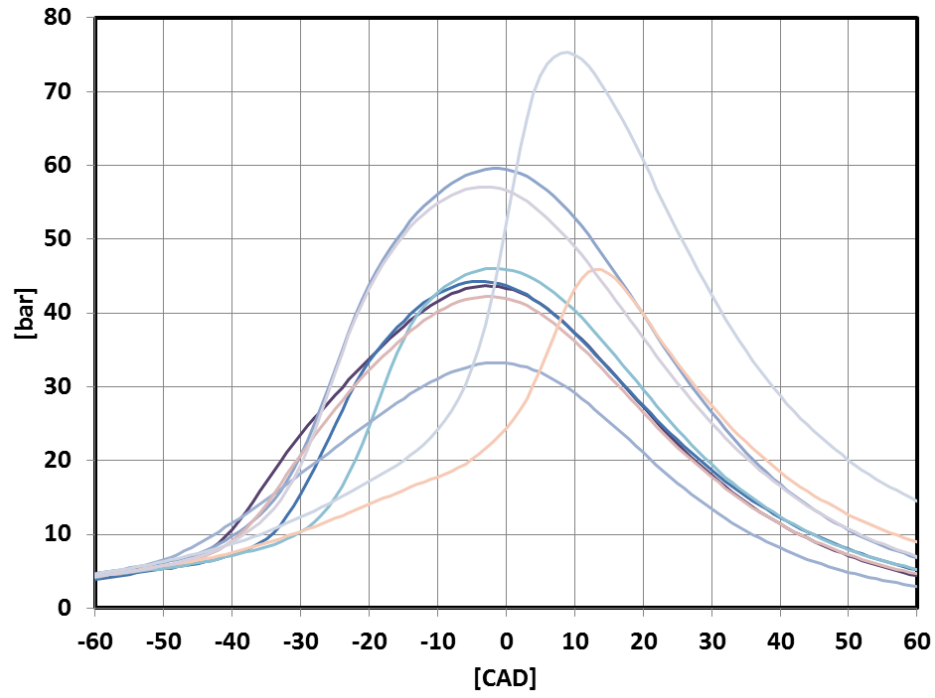


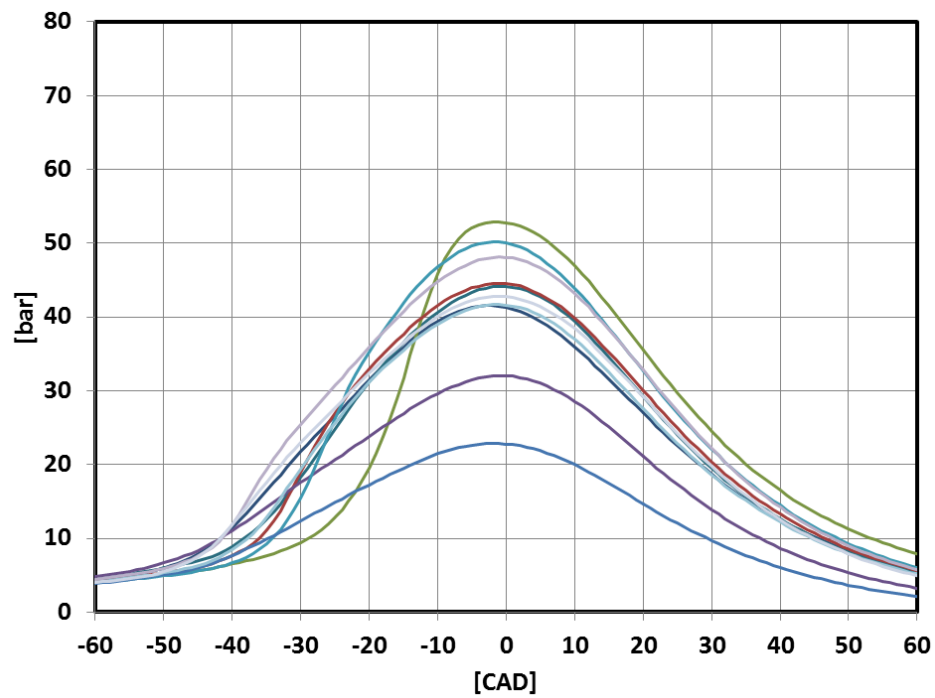
Figure 4.8.5 (a) Pre-ignition images



Figure 4.8.5 (b) Pre-ignition image (1° after ST)



(a)



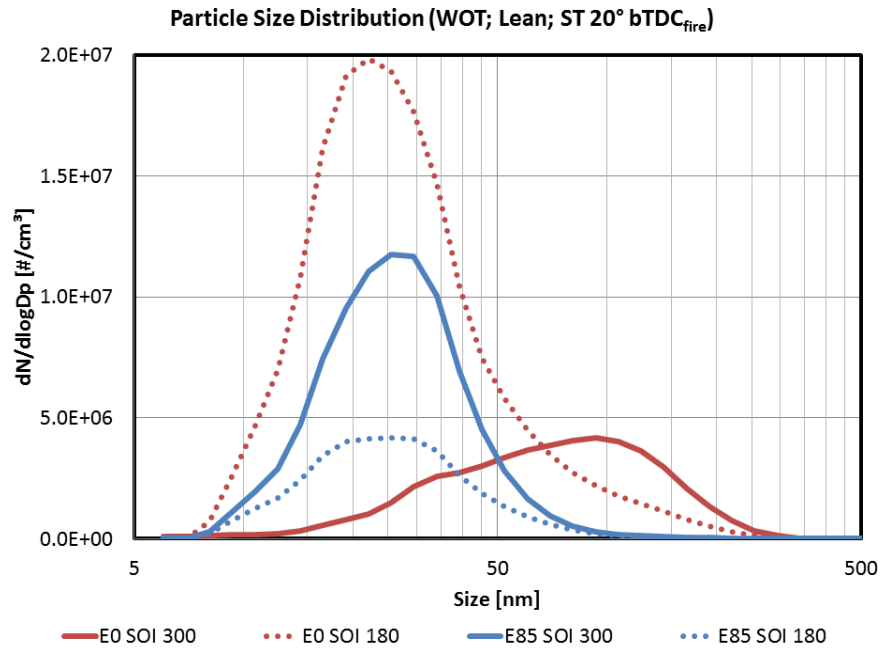
(b)

Figure 4.8.6. (a) E0 and (b) E85 pre-ignition pressure traces (out of 100 cycles)

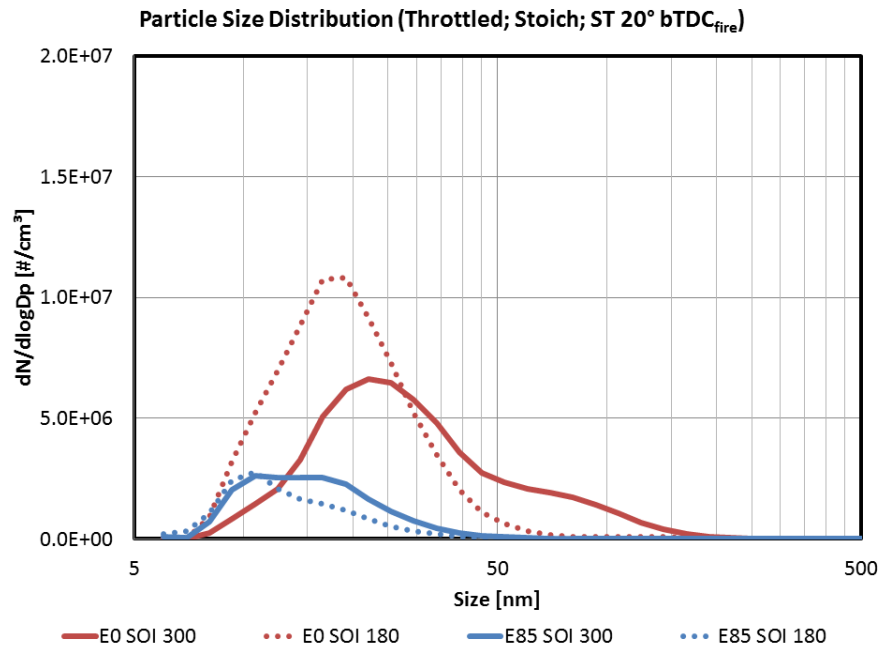
4.9 Injection Timing Effect on PM Emission

PM emission of E0 and E85 is demonstrated as the particle size distributions in Fig. 4.9.1 in both WOT and Throttled conditions, and Fig. 4.9.2 shows the total concentration and mass of both fuels with respect to injection timing. The raw and statistical intensity images (Method E) of one test condition are shown in Fig. 4.9.3.

Comparing the size distribution of E0 and E85 at early SOI (solid lines in Fig. 4.9.1(a)), it is found that E85 has more particles in nuclei mode (particle diameter <50 nm) and E0 has more particles in accumulation mode (particle diameter >100 nm). This is in the agreement with other research that the presence of ethanol in fuel could reduce the particle number in accumulation mode [68]. Figure 4.9.1(b) also shows the same trend that E0 with early SOI has more large particles, but the particle size distribution shifts to smaller sizes. The particle size distribution of SOI 180° bTDC_{fire} is dominated by nuclei mode particles for both fuels at both throttle positions. This is also described in [65, 69] that earlier SOI could produce more particles in accumulation mode due to piston wall wetting of fuel; pool fire could therefore be observed from optical access as seen in Fig. 4.9.3. Nonetheless, E85 does not produce high particle numbers in accumulation mode in both WOT and Throttled as Fig. 4.9.1 shows.



(a)

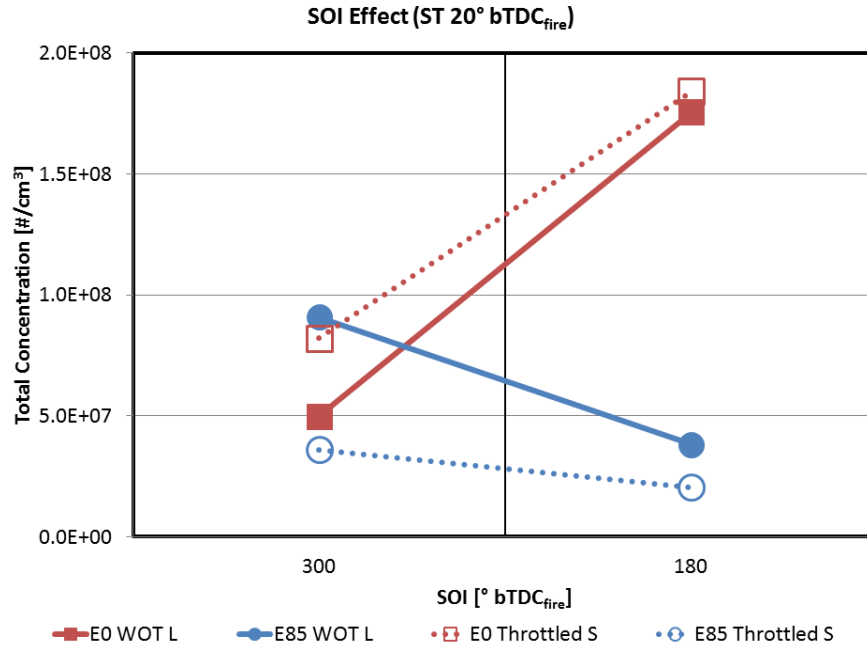


(b)

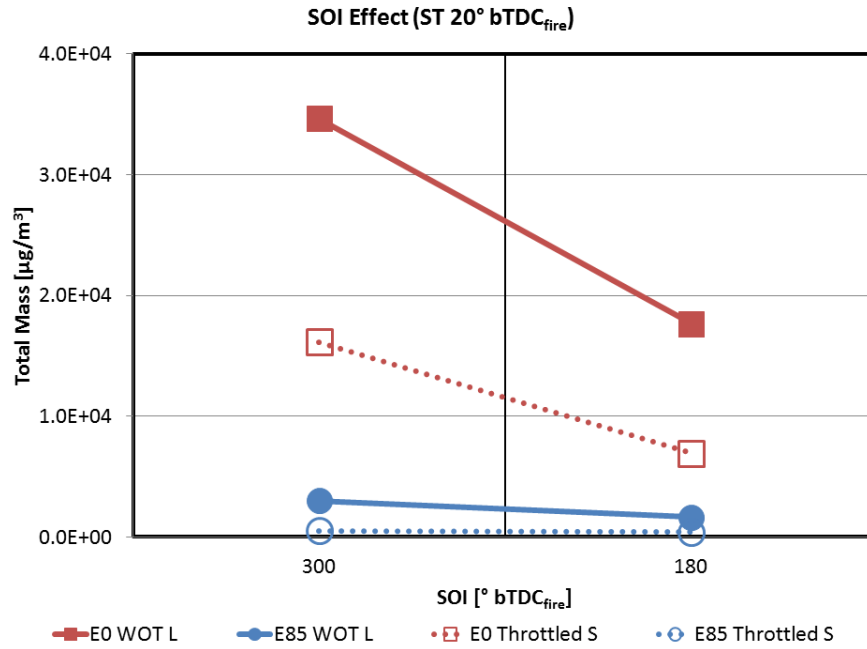
Figure 4.9.1 Particle size distribution of (a) WOT and (b) Throttled conditions at different SOI [° bTDC_{fire}]

Figure 4.9.2(a) indicates two opposite trends of the total concentration with respect to injection timing on both fuels. Regardless of the throttle positions, it is found that retarding injection timing would increase the particle number for E0 but decrease that for E85. It should be noticed that the air-fuel ratios are different in WOT and Throttled conditions but could be neglected because E85 WOT (Lean) still shows higher particle numbers at early SOI compared to all Throttled conditions (Stoich). In addition, the total concentration of PM for E85 is found much higher than that for E0 in WOT condition at early SOI although its total mass is much lower, as the solid blue dots shown in Fig. 4.9.2.

It is concluded that the E85 combustion does not form as many particles in accumulation mode as E0 even in the presence of diffusion flame since E85 does not have as many long-chain compounds, e.g. aromatics, as E0. On the other hand, it is faster to form fine particles from the incomplete combustion of short-chain compounds, whereas long-chain compounds will take longer time to be consumed that most particles are relatively larger. Therefore, more particles in nuclei mode are seen with E85, and its total concentration is higher as mentioned above. Furthermore, more E85 is injected in order to keep the same λ , and $\text{SOI } 180^\circ \text{ bTDC}_{\text{fire}}$ requires more fuel for both E0 and E85 due to stronger charge cooling effect. Had E85 consisted of more long-chain compounds, its particle size distribution and total concentration would have been similar to E0 results with respect to SOI.



(a)



(b)

Figure 4.9.2 (a) Total concentration and (b) total mass of PM emission at different SOI [° bTDC_{fire}]

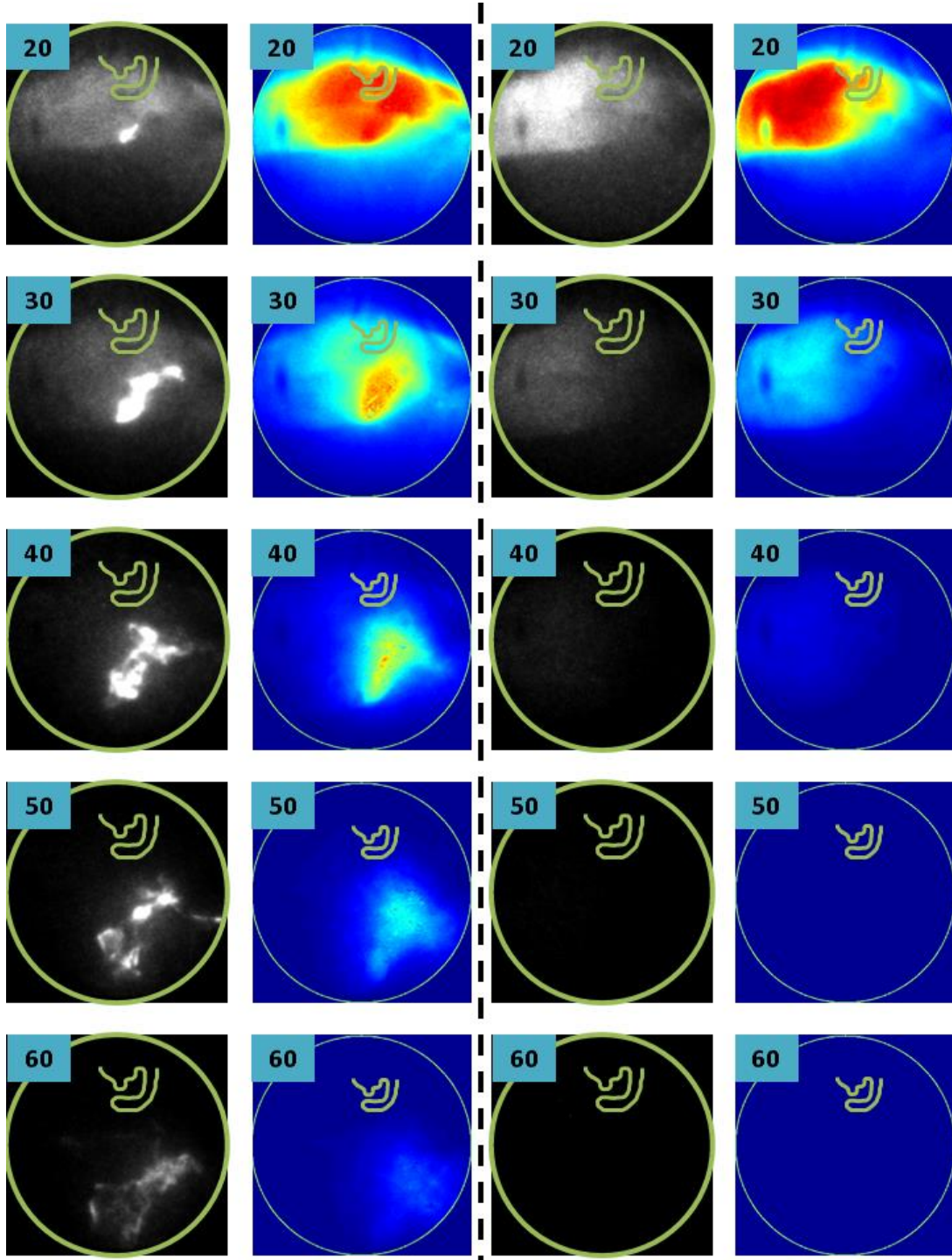


Figure 4.9.3 Raw and Method E images of E85 Throttled at different SOI: 300° bTDC_{fire} (left); 180° bTDC_{fire} (right) (numbers in the corner represent $^\circ$ aTDC_{fire}; test condition: Throttled; Stoich; ST 20° bTDC_{fire})

The raw and statistical intensity images of E85 combustion after 20° TDC_{fire} for both injection timing in Throttled shown in Fig. 4.9.3, the pool fire is present due to piston wall-wetting cause by early SOI. This is a contrast to some studies that E85 does not show strong diffusion combustion and therefore PM emission is lower [86, 87]. Therefore, it is believed that both image and PM emission measurement results are necessary to such research. Besides, the current study uses a minimum modified production engine, so it is believed that the air-fuel-wall interaction is close to realistic conditions for PM emission study.

In order to further study the difference between the fuels on the total concentration, images of a condition (WOT, Rich; SOI 300° bTDC_{fire}; ST 30° bTDC_{fire}; IMEP 12 bar) are shown in Fig. 4.9.4 with both fuels to emphasize the opposite trends. The total concentration of E0 and E85 is 1.8×10^8 and 3.0×10^8 #/cm³, respectively; the total mass of them is 3.3×10^4 and 1.5×10^4 #/cm³, respectively. It is clearly seen that both combustion images show strong diffusion flame. It should be noticed that the intensity of the images from the two fuels should not be compared side-by-side because different intensifier setup is used. Nevertheless, E0 combustion shows diffusion flame not only on the piston top but also the chamber roof and the injector side. Thus, the diffusion flame could be correlated with the combustion of long-chain compounds with heavier particles formed, yet the number of particles may vary depending on the type of fuel and operation conditions as indicated by the results found in the current study.

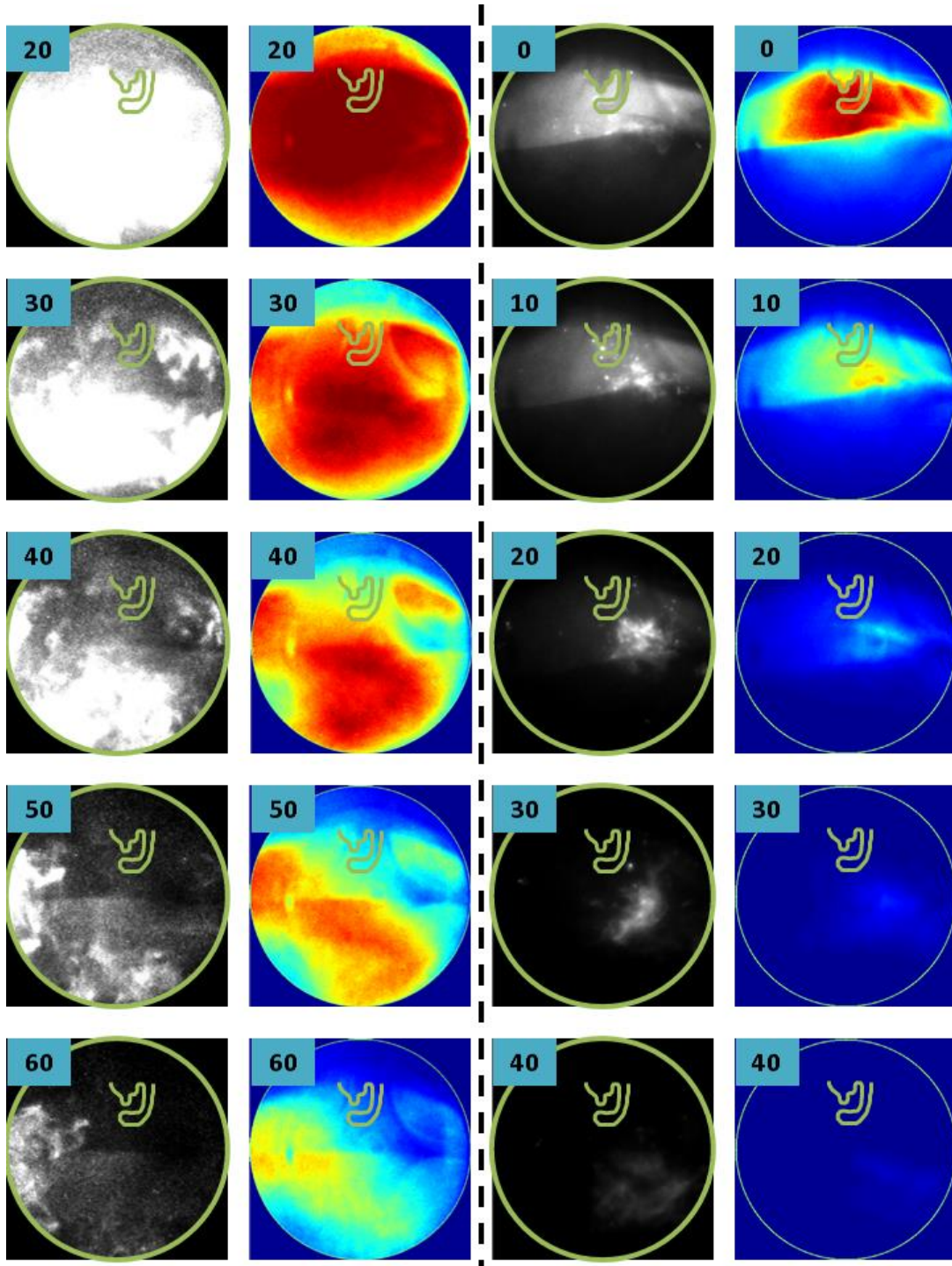


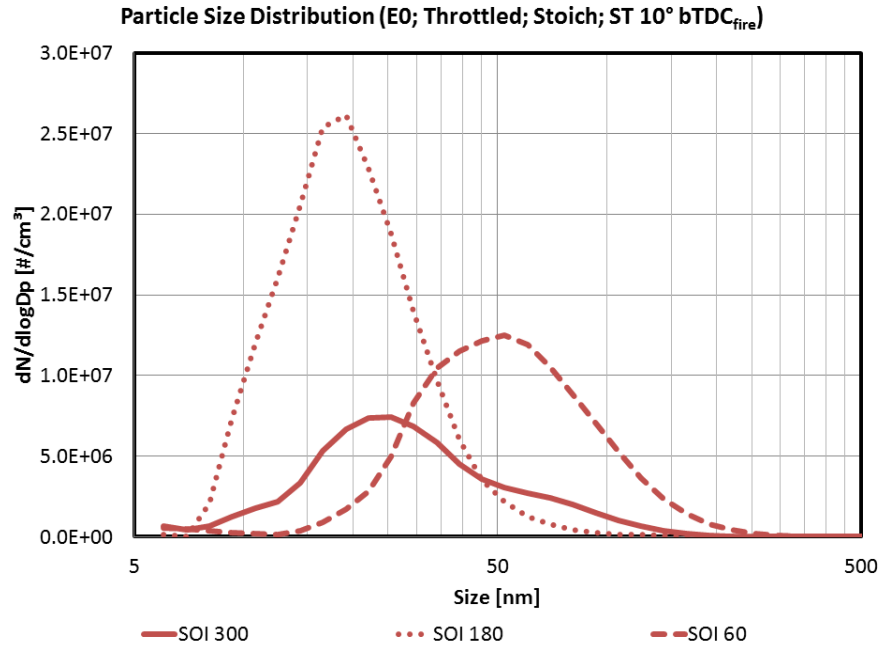
Figure 4.9.4 Raw and Method E images of E0 (left) and E85 (right; notice E85 images at different $^{\circ}$) (numbers in the corner represent $^{\circ}$ aTDC_{fire}; test condition:

WOT; Rich; SOI 300 $^{\circ}$ bTDC_{fire}; ST 30 $^{\circ}$ bTDC_{fire})

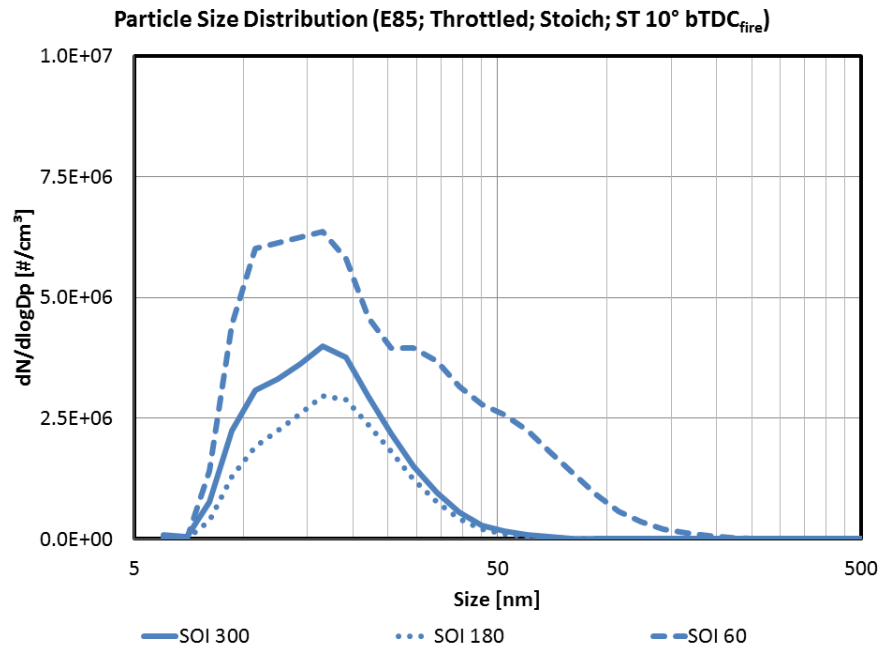
SOI at 60° bTDC_{fire} is also selected to study PM emission in stratified charge regime. Due to the instability of the combustion, only Stoich mixture is tested with both fuels in Throttled conditions. Although the engine was not designed for practical stratified charge combustion that ultra-lean burn conditions are not feasible, the results are interesting and also prove the effect of ethanol on soot formation. Figure 4.9.5 and Fig. 4.9.6 show the results of size distribution, total concentration, and total mass for E0 and E85; Fig. 4.9.7 shows the raw and statistical intensity images.

It is shown in Fig. 4.9.5(a) that particle size distribution of E0 shifts towards accumulation mode with SOI 60° bTDC_{fire}, whereas E85 only has slight increment. This further proves that E85 does not have significant particle size change even though strong diffusion flame is present as shown in Fig. 4.9.7. On the other hand, E0 particle size distribution is strongly affected by the presence of diffusion flame that accumulation mode occurs along with it. In terms of particle mass, it is proportional to the magnitude of diffusion flame as the data and images suggest.

A conclusion could be made that injection timing plays a critical role in GDI applications. A poor calibrated engine could result in excessive soot formation during a combustion cycle and therefore PM emission will be much higher. Injector position in the combustion chamber and spray pattern would also affect the PM emission since fuel wall wetting is very likely in a GDI engine. Using alternative fuel could reduce the total particle mass; however, total particle concentration may be high, especially particle number in the nuclei mode.

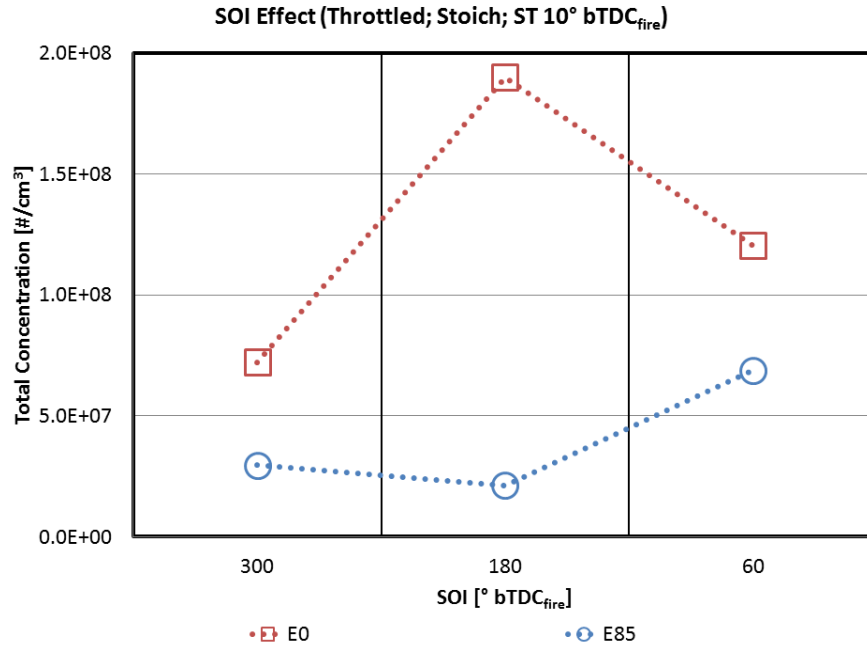


(a)

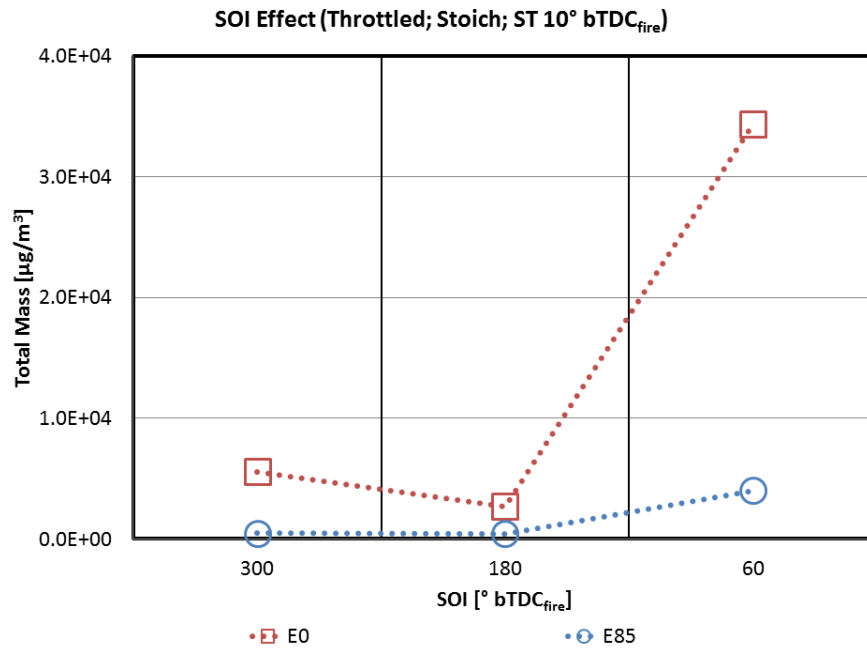


(b)

Figure 4.9.5 Particle size distribution of (a) E0 and (b) E85 at different SOI [° bTDC_{fire}]



(a)



(b)

Figure 4.9.6 (a) Total concentration and (b) total mass of PM emission at different SOI [° bTDC_{fire}]

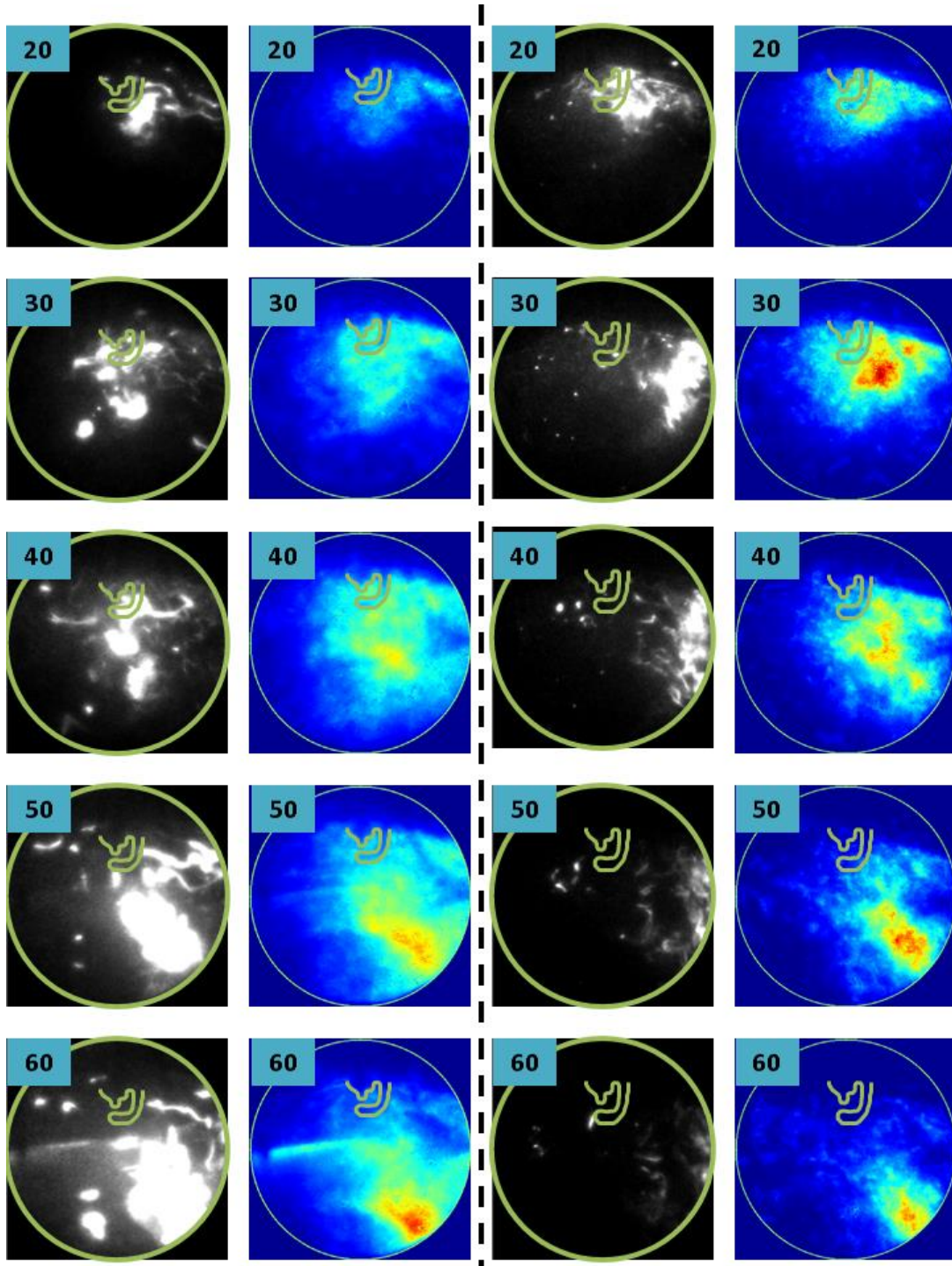


Figure 4.9.7 Raw and Method E images of E0 (left) and E85 (right) with late injection timing (numbers in the corner represent $^{\circ}$ aTDC_{fire}; test condition: Throttled; Stoich; SOI 60 $^{\circ}$ bTDC_{fire}; ST 10 $^{\circ}$ bTDC_{fire})

4.10 Ignition Timing Effect on PM Emission

In Table 4.10.1 and Table 4.10.2, the engine operation conditions and emission results in WOT and Throttled conditions are listed. Since spark timing is relevant to combustion phasing, it is seen that CA50 occurs later with retarded ST. The IMEP and COV_{IMEP} indicate that MBT is at ST 20° bTDC_{fire}, and combustion is slightly deteriorated with further retarded ST, especially with E85. HC and NO emissions are in the agreement with [49] that HC would decrease with retarded ST unless combustion is not sustainable; NO_x will decrease with retarded ST since the in-cylinder temperature is lower. PM emission with respect to ST is shown in Fig. 4.10.1 as the total concentration and mass; Fig. 4.10.2 shows the particle size distributions.

E0 and E85 total concentration and mass in Throttled conditions decrease with retarded ST due to deteriorated combustion (high COV_{IMEP} in Table 4.10.2). The trend is also found in [69]; however, the total concentration of particles for E0 in WOT conditions increases with retarded ST while the results of E85 show reduction at MBT but more particles at late ST. The difference could be explained with the image results shown in Fig. 4.10.3. With early ST in Fig. 4.10.3(a), both fuels show diffusion flame from the cylinder liner; however, only E85 shows diffusion flame at late ST in Fig. 4.10.3(b).

It is known that HC in crevice volume will come out once the piston starts moving down from the TDC position, so it could be burned if combustion flame propagates to the same location. Therefore, HC is usually expected to be lower with retarded ST [31, 44]. However, the engine coolant temperature is kept at 40°C in the present study that quench zone is expected to be larger and to contain more HC, so only part of HC in crevice volume may be burned completely with late ST. In other words, the increase in partial burnt HC could result in more particle formation. As the result, total concentration of particles for E0 in WOT conditions is lower at early ST and higher at late ST; total mass is higher at early ST and lower at late ST.

Moreover, the presence of diffusion flame in E0 images of Fig. 4.10.3(a) indicates more accumulation mode particles and no diffusion flame is observed in E0 images of Fig. 4.10.3(b); nevertheless, diffusion flame is seen in E85 images in Fig. 4.10.3. This is concluded that the injection quantity of E0 is much less in Thorttled conditions, which means very little HC will be present in the crevice volume. There is therefore no diffusion flame shown in Fig. 4.10.3(b) for E0. Using E85 fuel will require more injection quantity to match the same power output due to its lower energy content. This is the reason that E85 images in Fig. 4.10.3(b) show diffusion flame from fuel wall impingement due to more fuel injected into the combustion chamber.

As for E85 in WOT conditions, it is found that diffusion flame from the cylinder liner is present at both early and late ST as shown in Fig. 4.10.3(a) and Fig. 4.10.3(b), respectively. The diffusion flame of early ST is due to early CA50 (4° aTDC_{fire}) that HC from the liner is not burned completely to CO₂. The diffusion flame occurs at late ST is caused by late combustion phasing that the temperature and pressure of combustion chamber are not suitable to burn all HC from the liner. HC emission in Table 4.10.1 and Table 4.10.2 also supports this explanation that HC increases with either too early or too late ST. Nonetheless, E85 produces much less PM emission in terms of total mass in both WOT and Throttled conditions regardless of ignition timing.

Table 4.10.1 WOT conditions and emissions (SOI at 180° bTDC_{fire})

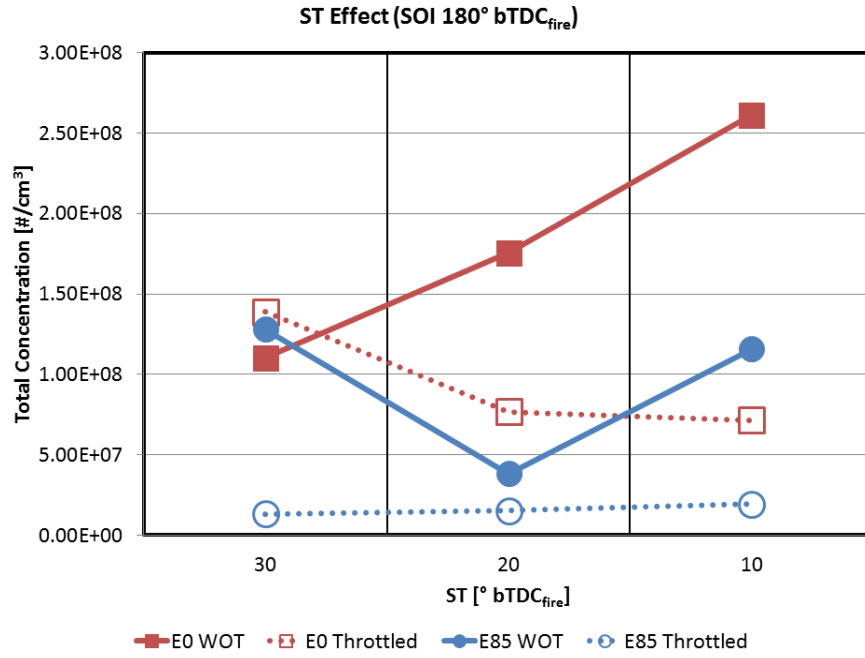
Lean	IMEP	COV _{IMEP}	ST	CA50	CA 50-90
	[bar]	[%]	[° bTDC _{fire}]	[° aTDC _{fire}]	[°]
E0	11.11	2.76	30	0	56
	11.16	1.45	20	10	39
	10.96	3.54	10	21	13
E85	10.38	2.63	30	4	48
	10.62	1.32	20	12	28
	9.08	5.96	10	29	17

Lean	ST	CO	HC	NO
	[° bTDC _{fire}]	[%]	[ppm]	[ppm]
E0	30	0.03	1081	2157
	20	0.02	1097	1782
	10	0.03	1080	955
E85	30	0.05	653	1050
	20	0.04	591	393
	10	0.03	707	20

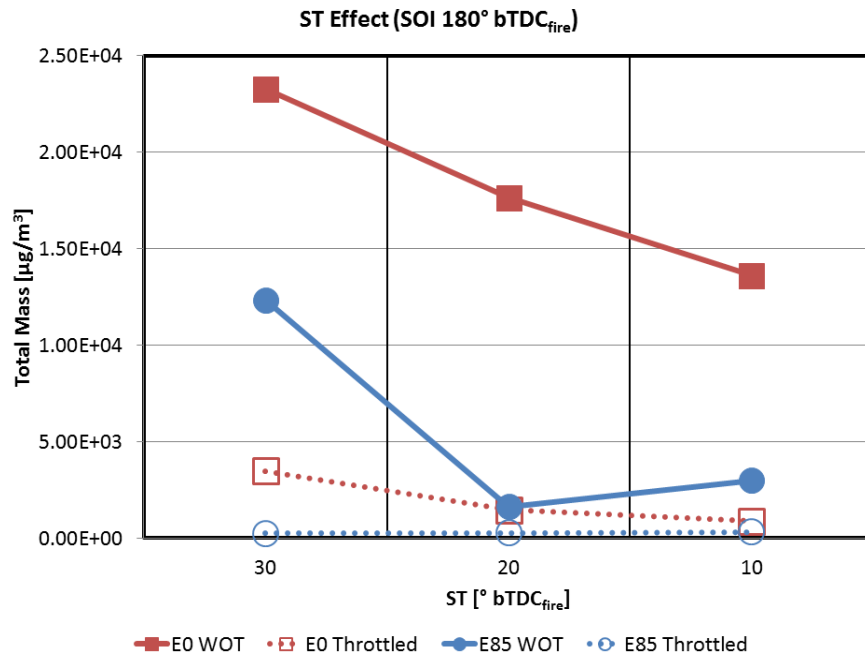
Table 4.10.2 Throttled conditions and emissions (SOI at 180° bTDC_{fire})

Lean	IMEP	COV _{IMEP}	ST	CA50	CA 50-90
	[bar]	[%]	[° bTDC _{fire}]	[° aTDC _{fire}]	[°]
E0	4.68	3.79	30	12	21
	3.96	11.15	20	26	19
	2.71	24.47	10	48	27
E85	4.55	3.48	30	8	24
	4.55	2.51	20	15	15
	3.99	8.92	10	30	15

Lean	ST	CO	HC	NO
	[° bTDC _{fire}]	[%]	[ppm]	[ppm]
E0	30	0.03	1181	1106
	20	0.04	1174	647
	10	0.04	1082	263
E85	30	0.05	613	543
	20	0.05	726	125
	10	0.04	717	18

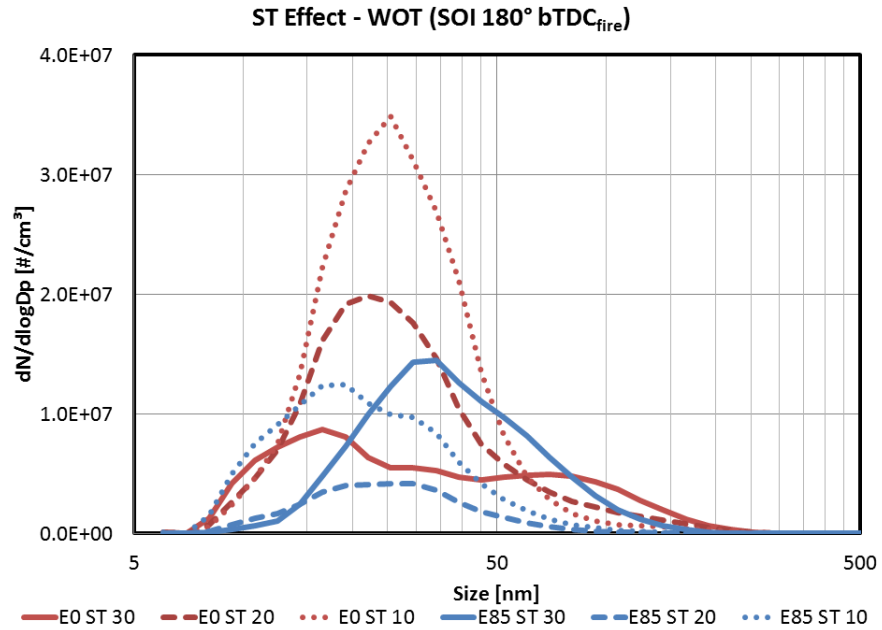


(a)

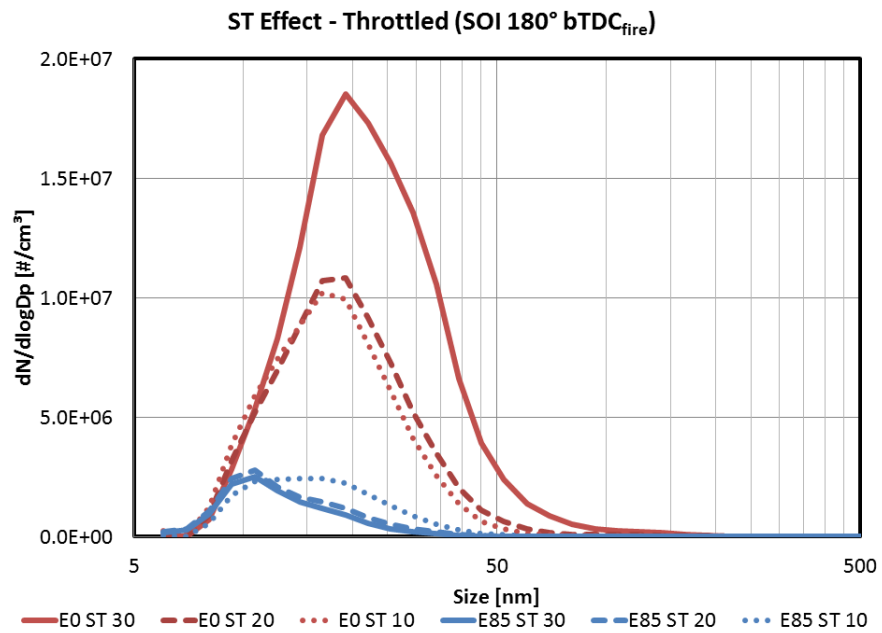


(b)

Figure 4.10.1 (a) Total concentration and (b) total mass of PM emission at different ST [° bTDC_{fire}]



(a)



(b)

Figure 4.10.2 Particle size distribution: (a) WOT and (b) Throttled conditions at different ST [° bTDC_{fire}]

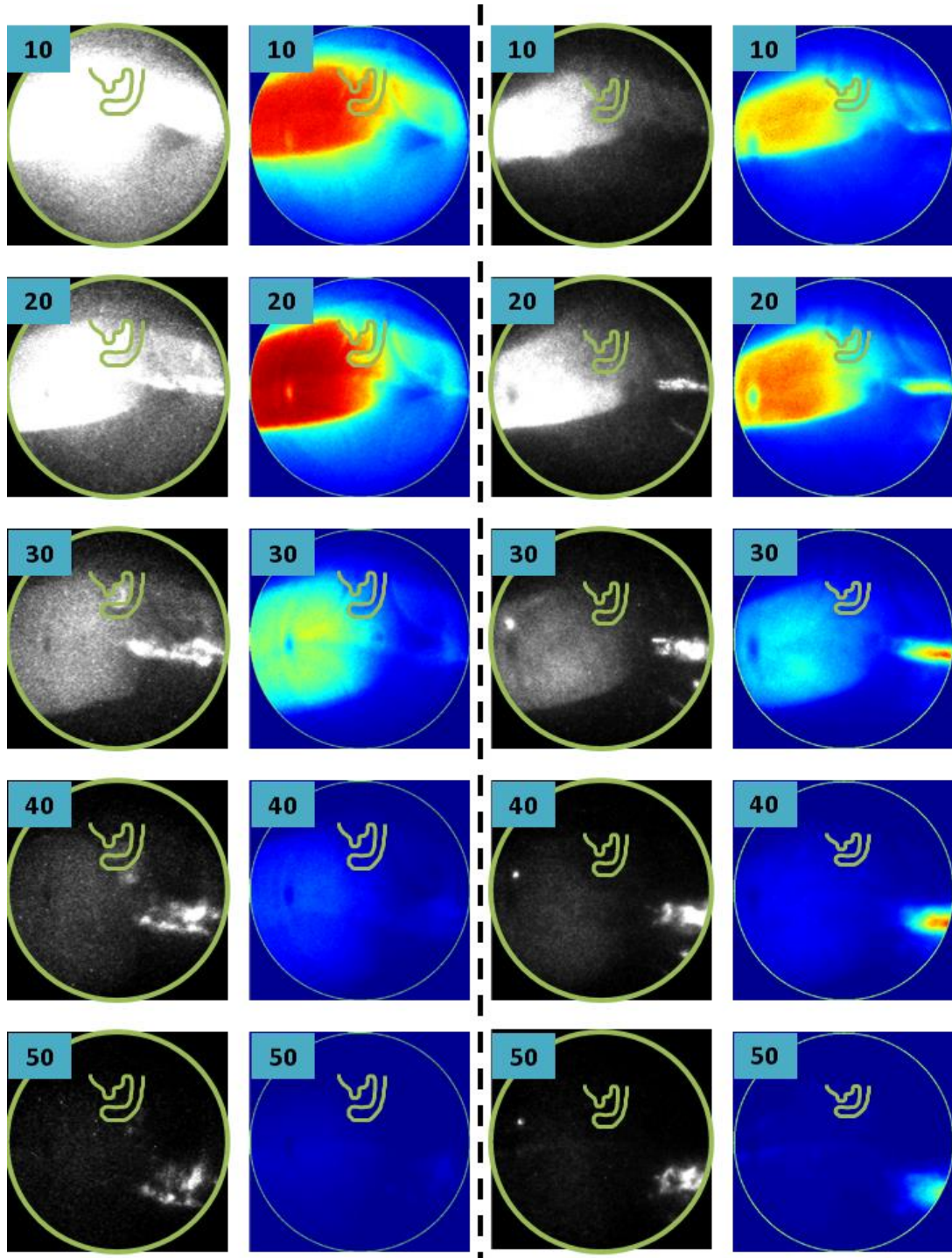


Figure 4.10.3 (a) Raw and Method E images of E0 (left) and E85 (right) (numbers in the corner represent $^{\circ}$ aTDC_{fire}; test condition: WOT; Lean; SOI 180 $^{\circ}$ bTDC_{fire}; ST 30 $^{\circ}$ bTDC_{fire})

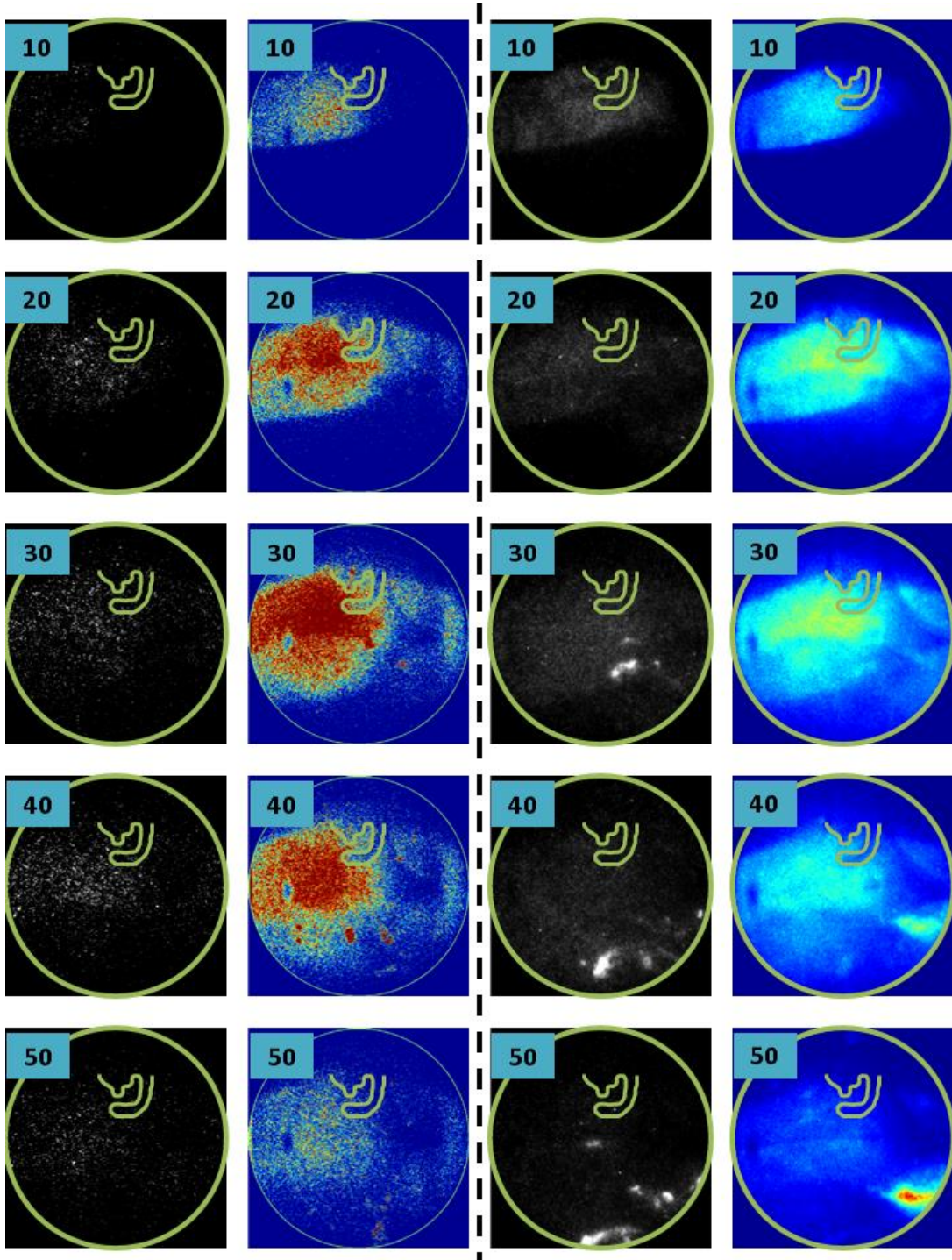


Figure 4.10.3 (b) Raw and Method E images of E0 (left; enhanced due to low intensity) and E85 (right) (numbers in the corner represent $^{\circ}$ aTDC_{fire}; test condition:

WOT; Lean; SOI 180° bTDC_{fire}; ST 10° bTDC_{fire})

4.11 Air-Fuel Ratio Effect on PM Emission

The effect of air-fuel ratio on engine-out emission (CO, CO₂, HC, and NO_x) has been studied thoroughly in the past decades; nevertheless, its influence on PM emission is still in discussion, especially with the presence of ethanol in GDI applications. In this session, a test condition (WOT; SOI 300° bTDC_{fire}; ST 10° bTDC_{fire}) is selected to compare PM emission in Rich ($\lambda \sim 0.9$), Stoich ($\lambda \sim 1.0$), and Lean ($\lambda \sim 1.15$) conditions. The engine operation conditions and emission data are shown in Table 4.11.1 and Table 4.11.2.

The trends of CO, HC, and NO_x emissions are in the agreement with [31, 44, 49]. CO emission increases as the air-fuel ratio gets richer; HC emission also shows the same trend. NO_x emission shows high in Stoich condition and low in Rich or Lean conditions. It should be noticed that NO_x decreases in rich air-fuel ratio because there is not enough O₂ and $C_2 + O_2 \rightarrow 2CO$ reacts much faster than $N_2 + O_2 \rightarrow 2NO$. Typically, highest NO_x emission from an engine could be measured while the air-fuel ratio is slightly lean.

The total concentration and mass of PM emission are shown in Fig. 4.11.1. It clearly shows that total concentration and mass of both E0 and E85 reduce with the increase of Lambda. This agrees with the findings in [69, 72]. The total mass of PM for E85 is much less than that of E0 regardless of air-fuel ratio, which could be the benefit of using E85 as fuel.

To further investigate the influence of air-fuel ratios on PM emission, the size distribution of the particles is shown in Fig. 4.11.2 for both fuels. From Rich to Stoich condition, both fuels do not show much reduction in particle numbers, but a slight shift of particle sizes, especially E0, is seen in the figure. This is due to enough oxygen available for more complete combustion. It is therefore proven that more fuel (unburnt hydrocarbons) is oxidized to smaller particles, if not CO or CO₂, at stoichiometry. From Stoich to Lean condition, it is found that both of the fuels have no size shift but significant reduction in numbers. This is due to less fuel injected with excessive oxygen present in the combustion chamber.

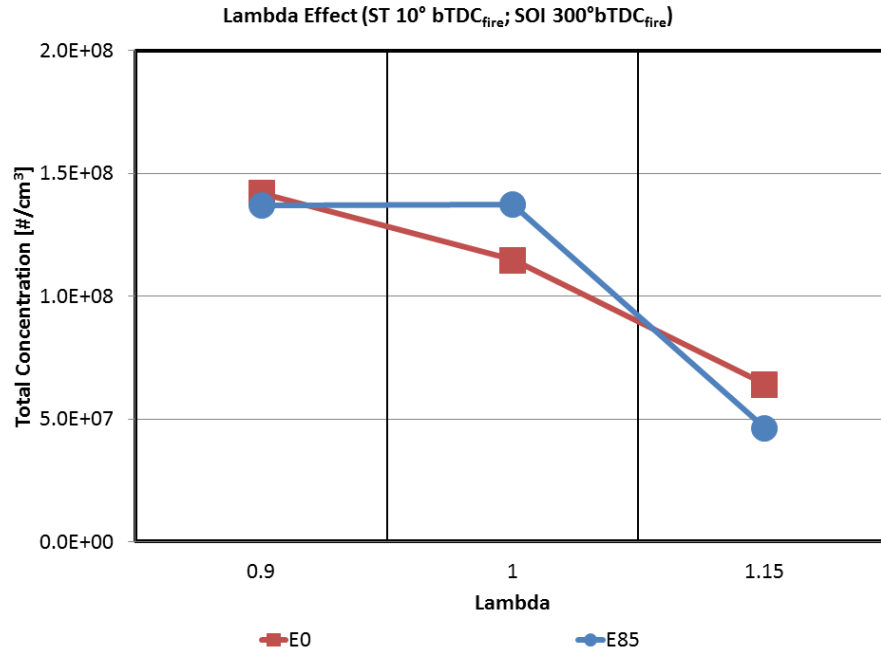
Image results in Fig. 4.11.3 represent Rich and Lean conditions, respectively. They show that E0 has more diffusion flame than E85 in both conditions, especially in Rich condition as shown in Fig. 4.11.3(a). This indicates that more accumulation mode particles are formed during the combustion as discussed previously. E85 images also show diffusion flame in both Rich and Lean conditions, but no accumulation mode is observed from the PM emission results. This also proves the previous conclusion that the short-chain compounds in E85 do not form many particles in accumulation mode.

Table 4.11.1 WOT conditions (SOI at 300° bTDC_{fire}; ST at 10° bTDC_{fire})

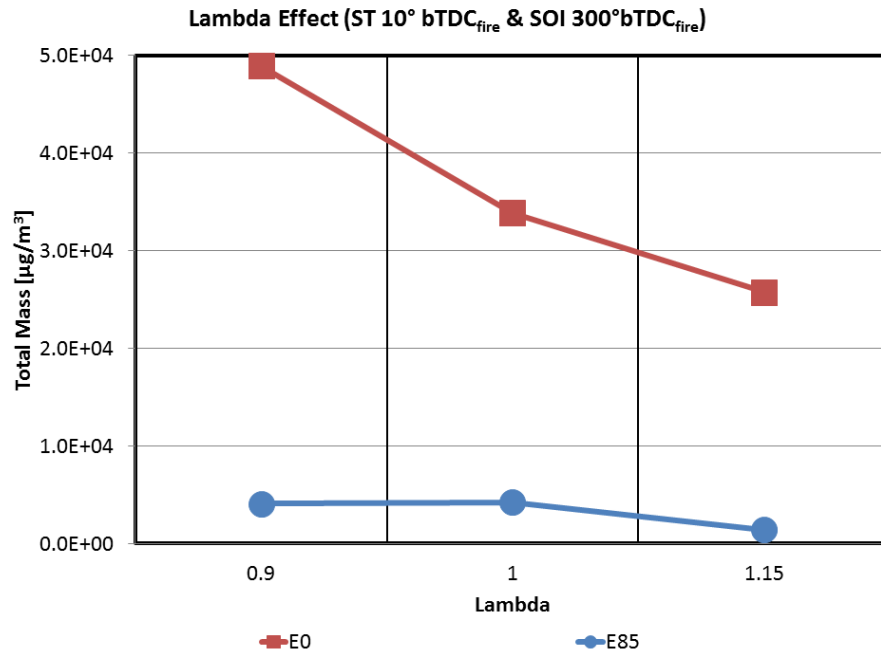
	IMEP	COV _{IMEP}	λ	CA50	CA 50-90
	[bar]	[%]	[$\pm 2\%$]	[° aTDC _{fire}]	[°]
E0	13.41	1.35	0.90	11	31
	12.46	1.54	1.00	15	25
	10.52	3.58	1.15	23	18
E85	13.35	1.01	0.90	11	28
	13.01	1.10	1.00	13	25
	10.99	3.33	1.15	21	17

Table 4.11.2 WOT emissions (SOI at 300° bTDC_{fire}; ST at 10° bTDC_{fire})

	λ	CO	HC	NO
	[$\pm 2\%$]	[%]	[ppm]	[ppm]
E0	0.90	1.41	1693	345
	1.00	0.40	947	1496
	1.15	0.03	760	937
E85	0.90	1.38	640	206
	1.00	0.22	520	912
	1.15	0.04	435	560

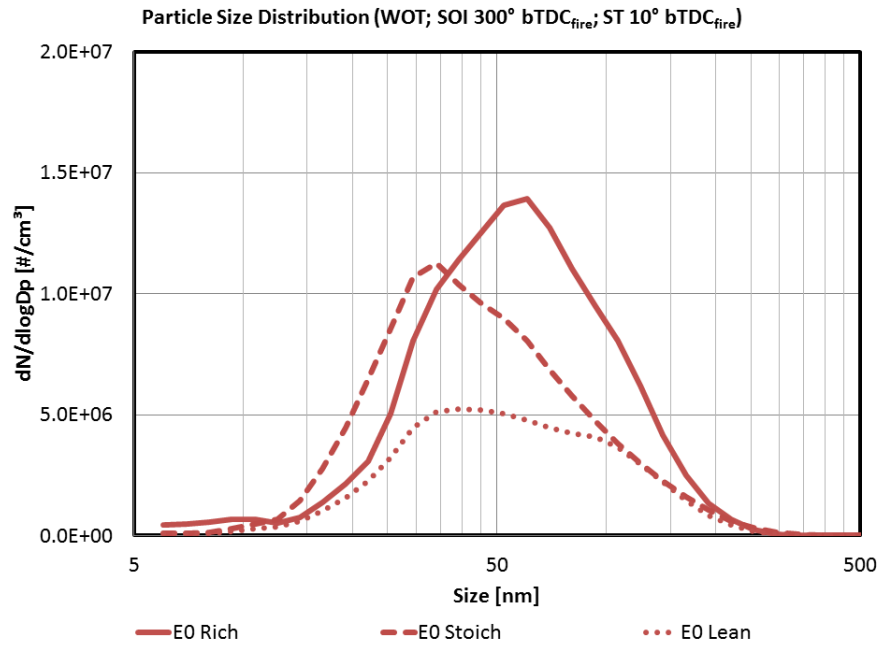


(a)

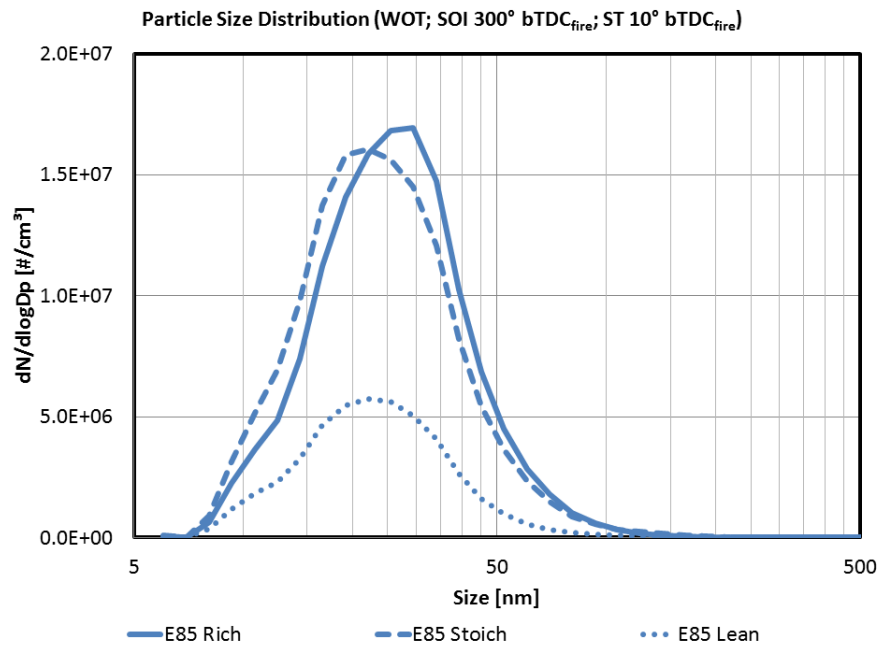


(b)

Figure 4.11.1 (a) Total concentration and (b) total mass of PM emission at different lambda



(a)



(b)

Figure 4.11.2 Particle size distribution of (a) E0 and (b) E85 at different lambda

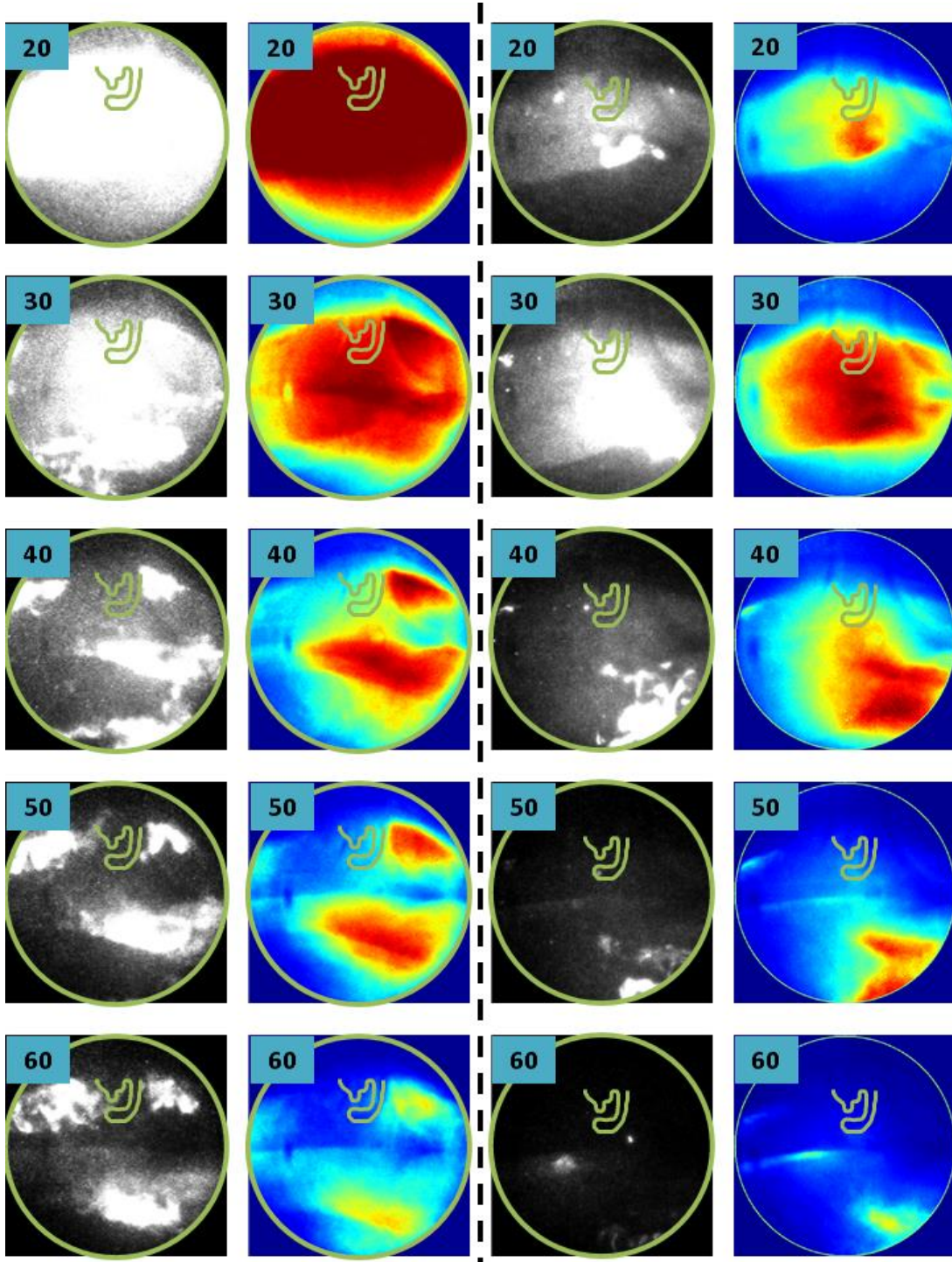


Figure 4.11.3 (a) Raw and Method E images of E0 (left) and E85 (right) (numbers in the corner represent $^{\circ}$ aTDC_{fire}; test condition: WOT; Rich; SOI 300 $^{\circ}$ bTDC_{fire}; 10 $^{\circ}$

bTDC_{fire})

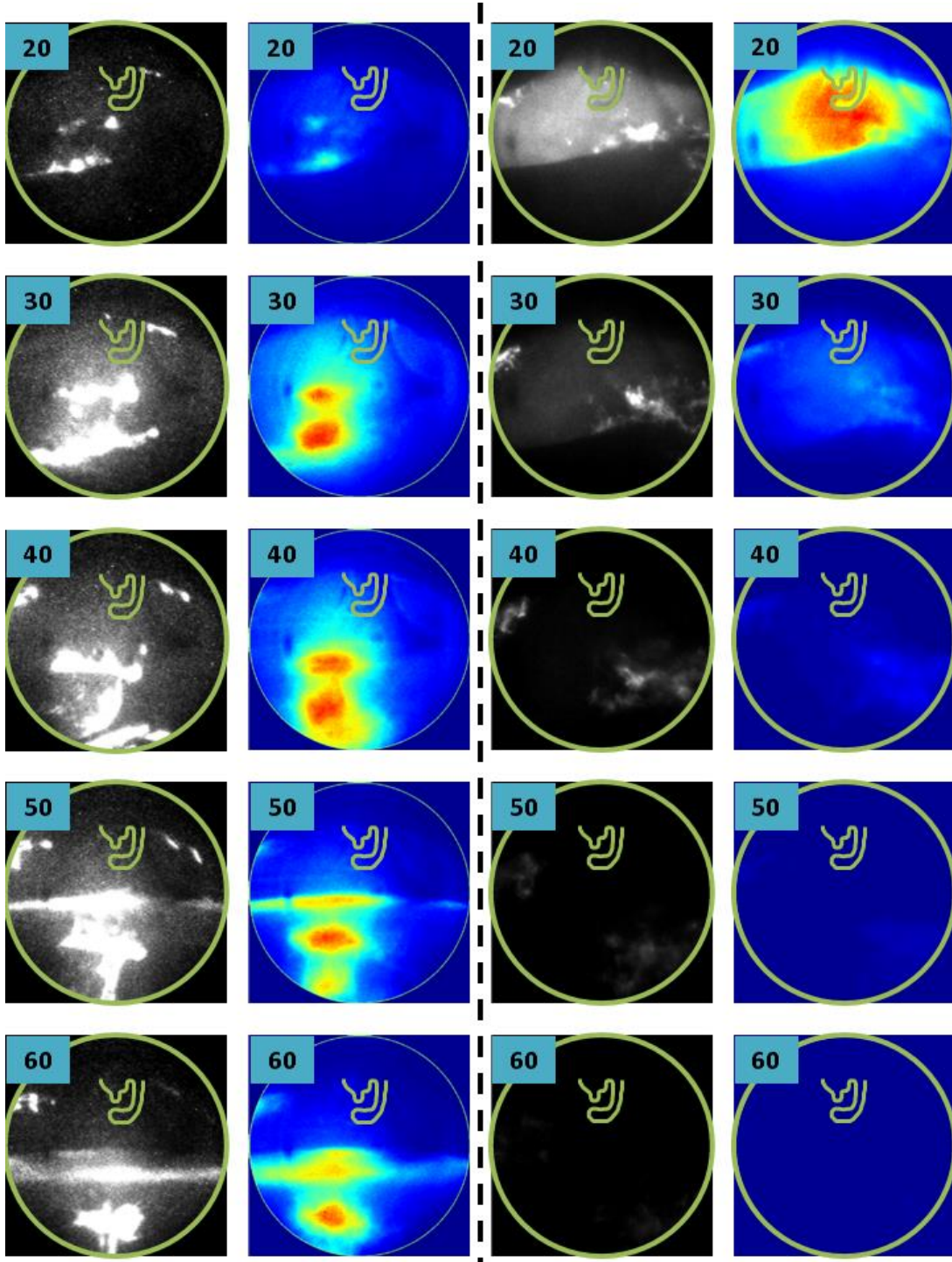


Figure 4.11.3 (b) Raw and Method E images of E0 (left) and E85 (right) (numbers in the corner represent $^{\circ}$ aTDC_{fire}; test condition: WOT; Lean; SOI 300 $^{\circ}$ bTDC_{fire}; ST 10 $^{\circ}$ bTDC_{fire})

4.12 Spark Energy on Combustion and Emission

Spark energy may influence the initial flame kernel development as well as the combustion process. Different spark energy is applied, and the flame kernel growth is studied via the optical access. The production coil of the current engine has the maximum output of approximately 36mJ (based on bench test). A specially made device is utilized to generate different spark discharge energy. The main variables of the ignition process were initial energy discharge and arc duration.

Test condition:

- 1200 rpm; MAP: 0.5 bar; Lambda: ~1.15; EGR 0%
- Injection timing: 300° bTDC_{fire}
- Injection pressure: 100 bar
- Ignition timing: 20, 15, and 10° aTDC_{fire}
- Camera Frame Rate: 8000 fps

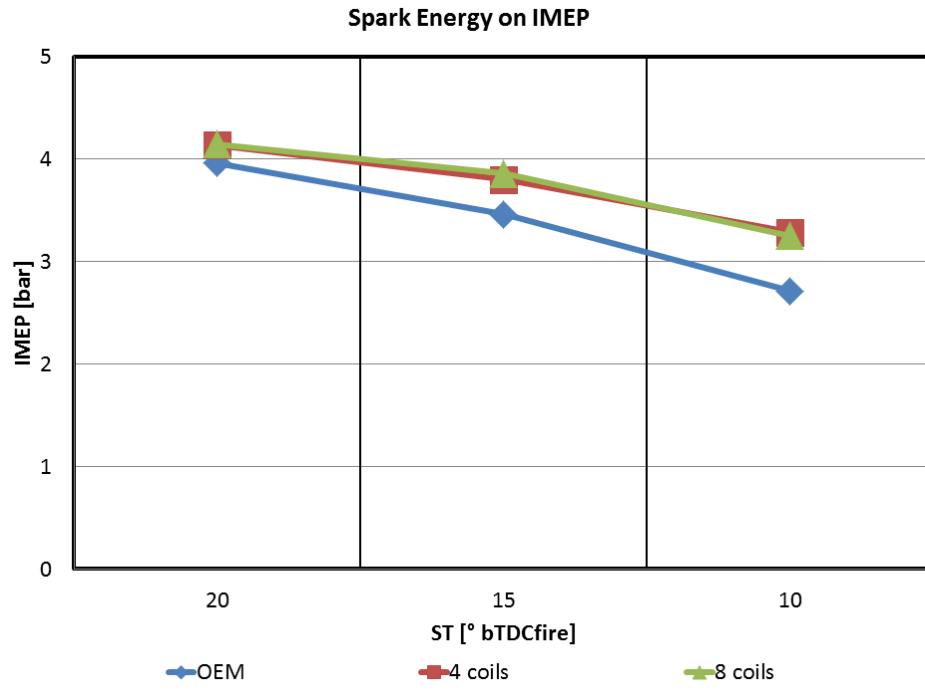
Three ignition coil configurations and their energy are listed below:

- OEM: single coil, 36 mJ
- 4 coils: 4 coils in series, 65 mJ
- 8 coils: 2 sets of 4 coils in parallel (8 coils totally), 240 mJ

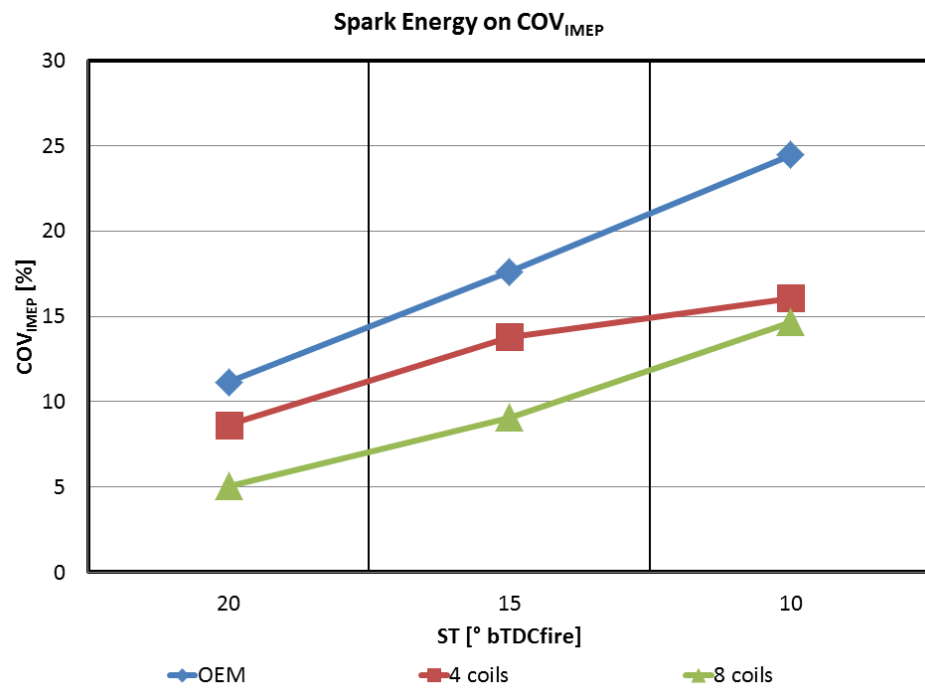
The test results show that increasing the energy could improve the combustion in a pro-misfire operating condition. Figure 4.12.1(a) and Fig. 4.12.1(b) show the results of IMEP and COV_{IMEP} where the improvement of the latter is significant (lower values). It should be noticed that even though 4 coils (4 series) and 8 coils (4 parallel) do not show much difference in IMEP, there is an improvement in COV_{IMEP} with the latter.

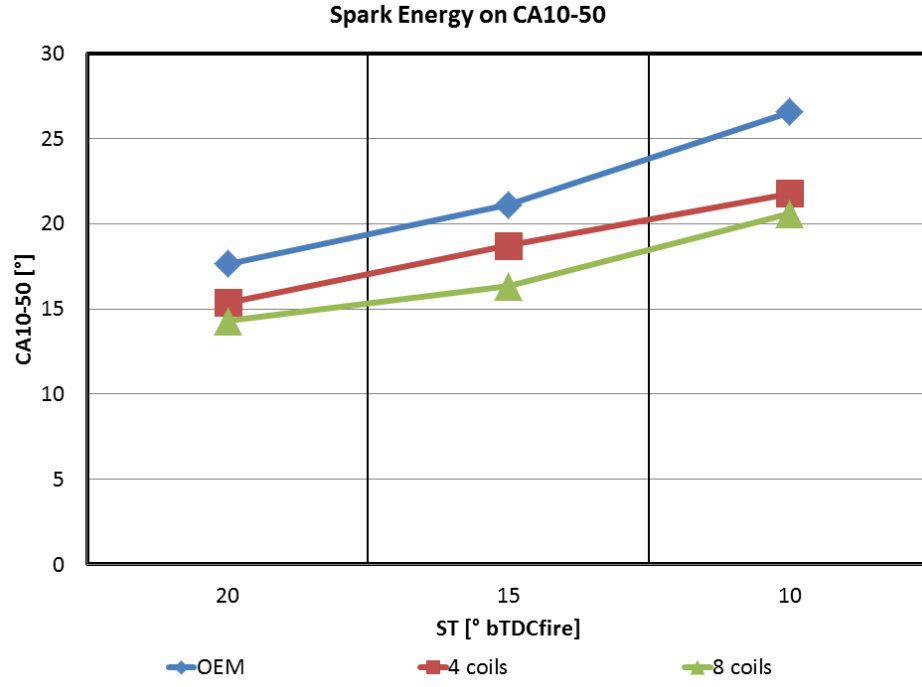
From Fig. 4.12.1(c) and Fig. 4.12.1(d), CA10-50 and CA50-90 also indicate that higher spark energy would enhance the flame propagation. However, the HC emission in Fig. 4.12.1(e) does not show much reduction. It is believed that the cool cylinder wall may increase the quench zone that the combustion could not sustain further when flame propagates close to the wall. Nevertheless, the HC emission at ST 10° bTDC_{fire} in Fig. 4.12.1(e) still shows somewhat significant reduction (16.67%), which is the result of more complete combustion due to higher spark energy.

Figure 4.12.2 shows the image results of early flame kernel development and the radii of different coil combinations with spark timing at 10° bTDC_{fire}. It is clearly seen that the flame kernel size is larger with more coils. Therefore, higher spark energy produces stronger and faster flame kernel development, which would improve combustion as the results shown in Fig. 4.12.1.



(a)

Figure 4.12.1 Spark energy on (a) IMEP and (b) COV_{IMEP}



(c)

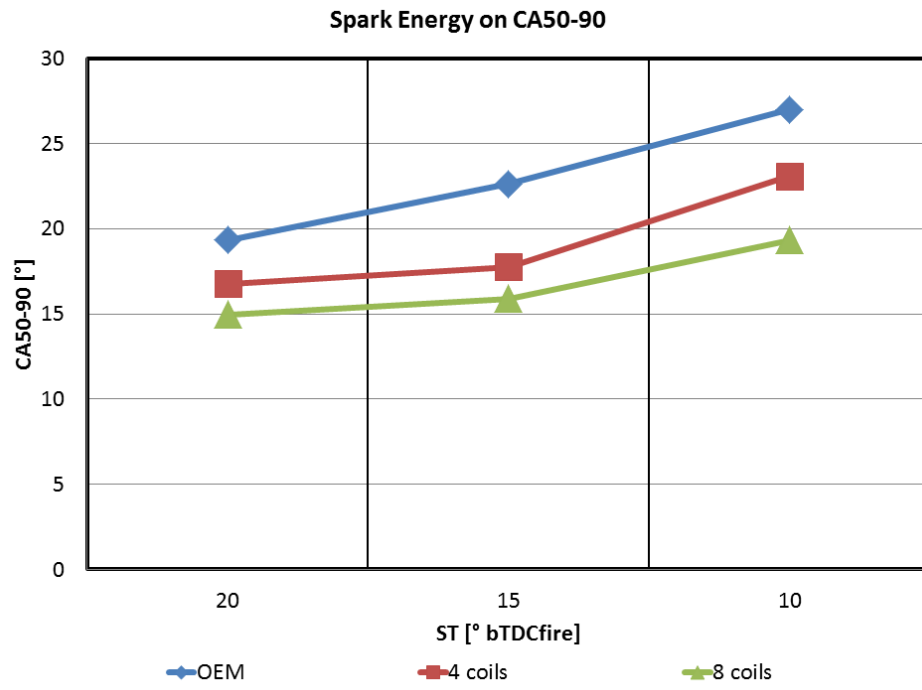


Figure 4.12.1 Spark energy on (c) CA10-50 and (d) CA50-90

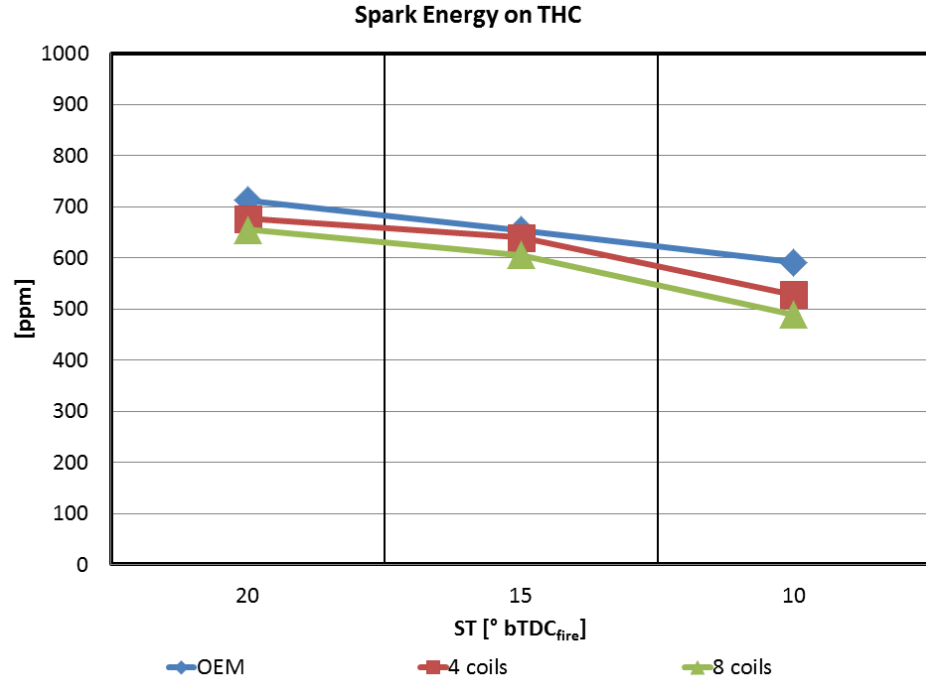


Figure 4.12.1 Spark energy on (e) HC emission

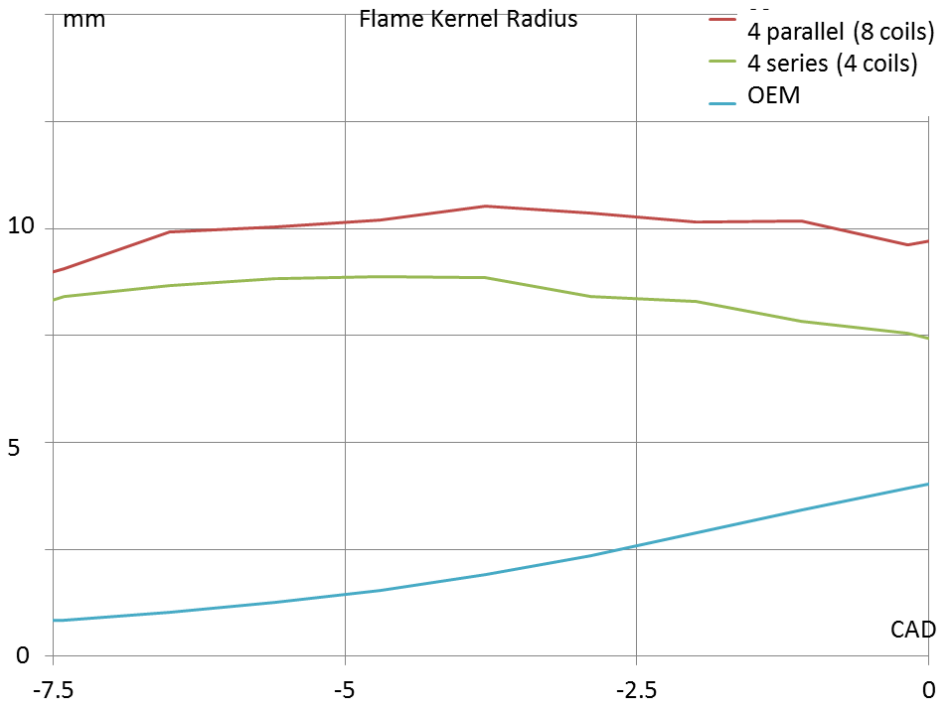


Figure 4.12.2 (a) Spark energy on flame kernel radius

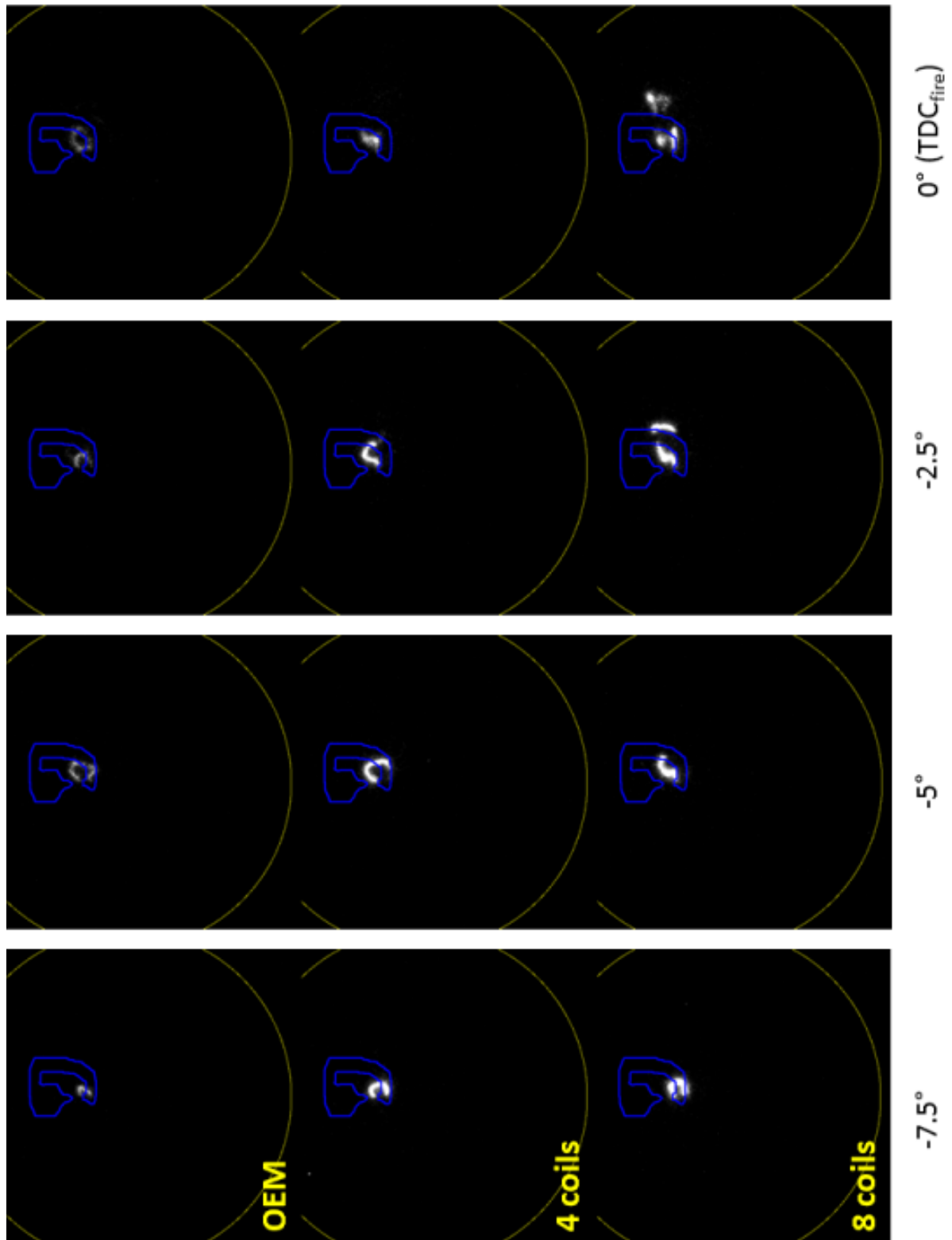


Figure 4.12.2 (b) Flame kernel development with different spark energy

CHAPTER 5 CONCLUSION

5.1 Summary of the Work

The combustion and emissions of using pure gasoline (E0) and E85 have been investigated via optically accessible engines with high speed cameras, data acquisition devices, and emission measurement benches. A single-cylinder optically accessible engine and a modified production engine provide sufficient “insights” for the investigator to study the combustion process and the resulting emission by various image processing methods under different engine operating conditions at low engine speed (600 and 1200 rpm). The study also provides many simpler and less expensive means for researchers to utilize optically accessible engines on fundamental engine research without encountering budget-hindering-and-labor-intensive laser techniques. CFD simulation is also used to demonstrate the validity of the test results. The summary of the current work is listed as below.

- The combustion of E85 is more stable in Lean conditions (lower COV_{IMEP} seen) with an exception of WOT, SOI 180° bTDC_{fire}, and ST 10° bTDC_{fire}. Since there is more fuel mass injected into the combustion chamber, more fuel could be available locally for the propagating flame to sustain the combustion. The only exception may be the contribution of over-mixing. The results are shown in Appendix A, which is measured from the mOAE because of more realistic engine operating conditions. Moreover, the fuel effect on mass burnt fraction is not significant regardless of test conditions.
- For engine starting at warm air (40°C) and coolant (80°C) temperature without fuel enrichment, the image results indicate that the first cycle of combustion has

relatively lower luminosity. The flame propagation also shows that the flame speed of first cycle is the slowest comparing with ensuing cycles. To improve the engine startability, richer air-fuel mixture or using other fuels may be needed; the former is typically more practical and has been adopted in the industry.

- Comparing the start-up process of E0 and E85, it is found that E0 does not fire up in the first cycle and ensuing cycles also have relatively lower combustion luminosity. On the other hand, E85 shows weak but visible combustion in the first cycle, and ensuing cycles display sustainable combustion as high luminosity seen.
- The spectrometer results show that the combustion has primarily OH^* , CH_2O^* , and CH^* in the early stage; high CO-O^* in the later stage. The color camera is able to present CH^* and partial CH_2O^* as the blue flame seen from the images. The yellow or red flame shows the chemiluminescence light from CO-O^* and some blackbody radiation from soot particles. The averaged RGB results also show that the blue flame could overlap with the AHRR curve (location-wise).
- Valve-deactivation of the intake valves may enhance the swirl motion in the combustion chamber. Nonetheless, over-mixing could happen at low engine speed below 1200 rpm as shown in this study. One-valve deactivation has weak first cycle combustion and slower flame propagation from both mOAE and sOAE. The CFD simulation also shows that the spark discharge arc is “pushed” by the air flow towards the locally lean area in one-valve deactivation conditions, whereas no-valve deactivation has more homogeneous air-fuel mixture distribution. Stronger and more stable combustion, faster and more symmetric

flame propagation are found in no-valve deactivation cases, which is in the agreement with the previous study [13] at low speed (less than 2000 rpm) and low load (1~2 bar BMEP)..

- Cycle-to-cycle variation is intrinsic phenomenon in spark-ignited gasoline engines. It could be contributed by the start of spark, flame propagation, and valve movement, and air motion in the combustion chamber. The probability results of flame propagation prove that an engine needs to be carefully calibrated to reduce the magnitude of variation.
- Although N₂ is used as the EGR in the study, darker combustion light and more “spots” are seen in the images. More comprehensive EGR equipment could be used to further investigate its effect on combustion.
- Typically, the ignition timing needs to be advanced with higher engine speed that the combustion process could be “completed” in time. However, over-advanced ignition timing could have negative impact on combustion. It is seen from the images that brighter images do not represent higher IMEP since the chemical work is converted to “fight” against the ascending piston. Besides, knocking could also happen with too early ignition timing.
- E85 requires more fuel to achieve the same power output of E0 due to the lower energy content. The injection quantity comparison is listed in Appendix B.
- Injection timing in GDI engines has very significant effects on combustion. In Appendix B, it is also shown that SOI at 180° bTDC_{fire} needs more fuel to achieve the same air-fuel ratio, which indicates the charge cooling effect. The flame also propagates differently with different SOI. Both experiment and CFD results show

that early SOI (300° bTDC_{fire}) has more symmetric flame propagation; however, pool fire is also seen as fuel impingement is unavoidable with early SOI.

- Late SOI (60° bTDC_{fire}) is typically used for stratified charge combustion. Nevertheless, it is found in the current study that strong heterogeneous combustion is recorded at low engine speed (1200 rpm) and high load (WOT conditions). Furthermore, pre-ignition could occur in certain conditions with relatively late ST (between 10° bTDC_{fire} and aTDC_{fire}). The phenomenon usually happens after a late burn cycle led by a misfire as some oil droplets might have been ignited and caused auto-ignition. Both E0 and E85 show 9 cycles of pre-ignition out of 100 cycles in this study that E85's "prone-to-pre-ignition" is not seen. It should also be addressed that the pre-ignition in this study is not as severe as super-knock found in boosting conditions for GDI engines.
- Injection timing in GDI engines also has very significant effects on emissions, especially PM emission. The current work has found that early SOI (300° bTDC_{fire}) results in pool fire on the piston top in the images, so PM emission of early SOI is higher than that of late SOI (180° bTDC_{fire}). Besides, E85 shows higher particle number than E0 in such conditions with much less mass. Since smaller particles (in nuclei mode) is found while using E85 as fuel, an explanation is that E85 has more short-chain compounds (e.g. ethanol) to produce smaller particles in incomplete combustion conditions, whereas E0 has more long-chain compounds to form larger particles in the same conditions. If incomplete combustion occurs, more E85 fuel will be burnt that more small particles would form; in other words, seeing pool fire or diffusion flame does not necessarily

mean higher PM “mass” emission; it may represent higher PM “number” emission.

- Ignition timing in GDI engines also affects soot formation in the combustion chamber. It is found that adjusting ignition timing to approach the MBT point is critical to reduce PM emission. Otherwise, incomplete combustion could increase the soot formation in both E0 and E85 cases.
- Air-fuel ratio influences engine-out PM emission as well. In rich conditions, a lot of diffusion flame or pool fire is seen in the images; in lean conditions, little diffusion flame or pool fire could be found.
- Varying spark energy could improve the combustion stability as suggested in COV_{IMEP} results. Faster burn rate and larger early flame kernel could also be found. However, it may not show much improvement in terms of emissions as HC emission indicates.
- CO, CO₂, and NO_x emissions in the current work are in the agreement with other literature. CO is found highest in rich conditions or non-ideal ignition timing. CO₂ is found highest in stoichiometric conditions, and NO_x is found highest in slightly lean conditions. In terms of fuel difference, E85 combustion shows lower CO, HC, and NO_x emissions in general. Injection timing does not show significant influence on such emissions. The data is shown in Appendix C.
- Formaldehyde (CH₂O) and Acetaldehyde (CH₃CHO) are found higher from E85 combustion than from E0 combustion. This is also in the agreement with other literature and should be considered while utilizing E85 as the alternative fuel. The data is shown in Appendix C.

5.2 Recommendation and Future Work

For equipment:

- Professional manufacturing is essential. It is found that a well-built optically accessible engine, either based on a single-cylinder engine or a production one, is very critical for such research. The sOAE was built in-house and did require excessive modification or extra work for maintenance, and it could only sustain about 10 consecutive cycles of test (not able to do skip fire). The typical down time for optics clean-up is 3 business days minimally. On the other hand, the mOAE was a production engine modified by an outside company, which could run as a regular engine and is easier to clean up.
- Precise and flexible engine control and data acquisition devices are highly recommended. A field-programmable gate array (FPGA) capable device suits better for optically accessible engines, especially for skip fire mode to avoid thermal stress on the optics. Well-grounded and high speed data acquisition device is also needed because the interference of the spark and coil could affect the measurement negatively.
- High speed emission measurement, such as fast FID, would also help the data correlation and analysis on engine-out emissions.
- Color camera is not recommended unless it is used for display purposes or two-color method. High noise, especially for the blue color, could cause difficulties on image post-processing. Many vendors would rather provide monochromatic cameras with wavelength filters. In addition, its sensitivity is also not as good.

- More camera memory should be needed to record more combustion cycles. The number of cycles recorded in the current work is 50 in maximum.
- CO₂ should be used as the EGR if the engine out exhaust is not drawn to the intake pipe. Besides using compressed CO₂ cylinders, drawing the exhaust gas from a portable bath water heater could be utilized. The EGR is more realistic by the latter method.
- High intensity light source, such as LED or laser, is also recommended. The intensifier used in the current work could only enhance to a certain level before the noise level is too high for the image analysis.
- A central mounted injector GDI engine could be studied as well with different injectors (i.e. different spray patterns).

For experiment:

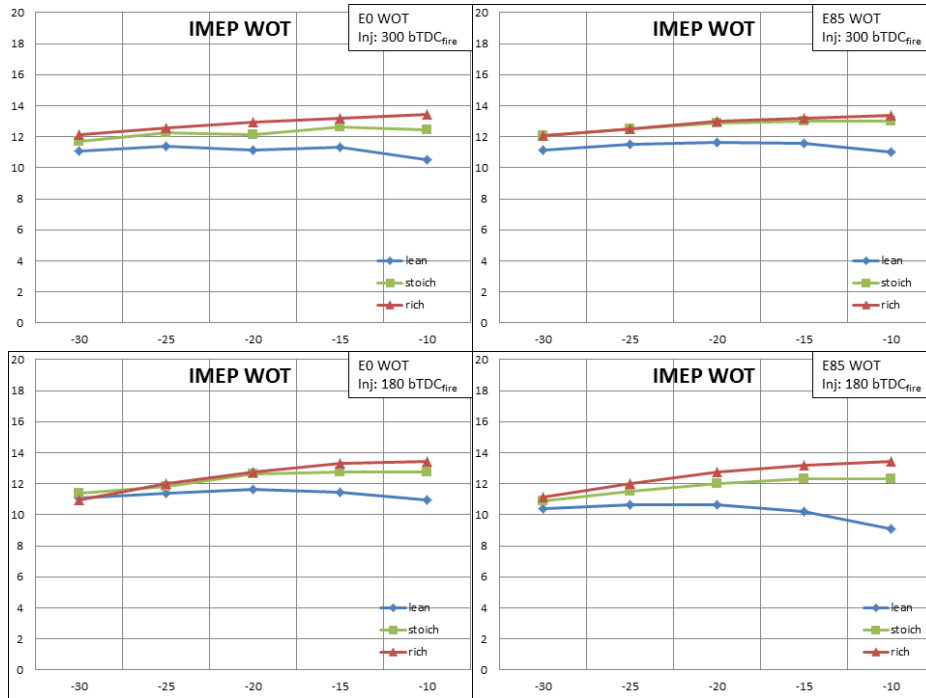
- Higher engine speed and load should be tested. The current work is limited due to unbalanced flywheel and drive shaft for mOAE, which are the leftovers from previous work, and an aging sOAE. Running higher engine speed and load had strong safety concerns.
- Boosting the intake air could also be considered since most GDI engines in the market are targeted for down size-down speed purposes. However, the aforementioned issue needs to be taken care of in prior.
- Laser techniques may be introduced, such as planar laser-induced fluorescence (PLIF) for OH*. The current study did not include such techniques due to limited budget and inoperable devices.

- Method B in the current work could be investigated further to correlate the AHRR curve with the averaged blue value. The BR and BG ratios could also be studied more in depth.
- Pre-ignition should be deeply investigated to understand the real cause(s) of the phenomenon.
- In-cylinder air-fuel ratio distribution should be studied to validate the CFD results and to identify under- or over-mixing.
- Late injection timing results in injecting fuel into high temperature and pressure surroundings. It is worth study the spray pattern in such conditions. One method is to use a rapid compression machine to create such surroundings, as shown in Appendix D.
- Spark energy could also be investigated further. Appendix E shows the setup of port-fuel-injection CNG system, which will be used in the future.
- Ethanol could also be used with other fuels in other kinds of engines. Appendix F shows the study of ethanol-biodiesel blends in a turbocharged light duty diesel engine.

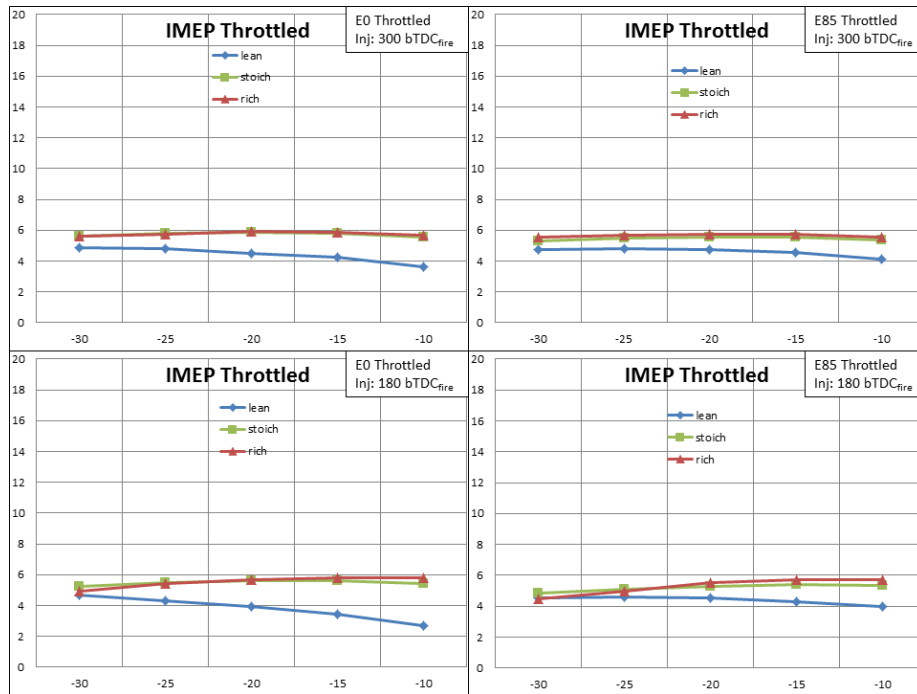
For simulation:

- Converge has been proved to be very efficient and powerful. However, a cluster or faster machine is needed to run finer mesh for more realistic results or to run LES models to capture details as the pressure traces and AHRR curves shown in Appendix G as well as the image comparisons have some discrepancies.

APPENDIX A: COMBUSTION DATA

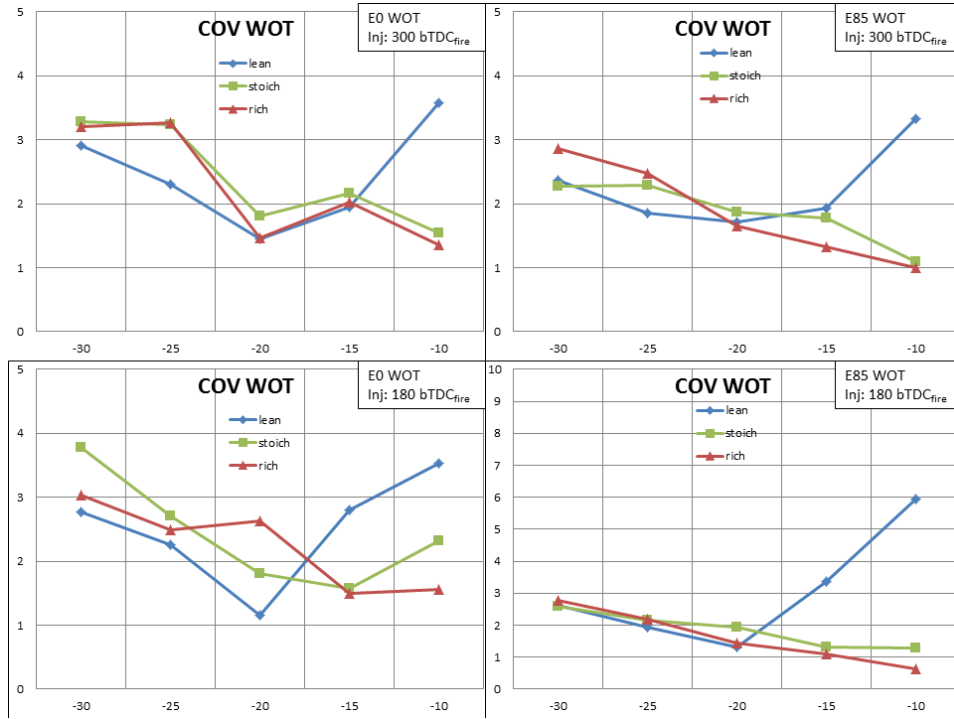


(a)

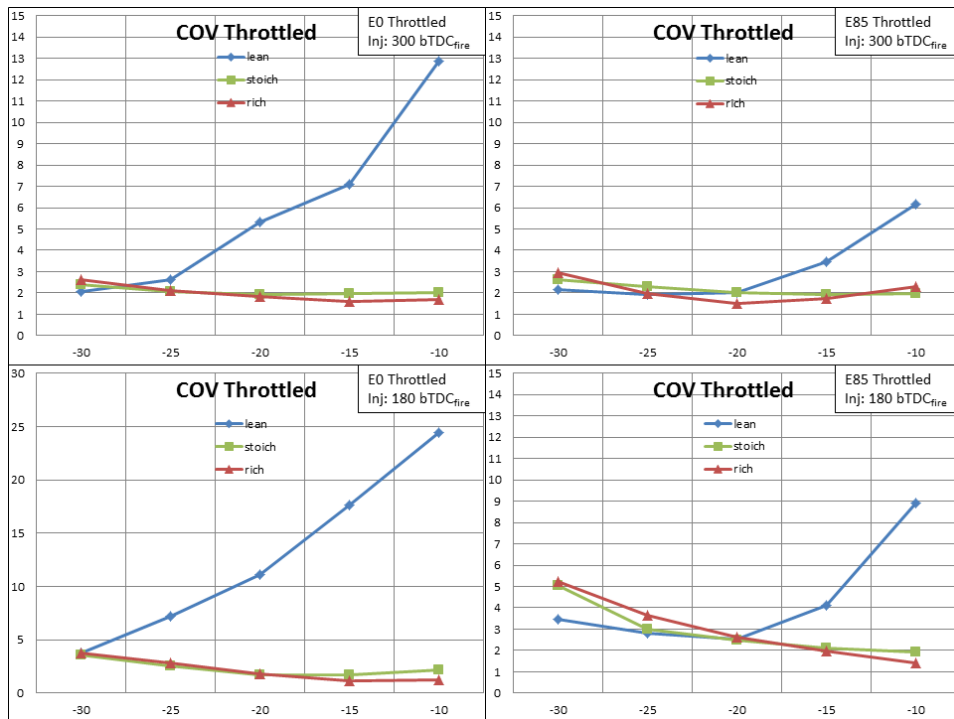


(b)

Figure A-1 IMEP of (a) WOT and (b) Throttled conditions

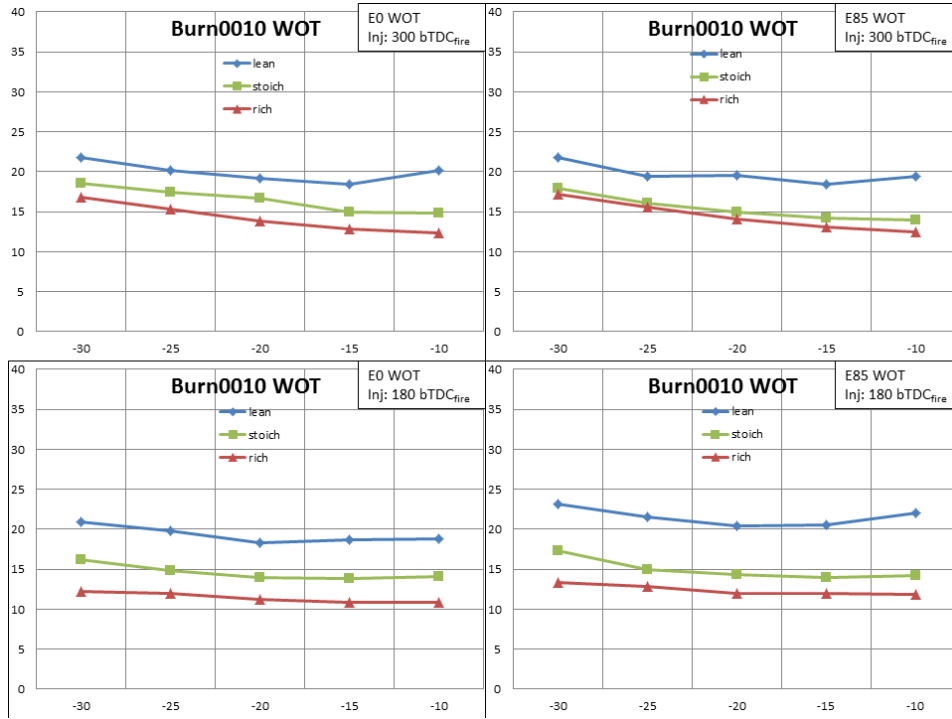


(a)

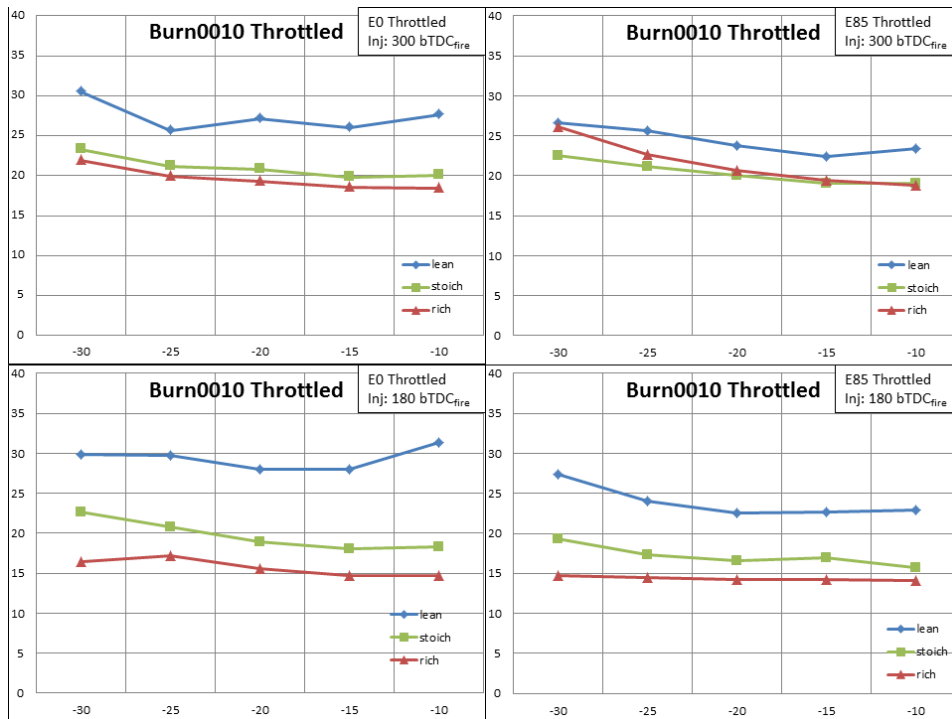


(b)

Figure A-2 COV_{IMEP} of (a) WOT and (b) Throttled conditions

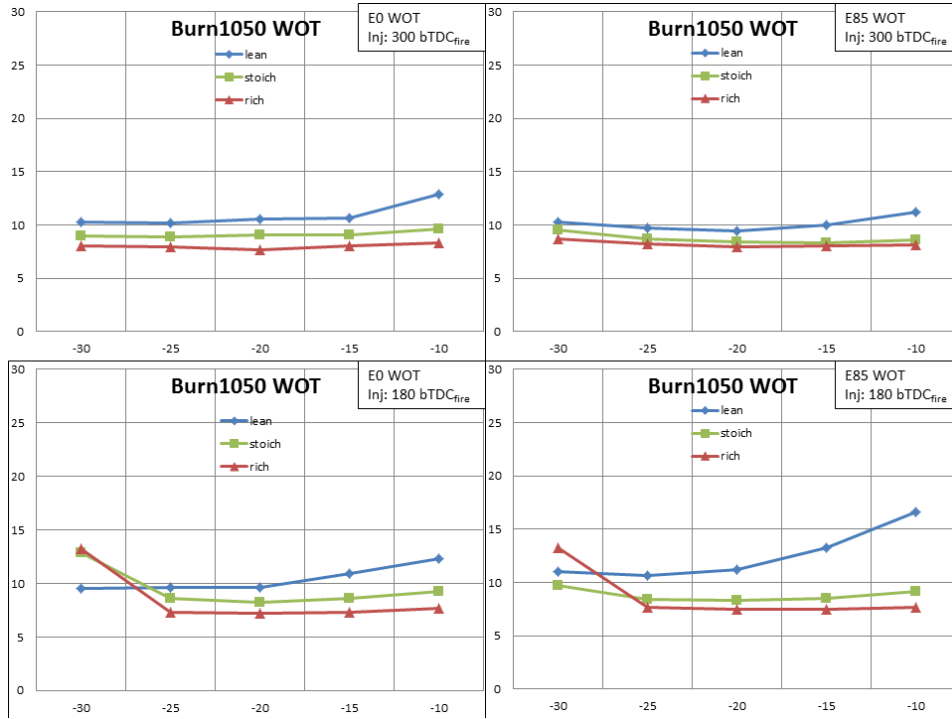


(a)

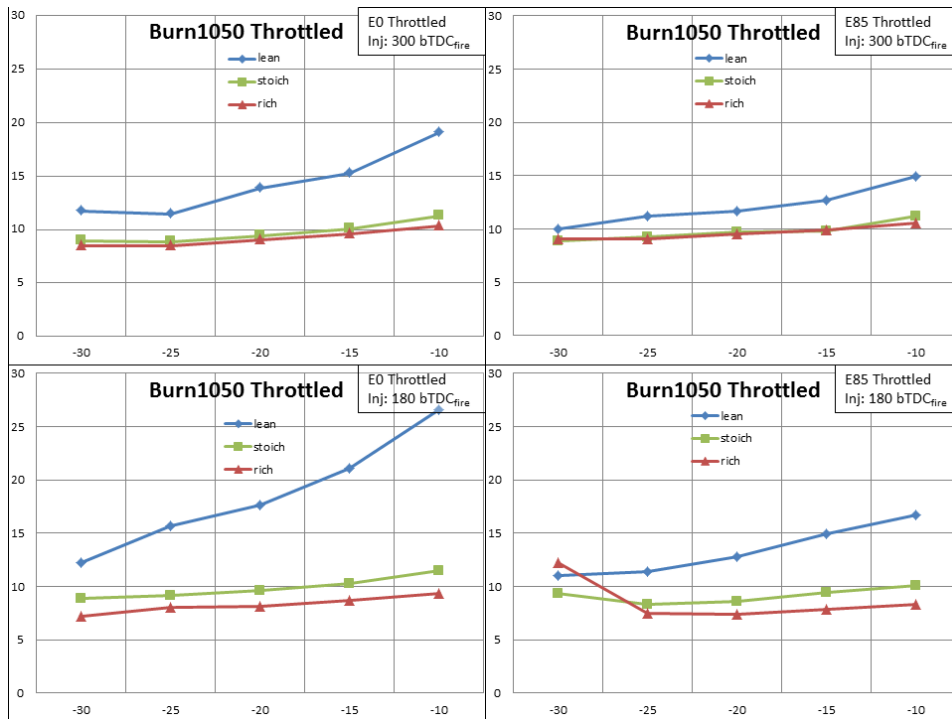


(b)

Figure A-3 CA00-10 of (a) WOT and (b) Throttled conditions

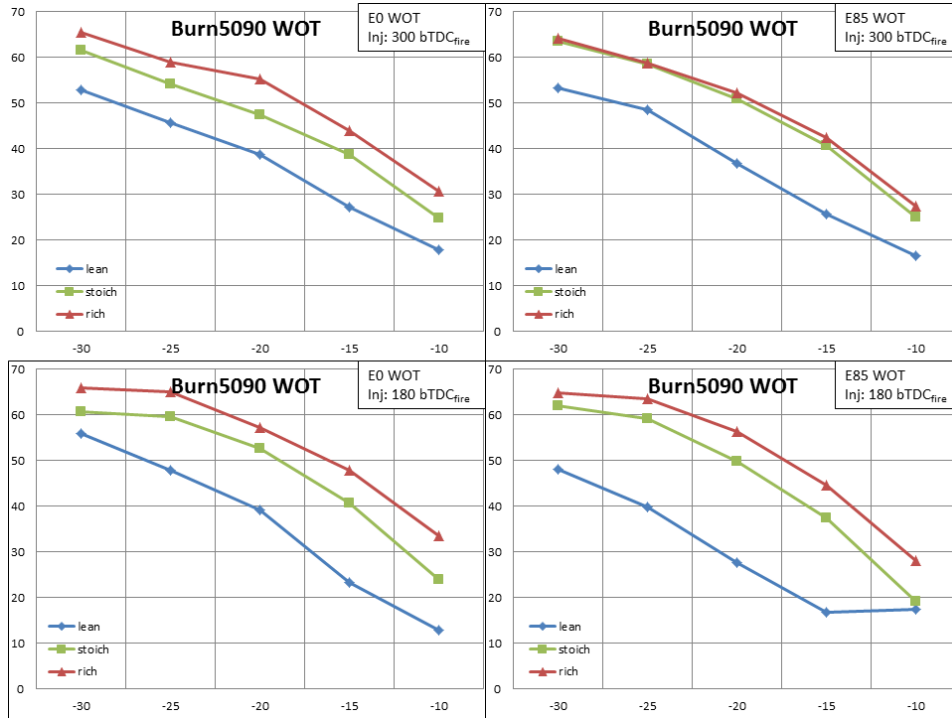


(a)

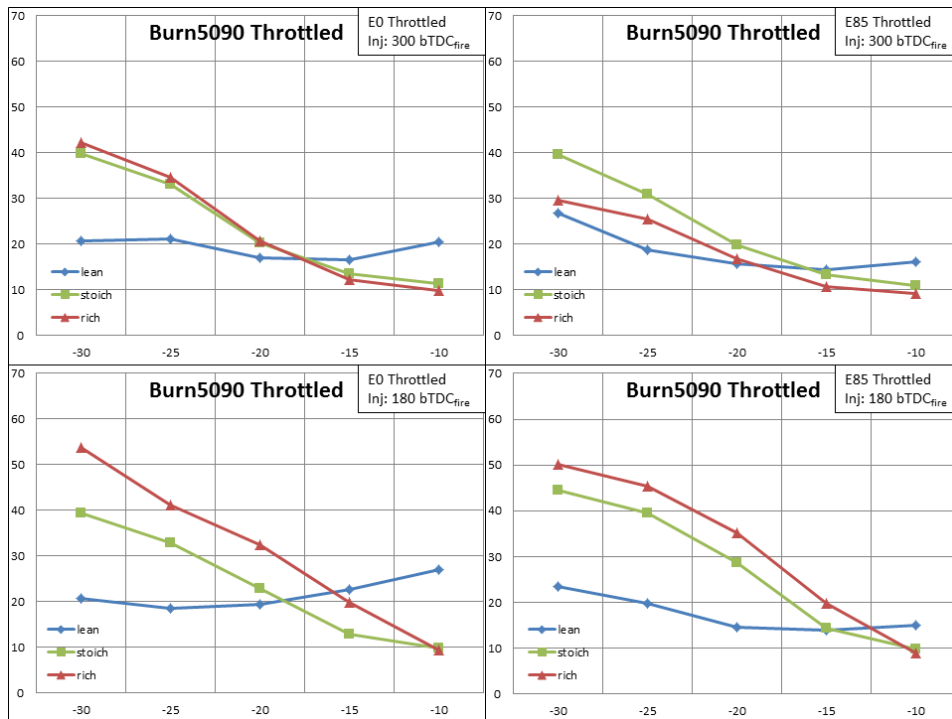


(b)

Figure A-4 CA10-50 of (a) WOT and (b) Throttled conditions



(a)



(b)

Figure A-5 CA50-90 of (a) WOT and (b) Throttled conditions

APPENDIX B: INJECTION QUANTITY DIFFERENCE

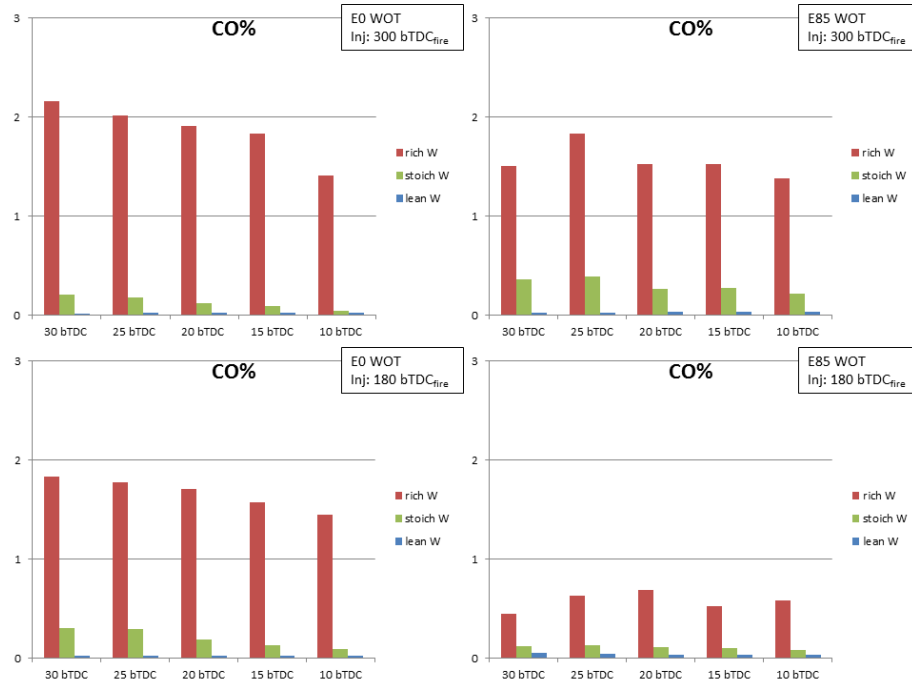
Table B-1 E0 injection quantity

E0	SOI 300° bTDC _{fire}	SOI 180° bTDC _{fire}
WOT	Injection [mg/cycle]	Injection [mg/cycle]
$\lambda \sim 0.90$	39.37	43.60
$\lambda \sim 1.00$	31.59	35.48
$\lambda \sim 1.15$	27.62	31.59
Throttled		
$\lambda \sim 0.90$	20.33	22.81
$\lambda \sim 1.00$	16.51	17.84
$\lambda \sim 1.15$	13.88	15.35

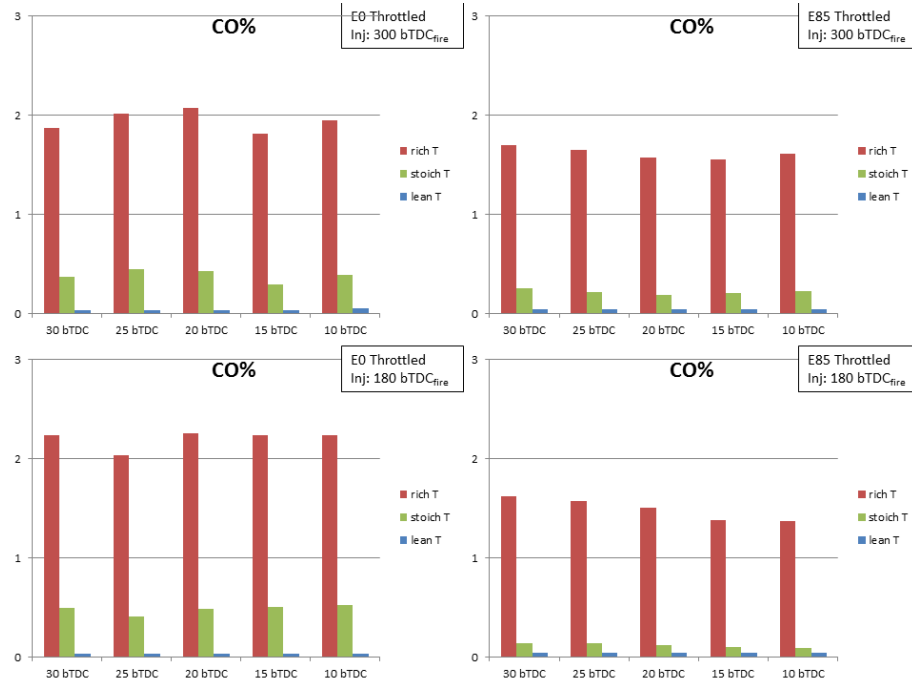
Table B-2 E85 injection quantity

E85	SOI 300° bTDC _{fire}	SOI 180° bTDC _{fire}
WOT	Injection [mg/cycle]	Injection [mg/cycle]
$\lambda \sim 0.90$	58.12	59.71
$\lambda \sim 1.00$	47.82	50.99
$\lambda \sim 1.15$	39.37	41.91
Throttled		
$\lambda \sim 0.90$	27.62	29.21
$\lambda \sim 1.00$	22.81	23.64
$\lambda \sim 1.15$	18.67	19.50

APPENDIX C: EMISSION DATA

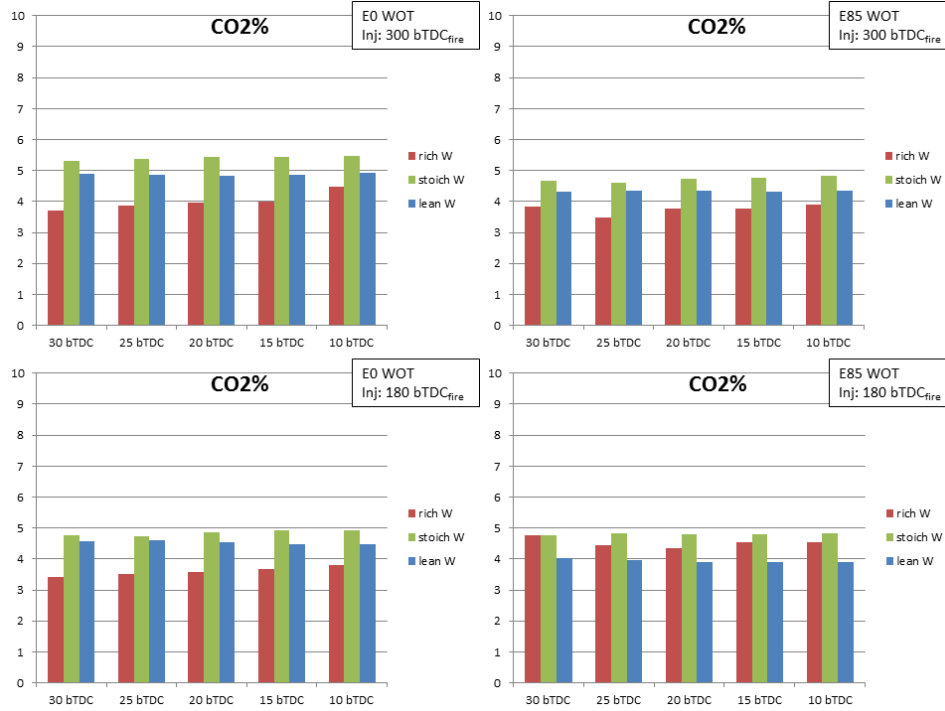


(a)

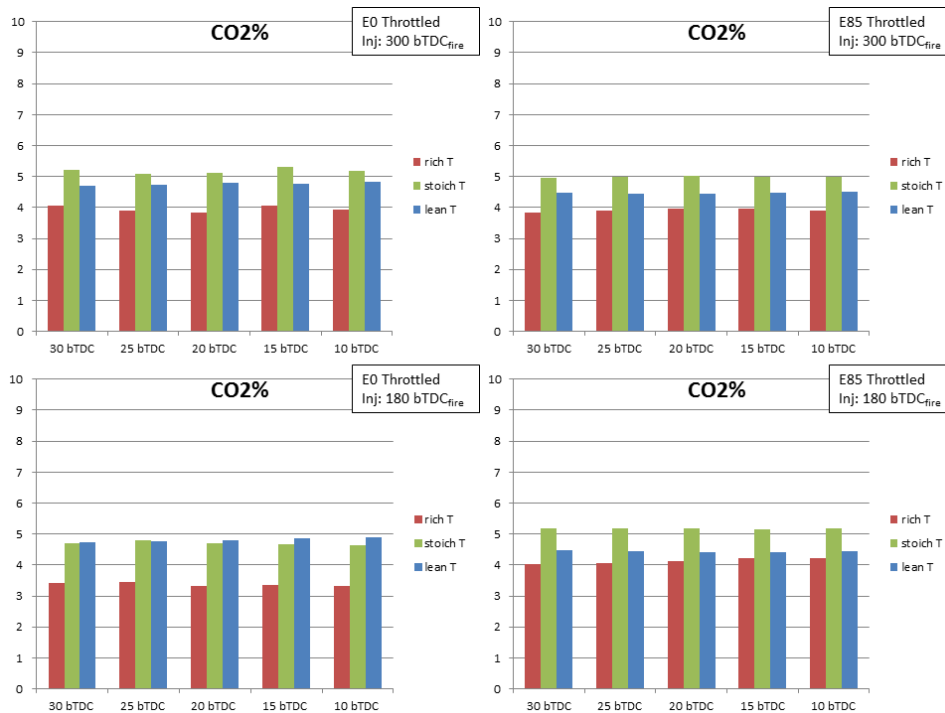


(b)

Figure C-1 CO of (a) WOT and (b) Throttled conditions

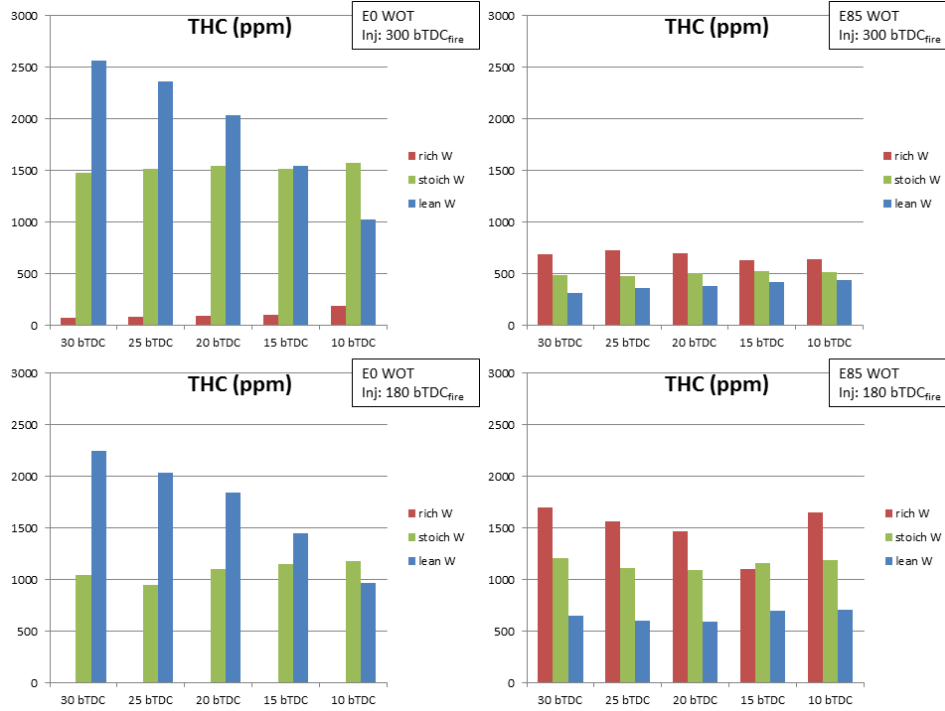


(a)

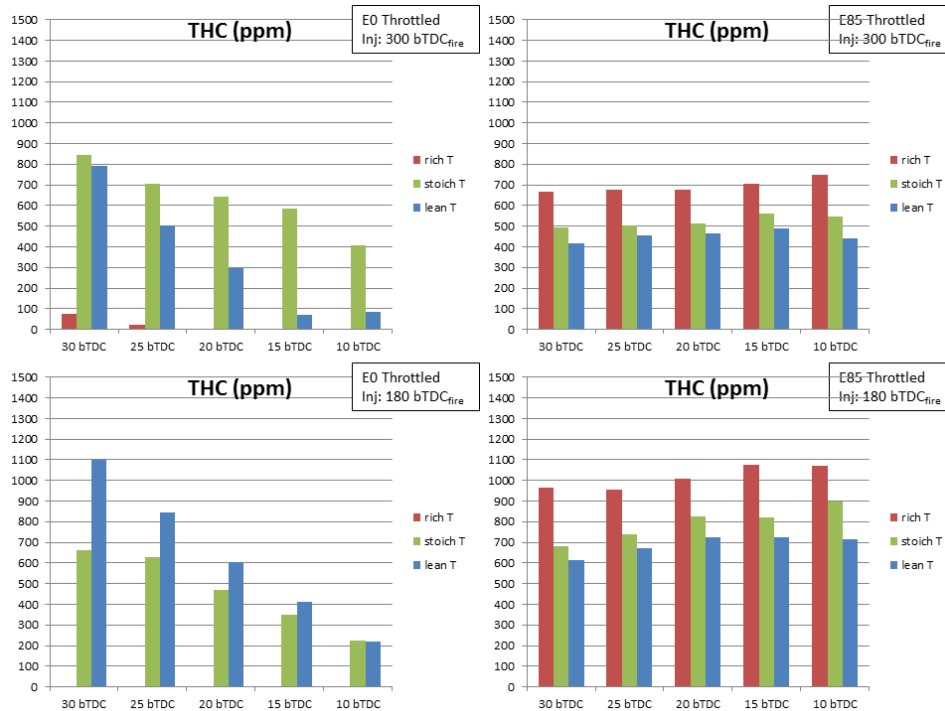


(b)

Figure C-2 CO₂ of (a) WOT and (b) Throttled conditions

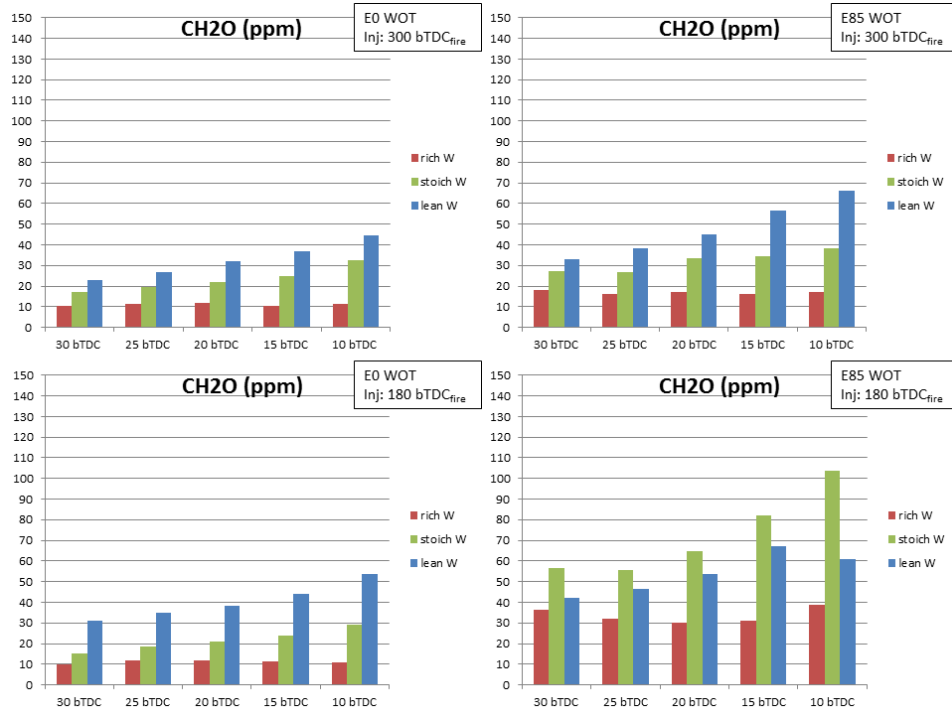


(a)

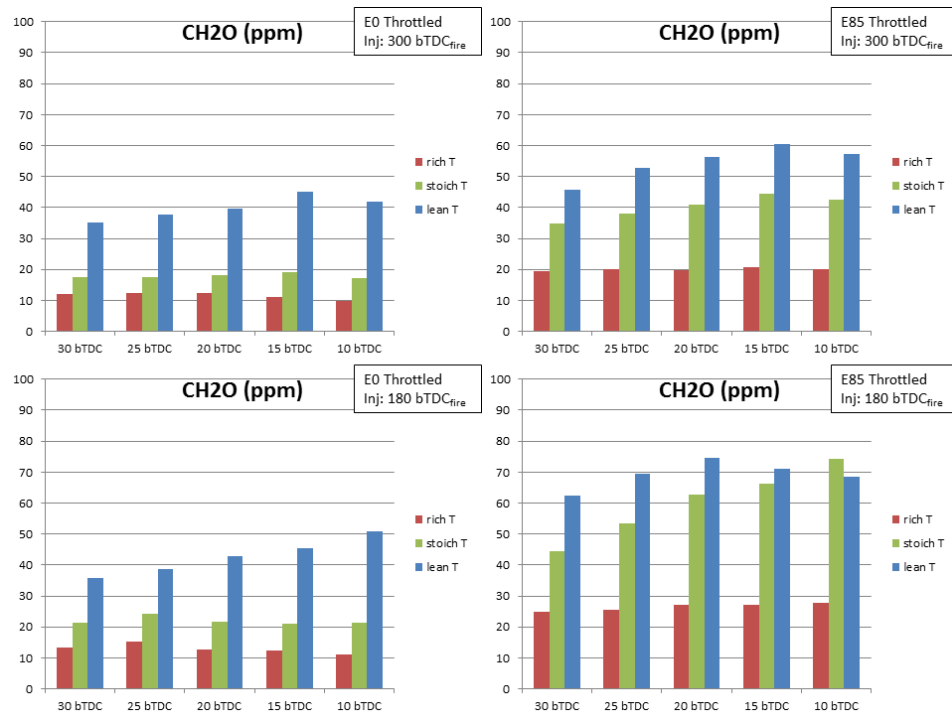


(b)

Figure C-3 HC of (a) WOT and (b) Throttled conditions

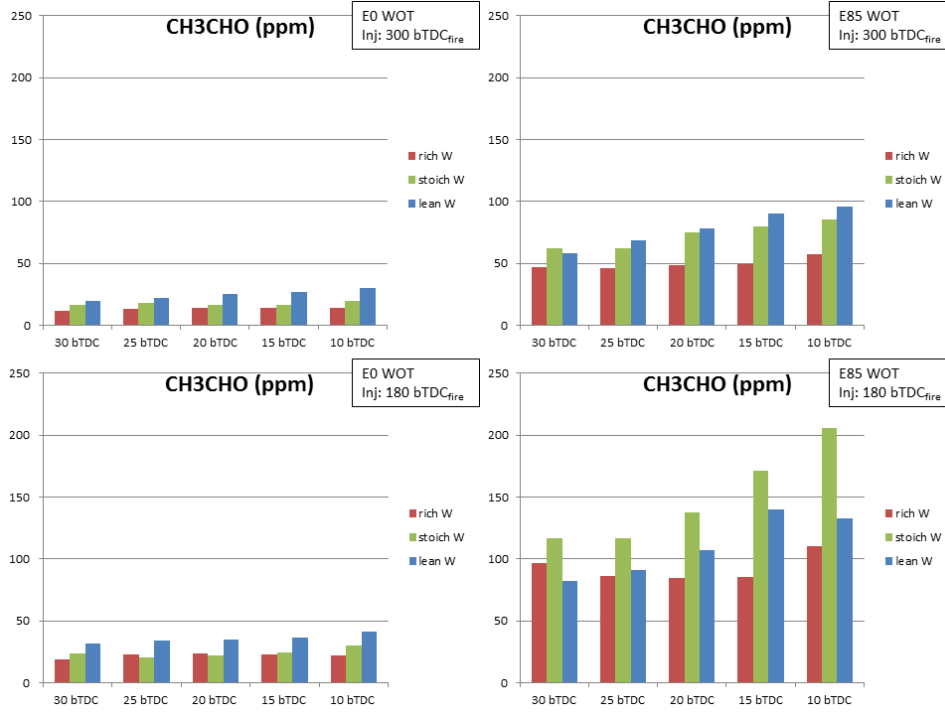


(a)

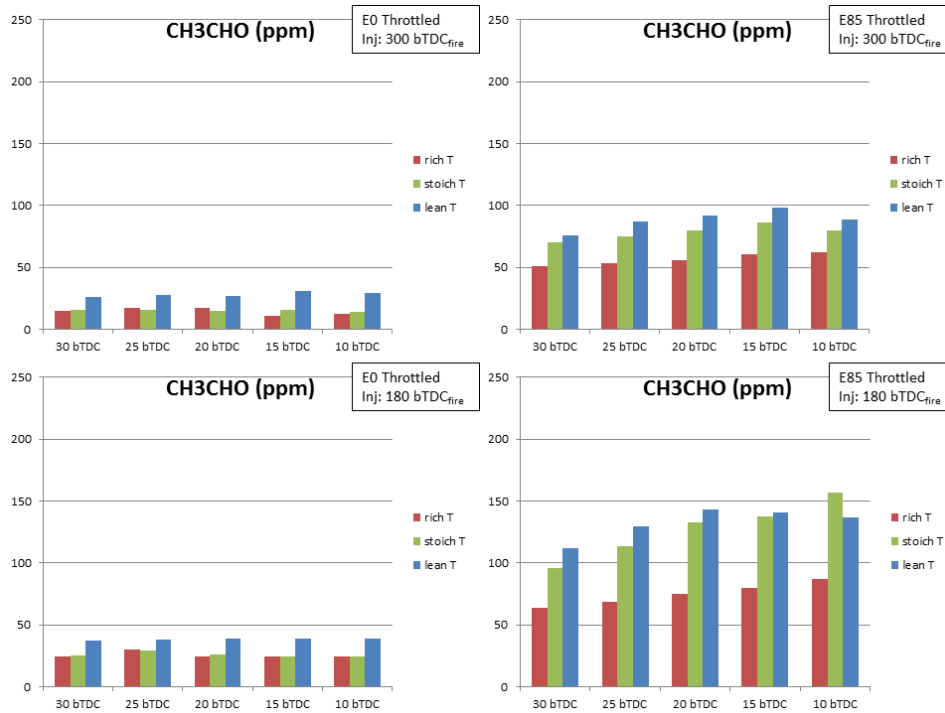


(b)

Figure C-4 Formaldehyde of (a) WOT and (b) Throttled conditions

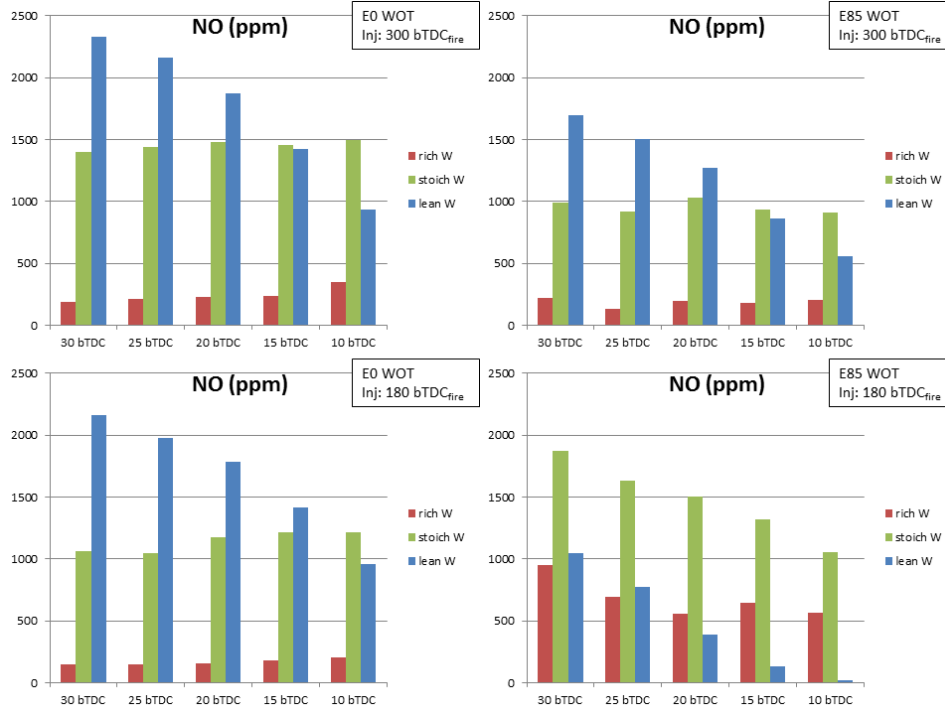


(a)

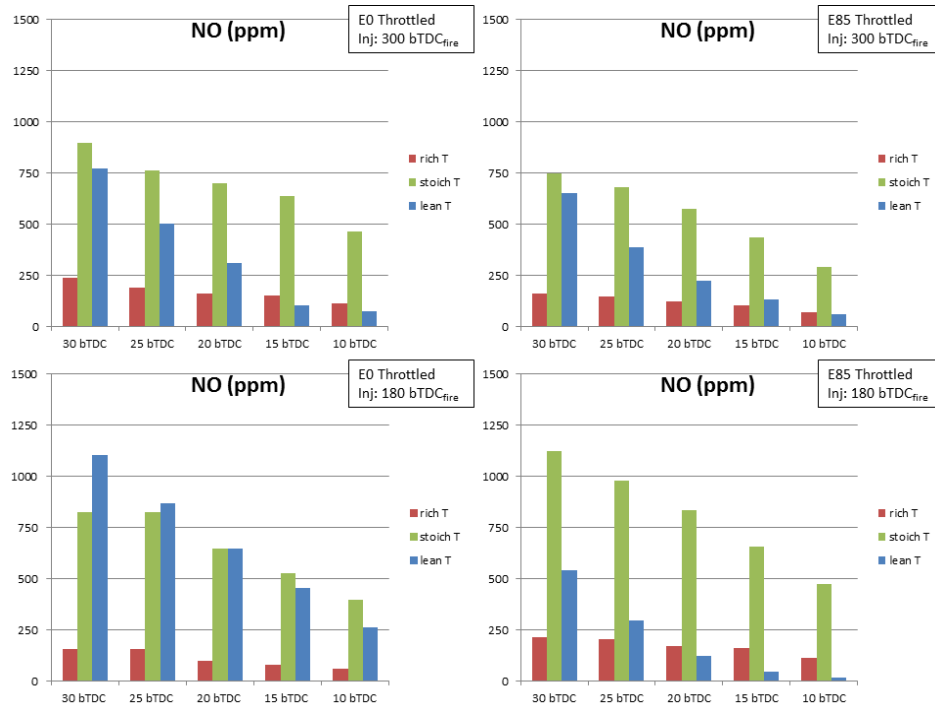


(b)

Figure C-5 Acetaldehyde of (a) WOT and (b) Throttled conditions



(a)



(b)

Figure C-6 NO of (a) WOT and (b) Throttled conditions (NO₂ is nominal)

APPENDIX D: INJECTION MEASUREMENT IN RCM

A schematic of the rapid compression machine setup used in the current study is shown in Fig. D-1, and the combustion chamber details are shown in Fig. D-2. The optics setup of the Schlieren imaging method is shown in Fig. D-3, and the real equipment is shown in Fig. D-4.

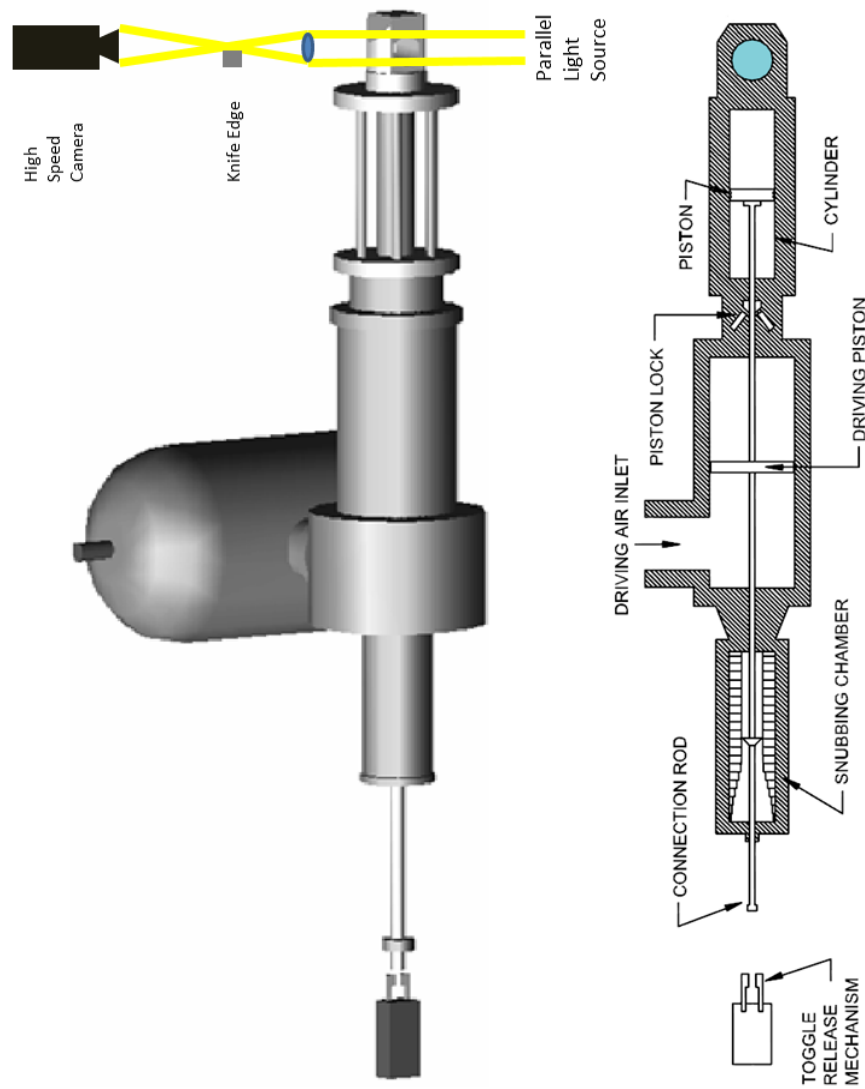


Figure D-1 RCM schematic

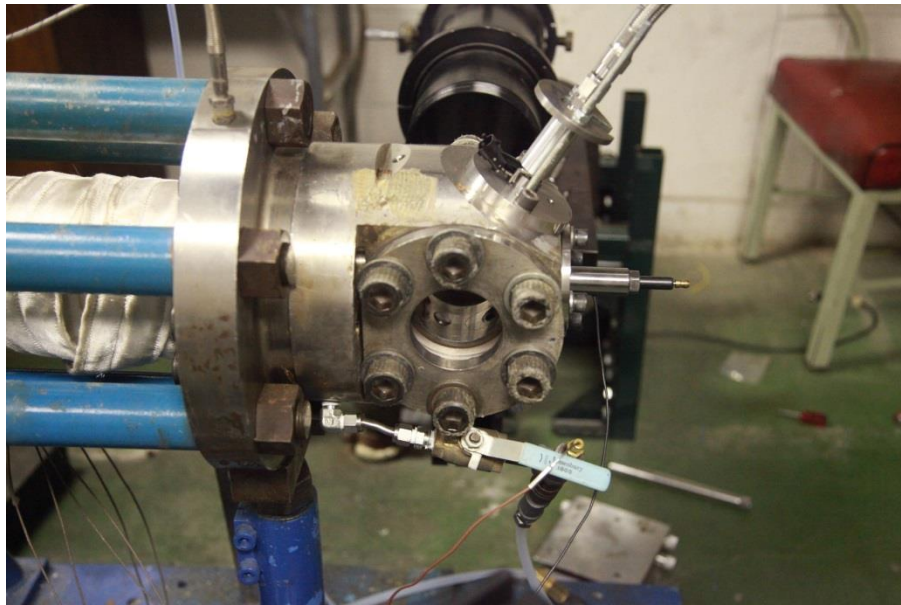
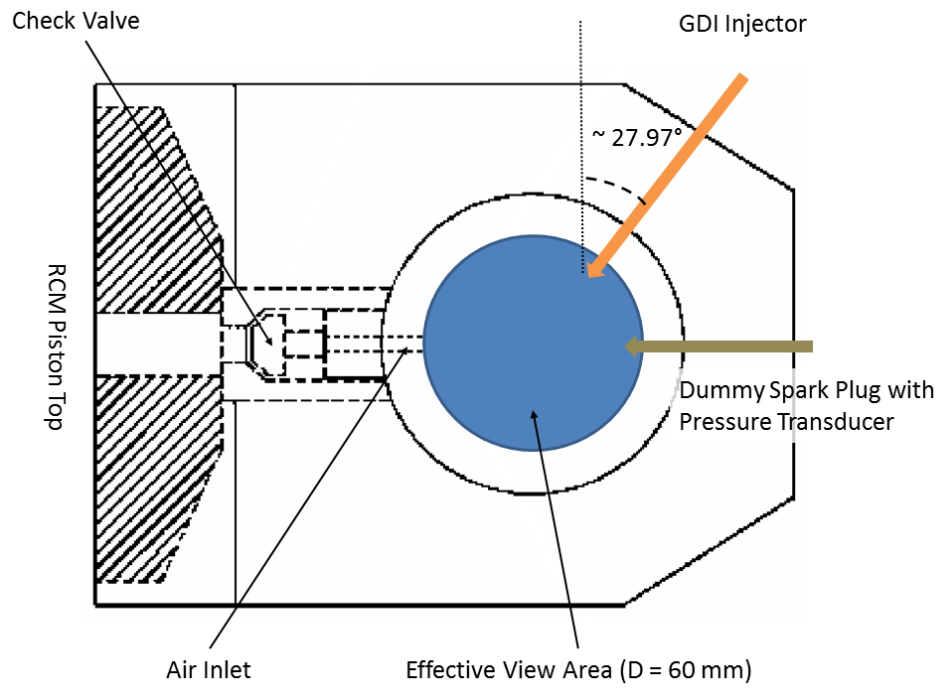


Figure D-2 Combustion chamber schematic (top) and details (bottom)

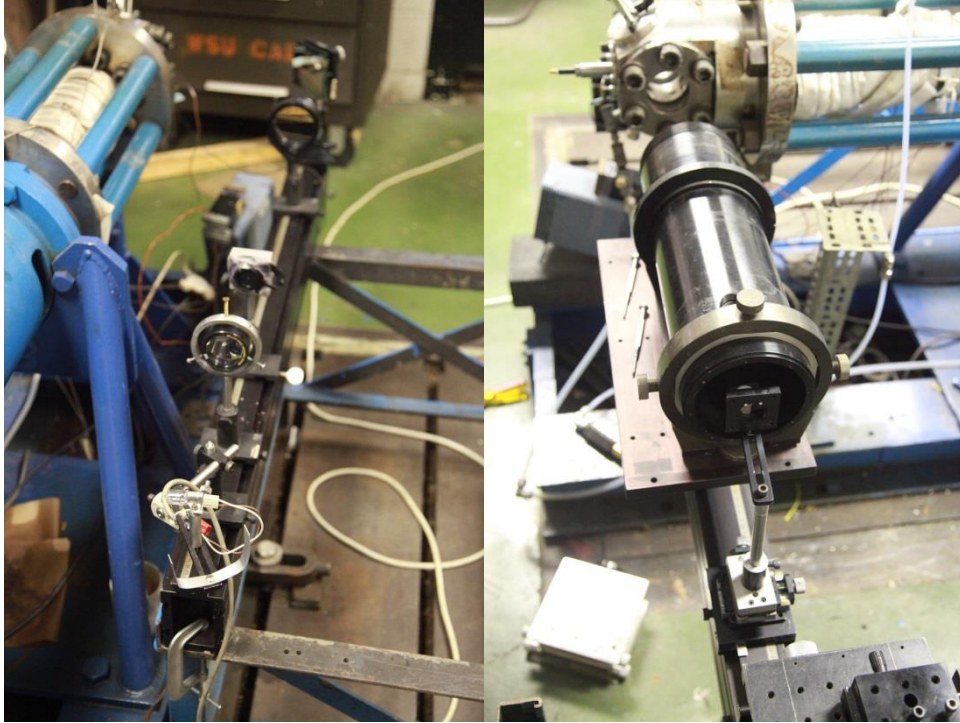


Figure D-3 Schlieren optics setup



Figure D-4 RCM system

The piston of RCM is driven by pressurized shop air stored in the tank. In the current study, the driving air is set at 60 psi. A safety lock holds the connecting rod from moving before the release of the toggle mechanism. Once the connecting rod is released, the piston will move towards the combustion chamber due to the pressure difference between the air tank and the combustion chamber. The higher the pressure of driving air is, the faster the piston motion will be.

The air in the combustion chamber is pre-heated to 100°C, and its pressure is kept at 1 bar. This translates to air density about 0.946 kg/m³, whereas it is roughly 1.205 kg/m³ at room temperature. Once the air is compressed, the peak pressure is about 18 to 19 bar. The mass averaged temperature at peak pressure is about 330°C. Figure D-5 shows the pressure trace of a typical test (considered as “motoring”). The cylinder is about 420 mm (stroke) by 101.5 mm (bore), and the combustion chamber is about 50 mm (thickness) by 70 mm (diameter). Therefore, the theoretical compression ratio is about 18.66:1.

One example of the spray measurement is done in four different ambient pressure conditions. These test points are listed in Table D-1, and Schlieren images right after the start of injection at these points are shown in Fig. D-6 to demonstrate the density gradient. It should be addressed that Fig. D-6(d) shows high density gradient, but its instant air motion is relatively slower than that in Fig. D-6(b) and (c), which indicates lower turbulence intensity.

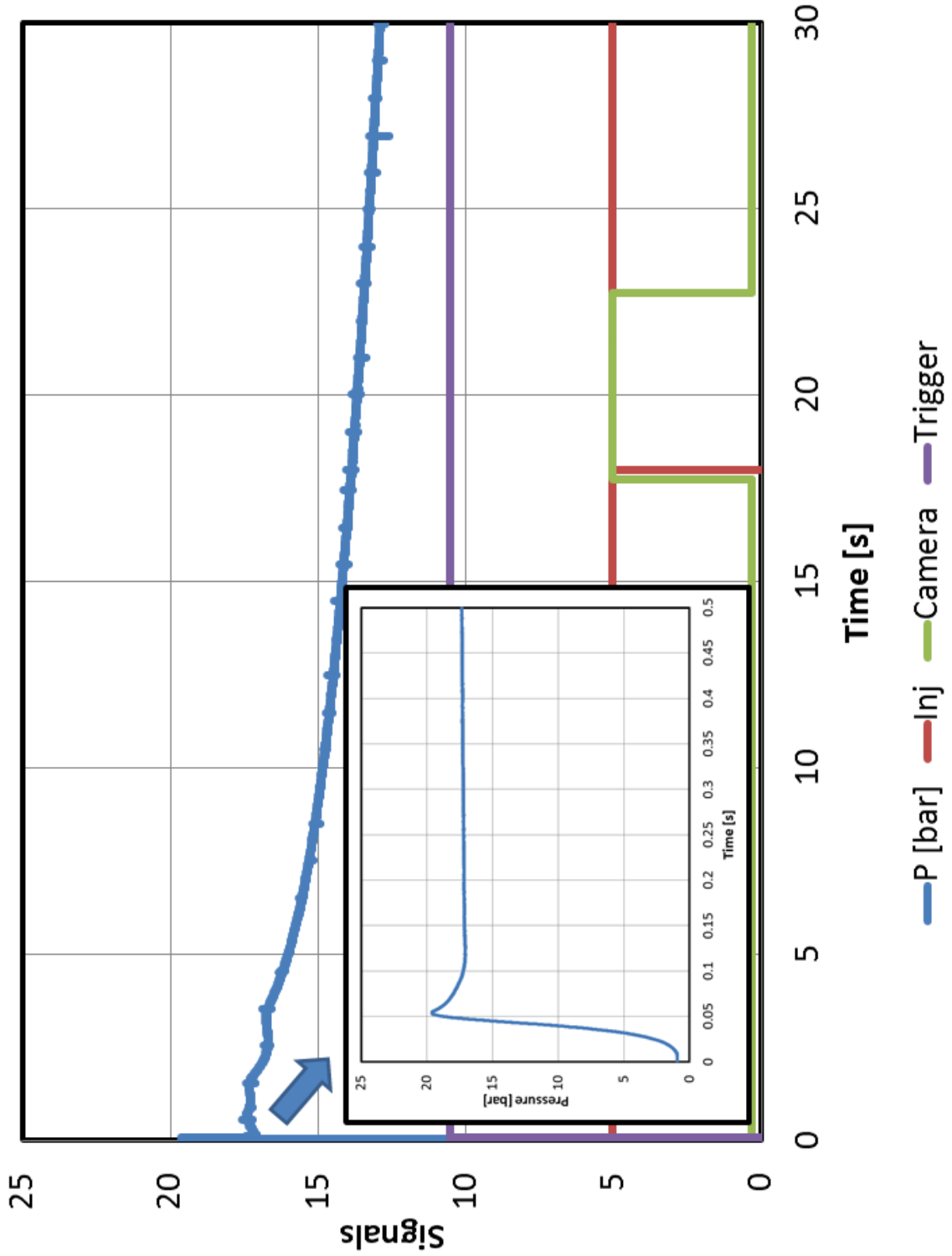


Figure D-5 Pressure trace of RCM

Table D-1 An example of spray measurement points for RCM test

	Point 1	Point 2	Point 3	Point 4
Initial Air Temperature (°C)	100	100	100	100
Ambient Pressure (bar)	1	4	10	18
Temperature at SOI (°C)	100	135	275	330
Corresponding Piston Position	BDC _{intake}	60° bTDC _{fire}	30° bTDC _{fire}	TDC _{fire}
Turbulence Intensity	Low	High	High	Medium

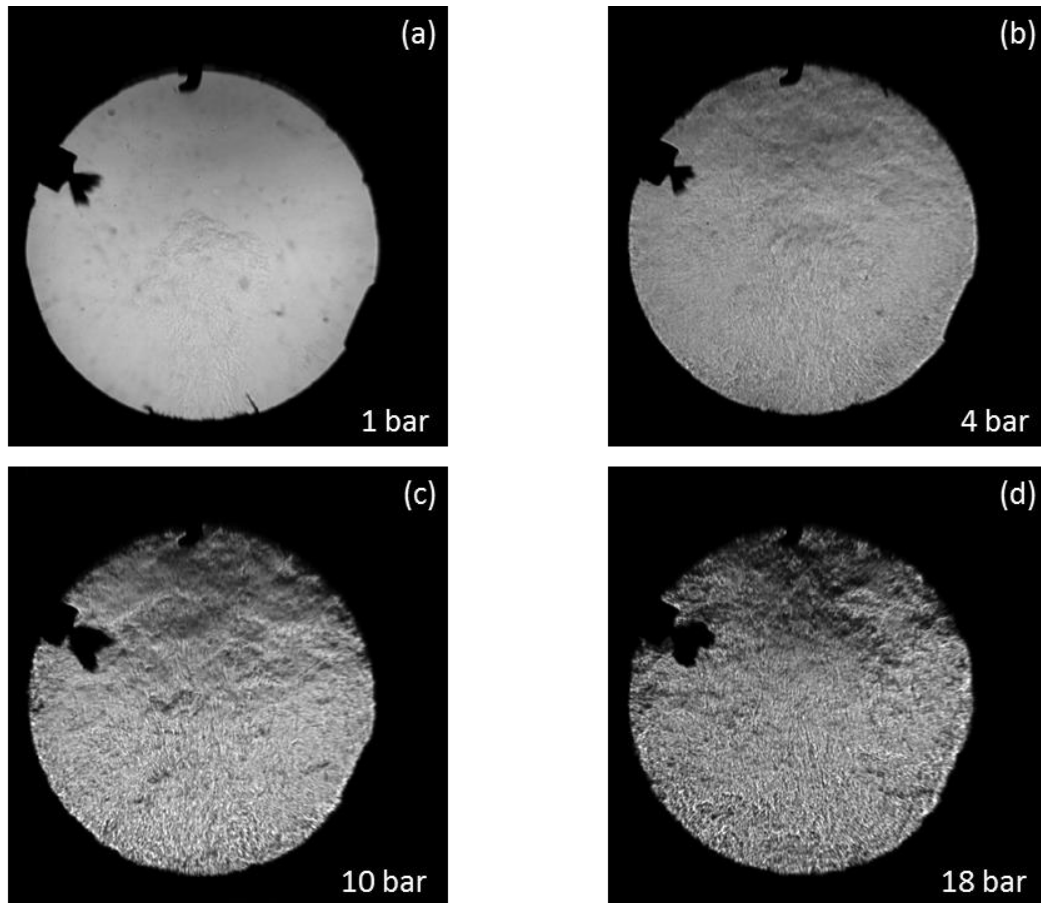


Figure D-6 Images at different test points (right after SOI)

APPENDIX E: PORT FUEL INJECTION CNG APPLICATION

Implementing CNG as a fuel in gasoline engines may be impressive and promising due to its resource worldwide and high H-C ratio ($= 4$) as well as high research octane number (RON > 130). CNG used in the present study is purchased from a local CNG station. The tank is pressurized to 3600 psi (~ 250 bar) in order to provide reasonable energy equivalent to gasoline for the engine testing. Figure E-1 shows the CNG tank and injector, and Fig. E-2 shows the particle size distribution of air, E0, and CNG. E0 and CNG are in Rich conditions, and it is clearly seen that CNG has much fewer particles in general but slight more in very fine sizes.

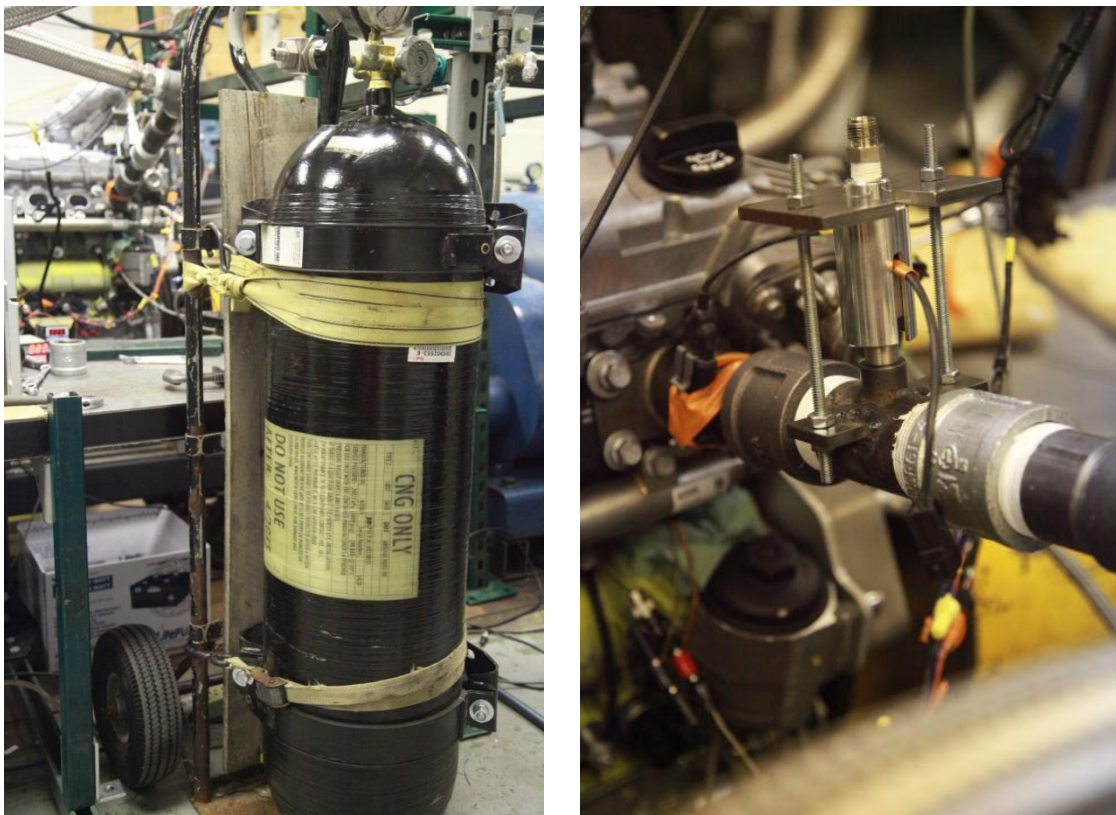


Figure E-1 CNG tank (left) and injector (right)

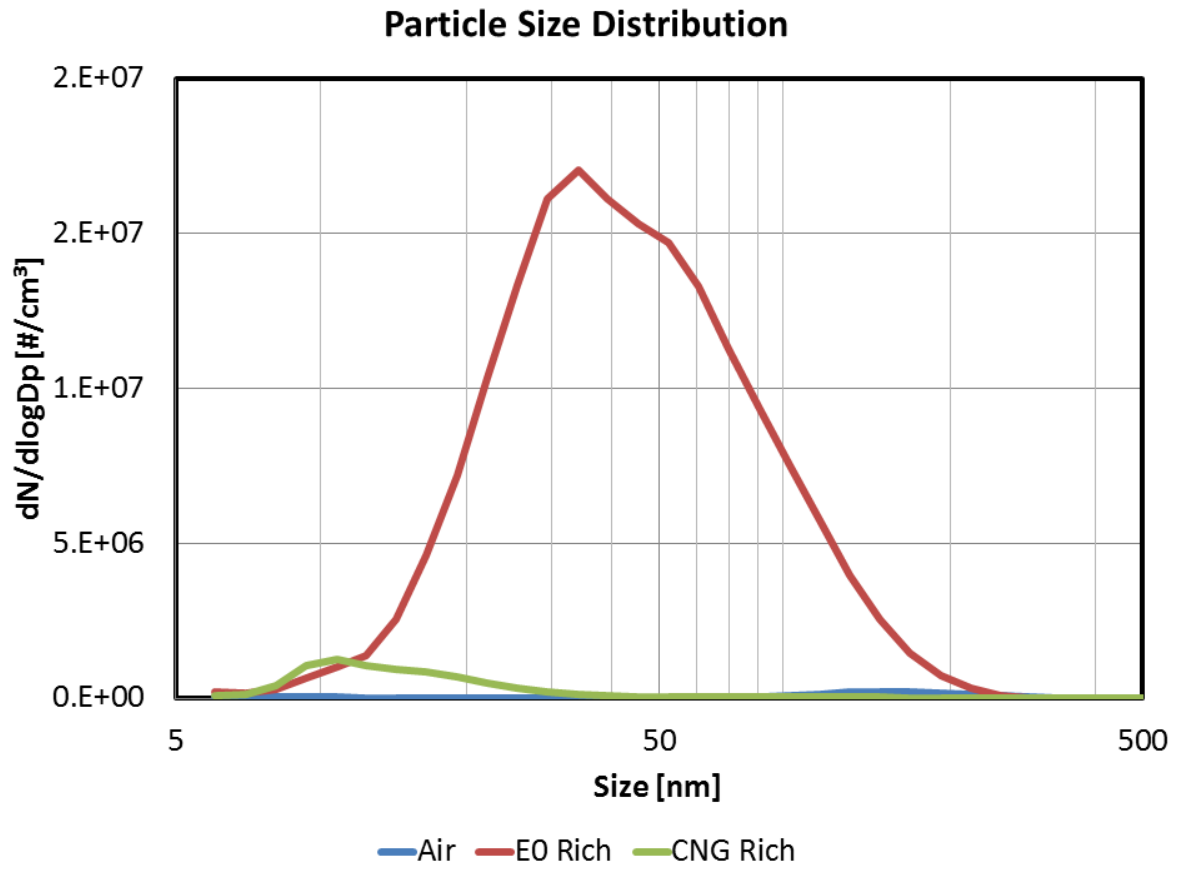


Figure E-2 Particle size distribution of air, E0, and CNG

APPENDIX F: ETHANOL-BIODIESEL APPLICATION

A soybean-based biodiesel is used in the CI engine; the blending of ethanol-biodiesel is to blend the biodiesel with aforementioned ethanol volumetrically by the splashing method. Their blends are denoted as BXXEYY in this study where XX represents the volumetric percentage (%v/v) of each fuel; for example, B60E40 is equal to a blend of 60% biodiesel and 40% ethanol by volume.

The density and kinematic viscosity of biodiesel, ethanol, and their blends are measured with a viscometer and a density meter, respectively. The viscosity measurement is taken at 40°C and complied with the ASTM D445 method. Figure F-1 shows the viscosity curve with respect to different ethanol-biodiesel blending ratios. 20% ethanol by volume in ethanol-diesel blend has about 2 mm²/s kinematic viscosity, which is the minimum value for No. 2 Diesel standard by ASTM. In the current study, up to 40% ethanol by volume could be blended with biodiesel when the minimum viscosity is maintained. Comparing with the viscosity of ultra-low-sulfur diesel (ULSD), the red solid line in Fig. F-1, and the results show that B80E20 has the equivalent viscosity to ULSD, which is the reason that B80E20 is selected for engine testing. Densities of ethanol-biodiesel blends are measured and plotted in Fig. F-2. The density of ULSD is also included in the same figure as the red solid line. B80E20 has slightly higher density than ULSD, which would have no effect on engine performance.

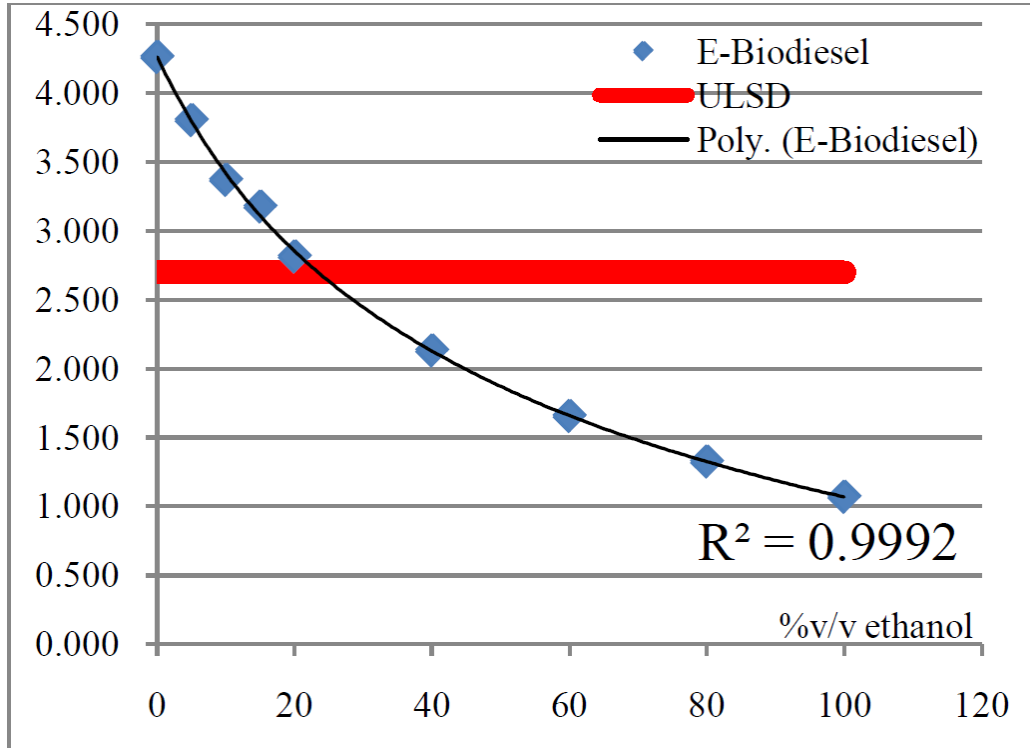


Figure F-1 Viscosity curve of different ethanol-biodiesel blending

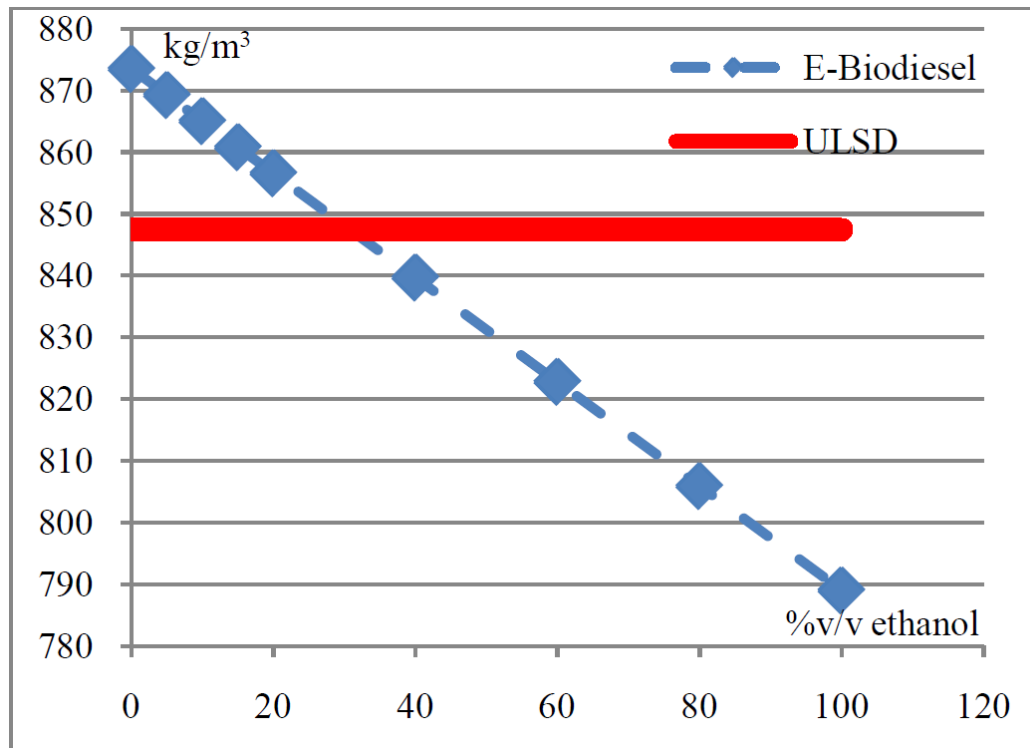


Figure F-2 Densities of different ethanol-biodiesel blending

A solenoid single-hole diesel injector is used in spray imaging with two nozzle orifice diameters (80 μm and 150 μm). Two blends (B80E20 and B60E40) are tested along with B100 for comparison. Figure F-3 shows the schematic of the spray measurement experiment setup, and the Schlieren imaging method is used. Table F-1 shows a detailed testing matrix where the two ethanol-biodiesel blends are selected in this testing according to viscosity results.

The injection system is a customized production common rail system. It contains a motor with a large flywheel, a production fuel pump, and a production common rail with high pressure fuel line to the injector. Pulse-width modulation (PWM) is used to control the common rail pressure by LabVIEW programming. A snapshot of the system is shown in Fig. F-4. The advantage of using the system is the portability without the need to motor a real engine to operate the common rail.

As for the injector, injection duration is fixed at 500 μs for both diameters with 1000 bar injection pressure. Ambient temperature, i.e. the temperature in the chamber, is set at 200 $^{\circ}\text{C}$, and ambient pressure is controlled at 1bar and 4bar for comparison. A monochromatic high speed camera is used in this experiment and the setup is shown in Table F-2. Light from the incandescent light source through optical lenses is partially blocked by a razor blade before captured by the camera, and all images are processed by computer programming to eliminate background noise and to calculate the penetration and area of the sprays.

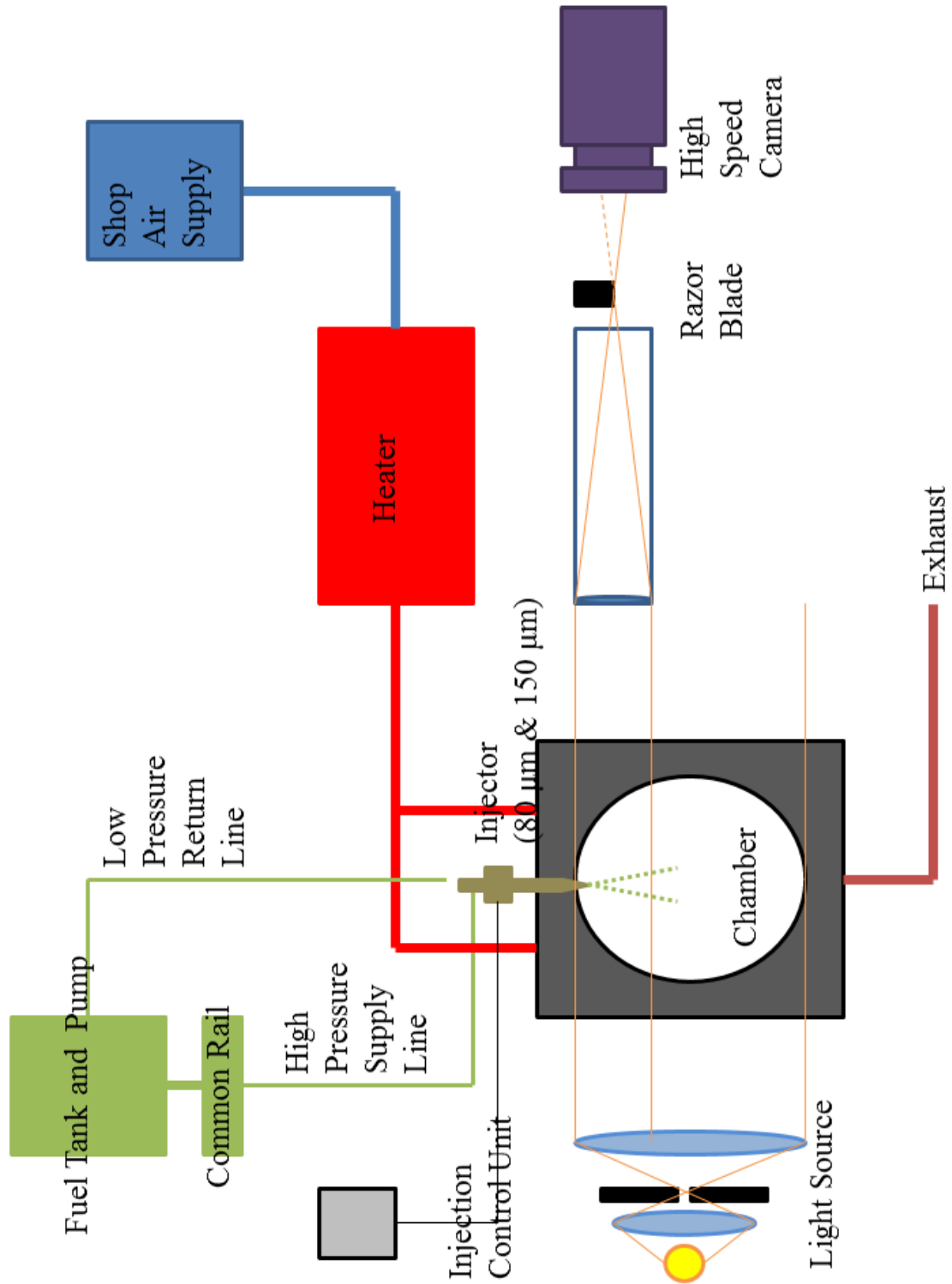


Figure F-3 Spray experiment setup schematic (constant volume chamber)

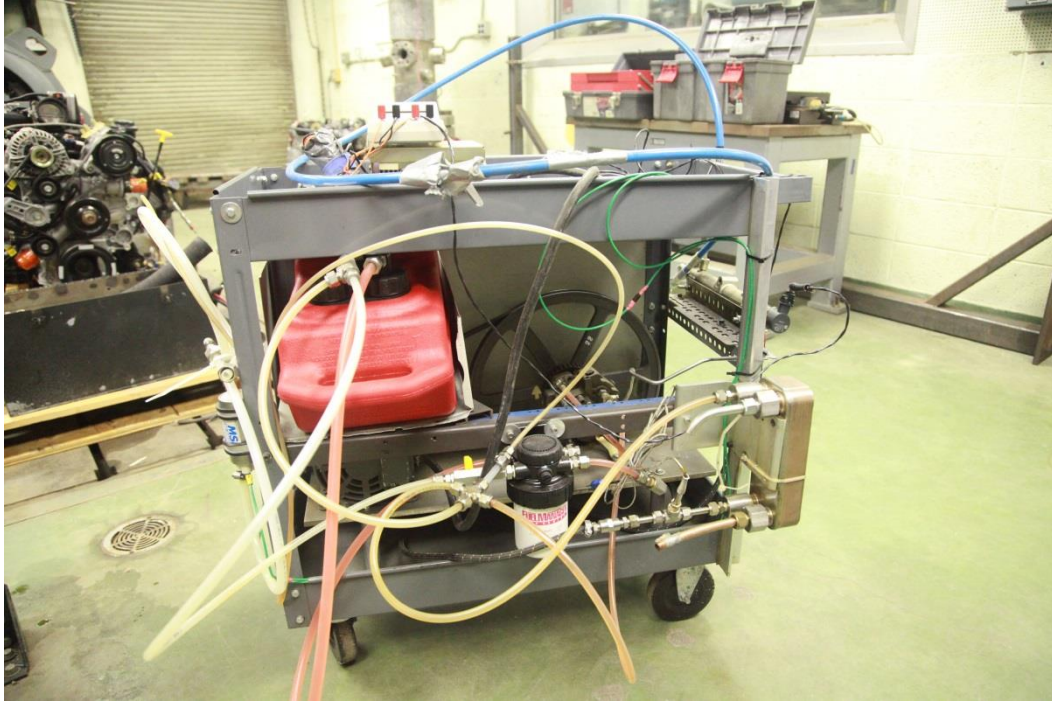


Figure F-4 Customized common rail fueling system

Table F-1 Spray measurement testing matrix (constant volume chamber)

Fuel		B100	B80E20	B60E40
Injection pressure	bar	1000	1000	1000
Injection duration*	μs	500	500	500
In-chamber temperature	$^{\circ}\text{C}$	200	200	200
In-chamber pressure	bar	1, 4	1, 4	1, 4
Nozzle orifice diameter	μm	80, 150	80, 150	80, 150
*: signal from an injection control unit				

Table F-2 Setup of high speed camera

Camera speed	fps*	15037
Frame to frame interval	μ s	66.5
Exposure	μ s	10
Resolution	pixel	512(Y) x 256(X)
1 pixel to mm	mm	0.18
*: frame per second		

The diesel engine used in the study is a 4-cylinder light-duty high-speed direct-injection engine equipped with a variable-geometry turbocharger (VGT) and a cooled EGR. The injection system is common-rail type with solenoid injectors. The engine displacement is 2.8L, and it was built by VM Motori for Jeep Liberty model year 2005 and 2006. The engine is coupled with a DC dynamometer capable of steady-state testing. The engine is controlled by an open ECU through ETAS INCA system. In-cylinder pressure is measured by pressure transducers at each cylinder; temperature is monitored by four thermocouples as one at the engine intake manifold, one at the exhaust manifold (after turbocharger), and two after DPF and SCR, respectively. A schematic of the engine setup is shown in Fig. F-5 with a snapshot of the test cell. Emissions are measured before and after the DPF by TSI Engine Exhaust Particle Sizer (EEPS) Spectrometer 3090 and Horiba Portable Emission Measurement Systems (PEMS) OBS-2200. Detailed emission measurement method and devices will be introduced later in the chapter. Table F-3 shows the engine specifications.

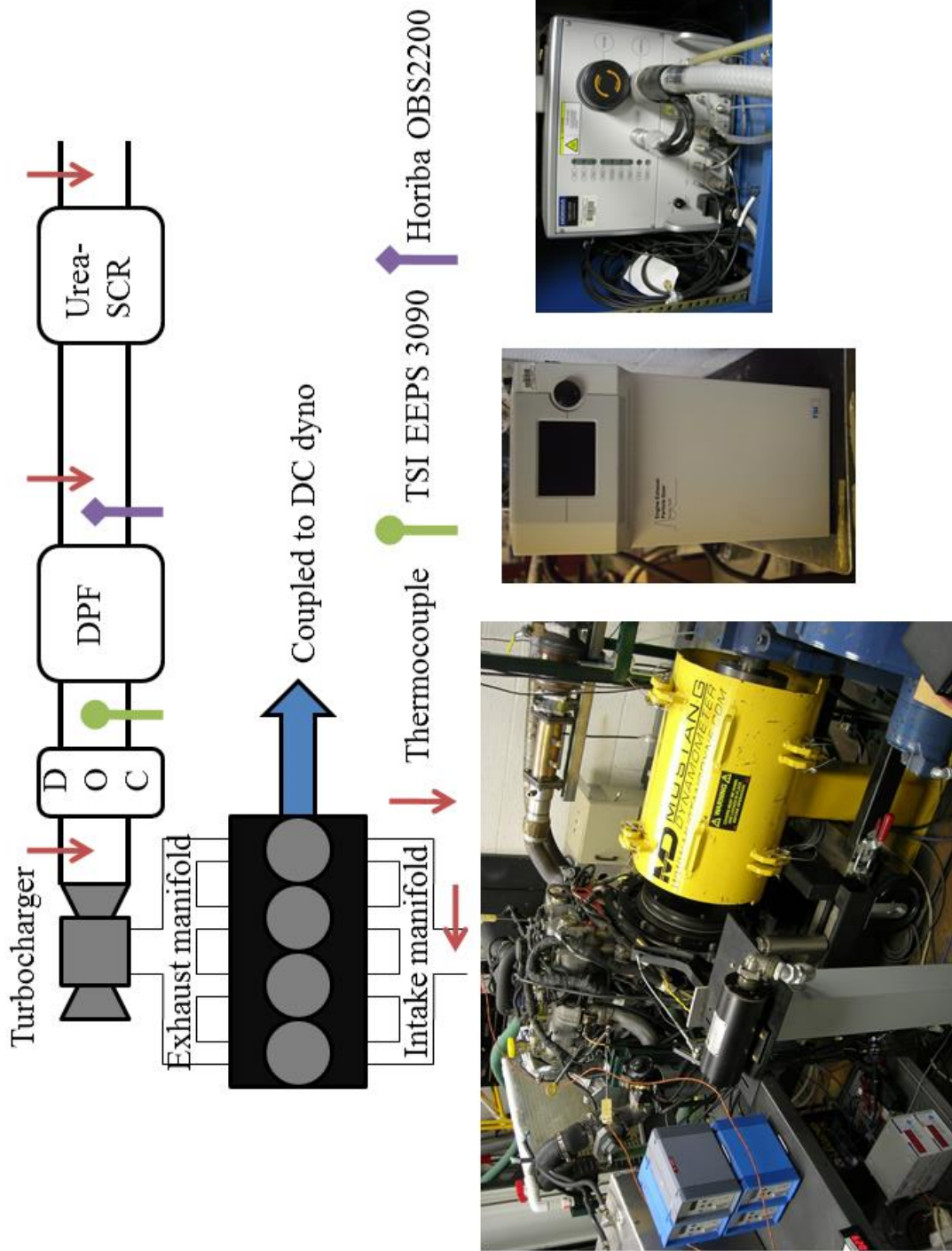


Figure F-5 Diesel engine setup schematic

Table F-3 Diesel engine specification

Engine model	VM Motori R428 DOHC
Displacement	2.8 L (4 cylinder)
Power	120 kW
Torque	400 Nm
Bore X Stroke	94 mm X 100 mm
Compression Ratio	17.5:1
Fuel system	Common rail; Solenoid
Other	Turbocharged, Cooled EGR

Data of the engine combustion and exhaust emission measurements is taken in a steady-state condition listed in Table F-4. Two fuels, B100 and B80E20, are selected for this experiment. A reference test is denoted as default where EGR and injection timing (two pilots and one main) are the original setups of the engine control unit (ECU); this default test is only experimented with B100. As for other tests, due to the stability and combustion quality of the engine, a main injection timing of 6.75° bTDC_{fire} is fixed with respect to two sets of EGR percentage, no-EGR or full-EGR. The two pilot injections are also used and designated by the ECU with respect to the main injection in other tests. The injection pressure is also determined by the ECU, which is between 850 and 950 bar. Figure F-5 shows one example of test results that with the presence of ethanol and biodiesel, both NO_x and PM emissions could be reduced simultaneously. It is because high EGR rate is possible with extra oxygen atoms available in the fuel.

Table F-4 Diesel engine test matrix

Test condition	2400 rpm, 3bar BMEP
EGR	default*, no**, full***
Injection timing (main)	2.62° aTDC _{fire} ****, 6.75° bTDC _{fire}
Fuel	B100, B80E20

*: ~15% EGR; **: EGR is deactivated and blocked;

: ~30% EGR; *: default, with B100 only

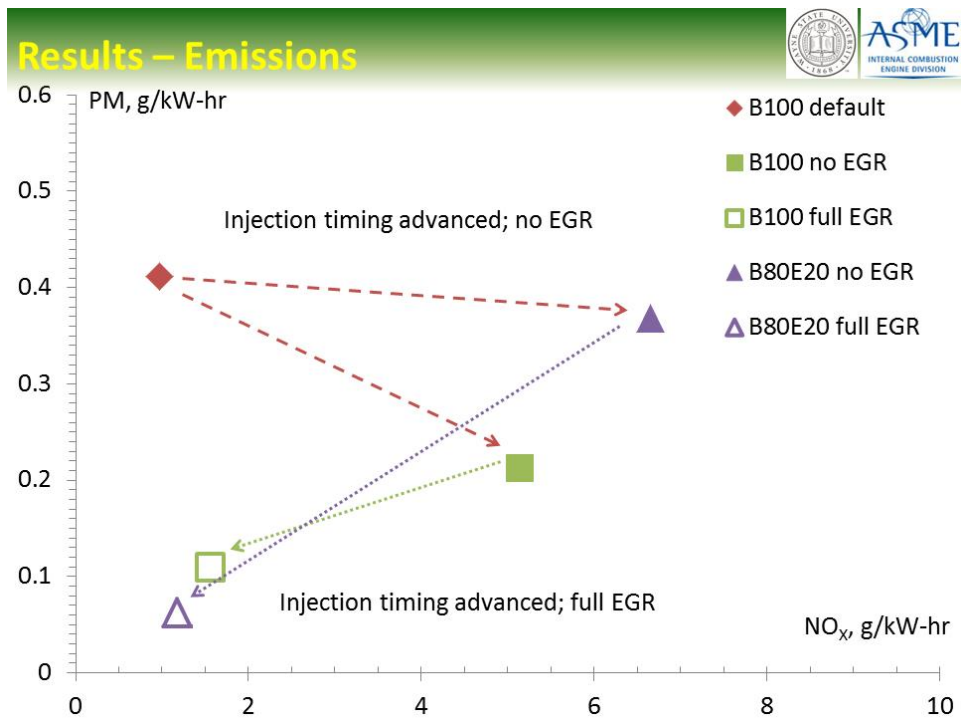
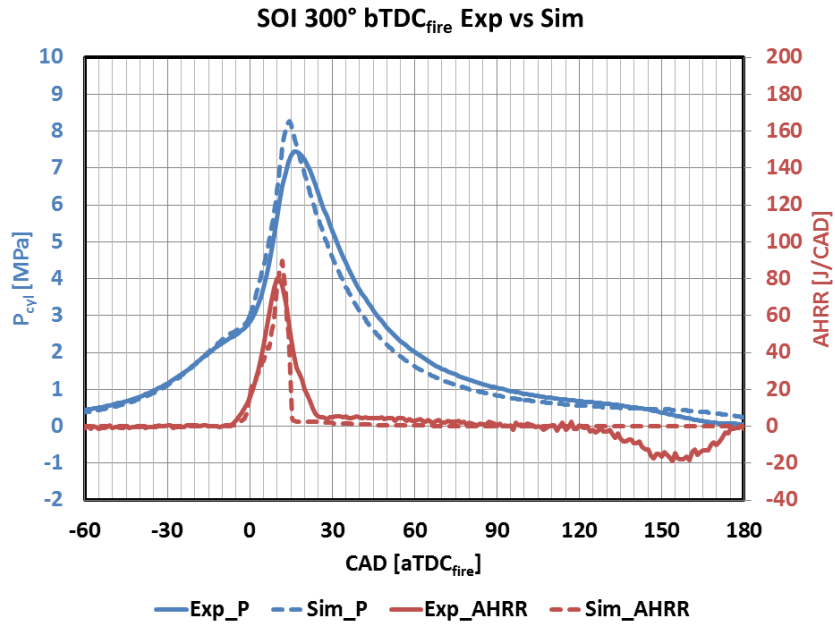
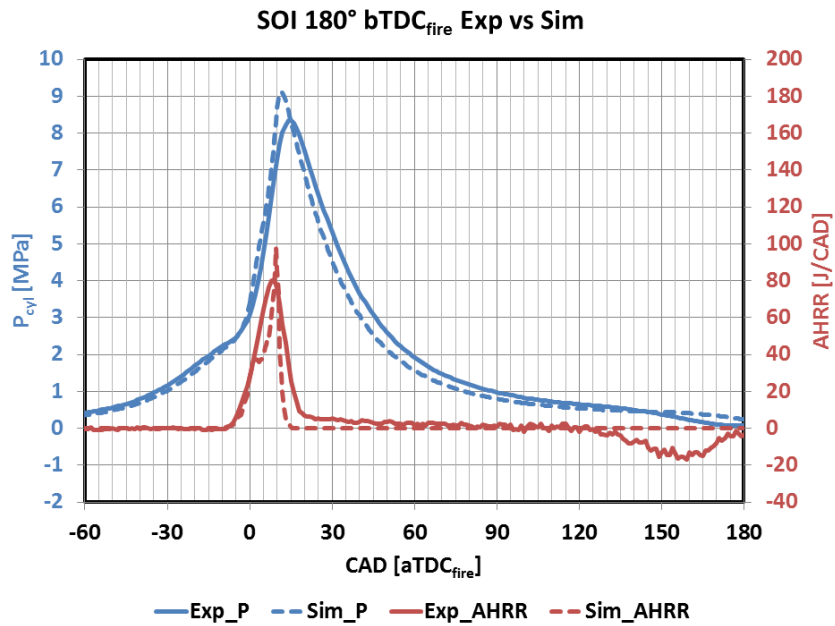


Figure F-5 Example results

APPENDIX G: CFD DATA



(a)



(b)

Figure G-1 Pressure traces and AHRR curves for (a) Fig. 4.7.2(a) and (b) Fig.

4.7.2(b)

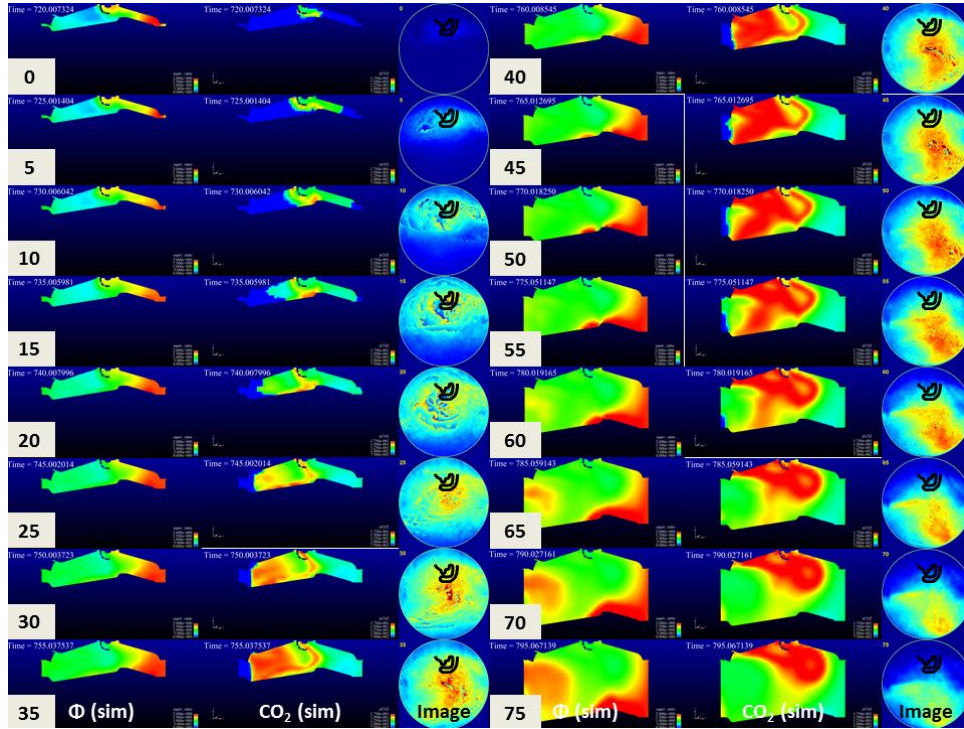


Figure G-2 CFD v.s. Method E (test condition: Throttled; Stoich; SOI: 60° bTDC_{fire}; ST 10° bTDC_{fire})

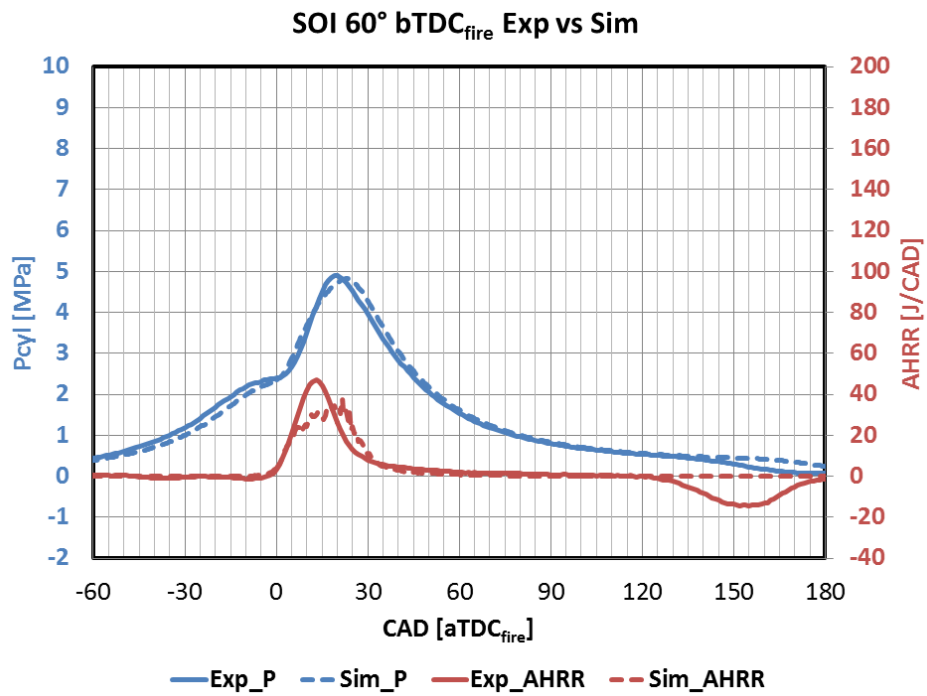


Figure G-3 Pressure traces and AHRR curves for Fig. G-2

REFERENCES

1. John Sousanis (2011-08-15). World Vehicle Population Tops 1 Billion Units. Ward AutoWorld. http://wardsauto.com/ar/world_vehicle_population_110815. Retrieved 2011-08-18.
2. Sperling, Daniel and Deborah Gordon (2009). Two billion cars: driving toward sustainability. Oxford University Press, New York. pp. 4 and 13. ISBN 978-0-19-537664-7. See Chapter 1, Note 1, pp. 261.
3. Chang, J., Kalghatgi, G., Amer, A., Adomeit, P. et al., "Vehicle Demonstration of Naphtha Fuel Achieving Both High Efficiency and Drivability with EURO6 Engine-Out NOx Emission," SAE Int. J. Engines 6(1):2013, doi:10.4271/2013-01-0267.
4. "ExxonMobil 2012 Energy Outlook," http://www.exxonmobil.com/corporate/files/news_pub_eo2012.pdf. Accessed 2 January 2013.
5. "International energy outlook 2011," DOE/EIA-0484(2011), U.S. Energy Information Administration, [http://www.eia.gov/forecasts/ieo/pdf/0484\(2011\).pdf](http://www.eia.gov/forecasts/ieo/pdf/0484(2011).pdf). Accessed 13 October 2012
6. "BP energy Outlook 2030, Jan 2012," http://www.bp.com/liveassets/bp_internet/globalbp/STAGING/global_assets/downloads/O/2012_2030_energy_outlook_booklet.pdf. Accessed 13 October 2012
7. "World Energy Outlook 2011," International Energy Agency (IEA),2011, <http://www.iea.org/publications/worldenergyoutlook/publications/weo-2011/>. Accessed 13 October 2012

8. U.S. Environmental Protection Agency, National Emission Inventory Air Pollutant Emission Trends Web site www.epa.gov/ttn/chief/trends. (Additional resources: www.epa.gov/ttn/chief)
9. Johnson, T., "Vehicular Emissions in Review," SAE Int. J. Engines 6(2):2013, doi:10.4271/2013-01-0538.
10. U.S. Environmental Protection Agency, National Emission Inventory Air Pollutant Emission Trends Web site <http://cfpub.epa.gov/eroe/index.cfm?fuseaction=detail.viewInd&lv=list.listbyalpha&r=219687&subtop=341>
11. Zhao, F., M.-C. Lai, and D.L. Harrington, Automotive spark-ignited direct-injection gasoline engines. Progress in Energy and Combustion Science, 1999. 25: p.437-562.
12. http://en.wikipedia.org/wiki/Ford_EcoBoost_engine. Accessed May 04, 2013
13. Matsumoto, Atsushi, "Spray characterization of flex-fuel gasoline di injectors and spray interaction with charge motion in a variable valve actuation engine" (2012).Wayne State University Dissertations. Paper 457.
14. Introduction to Internal Combustion Engines, 3rd Edition, Richard Stone, SAE International, 1999.
15. Theobald, Jorg, et al., "Fuel injection system – key component for future emission targets." MTZ(72), 2011.
16. M.C. Drake, D.C. Haworth., Advanced gasoline engine development using optical diagnostics and numerical modeling. Proceedings of the Combustion Institute, 2007. 31 : p. 99-124.

17. A.C. Alkidas, S.H. El Tahry, Contributors to the Fuel Economy Advantage of DISI Engines Over PFI Engines. SAE Paper 2003-01- 3101, 2003.
18. Matsumoto, A., Zheng, Y., Xie, X., Lai, M. et al., "Interactions of Multi-hole DI Sprays with Charge Motion and their Implications to Flexible Valve-trained Engine Performance," SAE Technical Paper 2011-01-1883, 2011, doi:10.4271/2011-01-1883.
19. Zheng, Yi, "SIMULATIONS AND EXPERIMENTS OF FUEL INJECTION, MIXING AND COMBUSTION IN DI GASOLINE ENGINES" (2013). Wayne State University Dissertations.
20. Ferguson, C.R. and A.T. Kirkpatrick, *Internal Combustion Engines: Applied Thermosciences*. Second Edition ed2001, New York: John Wiley & Sons.
21. Sellnau, M., et al., 2-step Variable Valve Actuation: System Optimization and Integration on an SI Engine. SAE Paper 2007-01-0040, 2007.
22. Cleary, D. and G. Silvas, Unthrottled Engine Operation with Variable Intake Valve Lift, Duration, and Timing. SAE Paper 2007-01-1282, 2007.
23. Kamo, R., et al., Emissions Comparisons of an Insulated Turbocharged Multi-Cylinder Miller Cycle Diesel Engine. SAE Technical Paper 980888, 1998.
24. Moore, W., Foster, M., Lai, M., Xie, X. et al., "Charge Motion Benefits of Valve Deactivation to Reduce Fuel Consumption and Emissions in a GDi, VVA Engine," SAE Technical Paper 2011-01-1221, 2011, doi:10.4271/2011-01-1221.
25. Moore, W., Foster, M., and Hoyer, K., "Engine Efficiency Improvements Enabled by Ethanol Fuel Blends in a GDi VVA Flex Fuel Engine," SAE Technical Paper 2011-01-0900, 2011, doi:10.4271/2011-01-0900.

26. Mustafa Bahattin Çelik and Bulent Ozdalyan (2010). Gasoline Direct Injection, Fuel Injection, Daniela Siano (Ed.), ISBN: 978-953-307-116-9, InTech, Available from: <http://www.intechopen.com/books/fuelinjection/gasoline-direct-injection>
27. Yamamoto, S., Tanaka, D., Takemura, J., Nakayama, O. et al., "Mixing Control and Combustion in Gasoline Direct Injection Engines for Reducing Cold-Start Emissions," SAE Technical Paper 2001-01-0550, 2001, doi:10.4271/2001-01-0550.
28. Keck, J. C., Heywood, J. B. and Noske, G., "Early Flame Development and Burning Rates in Spark Ignition Engines and Their Cyclic Variability," SAE Paper No. 870164, 1987.
29. Samuel, S., Morrey, D., Whelan, I., and Hassaneen, A., "Combustion Characteristics and Cycle-By-Cycle Variation in a Turbocharged-Intercooled Gasoline Direct-Injected Engine," SAE Technical Paper 2010-01-0348, 2010, doi:10.4271/2010-01-0348.
30. E. Zervas, "Correlations between cycle-to-cycle variations and combustion parameters of a spark ignition engine." Applied Thermal Engineering 24 (2004) 2073–2081
31. Heywood, J.B., Internal Combustion Engine Fundamentals, McGraw-Hill, Inc., New York, 1988.
32. Ault, J. and Witze, P., "Evaluation and Optimization of Measurements of Flame Kernel Growth and Motion Using a Fiber-Optic Spark Plug Probe," SAE Technical Paper 981427, 1998, doi:10.4271/981427.

33. Lipatnikov, A. and Chomiak, J., "Randomness of Flame Kernel Development in Turbulent Gas Mixture," SAE Technical Paper 982617, 1998, doi:10.4271/982617.
34. Ancimer, R., Jaaskelainen, H., and Wallace, J., "Experiments into the Flame Kernel Development in High Swirl Production Spark Ignition Engines," SAE Technical Paper 1999-01-3544, 1999, doi:10.4271/1999-01-3544.
35. Subramanian, K., Shukla, S., Athwe, M., Babu, M. et al., "Study of Flame Characteristics of a Spark Ignition Engine for Gasoline Fuel," SAE Technical Paper 2009-28-0028, 2009, doi:10.4271/2009-28-0028.
36. Song, J. and Sunwoo, M., "A Modeling and Experimental Study of Initial Flame Kernel Development and Propagation in SI Engines," SAE Technical Paper 2000-01-0960, 2000, doi:10.4271/2000-01-0960.
37. Aleiferis, P., Taylor, A., Whitelaw, J., Ishii, K. et al., "Cyclic Variations of Initial Flame Kernel Growth in a Honda VTEC-E Lean-Burn Spark-Ignition Engine," SAE Technical Paper 2000-01-1207, 2000, doi:10.4271/2000-01-1207.
38. Pajot, O. and Mounaïm-Rousselle, C., "Instantaneous Flow Field Effects on the Flame Kernel in S.I.Engine by Simultaneous Optical Diagnostics," SAE Technical Paper 2000-01-1796, 2000, doi:10.4271/2000-01-1796.
39. Soltis, D., "Correlating an Air Motion Number to Combustion Metrics and Initial Flame Kernel Development," SAE Technical Paper 2007-01-0653, 2007, doi:10.4271/2007-01-0653.

40. Ikeda, Y., Nishiyama, A., Kawahara, N., Tomita, E. et al., "In-spark-plug Sensor for Analyzing the Initial Flame and Its Structure in an SI Engine," SAE Technical Paper 2005-01-0644, 2005, doi:10.4271/2005-01-0644.
41. Lee, Y. and Boehler, J., "Flame Kernel Development and its Effects on Engine Performance with Various Spark Plug Electrode Configurations," SAE Technical Paper 2005-01-1133, 2005, doi:10.4271/2005-01-1133.
42. Alger, T., Mangold, B., Mehta, D., and Roberts, C., "The Effect of Sparkplug Design on Initial Flame Kernel Development and Sparkplug Performance," SAE Technical Paper 2006-01-0224, 2006, doi:10.4271/2006-01-0224.
43. Naeim A. Henein and Donald Patterson, Economy and Emission Control in Combustion Engines, Wayne State University
44. Pulkrabek, W.W., Engineering Fundamentals of the Internal Combustion Engine, 2nd Ed., Prentice Hall, New Jersey, 2004
45. Russ, S., Thiel, M., and Lavoie, G., "SI Engine Operation with Retarded Ignition: Part 2 -HC Emissions and Oxidation," SAE Technical Paper 1999-01-3507, 1999, doi:10.4271/1999-01-3507.
46. Hallgren, B. and Heywood, J., "Effects of Substantial Spark Retard on SI Engine Combustion and Hydrocarbon Emissions," SAE Technical Paper 2003-01-3237, 2003, doi:10.4271/2003-01-3237.
47. Stanglmaier, R., Li, J., and Matthews, R., "The Effect of In-Cylinder Wall Wetting Location on the HC Emissions from SI Engines," SAE Technical Paper 1999-01-0502, 1999, doi:10.4271/1999-01-0502.

48. Cole, R., Poola, R., and Sekar, R., "Exhaust Emissions of a Vehicle with a Gasoline Direct-Injection Engine," SAE Technical Paper 982605, 1998, doi:10.4271/982605.
49. Kaiser, E., Siegl, W., Brehob, D., and Haghgooie, M., "Engine-Out Emissions from a Direct-Injection Spark-Ignition (DISI) Engine," SAE Technical Paper 1999-01-1529, 1999, doi:10.4271/1999-01-1529.
50. Alger, T., Hall, M., and Matthews, R., "The Effects of In-Cylinder Flow Fields and Injection Timing on Time-Resolved Hydrocarbon Emissions in a 4-Valve, DISI Engine," SAE Technical Paper 2000-01-1905, 2000, doi:10.4271/2000-01-1905.
51. Sandquist, H., Lindgren, R., and Denbratt, I., "Sources of Hydrocarbon Emissions from a Direct Injection Stratified Charge Spark Ignition Engine," SAE Technical Paper 2000-01-1906, 2000, doi:10.4271/2000-01-1906.
52. Choi, M., Sun, H., Lee, C., Myung, C. et al., "The Study of HC Emission Characteristics and Combustion Stability with Spark Timing Retard at Cold Start in Gasoline Engine Vehicle," SAE Technical Paper 2000-01-1082, 2000, doi:10.4271/2000-01-1082.
53. Bartley, G. and Gabehart, T., "Evaluation of NOx Emission Control Technologies for SIDI Engines," SAE Technical Paper 2002-01-1674, 2002, doi:10.4271/2002-01-1674.
54. Pauly, T., Franoschek, S., Hoyer, R., and Eckhoff, S., "Cost and Fuel Economy Driven Aftertreatment Solutions -for Lean GDI-," SAE Technical Paper 2010-01-0363, 2010, doi:10.4271/2010-01-0363.

55. Li, W., Perry, K., Narayanaswamy, K., Kim, C. et al., "Passive Ammonia SCR System for Lean-burn SIDI Engines," SAE Int. J. Fuels Lubr. 3(1):99-106, 2010, doi:10.4271/2010-01-0366.
56. Guralp, O., Qi, G., Li, W., and Najt, P., "Experimental Study of NOx Reduction by Passive Ammonia-SCR for Stoichiometric SIDI Engines," SAE Technical Paper 2011-01-0307, 2011, doi:10.4271/2011-01-0307.
57. Kirwan, J., Shost, M., Roth, G., and Zizelman, J., "3-Cylinder Turbocharged Gasoline Direct Injection: A High Value Solution for Low CO2 and NOx Emissions," SAE Int. J. Engines 3(1):355-371, 2010, doi:10.4271/2010-01-0590.
58. Peckham, M., Finch, A., and Campbell, B., "Analysis of Transient HC, CO, NOx and CO2 Emissions from a GDI Engine using Fast Response Gas Analyzers," SAE Int. J. Engines 4(1):1513-1522, 2011, doi:10.4271/2011-01-1227.
59. Sjöberg, M. and Reuss, D., "NOx-Reduction by Injection-Timing Retard in a Stratified-Charge DISI Engine using Gasoline and E85," SAE Int. J. Fuels Lubr. 5(3):1096-1113, 2012, doi:10.4271/2012-01-1643.
60. Iason Dimou, "Particulate Matter Emissions from a DISI engine under Cold-Fast-Idle Conditions for Ethanol-Gasoline Blends." Master Thesis in Mechanical Engineering and Naval Engineer, MIT. 2011.
61. Braisher, M., Stone, R., and Price, P., "Particle Number Emissions from a Range of European Vehicles," SAE Technical Paper 2010-01-0786, 2010, doi:10.4271/2010-01-0786.

62. Zhang, S. and McMahon, W., "Particulate Emissions for LEV II Light-Duty Gasoline Direct Injection Vehicles," *SAE Int. J. Fuels Lubr.* 5(2):637-646, 2012, doi:10.4271/2012-01-0442.
63. Drake, M., Fansler, T., Solomon, A., and Szekely, G., "Piston Fuel Films as a Source of Smoke and Hydrocarbon Emissions from a Wall-Controlled Spark-Ignited Direct-Injection Engine," *SAE Technical Paper 2003-01-0547*, 2003, doi:10.4271/2003-01-0547.
64. Yu, C., Park, K., Han, S., and Kim, W., "Development of Theta II 2.4L GDI Engine for High Power & Low Emission," *SAE Technical Paper 2009-01-1486*, 2009, doi:10.4271/2009-01-1486.
65. Matthias, N., Farron, C., Foster, D., Andrie, M. et al., "Particulate Matter Sampling and Volatile Organic Compound Removal for Characterization of Spark Ignited Direct Injection Engine Emissions," *SAE Int. J. Fuels Lubr.* 5(1):399-409, 2012, doi:10.4271/2011-01-2100.
66. Winklhofer, E., Neubauer, M., Hirsch, A., and Philipp, H., "Cylinder- and Cycle Resolved Particle Formation Evaluation to Support GDI Engine Development for Euro 6 Targets," *SAE Technical Paper 2011-24-0206*, 2011, doi:10.4271/2011-24-0206.
67. Choi, K., Kim, J., Ko, A., Myung, C. et al., "Evaluation of Time-Resolved Nano-Particle and THC Emissions of Wall-Guided GDI Engine," *SAE Technical Paper 2011-28-0022*, 2011, doi:10.4271/2011-28-0022.
68. He, X., Ireland, J., Zigler, B., Ratcliff, M. et al., "The Impacts of Mid-level Biofuel Content in Gasoline on SIDI Engine-out and Tailpipe Particulate Matter

- Emissions," SAE Technical Paper 2010-01-2125, 2010, doi:10.4271/2010-01-2125.
69. Sabathil, D., Koenigstein, A., Schaffner, P., Fritzsche, J. et al., "The Influence of DISI Engine Operating Parameters on Particle Number Emissions," SAE Technical Paper 2011-01-0143, 2011, doi:10.4271/2011-01-0143.
70. Steimle, F., Kulzer, A., Richter, H., Schwarzenhal, D. et al., "Systematic Analysis and Particle Emission Reduction of Homogeneous Direct Injection SI Engines," SAE Technical Paper 2013-01-0248, 2013, doi:10.4271/2013-01-0248.
71. Köpple, F., Jochmann, P., Kufferath, A., and Bargende, M., "Investigation of the Parameters Influencing the Spray-Wall Interaction in a GDI Engine - Prerequisite for the Prediction of Particulate Emissions by Numerical Simulation," SAE Int. J. Engines 6(2):2013, doi:10.4271/2013-01-1089.
72. Sakai, S., Hageman, M., and Rothamer, D., "Effect of Equivalence Ratio on the Particulate Emissions from a Spark-Ignited, Direct-Injected Gasoline Engine," SAE Technical Paper 2013-01-1560, 2013, doi:10.4271/2013-01-1560.
73. Berndorfer, A., Breuer, S., Piock, W., and Von Bacho, P., "Diffusion Combustion Phenomena in GDi Engines caused by Injection Process," SAE Technical Paper 2013-01-0261, 2013, doi:10.4271/2013-01-0261.
74. Whitaker, P., Kapus, P., Ogris, M., and Hollerer, P., "Measures to Reduce Particulate Emissions from Gasoline DI engines," SAE Int. J. Engines 4(1):1498-1512, 2011, doi:10.4271/2011-01-1219.

75. Efthymiou, P., Davy, M., Garner, C., Hargrave, G. et al., "Insights into Cold-Start DISI Combustion in an Optical Engine Operating at -7°C," SAE Int. J. Engines 6(2):2013, doi:10.4271/2013-01-1309.
76. Matsumoto, A., Moore, W., Lai, M., Zheng, Y. et al., "Spray Characterization of Ethanol Gasoline Blends and Comparison to a CFD Model for a Gasoline Direct Injector," SAE Int. J. Engines 3(1):402-425, 2010, doi:10.4271/2010-01-0601.
77. Matsumoto, A., Zheng, Y., Xie, X., Lai, M. et al., "Characterization of Multi-hole Spray and Mixing of Ethanol and Gasoline Fuels under DI Engine Conditions," SAE Technical Paper 2010-01-2151, 2010, doi:10.4271/2010-01-2151.
78. <http://www.afdc.energy.gov/fuels/ethanol.html>, accessed May 02, 2013.
79. Stan, C., Troeger, R., Lensi, R., Martorano, L., et al., "Potentialities of Direct Injection in Spark Ignition Engines - from Gasoline to Ethanol," SAE Technical Paper 2000-01-3270, 2000, doi: 10.4271/2000-01-3270.
80. Stan, C., Troeger, R., Gunther, S., Stanciu, A., et al., "Internal Mixture Formation and Combustion - from Gasoline to Ethanol," SAE Technical Paper 2001-01-1207, 2001, doi: 10.4271/2001-01-1207.
81. Christie, M.J., N. Fortino, and H. Yilmaz, Parameter Optimization of a Turbo Charged Direct Injection Flex Fuel SI Engine. SAE Technical Paper 2009-01-0238, 2009.
82. Kapus, P.E., et al., Ethanol Direct Injection on Turbocharged SI Engines – Potential and Challenges. SAE Technical Paper 2007-01-1408, 2007.

83. Khalek, I., Bougher, T., and Jetter, J., "Particle Emissions from a 2009 Gasoline Direct Injection Engine Using Different Commercially Available Fuels," *SAE Int. J. Fuels Lubr.* 3(2):623-637, 2010, doi:10.4271/2010-01-2117.
84. Catapano, F., Di Iorio, S., Lazzaro, M., Sementa, P. et al., "Characterization of Ethanol Blends Combustion Processes and Soot Formation in a GDI Optical Engine," *SAE Technical Paper 2013-01-1316*, 2013, doi:10.4271/2013-01-1316.
85. Allocca, L., Catapano, F., Montanaro, A., Sementa, P. et al., "Study of E10 and E85 Effect on Air Fuel Mixing and Combustion Process in Optical Multicylinder GDI Engine and in a Spray Imaging Chamber," *SAE Technical Paper 2013-01-0249*, 2013, doi:10.4271/2013-01-0249.
86. Fatouraie, M., Wooldridge, M., and Wooldridge, S., "In-Cylinder Particulate Matter and Spray Imaging of Ethanol/Gasoline Blends in a Direct Injection Spark Ignition Engine," *SAE Int. J. Fuels Lubr.* 6(1):1-10, 2013, doi:10.4271/2013-01-0259.
87. Stein, R., Anderson, J., and Wallington, T., "An Overview of the Effects of Ethanol-Gasoline Blends on SI Engine Performance, Fuel Efficiency, and Emissions," *SAE Int. J. Engines* 6(1):2013, doi:10.4271/2013-01-1635.
88. Çengel, Y.A., and Boles, M.A., *Thermodynamics: An Engineering Approach*, 3rd Ed., McGraw-Hill, Inc., New York, 1998.
89. Lee, S., Tong, K., Quay, B. D., Zello, J. V., et al., "Effects of Swirl and Tumble on Mixture Preparation During Cold Start of a Gasoline Direct-Injection Engine," *SAE Technical Paper 2000-01-1900*, 2000, doi: 10.4271/2000-01-1900.

90. Yamamoto, S., Tanaka, D., Takemura, J., Nakayama, O., et al., "Mixing Control and Combustion in Gasoline Direct Injection Engines for Reducing Cold-Start Emissions," SAE Technical Paper 2001-01-0550, 2001, doi: 10.4271/2001-01-0550.
91. Downs, D., and Theobald, F. B., "The Effect of Fuel Characteristics and Engine Operating Conditions on Pre-Ignition," Proceedings of the Institution of Mechanical Engineers: Automobile Division 1963 178: 89. DOI: 10.1243/PIME_AUTO_1963_178_016_02.
92. Hamilton, L. J., Rostedt, M. G., Caton, P. A., and Coewart, J. S., "Pre-Ignition Characteristics of Ethanol and E85 in a Spark Ignition Engine," SAE Technical Paper 2008-01-0321, 2008, doi: 10.4271/2008-01-0321.
93. Zaccardi, J.-M., Duval, L., and Pagot, A., "Development of Specific Tools for Analysis and Quantification of Pre-Ignition in a Boosted SI Engine," SAE Technical Paper 2009-01-1795, 2009, doi: 10.4271/2009-01-1795.
94. Dahnz, C., Han, H.-M., Spicher, U., Magar, M., et al., "Investigations on Pre-Ignition in Highly Supercharged SI Engines," SAE Technical Paper 2010-01-0355, 2010, doi: 10.4271/2010-01-0355.
95. Amann, M., Alger, T., and Mehta, D., "The Effect of EGR on Low-Speed Pre-Ignition in Boosted SI Engines," SAE Technical Paper 2010-01-0339, 2011, doi: 10.4271/2011-01-0339.
96. Haenel, P., Seyfried, P., Kleeberg, H., and Tomazic, D., "Systematic Approach to Analyze and Characterize Pre-Ignition Events in Turbocharged Direct-Injected

- Gasoline Engines," SAE Technical Paper 2011-01-0343, 2011, doi: 10.4271/2011-01-0343.
97. Sasaki, N., Nakata, K., Kawatake, K., Sagawa, S., et al. "The Effect of Fuel Compounds on Pre-Ignition under High Temperature and High Pressure Condition," SAE Technical Paper 2011-01-1984, 2011, doi: 10.4271/2011-01-1984.
98. Zahdeh, A., Rothenberger, P., Nguyen, W., Anbarasu, M., et al., "Fundamental Approach to Investigate Pre-Ignition in Boosted SI Engines," SAE Technical Paper 2011-01-0340, 2011, doi: 10.4271/2011-01-0340.
99. Sasaki, N., and Nakata, K., "Effect of Fuel Components on Engine Abnormal Combustion," SAE Technical Paper 2012-01-1276, 2012, doi: 10.4271/2012-01-1276.
100. Kalghatgi, G. T., and Bradley, D., "Pre-ignition and 'super-knock' in turbo-charged spark-ignition engines," International Journal of Engine Research 2012 13: 399. DOI: 10.1177/1468087411431890.
101. Computational Fluid Dynamics for Engineers, by Bengt Andersson, Ronnie Andersson, Love Håkansson, Mikael Mortensen, Rahman Sudiyo, Berend van Wachem, 2011, Cambridge University Press, 9781107018952.
102. Givler, S., Raju, M., Pomraning, E., Senecal, P. et al., "Gasoline Combustion Modeling of Direct and Port-Fuel Injected Engines using a Reduced Chemical Mechanism," SAE Technical Paper 2013-01-1098, 2013, doi:10.4271/2013-01-1098.

103. Som, S., Longman, D., Aithal, S., Bair, R. et al., "A Numerical Investigation on Scalability and Grid Convergence of Internal Combustion Engine Simulations," SAE Technical Paper 2013-01-1095, 2013, doi:10.4271/2013-01-1095.
104. Hori, T., et al., Large Eddy Simulation of Non-Evaporative and Evaporative Diesel Spray in Constant Volume Vessel by Use of KIVALES. SAE Technical Paper 2006-01-3334, 2006.
105. Yi, Y. and C.M. DeMinco, Numerical Investigation of Mixture Preparation in a GDI Engine. SAE Technical Paper 2006-01-3375, 2006.
106. John, M., et al., Numerical Prediction and Validation of Fuel Spray Behavior in a Gasoline Direct-Injection Engine. SAE Technical Paper 2001-01-3668, 2001.
107. TSI EEPS manual, TSI
108. Phantom V310 manual, Vision Research
109. Phantom V7.1 manual, Vision Research
110. HiCATT 18 manual, Lambert Instruments
111. ACTION SpectaPro 2150i manual, Princeton Instruments
112. P. Keros, "Emissions and imaging studies of spark assisted HCCI," University of Michigan, 2011.
113. Zeng, W., Idicheria, C., Fansler, T., and Drake, M., "Conditional Analysis of Enhanced Combustion Luminosity Imaging in a Spray-Guided Gasoline Engine with High Residual Fraction," SAE Technical Paper 2011-01-1281, 2011, doi:10.4271/2011-01-1281.

114. Blessinger, M., Stein, J., and Gandhi, J., "An Optical Investigation of Fuel Composition Effects in a Reactivity Controlled HSDI Engine ," SAE Int. J. Engines 5(2):516-525, 2012, doi:10.4271/2012-01-0691.
115. Senecal, P., Pomraning, E., Richards, K., Briggs, T. et al., "Multi-Dimensional Modeling of Direct-Injection Diesel Spray Liquid Length and Flame Lift-off Length using CFD and Parallel Detailed Chemistry," SAE Technical Paper 2003-01-1043, 2003, doi:10.4271/2003-01-1043.

ABSTRACT**COMBUSTION VISUALIZATION AND PARTICULATE MATTER EMISSION OF A GDI ENGINE USING GASOLINE AND E85**

by

PO-I LEE

May 2014

Advisor: Dr. Ming-Chia Lai**Major:** Mechanical Engineering**Degree:** Doctor of Philosophy

In order to increase engine efficiency as well as to reduce emission, optimizing combustion is always the challenge in research and product development. Gasoline direct injection (GDI) engines have been popularized due to its higher power density, fuel efficiency, and the possibility for advanced engine technologies over conventional port-fuel-injection (PFI) gasoline engines. However, many issues are heavily investigated, such as air-fuel mixing preparation, fuel wall-wetting, higher HC and PM emissions, catalytic convertor efficiency, knocking, and pre-ignition. Besides, advanced technologies represent higher production cost.

Because of the limited resource of petroleum-based fuels, ethanol is deemed as the alternative fuel for gasoline due to its availability, renewability, and fuel properties. It is also known for its lower energy content (LHV ~ 27 MJ/kg) that the fuel economy would decrease if such a fuel is used. Besides that, lower HC, CO, NO_x, and PM emissions may be achieved with the presence of ethanol in fuel.

The present study is focused on visualizing GDI combustion with different fuels (E0 and E85) along with engine-out emission measurement specially focusing

on PM emission. Different engine operation conditions are taken into consideration to study the effects on engine performance in terms of engine start-up, combustion quality and variation, and engine-out emission. High speed imaging techniques are used for visualizing the combustion process, and high speed emission measurement devices are used for engine-out emission study. PM emission is the primary focus in the current study on emissions with the assistance of in-cylinder visualization to identify the location of diffusion flame where the soot is formed. CFD modeling is also implemented to analyze the air-fuel mixture preparation as well as the combustion process.

The results indicate that the combustion process may not be ideal under certain operating conditions. By various image processing techniques, it is found that the flame kernel development could be either too slow or too heterogeneous. Fuel wall impingement is also found that pool fire is inevitable in some cases that HC, CO, and PM emissions are high. Injection timing, ignition timing, and air-fuel ratio are the three primary factors that need to be carefully controlled for engine calibration in order to achieve higher efficiency and lower emissions. Some advanced technologies, e.g. one-valve deactivation, may not be ideal at certain speed and load. The use of alternative fuel could reduce PM emission in mass, but the particle number could sometimes be higher than using E0. The CFD simulation also validates the similar results found from the experiments.

AUTOBIOGRAPHICAL STATEMENT

Po-I Lee was born in Taipei, Taiwan (ROC) in 1983. He obtained his Bachelor's degree in Bio-Environmental Systems Engineering from the National Taiwan University in 2005. Because of his enthusiasm of engines, he started up a motorcycle repair shop before went study abroad in 2006. He worked on a modern diesel engine in this lab in Mechanical Engineering at Wayne State University with earning his Master's degree in 2009. With his passion, he continued his research work in the Ph.D. program in 2010. His research interests, both diesel and gasoline engines, include engine combustion analysis, emission measurement, alternative fuels, optical diagnostics, spray measurement, and CFD simulation. He was invited to GM Powertrains in Pontiac, MI, for presenting the current work on June 12, 2013, and he has also worked in Chrysler Group LLC since Sept, 2013 to extend his research work on internal combustion engines and optical diagnostics.

Major publications:

- "Investigation of Ignition Energy with Visualization on a Spark Ignited Engine powered by CNG." SAE 2014-01-1331. (in press)
- "Role of Volatility in the Development of JP-8 Surrogate for Diesel Engine Application." SAE 2014-01-1389. (in press; also *SAE Int. J. Fuels Lubr. V123-4EJ*)
- "Gasoline and E85 Combustion Visualization and Particulate Matter Emission in a Production SIDi Engine with Optical Access." ASME 2013 International Combustion Engine Division Fall Technical Conference. ICEF2013-19210.
- "Direct Visualization of Combustion in an E85-Fueled DISI Engine under Various Operation Conditions." SAE 2013-01-1129.
- "CFD Simulation and Optical Engine Diagnostics of Mixture Formation Processes in DI Gasoline Engine with Flexible Valve-train." Proceedings of the FISITA 2012 World Automotive Congress, 865-877.
- "The Spray and Engine Combustion Performance of Ethanol-Biodiesel Fuel Blends." ASME 2011 International Combustion Engine Division Fall Technical Conference. ICEF2011-60073.
- "Effect of Ethanol-Biodiesel Blend Ratio on Fuel Properties and Spray Behaviors." ILASS Americas, 23rd Annual Conference on Liquid Atomization and Spray Systems. Ventura, CA. ILASS2011-158.
- "Effects of B20 Fuel and Catalyst Entrance Section Length on the Performance of Urea SCR in a Light-Duty Diesel Engine." SAE 2010-01-1173.
- "Effects of B20 on Emissions and the Performance of a Diesel Particulate Filter in a Light-Duty Diesel Engine." J. Eng. Gas Turbines Power 132(11).
- "Effects of B20 on Combustion, Emissions and Performance of a Light-Duty Diesel Engine." ASME 2009 International Combustion Engine Division Fall Technical Conference. ICEF2009-76167.
- "Impact of Biodiesel Emission Products from a Multi-Cylinder Direct Injection Diesel Engine on Particulate Filter Performance." SAE 2009-01-1184.